# Revealing the dynamics of the tumour microenvironment in Diffuse Large B Cell Lymphoma using mouse models and multiplexed imaging

Madelyn Abraham
Division of Experimental Medicine, Faculty of Medicine
McGill University
Montréal, Québec, Canada

March 2025

A thesis submitted to McGill University in partial fulfillment of the requirements of the degree of Doctor of Philosophy (Ph.D.)

# Table of Contents

## Abstract

Diffuse Large B-Cell Lymphoma (DLBCL) is the most common and aggressive subtype of Non-Hodgkin's Lymphoma (B-NHL), accounting for a significant proportion of lymphoma-related mortality. Despite advances in treatment, approximately 30-40% of DLBCL patients experience relapse or exhibit refractory disease (rrDLBCL), underscoring the critical need to better understand the mechanisms driving therapeutic resistance. This thesis used mouse modelling and multiplexed immunofluorescence imaging to explore the complex interplay between tumour cells and the tumour microenvironment (TME), focusing on how the TME contributes to the progression, immune evasion, and therapeutic resistance of DLBCL.

The first part of this work examined the TME in mouse models of cancer using advanced spatial profiling technologies. Employing highly multiplexed immunofluorescent imaging via the PhenoCycler platform, we characterized the TME in pre-clinical models of lymphoma, alongside other cancer types such as breast cancer and melanoma. This technology allowed for high-resolution mapping of immune cells, endothelial cells, and fibroblasts within tumours, revealing distinct patterns of cell-cell interactions across different cancer models. The methodology developed in this study also provided a tunable approach for the analysis of archival tissues, offering a valuable resource for understanding the TME of various cancer models.

The second part of the thesis utilized the PhenoCycler methodology on mouse and human tissues to examine a novel driver of therapeutic resistance in rrDLBCL: Signal Transducer and Activator of Transcription 6 (STAT6). In a previous study, our group identified recurrent gain-of-function $STAT6^{D419}$ mutations in rrDLBCL, and we

hypothesized that these mutations induced therapeutic resistance via modulation of the TME. To this end, we established a mouse model that recapitulates critical features of human STAT6-mutant DLBCL, including elevated phospho-STAT6 levels, increased infiltration of CD4+ T cells, and resistance to doxorubicin chemotherapy. We used this model to describe mechanistically how $STAT6^{D419}$-mutant tumour cells attract CD4+ T cells: $STAT6^{D419}$ tumour cells express significantly higher levels of the chemokine CCL17, which leads to the enhanced recruitment CCR4+ CD4+ T cells into the tumour. Functional assays further confirmed that inhibition of CCR4 using a small molecule antagonist reduced CD4+ T cell infiltration and restored doxorubicin sensitivity in $STAT6^{D419N}$ tumours. The findings were extended to human rrDLBCL samples, where we confirmed elevated CCR4+ CD4+ T cell infiltration in STAT6-mutant tumours. Overall, these results suggested that targeting the CCR4-CCL17 axis may offer a novel strategy to overcome therapeutic resistance and improve outcomes for patients with $STAT6^{D419}$ mutant rrDLBCL.

In conclusion, this thesis employed newly developed techniques in spatial biology to advance our understanding of the TME in DLBCL, with a particular focus on the STAT6 signalling axis and its impact on immune infiltration and therapeutic resistance in rrDLBCL. By leveraging mouse modelling and cutting-edge spatial biology techniques, we provided new insights into the cellular and molecular mechanisms underlying rrDLBCL, offering promising therapeutic avenues for targeting the TME to enhance treatment efficacy in relapsed and refractory cases.

**Résumé**

Le lymphome diffus à grandes cellules B (DLBCL) est le sous-type le plus courant et agressif du lymphome non hodgkinien (B-NHL) représentant une part significative de la mortalité liée aux lymphomes. Malgré les avancées thérapeutiques, environ 30 à 40 % des patients atteints de DLBCL connaissent une rechute ou présentent une maladie réfractaire (rrDLBCL), soulignant le besoin crucial de mieux comprendre les mécanismes sous-jacents à la résistance thérapeutique. Cette thèse utilise la modélisation murine et l'imagerie immunofluorescente multiplexée pour explorer les interactions complexes entre les cellules tumorales et le microenvironnement tumoral (TME), en se concentrant sur la contribution du TME à la progression, à l'évasion immunitaire et à la résistance thérapeutique du DLBCL.

La première partie de ce travail examine le TME dans des modèles murins de cancer en utilisant des technologies avancées de profilage spatial. Grâce à l'imagerie immunofluorescente multiplexée, via la plateforme PhenoCycler, nous avons caractérisé le TME dans des modèles précliniques de lymphome, ainsi que dans d'autres types de cancer tels que le cancer du sein et le mélanome. Cette technologie a permis une cartographie haute résolution des cellules immunitaires, des cellules endothéliales et des fibroblastes au sein des tumeurs, révélant des schémas distincts d'interactions cellule-cellule entre différents modèles de cancer. La méthodologie développée dans cette étude offre également une approche modulable pour l'analyse des tissus archivés, constituant une ressource précieuse pour comprendre le TME de divers modèles de cancer.

La seconde partie de la thèse a utilisé la méthodologie PhenoCycler sur des tissus murins et humains pour examiner un nouveau moteur de la résistance thérapeutique

dans le rrDLBCL: le transducteur de signal et activateur de transcription 6 (STAT6). Dans une étude précédente, notre groupe a identifié des mutations récurrentes STAT6$^{D419}$ à gain de fonction dans le rrDLBCL, et nous avons émis l'hypothèse que ces mutations induisaient une résistance thérapeutique via la modulation du TME. Pour cela, nous avons établi un modèle murin qui reproduit des caractéristiques clés du DLBCL humain avec mutation STAT6, notamment des niveaux élevés de phospho-STAT6, une infiltration accrue de cellules T CD4+ et une résistance à la chimiothérapie à base de doxorubicine. Nous avons utilisé ce modèle pour décrire de manière mécanistique comment les cellules tumorales STAT6$^{D419}$ attirent les cellules T CD4+ : les cellules tumorales STAT6$^{D419}$ expriment des niveaux significativement plus élevés de la chimiokine CCL17, entraînant un recrutement accru de cellules T CD4+ CCR4+ dans la tumeur. Des tests fonctionnels ont confirmé que l'inhibition de CCR4 à l'aide d'une molécule antagoniste réduit l'infiltration des cellules T CD4+ et rétablit la sensibilité à la doxorubicine dans les tumeurs STAT6$^{D419N}$. Ces résultats ont été étendus à des échantillons humains de rrDLBCL, où nous avons confirmé une infiltration élevée de cellules T CD4+ CCR4+ dans les tumeurs mutées STAT6$^{D419}$. Dans l'ensemble, ces résultats suggèrent que le ciblage de l'axe CCR4-CCL17 pourrait offrir une nouvelle stratégie pour surmonter la résistance thérapeutique et améliorer les résultats pour les patients atteints de rrDLBCL mutant STAT6$^{D419.}$

En conclusion, cette thèse a employé des techniques récemment développées en biologie spatiale pour approfondir notre compréhension du TME dans le DLBCL, en mettant particulièrement l'accent sur l'axe de signalisation STAT6 et son impact sur l'infiltration immunitaire et la résistance thérapeutique dans le rrDLBCL. En tirant parti de

la modélisation murine et des techniques de biologie spatiale de pointe, nous avons apporté de nouvelles connaissances sur les mécanismes cellulaires et moléculaires sous-jacents au rrDLBCL, offrant des pistes thérapeutiques prometteuses pour cibler le TME et améliorer l'efficacité des traitements dans les cas de rechute et réfractaires.

## Acknowledgements

First and foremost, I am eternally grateful to my supervisors Dr. Sonia del Rincon and Dr. Koren Mann. I originally approached them separately for a PhD position, but ending up interviewing with them together, and ultimately joined both of their labs. I suspect that the choice to join both of their teams will end up being one of the best decisions of my life. Not only was I given exciting research projects, but I was also allowed the freedom to pursue specific areas of investigation that were of interest to me and was given ample opportunities to develop my communication and leadership skills, in an environment where I was constantly supported. Sonia and Koren both have similar philosophies in how their labs are run, with teamwork as a cornerstone and a strong emphasis on scientific truth and discovery. Indeed, the backbone of their professional collaboration is based on a longstanding friendship, and this is apparent in how they work as a team. I recognize all the hard work they did to support me over the last five years: spending weekends reading my drafts and editing my figures, writing endless grants to financially support my research, and organizing collaborations to get the best of everything into my research. I truly could not have done it without them.

The support from Sonia and Koren extended to the teams they built. Christophe Goncalves and Cynthia Guilbert worked closely beside me through every element of this research, and often functioned as the angel and devil on my shoulder (they can argue amongst themselves to decide who is the angel and who is the devil!). Chris and Cyn are known throughout the LDI as people you can contact when you need to see a result. They work harder than anyone, and always know the best way to do anything. I am unbelievably lucky to have worked with them so closely. Natascha Gagnon was always up at the crack

of dawn with me, so that I could get “the hard parts” of my experiments done before everyone else arrived. Spending quiet mornings with the lab lights turned off with Nat have always been a peaceful ritual I can count on, and I am thankful not only for Nat’s technical support, but also for her friendship.

Sonia and Koren built an amazing team of graduate students and post-docs, who have become my close friends and confidantes over the years. Vrinda Gupta worked closely with me in 2022 and was instrumental in the publishing of the work in Chapter 2. Thankfully, she returned to the LDI in 2024, and I again have been able to benefit from her warmth, humour, and top-notch organizational skills. Dr. Sam Preston and Dr. Fan Huang graduated from the McGill Experimental Medicine PhD program in 2023 and 2022, but have remained my close friends, and are the first people I contact when I need an extra set of eyes on my data. I am also thankful to other past and present members of the del Rincon and Mann labs, including Dr. Margarita Bartish, Raul Ernesto Flores Gonzalez, Hsaing Chou, Feiyang Cai, Mengqi Li, Theodore Papadapoulos, Paige McCallum, Rowa Bakadlag, Nivetha Subramaniam, Braeden Giles, Harinee Srikanna, and Nazli Zengin. I am truly blessed to have worked with all of them, and to have benefitted from their brilliant minds.

I am thankful to the close collaborators and committee members who guided all elements of this thesis work: Dr. Nathalie Johnson, Dr. Wilson H. Miller Jr., Dr. Francois Mercier, and Dr. Kostas Pantopoulos. Each of these senior scientists has given me invaluable advice, and their influence is apparent in many of the experiments that were performed.

Much of my thesis work included mouse studies, and I am thankful to those who trained me in the specialized procedures I used and kept a close eye on my mice while I was away doing other experiments: Veronique Michaud, Yvhans Chery, Darlene Element, and Sam Sumayo. I also extend my thanks to Christian Young, for training and guidance in flow cytometry.

A PhD is a marathon and not a sprint, and I extend my thanks to my friends and family for their patience and support while I worked long hours far from home. My sister and brother, Meagan and Callum Abraham, spent endless hours on the phone with me, and kept me sane and connected. Despite not working in science or research, they both made sincere efforts to understand my work, and I am truly thankful for that. My mother, Kelly Lowther, and her partner, Gary Thoms, often made the long drive to visit me in Montreal, even bringing my grandfather, Ron Lowther, to visit. My father, Scott Abraham, and his wife, Sarah Sones, were always sending food and clothes, to help keep my engine running. My grandmother, Laura Abraham, provided support in a million different ways, and always kept me laughing. I also thank and remember family members who are dear to me, but are no longer here: my grandfather Thomas Abraham, who passed away the day before I moved to Montreal to begin my PhD, but spent his career as a chemist and would have been the proudest to see me finish; and my grandmother, Betty Lowther, who passed away during the COVID-19 pandemic.

Finally, to my partner Oren: the person who taught me it was okay to quit when nothing was working and supported me while I forged ahead when everything was. I am so thankful for all he has done for me and am unwilling to imagine how I could have done it without him. Thank you truly.

## Publications Arising from this Work

Chapters 1 and 4 contain material pertaining to STAT6 modulation of the tumour microenvironment, published as an original research article (* = as co-first author):

> A Benoit*, **MJ Abraham***, S Li, J Kim, R Estrada-Tejedor, R Bakadlag, N Subramaniam, K Makhani, C Guilbert, R Tu, M Salaciak, KO Klein, KM Coyle, LK Hilton, R Santiago, S Dmitirenko, S Assouline, RD Morin, SV del Rincon, NA Johnson, & KK Mann. STAT6 Mutations Enriched at Diffuse Large B-cell Lymphoma Relapse Reshape the Tumour Microenvironment. **International Journal of Hematology. 2024.** doi: 10.1007/s12185-023-03692-x; PubMed PMID 38285120

Chapter 2 was published as an original research methodology article:

> **MJ Abraham**, C Goncalves, P McCallum, V Gupta, H Chou, N Gagnon, SEJ Preston, F Huang, NA Johnson, WH Miller, KK Mann, & SV del Rincon. Tunable PhenoCycler Imaging of the Murine Pre-Clinical Tumour Microenvironments. **Cell and Bioscience. 2024.** doi: 10.1186/s13578-024-01199-4; PubMed PMID 38311785.

Chapter 3 is available online as a preprint:

> **MJ Abraham**, C Guilbert, N Gagnon, C Goncalves, A Benoit, R Rys, SEJ Preston, RD Morin, WH Miller Jr., NA Johnson, SV del Rincon, & KK Mann. The CCL17-CCR4 Axis is Critical for Mutant STAT6-Mediated Microenvironmental Remodelling and Therapeutic Resistance in Relapsed and Refractory Diffuse Large B Cell Lymphoma. **BioRxiv. 2024.** doi: 10.1101/2024.12.13.628396.

Publications that include work performed by the candidate, but not included in the presentation of this thesis (* = as co-first author):

> M Bartish*, **MJ Abraham***, C Goncalves, O Larsson, C Rolny, & SV del Rincon. The role of eIF4F-driven mRNA translation in regulating the tumor microenvironment. **Nature Reviews Cancer. 2023.** doi: 10.1038/s41568-023-00567-5; PubMed PMID 37142795.
>
> SEJ Preston, A Edmond, F Pettersson, D Dupere-Richer, **MJ Abraham**, A Riva, M Kinal, R Rys, NA Jonhson, KK Mann, SV del Rincon, JD Licht, & WH Miller. Acquired resistance to EZH2 inhibitor GSK343 promotes the differentiation of human DLBCL cell lines towards an ABC-like phenotype. **Molecular Cancer Therapeutics. 2022.** doi: 10.1158/1535-7163.MCT-21-0216; PubMed PMID 35086959.

## Contribution to Original Knowledge

DLBCL is the most commonly diagnosed lymphoid malignancy in adults. Numerous studies have taken genomic approaches to understand the heterogeneity of this disease, but this has not resulted in a change to the standard of care, as all patients receive the same therapy, R-CHOP. In this thesis of work, the TME is studied as another layer of DLBCL disease heterogeneity, with the overarching goal of identifying treatment modalities that could improve outcomes for a subset of patients. Specifically, this thesis used highly multiplexed immunofluorescence imaging and mouse models to uncover a novel therapeutic strategy for patients with rrDLBCL that have mutations in the gene *STAT6*. Indeed, we found that the TME can be therapeutically targeted in *STAT6*-mutant rrDLBCL, to restore sensitivity to chemotherapy.

- In Chapter 2, we utilized mouse models of lymphoma for multiplexed immunofluorescent imaging, with the PhenoCycler-Fusion platform, to determine the constitution and cellular organization of the murine lymphoma TME.
- In this publication, we were the first to report PhenoCycler imaging for murine FFPE tissues. This manuscript represented a major effort to identify and optimize antibody clones that stain various murine FFPE tissues with high fidelity. Following the publication of this work, many research groups have requested collaborations to perform similar experiments on their own experimental tissues.
- In Chapter 3, we developed and described a mouse model of $STAT6^{D419N}$-mutant DLBCL. The development of this mouse model allowed us to ask detailed

questions regarding the mechanism of therapeutic resistance in STAT6$^{D419}$-mutant rrDLBCL and allowed us to screen a novel therapeutic target: CCR4.

- The work performed in Chapter 3 allowed us to suggest the FDA-approved monoclonal antibody Mogamulizumab for the treatment of STAT6$^{D419}$-mutant rrDLBCL.
- In Chapter 3, we were the first team to spatially characterize the TME of rrDLBCL, using biopsies tissues from patients. This data will be analyzed for other experimental questions of interest, especially pertaining to TME-mediated mechanisms of resistance to therapy.

## Contribution of Authors

**Chapter 1**
Madelyn Abraham: Literature review, Writing, Editing, Generation of Schematics and Tables
Koren K. Mann: Editing
Sonia V. del Rincon: Editing

**Chapter 2**
Madelyn Abraham: Conceptualization, Methodology, Formal Analysis, Investigation, Writing – Original Draft, Writing - Review & Editing, Visualization, Project Administration
Christophe Goncalves: Formal Analysis, Software
Paige McCallum: Software
Vrinda Gupta: Investigation
Samuel E. J. Preston: Animal modelling (breast cancer), Writing - Review & Editing
Fan Huang: Animal modelling (melanoma), Writing - Review & Editing
Hsiang Chou: Investigation
Natascha Gagnon: Animal modelling
Nathalie A. Johnson: Supervision, Writing - Review & Editing
Wilson H. Miller Jr.: Study supervision, Funding Acquisition, Writing - Review & Editing
Koren K. Mann: Study supervision, Conceptualization, Funding Acquisition, Writing - Review & Editing
Sonia V. del Rincon: Study supervision, Conceptualization, Funding Acquisition, Writing - Review & Editing

**Chapter 3**
Madelyn Abraham: Conceptualization, Methodology, Formal Analysis, Investigation, Writing – Original Draft, Writing - Review & Editing, Visualization, Project Administration
Cynthia Guilbert: Investigation
Natascha Gagnon: Investigation
Christophe Goncalves: Software, Visualization
Alexandre Benoit: Investigation, Resources
Ryan Rys: Data Curation
Samuel E. J. Preston: Formal Analysis
Ryan D. Morin: Resources
Nathalie A. Johnson: Resources, Data Curation, Writing - Review & Editing, Supervision
Sonia V. del Rincon: Resources, Writing - Review & Editing, Supervision
Koren K. Mann: Conceptualization, Resources, Writing - Review & Editing, Supervision, Funding Acquisition

**Chapter 4**
Madelyn Abraham: Literature review, Writing, Editing, Generation of Schematics and Tables
Koren K. Mann: Editing
Sonia V. del Rincon: Editing

## List of Figures

## List of Tables

## List of Abbreviations

| | |
|---|---|
| ABC | Activated B cell-like |
| AID | Activation-Induced Cytidine Deaminase |
| ANN | Artificial Neural Networks |
| APC | Antigen-presenting cell |
| BCR | B cell Receptor |
| B-NHL | B cell Non-Hodgkin's Lymphoma |
| CAR-T | Chimeric-Antigen Receptor T Cells |
| CCR4 | C-C Chemokine Receptor Type 4 |
| cHL | Classical Hodgkin's Lymphoma |
| cLN | Cervical Lymph Node |
| CODEX | Co-Detection by Indexing |
| COO | Cell of Origin |
| CTCL | Cutaneous T Cell Lymphoma |
| DC | Dendritic Cell |
| DLBCL | Diffuse Large B Cell Lymphoma |
| DNA | Deoxyribonucleic Acid |
| ECM | Extracellular Matrix |
| FBS | Fetal Bovine Serum |
| FDC | Follicular Dendritic Cell |
| FFPE | Formalin-Fixed Paraffin-Embedded |
| FL | Follicular Lymphoma |
| GC | Germinal Center |
| GCB | Germinal Center B cell-like |
| GEMM | Genetically Engineered Mouse Model |
| GOF | Gain-of-Function |
| GSEA | Gene Set Enrichment Analysis |
| ICI | Immune Checkpoint Inhibitor |
| IF | Immunofluorescence |
| IHC | Immunohistochemistry |
| iLN | Inguinal Lymph Node |
| IL-4 | Interleukin 4 |
| IL-4R | Interleukin 4 Receptor |
| IL-13 | Interleukin 13 |
| IL-13R | Interleukin 13 Receptor |
| IMC | Imaging Mass Cytometry |
| LOF | Loss-of-Function |
| MALT | Mucosa-Associated Lymphoid Tissue |
| MEF | Mouse Embryonic Fibroblasts |
| MHC | Major Histocompatibility Complex |
| MIBI | Multiplexed Ion Beam Imaging |
| NK | Natural Killer |
| OS | Overall Survival |
| PBMC | Peripheral Blood Mononuclear Cell |
| PFA | Paraformaldehyde |

| | |
|---|---|
| PBS | Phosphate Buffered Saline |
| PDX | Patient-Derived Xenograft |
| PFS | Progression Free Survival |
| PMBCL | Primary Mediastinal B Cell Lymphoma |
| R-CHOP | Rituximab, Cyclophosphamide, doxorubicin Hydrochloride (Hydroxydaunorubicin), vincristine (Oncovin), Prednisone |
| rrDLBCL | Relapsed and Refractory Diffuse Large B Cell Lymphoma |
| scRNAseq | Single Cell RNA Sequencing |
| SLO | Secondary Lymphoid Organ |
| STAT6 | Signal Transducer and Activator of Transcription 6 |
| SNR | Signal to Noise Ratio |
| TAD | Transactivation Domain |
| TBS | Tris Buffered Saline |
| Tfh | T Follicular Helper Cell |
| Th1 | T Helper Cell, Type 1 |
| Th2 | T Helper Cell, Type 2 |
| TIL | Tumour Infiltrating T Cell/ Lymphocyte |
| TME | Tumour Microenvironment |
| Treg | Regulatory T Cell |
| VDJ | Variable, diversity, and joining |
| WES | Whole Exome Sequencing |

# Chapter 1: Introduction and Literature Review

## 1.1 Preface

Lymphoma is a disease arising from the uncontrolled proliferation of either T or B lymphocytes. When involving B lymphocytes, lymphoma is classified as Hodgkin's (cHL) or Non-Hodgkin's Lymphoma (B-NHL). cHL is among the most curable cancers, with a five-year survival rate of 85% (1). B-NHL, on the other hand, is 6.5 times more prevalent than cHL (2), and its most common subtype, Diffuse Large B Cell Lymphoma (DLBCL), is much more aggressive. In 2024, it is estimated that 11700 Canadians will be diagnosed with DLBCL, and of those, 3100 will die from their disease (1). Moreover, while other common cancer types are decreasing in incidence and mortality rates, DLBCL incidence and mortality are projected to increase. These humbling statistics serve to emphasize the importance of studying DLBCL, to better improve patient outcomes.

In this body of work, DLBCL is studied using mouse modelling. In particular, this research considers how the non-malignant components of the tumour, the so-called Tumour Microenvironment (TME), can support DLBCL growth and therapeutic resistance. Moreover, the research methodology takes advantage of recent developments in spatial tumour profiling, which employs oligonucleotide-conjugated antibodies for highly multiplexed immunofluorescent tumour imaging of proteins within the TME of both mouse and human tissues.

## 1.2 B Cells

### *1.2.1 B Cell Maturation*

To understand how lymphoma develops, one must first understand the unique features of B cells that render them susceptible to malignant transformation. In normal physiology, B cells contribute to the humoral and adaptive immune responses by maturing following activation by an antigen into antibody-producing plasma cells or into long-lived memory B cells. However, they must first undergo maturation in the bone marrow, where they originate from hematopoietic stem cells (HSCs). The maturation steps that they undergo will ensure that each B cell in circulation will express a unique and functional B cell receptor (BCR) that is not reactive to self-antigens. B cell maturation consists of a series of tightly regulated developmental steps, where cells transition linearly between pro-B cell, pre-B cell, immature B cell, and mature naïve B cell states (3, 4).

In the pro-B cell state, B cells rearrange their immunoglobulin heavy chain (IgH) through a process known as Variable, Diversity and Joining (VDJ) recombination to create a unique antigen-binding sequence. VDJ recombination involves the random recombination of IgH variable (V), diversity (D), and joining (J) gene segments, leading to transcription and translation of a functional μ heavy chain, which will form part of the pre-BCR to be expressed on the cell surface (5). Once the pre-BCR is expressed, B cells are now in the pre-B cell state, which is characterized by light chain (IgL or IgK) recombination, including recombination of the V and J segments (6). The new recombinant sequence is then also transcribed and translated to produce a K or L light chain protein that is combined with the recombinant heavy chain and is expressed on the cell surface, as a complete BCR. Of note, the BCR not only consists of the surface-bound

recombinant heavy and light chain Ig proteins, but also includes the heterodimeric CD79A/ CD79B signaling unit. CD79A/B is critical for downstream tonic and antigen dependent survival signals.

Once the recombinant BCR is expressed, the B cell is at the immature B cell phase, whereby the BCR will be tested for self-reactivity through negative selection. If the BCR strongly recognizes self-antigen, the B cell will undergo apoptosis, as a mechanism to decrease autoimmunity. Mature naïve B cells that survive negative selection will exit the bone marrow, circulate through the blood, and home to the secondary lymphoid organs (SLOs), including the spleen, lymph nodes, tonsil, and mucosa-associated lymphoid tissue (MALT).

### *1.2.2 The Germinal Center Reaction*

When B cells in SLOs encounter antigen, they become activated and begin to transition through the germinal center (GC) reaction. Activation occurs through antigen binding to the mature BCR, leading to B cell antigen processing and presentation via Major Histocompatibility Complex II (MHCII) molecules (7, 8). Antigen-presenting B cells will be able to interact with T follicular helper (Tfh) cells to receive “help” signals that allow them to migrate to the follicular area of the SLO (8, 9), and form the GC. The GC consists of two distinct zones: the dark zone and the light zone. In the dark zone, B cells are termed “centroblasts”, rapidly divide, and undergo somatic hypermutation, which will introduce mutations into the Ig gene variable regions. This leads to the development of a pool of B cells with diverse affinities for the antigen (10). Following somatic hypermutation, centroblasts will migrate to the light zone, where they will now be termed “centrocytes”, and cell division will halt (11).

To best ensure the B cells with the highest and most specific affinity for antigen will continue to mature into memory B cells and plasma cells, centrocytes in the light zone undergo affinity maturation. In affinity maturation, follicular dendritic cells (FDCs) in the light zone present antigen to the newly mutated centrocytes. Only the centrocytes with high-affinity antibodies are able to bind the antigen, and will be able to receive survival signals from Tfh cells (12), through receptors termed CD40, ICOS, and PD-L1 on the centrocyte binding to CD40L, ICOSL, and PD-1 on the Tfh cell (13). The centrocytes that are not selected will undergo apoptosis (14).

Tfh cells also secrete cytokines that induce centrocytes to undergo class switch recombination, which is the process that allows B cells to produce different antibody classes (15). TGF-β secreted by Tfh cells will induce class switch to IgA or IgG2, IL-4 will induce class switch to IgE or IgG1, and IFN-γ will induce class switch to IgG2a (16). Each of these classes are adapted to respond to different types of pathogens, thus allowing the humoral immune system to respond to infection in a highly specific fashion.

After successful selection and class switch, high-affinity B cells differentiate into plasma cells, which function to produce antibodies, or into memory B cells, which provide long-term immunity and can quickly respond to future encounters with the same antigen (**Figure 1.1**). Indeed, the diversity and affinity of antibodies that are generated in response to immune challenge is dependent on the fidelity of the GC reaction, which is controlled by the coordination of several transcription factors, including NF-κB, IRF4, BCL6, BLIMP1, and Myc (17), and intracellular signaling pathways, including PI3K/ AKT, MAPK, and JAK/ STAT pathways (18-20).

Critically, GC B cells are unique, as the features described above are reminiscent of the some of the canonical hallmarks of cancer (21), including phenotypic plasticity, genomic instability, resistance to DNA damage, and extended replicative potential (22). When malignant transformation occurs, lymphoma cells derived from GC B cells retain many of these phenotypes, as will be discussed below.

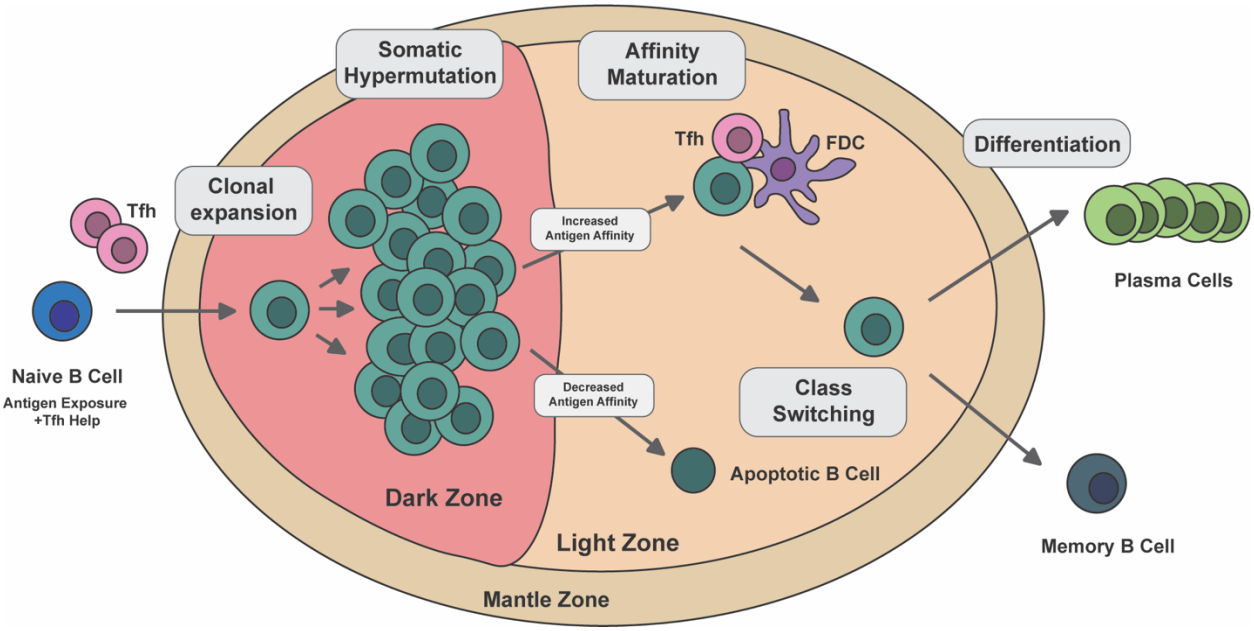


**Figure 1.1 The Germinal Center Reaction.** (Adapted from De Silva & Klein, 2015 (23)) Once naive B cells in SLOs encounter antigen, they will enter the GC reaction, which functions to generate B cells with high antigen affinity that can differentiate into plasma cells or long-lasting memory B cells.

## 1.3 Diffuse Large B Cell Lymphoma

### *1.3.1 Malignant Transformation*

For successful somatic mutation and affinity maturation to occur, GC B cells attenuate cell proliferation and DNA damage checkpoints (24). This renders them particularly susceptible to malignant transformation, and DLBCL, and other similar

aggressive and indolent lymphomas, arise from B cells transiting through the GC reaction (22). Indeed, the mutations that present in lymphoma cells are often reflective of the stage of the GC reaction where the mutation was acquired.

As a further matter, GC B cells are prone to mutation. In the dark zone, somatic hypermutation is achieved via expression of 1) activation-induced cytidine deaminase (AID), and 2) the error-prone DNA polymerase eta (Polη) (25, 26). AID targets the V region of the Ig heavy and light chain and introduces single strand breaks into DNA by converting cytosine to uracil. When repairing AID-induced damage, Polη will introduce point-mutations, leading to the generation of new B cell antibody clones. While this process is a necessary feature of the humoral immune response, off-target mutations can occur. Both gain-of-function (GOF) and loss-of-function (LOF) mutations in non-Ig genes can engender B cells with selective survival advantages that evolve to malignancy.

For instance, in the GC reaction, expression of the transcriptional repressor BCL6 is critical for downregulating expression of cell cycle checkpoint genes (including *CDKN1A* and *CDKN1B (27)*) and genes involved in the DNA damage response pathway (including *TP53 (28)*). Repression of these genes allows dark zone B cells to bypass survival checkpoints as they undergo somatic hypermutation (29). Concordantly, GOF *BCL6* mutations are recurrent in B cell lymphomas, and drive tumour cell proliferation and survival. Interestingly, BCL6 also plays a role in the light zone, through silencing gene expression of the anti-apoptotic protein BCL2. This repression poises GC B cells to undergo apoptosis if they are not selected during affinity maturation. However, in lymphoma, *BCL2* translocations bypass this repression, by driving *BCL2* expression

through alternative enhancers and promoters, leading to tumour cell resistance to apoptosis.

Moreover, in the light zone, GC B cells require interactions with FDCs and Tfh cells (the so-called “immune synapse”) for survival signals through their BCR, allowing them to avoid apoptosis and exit the GC reaction for further differentiation (30). In lymphoma cells, the requirement for survival signals from the immune synapse can be evaded through genetic lesions that enable T cell-independent B cell survival (ie. LOF mutation of *B2M* or *MHCII*) or cause constitutive BCR activation (ie. GOF mutation of *CD79B*). In **Table 1.1**, additional examples of genes that are recurrently mutated in DLBCL and their normal function in the GC are listed (non-exhaustive).

**Table 1.1 Recurrent Mutations in DLBCL and Association with Germinal Center Function** (Adapted from Mlynarczyk et al. 2019 (22))

| Gene | Normal Function | In DLBCL |
|---|---|---|
| Gain of Function Mutations or Gene Amplifications/ Translocations | | |
| *BCL2* | Restrict apoptosis in the light zone | Restrict apoptosis in tumour cells |
| *BCL6* | Resistance to apoptosis, DNA-damage tolerance, cell cycle progression | Survival, proliferation, differentiation blockade, DNA damage |
| *CARD11* | GC initiation and B cell activation | Survival |
| *CCND3* | Cell expansion in the dark zone | Proliferation |
| *CD79A/B* | B cell activation | Survival |
| *EZH2* | GC formation and repression of cell proliferation checkpoints | Differentiation blockade, proliferation |
| *FOXO1* | Transcription factor for dark zone gene expression | Survival and proliferation |
| *MYC* | GC entry | Cell growth |
| *MYD88* | B cell activation | Survival |
| *NFKBIZ* | B cell activation | Survival |
| *PD-L1* | Mediates interaction with Tfh cells | Immune escape |

| | | |
|---|---|---|
| *STAT6* | GC entry and maintenance, class switch recombination | Cell survival, resistance to apoptosis, immune escape |
| *TCF3* | Transcription factor for dark zone gene expression | Survival and proliferation |
| Loss of Function Mutations | | |
| *B2M* | MHC-I expression on cell surface | Immune escape |
| *CIITA* | MHC-II expression on cell surface | Immune escape |
| *CREBBP* | GC exit | Differentiation blockade, proliferation, immune escape |
| *EP300* | GC exit | Differentiation blockade, immune escape |
| *GNA13* | GC maintenance | Dissemination of lymphoma outside of the GC |
| *KMT2D* | GC exit, plasma cell differentiation | Differentiation blockade, cell survival |
| *TMEM30A* | BCR expression | Survival signaling, immune escape |
| *PRDM1* | Plasma cell differentiation | Differentiation blockade |
| *TNFSRF14* | Mediates interaction with Tfh cells, to restrict B cell expansion | Activation of BCR signaling |
| *TP53* | DNA damage checkpoint | Genomic instability |

### *1.3.2 Diagnosis, Staging, and Treatment of DLBCL*

Once malignant transformation occurs, patients may present to their doctor with complaints of fatigue, weight loss, fever, night sweats, and/ or swollen lymph nodes. To diagnose DLBCL from these non-specific symptoms, a biopsy of the affected lymph node is required. Histopathological examination will confirm the presence of large, atypical B cells (31). Moreover, a PET-CT scan will be used to identify other organs with disease involvement (32), which is critical for disease staging (33). Based on the Ann Arbor and Lugano staging systems, Stage I DLBCL has disease involvement of a single lymph node region or single lymphoid structure, Stage II DLBCL involves two or more lymph node regions/ lymphoid structures on the same side of the diaphragm, Stage III DLBCL involves two or more lymph node regions/ structures on both sides of the diaphragm, and Stage IV DLBCL has additional extranodal involvement (34).

Regardless of disease stage at diagnosis, the standard of care therapy for newly diagnosed DLBCL is the poly-chemoimmunotherapy R-CHOP, which consists of 8 cycles of Rituximab, Cyclophosphamide, doxorubicin Hydrochloride, Oncovin (Vincristine), and Prednisone. The CHOP components in R-CHOP include standard chemotherapy agents designed to kill rapidly dividing cells by interfering with DNA synthesis and cellular replication. Cyclophosphamide, an alkylating agent, damages DNA, preventing cancer cell division; Doxorubicin, an anthracycline, intercalates DNA and inhibits topoisomerase II, causing DNA strand breaks; Vincristine, a vinca alkaloid, disrupts microtubule formation, halting mitosis; and Prednisone, a corticosteroid, reduces inflammation and can induce cell death in certain lymphoma cells. Rituximab is a monoclonal antibody specifically targeting CD20, an antigen on the surface of B cells, which promotes immune-mediated killing of both malignant lymphoma cells and normal B cells. This regimen is very effective, and with R-CHOP, more than 60% of patients will be cured. There have been attempts to improve clinical outcomes by intensifying R-CHOP, through increased dose concentration (R-megaCHOEP, (35)) or decreased time between treatment cycles (R-CHOP-14, (36)). However, these strategies increased toxicity and did not impart a survival benefit.

Recent clinical trials have also explored other therapies that might be used in the frontline setting for DLBCL. For instance, given that recurrent GOF mutations in CD79A/B are found in DLBCL, the POLARIX study evaluated the use of the CD79B-directed antibody-drug conjugate polatuzumab vedotin in the place of vincristine in R-CHOP (37). This therapy, termed pola-R-CHP, led to a modest improvement in progression free survival (PFS; 76.7% patients without progression for pola-R-CHP vs 70.2% in R-CHOP

treated), but did not impact overall survival (OS). Another less successful attempt to target BCR-signaling was in the PHOENIX trial, which used the BTK inhibitor ibrutinib in combination with R-CHOP. Ibrutinib + R-CHOP had favourable outcomes in patients younger than 60 years of age, but in patients older than 60, ibrutinib + R-CHOP worsened OS and PFS, and resulted in an increase in serious adverse events (38). Beyond BCR-signaling, apoptosis pathways have also been targeted in clinical trials. In the CAVALLI study, the BCL2 inhibitor venetoclax was tested in combination with R-CHOP for newly diagnosed DLBCL showing BCL2 positivity (39). Venetoclax + R-CHOP showed a modest improvement in OS and PFS, but also showed increased toxicity and incidence of adverse events. To date, none of these therapies have been widely adopted for the treatment of DLBCL.

### *1.3.3 Relapsed and Refractory DLBCL*

While most DLBCL patients respond to R-CHOP, approximately 10-15% of patients will be refractory to treatment, and another 20-25% will experience relapse within 24 months of treatment. In the scenario of relapsed and refractory DLBCL (rrDLBCL), many different treatment paradigms have been tested. Prior to 2024, the standard of care for rrDLBCL was salvage chemotherapy, usually consisting of gemcitabine, cisplatin, and dexamethasone (40), followed by autologous stem cell transplant (**Figure 1.2A**; ASCT). Despite this aggressive treatment, two year OS for rrDLBCL patients is often reported to be less than 20% (41). However, the approval of chimeric antigen T cell receptor (CAR-T) therapy has vastly improved projected outcomes for rrDLBCL patients, with up to 46% of patients showing a complete response (42). CAR-T therapy is a type of personalized immunotherapy, that involves genetically modifying a patient's T cells to express chimeric

antigen receptors that specifically target cancer cells (**Figure 1.2B**). In the case of DLBCL, CAR-T cells are targeted to the B cell marker CD19. The ZUMA-7 and TRANSFORM clinical trials demonstrated that CAR-T has improved efficacy compared to salvage chemotherapy and ASCT (43, 44), and vastly improved the outcome for patients with rrDLBCL, becoming the new standard of care for second-line treatment of DLBCL.

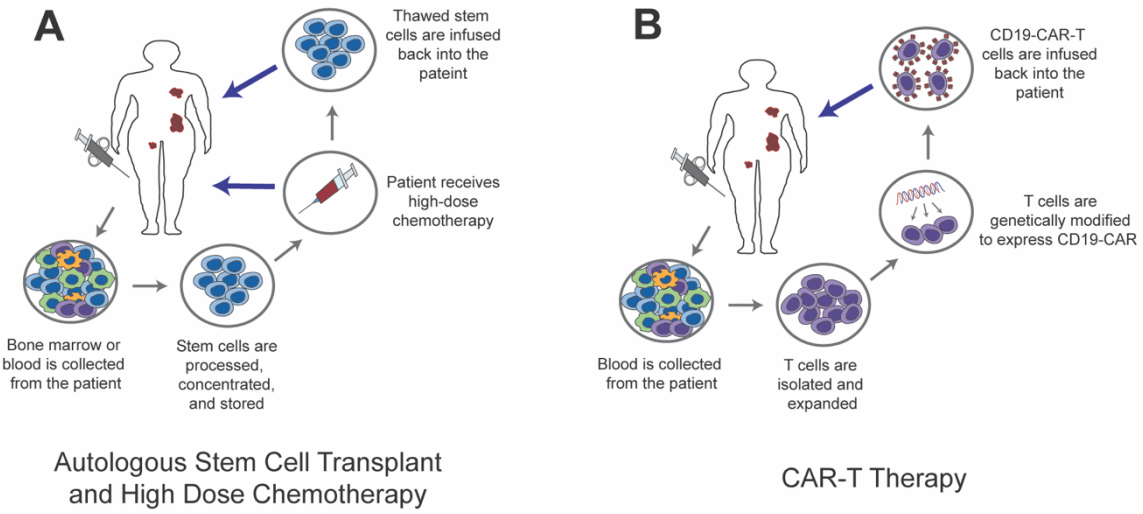


**Figure 1.2 Treatment Strategies for rrDLBCL. A.** Schematic showing ASCT and high dose chemotherapy. Stem cells are collected from the blood or bone marrow of patients and are stored while the patient receives high dose chemotherapy. Following chemotherapy, stem cells are infused back into the patient. **B.** Schematic showing CAR-T therapy. T cells are collected from the blood of patients and are genetically modified *ex vivo* to express a CAR directed to CD19. The CAR-T cells are then infused back into the patient. *Figure made with Adobe Illustrator.*

Despite the successes of CAR-T, the biology of rrDLBCL is still relatively understudied compared to diagnostic DLBCL, and the factors which influence therapeutic resistance are poorly understood. This is typically attributed to a paucity of tissue and biopsy samples collected at DLBCL relapse available to study. Regardless, using the available materials, several studies have taken a genomic approach to identify mutations

that are enriched at relapse. These studies aimed to determine if there are gene mutations that predict response to R-CHOP, or if any gene mutations emerge at DLBCL relapse that could represent sub-dominant clones that expand under the select pressure of chemotherapy.

To this end, a series of four unrelated studies performed whole exome sequencing (WES) on diagnostic and relapse DLBCL samples, with the aim of identifying gene mutations that could form the basis for therapeutic resistance (45-48). Critically, the sample size in each of the studies was low to moderate, ranging from 6 patients to 47 patients, with only a subset of those being matched with diagnostic samples to track clonal evolution of mutations. Within these studies, Morin et al. identified mutations in *TP53, CCND3, KMT2C, FOXO1, NFKBIZ,* and *STAT6* as enriched at relapse compared to diagnosis, while Mareschal et al. additionally identified mutations in *IRF4, REL, CDKN2A* and *HYAL2*, and Park et al. identified mutations *MYD88, B2M, SORCS3,* and *WDFY3*. While Greenawald et al. reported that several mutations are increased in prevalence at relapse, including *BCL2* and *CREBBP*, they were also the first to report mutations that decreased in prevalence at relapse: in the genes *CARD11, PIM1,* and *CD79B*. Of these mutated genes, additional studies on *TP53 (49), FOXO1 (50) , NFKBIZ (51),* and *STAT6 (52)* have begun to model how mutations affect protein structure and function, to change cellular dynamics and confer a growth advantage to rrDLBCL cells. However, no studies to date have posited potential treatment paradigms for when mutations in any of these genes are identified at relapse.

With the advent of liquid biopsy to perform genetic profiling of tumours non-invasively (53), the potential pool of rrDLBCL samples for characterization expanded.

Indeed, Rushton et al. took advantage of circulating tumour DNA (ctDNA), to explore the mutational spectrum of 135 rrDLBCL samples, compared with a "meta-cohort" of 1670 diagnostic DLBCLs (54). In their dataset, 6 genes were recurrently mutated at relapse: *TP53, KMT2D, CREBBP, FOXO1, NFKBIE,* and *MS4A1*. Mutations in *MS4A1*, which encodes CD20 (the B cell marker and target of Rituximab), were predominantly truncating, resulting in CD20 expression loss, or missense mutations in the transmembrane domain that inhibited the binding of Rituximab or other CD20-targeted antibodies. Outside of the context of relapse, *MS4A1* mutations are exceedingly rare, and therefore represent the emergence of Rituximab-resistance clones at relapse. Rushton et al. also found that mutations in *TP53* and *KMT2D* were present in the majority of rrDLBCLs, but upon analysis of paired diagnostic and relapse samples, it was revealed that these mutations are "clonally stable", meaning that they are also present at diagnosis. Thus, *TP53* and *KMT2D* may be implicated in R-CHOP resistance and could be utilized to identify patients at high-risk for failure of frontline therapy.

### *1.3.4 Subtyping of DLBCL*

There are approximately 150 genes that are recurrently mutated in DLBCL, defined as occurring in >5% of patients (55). To this end, DLBCL is an incredibly heterogenous disease, and substantial research efforts have aimed to subtype DLBCL into groups that differ in prognosis or therapeutic vulnerability.

The first widely adopted subclassification of DLBCL used gene expression profiling to distinguish two subtypes of DLBCL based on cell of origin (COO): germinal center B cell-like (GCB) and activated B cell-like (ABC). GCB-DLBCL tumours tend to express genes that are commonly expressed in GC B cells, while ABC-DLBCL tumours express genes

associated with chronic BCR signaling (including NF-κB activation) (56). Clinically, these subtypes can be distinguished using the Hans algorithm, which utilizes immunohistochemical (IHC) staining for CD10, BCL6, and MUM1, to classify patients as GCB or NON-GCB DLBCL (57). A 2009 update to the Hans algorithm further demonstrated that the additional evaluation of GCET1 and FOXP1 by IHC can discriminate more clearly between GCB and ABC-DLBCL (58). While this classification has been extremely helpful in identifying targeted therapies that might be effective in specific patients, especially since ABC-DLBCL has inferior PFS to GCB-DLBCL, approximately 10-15% of cases cannot be classified with this binary.

More recent attempts to subclassify DLBCL have examined gene mutations with the shared underlying hypothesis that the combinations of mutations that drive individual cases of DLBCL are predictive of therapeutic vulnerability. In April of 2018, both Chapuy et al. and Schmitz et al. published their work in this regard. Chapuy et al. performed WES to identify the structural variants, copy number alterations, and single nucleotide variants that were present in 304 DLBCL tumours. They then used a consensus clustering method to define the common drivers of DLBCL, leading to identification of five genetic signatures of DLBCL (59), termed Cluster 1 (C1) through Cluster 5 (C5; **Figure 1.3**).

C1 tumours frequently showed *BCL6* structural variants, mutations in *NOTCH2* and its negative regulator *SPEN*, mutations in members of the NF-κB signaling pathway, and inactivating mutations that could confer immune escape (ie. *B2M, PDL1, PDL2*). The majority of C1 tumours were classified as ABC-DLBCL. C2 DLBCLs were characterized by bi-allelic inactivation of *TP53* via mutations and chromosome *17p* copy loss, and C2 consisted of both ABC and GCB-DLBCL. C3 DLBCLs exhibited *BCL2* structural variants,

in addition to mutations in epigenetic and chromatin modification genes, such as *KMT2D, CREBBP,* and *EZH2.* C4 DLBCLs were similar to C3 DLBCLs, as they are both primarily GCB-DLBCLs, and have mutations in genes that code for proteins with epigenetic function. However, while C3 DLBCLs primarily show alterations in chromatin modifying proteins, C4 DLBCLs have frequent mutations in histone-associated genes. C4 DLBCLs also have mutations in BCR/ PI3K signalling intermediates, and mutations in genes within the RAS/ JAK/ STAT pathway. The final cluster by Chapuy et al, C5, was another ABC-DLBCL cluster, defined by mutations in *MYD88* and *CD79B*, and by *18q* chromosomal gain, leading to increased BCL2 expression.

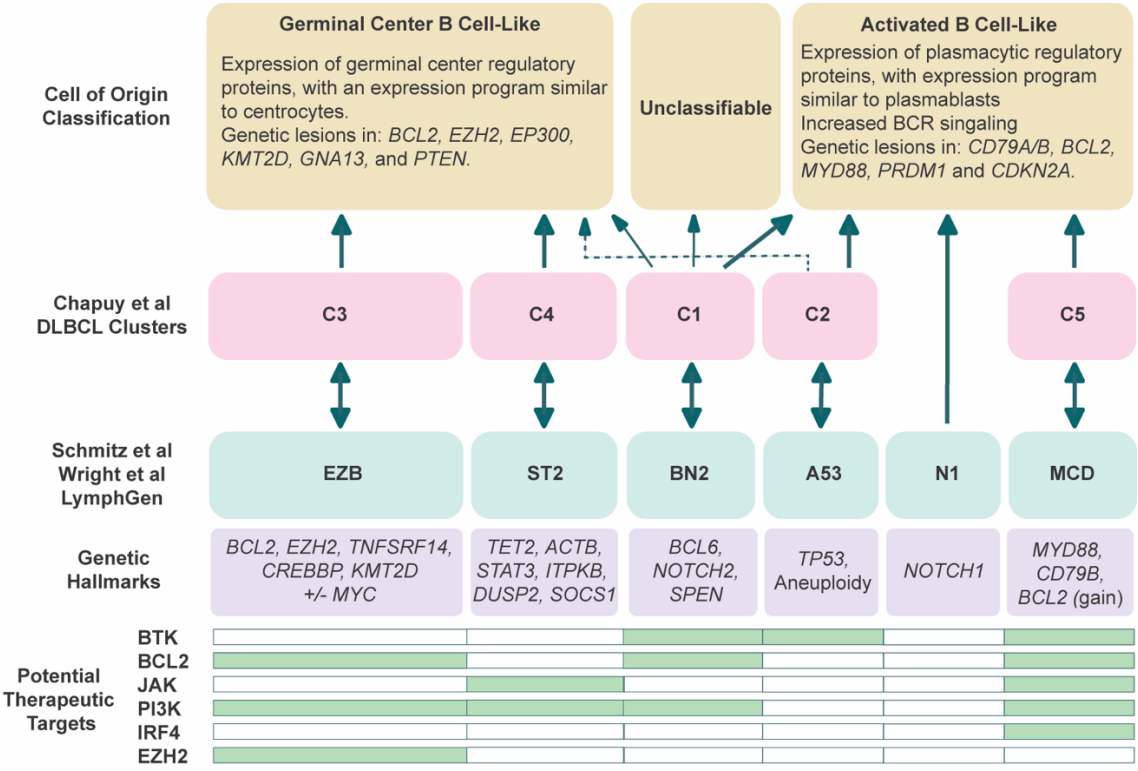


**Figure 1.3 DLBCL Subtypes.** (Adapted from Sehn & Salles, 2021 (34)). Schematic showing each identified subtype of DLCBL, including driving gene mutation. Arrows show how each subtype corresponds to other published subtypes. Potential therapeutic targets are indicated by green bars.

In their subclassification system, Schmitz et al. used exome and transcriptome sequencing, in addition to targeted amplicon resequencing and array-based copy-number analysis to profile 574 DLBCL tumours (60). With this pipeline, four genetic subtypes were identified, termed MCD, BN2, EZB, and N1. Roughly speaking, MCD tumours were similar to C5, BN2 tumours were similar to C1, and EZB tumours were similar to C3 (**Figure 1.3**). N1 tumours did not have a clear parallel to the Chapuy et al. subtypes, but instead were primarily ABC-DLBCLs, and were defined by *NOTCH1* mutations and aberrations in genes that control B cell differentiation, such as *IRF4, ID3,* and *BCOR*.

As a follow-up, in 2020 Wright et al. published a probabilistic classification tool, termed "LymphGen", using the same 574 patients samples from Schmitz et al. as a discovery cohort, and a 332 patient cohort from Ennishi et al. (61), in addition to the 304 patient cohort from Chapuy et al. for validation. With LymphGen, two additional subtypes were added to the Schmitz classification: ST2 and A53 (62). ST2 corresponded to the Chapuy C4 subtype, while A53 corresponded to C2. Moreover, Wright et al. demonstrated that the EZB subtype could be stratified as Myc-positive or Myc-negative, with Myc-positive EZB tumours having significantly worse prognosis and enrichment of double hit high-grade B cell lymphoma (HGBCL-DH) cases (so-called "double hit", due to genetic abnormalities in both the *MYC* and *BCL2* or *BCL6* genes). Wright et al. also suggested potential therapeutic targets for each DLBCL subtype. For instance, BTK inhibitors, which function to reduce chronic-BCR signaling, could be used to treat MCD tumours, due to their increased prevalence of mutations in *MYD88* and *CD79B*, but BTK inhibitors could also be effective in the treatment of BN2 tumours, due to their reliance on NF-κB signaling. Similarly, a BCL2 inhibitor such as Venetoclax could be used to treat MCD lymphomas

due to their enrichment *BCL2* amplifications. Thus, these findings led the authors to speculate that LymphGen could be used for the retrospective analysis of clinical trials, to determine if the top responders to each targeted agent corresponds with their predicted therapeutic vulnerabilities.

Moreover, LymphGen subtypes can be integrated into pre-clinical studies, to screen the efficacy of novel therapeutics based on molecular classification, as the studies discussed above emphasize the importance of genetically diverse models that reflect the range of mutations seen in patient samples. Indeed, attempts to generate mouse models of DLBCL have taken into consideration COO and LymphGen classifications, to study specific genetic alterations and their impacts on tumor biology and drug response.

## 1.4 Mouse Models of DLBCL

### *1.4.1 Genetically Engineered Mouse Models*

To mimic the molecular features that are observed in human DLBCL, a variety of Genetically Engineered Mouse Models (GEMMs) have been developed, whereby DLBCL-associated genes are overexpressed, deleted, or mutated, leading to "spontaneous" tumour formation. Many of these GEMMs employ the Cre/LoxP system, using mice that allow for B cell and GC B cell conditional gene knockout, such as $Cd19^{Cre}$, $Mb1^{Cre}$, $Aicda^{Cre}$, and $Cd21^{Cre}$ mice. Other GEMMs take advantage of B cell and hematopoietic cell specific promoter regions, such as Eμ enhancer, Iμ promoter, and Vav promoter sequences, to overexpress genes of interest (63). With these GEMMs, gene alterations that are characteristic of LymphGen subtypes can be specifically induced in B cells, allowing for the study of tumourigenesis and tumour progression. Using GEMMs,

EZB, BN2, and MCD LymphGen subtypes have been modelled; however, no GEMMs of ST2, A53 or N1 DLBCL subtypes have yet been reported.

As stated above, EZB-DLBCL is characterized by overexpression of BCL2, and mutations in epigenetic modifiers, such as *EZH2*, *KMT2D,* and *CREBBP*. In one model, known as the VavP-BCL2 model, *BCL2* gene expression is driven by the Vav promoter, leading to BCL2 overexpression in hematopoietic cells and subsequent GC B cell malignant transformation. VavP-BCL2 mice develop somatically mutated, clonal B cell lymphomas (64). When VavP-BCL2 mice are crossed with mice that either carry mutations in *Ezh2 (65),* have deletion of *Kmt2d (66)*, or have homo- or heterozygous *Crebbp* deletion (67), lymphomagenesis is enhanced. These findings underscore how different gene alterations cooperate to induce lymphomagenesis.

BN2-DLBCL is characterized by BCL6 structural variants. To model this, HA-tagged *Bcl6* was inserted into the *IgH* Iμ promoter (68). These mice, termed $Iμ^{HA.Bcl6/wt}$ mice, develop spontaneous lymphoma when they are between 13 – 15 months old. $Iμ^{HA.Bcl6/wt}$ tumors display a mature B cell phenotype and are histologically reminiscent of human DLBCL. However, these mice have yet to be combined with other gene mutations that are characteristic of BN2-DLBCL, such as *Notch2* and *Spen*, and therefore do not yet model the full genetic spectrum of BN2-DLBCL.

MCD-DLBCLs are defined by mutations in *MYD88* and *CD79B* and are commonly classified as ABC-DLBCL. To model this, a GEMM was developed with a conditional *Myd88* p.L252P mutant allele. These mice were crossed with $Cd19^{Cre}$, $Aicda^{Cre}$, and $Cd21^{Cre}$, leading to mouse strains that develop splenomegaly and DLBCL-like disease in 30% of mice (69). Several attempts to refine this model have increased the prevalence of

mice displaying aggressive lymphoma phenotypes. For instance, by overexpressing BCL2 using the *Rosa26* locus, DLBCL was observed in 80% of mice (69). Further incorporation of *Prdm1* deletion and *Spib* overexpression led to lymphomas with pre-memory and light-zone B cell characteristics, which are reminiscent of ABC-like DLBCL (70).

GEMMs have the power to replicate the complex temporal development of DLBCL, and they enable the study of specific genetic alterations in the context of immune competence. However, they are still unable to fully model the true genetic complexity of DLBCL, as more than 150 genes are recurrently mutated in DLBCL. Confounding this, DLBCL GEMMs often have long latency periods before tumours develop, and tumours do not penetrate across all offspring in the cohort. While these inconsistencies in tumour development mimic a human population, low penetrance and long latency make GEMMs more resource intensive and costly for large-scale studies, particularly those studies performing drug development and drug testing. Due to these drawbacks, syngeneic mouse models offer distinct advantages over GEMMs for the study of DLBCL.

### *1.4.2 Syngeneic Mouse Models*

Syngeneic mouse models utilize tumor cells that are derived from a specific strain of mouse, that are maintained *ex vivo* and are transplanted back into the same strain of mouse to induce tumour formation. This approach ensures that the immune system of the recipient mouse is compatible with the tumour cells, avoiding immune rejection. As compared to GEMMs, syngeneic mouse models are highly reproducible and scalable, which is beneficial for pre-clinical studies that require multiple cohorts and treatment arms. Moreover, murine tumour cell lines can be genetically modified *ex vivo*, to

overexpress, mutate, or delete genes of interest, allowing for studies that examine the functional consequences of specific gene modifications on tumour development and treatment responses, without the time and resources required to develop a new GEMM. Thus, syngeneic mouse models are often favoured for DLBCL studies that aim to screen novel therapeutics.

One of the most used syngeneic mouse models in DLBCL research is A20. A20 cells were derived from a spontaneous tumour that arose in an aged female BALB/C mouse (71), and are known to express B cell markers, such as CD19 and CD20, and can produce both IgM and IgH (72). Molecular cytogenetics have confirmed that A20 is driven by *c-Myc* translocation and copy number gain (73). Due to their aggressive nature when implanted into immunocompetent BALB/C mice, A20 tumours have been used to study minimal residual disease following R-CHOP treatment (74). A20 cells are also known to express PD-L1 (75), and have therefore been extensively used to test novel immunotherapies for the treatment of DLBCL, including various immune checkpoint inhibitors and CAR-T (76, 77). Critically, A20 cells can grow subcutaneously when implanted under the skin, but they have also been reported to grow in organs such as the spleen, eye, brain, and liver, depending on the implantation strategy (78-80). Thus, A20 cells allow for the study of lymphoma growth in extranodal sites having varied TMEs.

The other most commonly used syngeneic lymphoma model is Eμ-Myc. Eμ-Myc tumour cells were originally derived from the Eμ-Myc GEMM, which express Myc under the control of the IgH Eμ promoter on a C57BL/6 background (81). While Eμ-Myc tumours are Myc driven, additional alterations in genes including *Tp53*, *Ezh2*, and *Bcl2* have been reported (82-84). Eμ-Myc tumours are exceedingly aggressive. When Eμ-Myc cells are

transplanted into immunocompetent C57BL/6 mice, large tumour masses form in the lymph nodes and spleen. Indeed, the Eμ-Myc transplant model has been used to study how genomic changes impact tumour progression (85, 86), and has been used to screen novel targeted agents (87, 88), proving to be a valuable mouse model of aggressive lymphoma.

While syngeneic mouse models have been widely used, some elements of these models have been criticized. Since syngeneic models use murine cancer cells, results may not always translate to human biology or predict human therapeutic outcomes accurately. Moreover, syngeneic models rely on cancer cell lines that are clonally homogenous and often driven by a single oncogene, and therefore inherently will not fully capture the complexity and heterogeneity of human cancer.

### *1.4.3 Patient-Derived Xenograft Models*

Patient-derived xenograft models (PDXs) are established by implanting a piece of tumour tissue from a human patient into an immunocompromised mouse, where it can grow and then be propagated via serial transplant into new mice. PDX models maintain the genetic heterogeneity observed in the original patient for at least 10 passages (89), and are therefore a powerful reflection of human cancer.

PDX models of DLBCL have proven to retain the same histological and COO classification as the original human tumour (90, 91). Moreover, PDXs have been used to successfully predict therapeutic vulnerability. Using a panel of 8 different DLBCL PDXs, Chapuy et al. showed that only DLBCL PDXs that were dependent on chronic BCR-signaling through spleen tyrosine kinase (SYK)/ PI3K/ AKT for survival were sensitive to the SYK inhibitor entospletinib (90). Similarly, Zhang et al. used PDX DLBCL models to

demonstrate that acquired resistance to Ibrutinib could be overcome with the PI3K inhibitor idelalisib (91). Thus, PDX models have proven to be incredibly useful for the testing of hypotheses related to the efficacy of targeted therapies.

The critical drawback to PDX models is that they must be implanted into immunodeficient mice. Therefore, while PDXs powerfully model human DLBCL genetic heterogeneity, they are lacking the non-malignant component of the tumour: the TME. Indeed, the TME of DLBCL has proven to be another layer of disease heterogeneity, which must be taken into consideration when designing rational novel therapeutics. Accordingly, the most recent attempts to subclassify DLBCL include consideration of the TME.

## 1.5 The Tumour Microenvironment of DLBCL

### *1.5.1 Components and Subtypes of the TME in DLBCL*

Biological heterogeneity in DLBCL is not only achieved through genomic lesions, but also through differences in abundance and spatial organization of the components of the TME. In DLBCL and other cancers, the TME is a complex and dynamic ecosystem of tumour cells, immune cells, stromal cells, vasculature, extracellular matrix (ECM), and cytokines/ chemokines (**Table 1.2**). The TME not only influences disease progression and prognosis, but also plays an important role in therapeutic resistance or therapeutic susceptibility.

The TME contributes to tumour growth and survival through multiple mechanisms, including immune evasion, metabolic reprogramming, angiogenesis, and remodeling of the ECM (92, 93). Immune cells within the TME, such as macrophages, Tregs, and

myeloid-derived suppressor cells (MDSCs), often create an immunosuppressive milieu that enables tumor persistence. These cells secrete immunosuppressive cytokines, which can contribute to the upregulation of immune checkpoint molecules such as PD-L1 and CTLA-4 (94), leading to T-cell exhaustion and reduced anti-tumour immunity. Conversely, CD8+ cells and NK cells within the TME have the potential to mediate anti-tumour responses but are often rendered ineffective due to these immunosuppressive signals.

Key signaling pathways that support tumour growth and can be activated in tumour cells by cells of the TME include the NF-κB, JAK/STAT, and PI3K/AKT/mTOR pathways. The NF-κB pathway, frequently activated in DLBCL, is a critical mediator of inflammation and immune evasion, promoting the survival of both malignant B cells and immunosuppressive cells in the microenvironment (95). The JAK/STAT signaling axis drives tumor growth by enhancing survival signals in both tumor and stromal cells while simultaneously suppressing anti-tumor immunity (96, 97). Additionally, overactivation of the PI3K/AKT/mTOR pathway can facilitate tumor cell proliferation, survival, and resistance to apoptosis (98).

**Table 1.2 Components of the Tumour Microenvironment**

| TME Component | Function in Normal Biology | Contribution to Tumour Growth/ Survival | Anti-Tumour Function |
|---|---|---|---|
| CD8 T cell | Adaptive immune response | Immune exhaustion | Direct tumour cell killing |
| CD4 T cell | Adaptive immune response | Tumour promoting inflammation, immunosuppression | Maintenance of CD8 response, occasional tumour cell cytotoxicity |
| Regulatory T cell | Regulation of immune response | Suppression of T cell mediated tumour cytotoxicity | Production of anti-tumour cytokines, suppression of tumour promoting inflammation |

| | | | |
|---|---|---|---|
| Natural Killer cell | Innate immune response | Tumour promoting inflammation | Direct tumour cell killing |
| Plasma cell | Humoral immune response | Pro-tumour cytokine production | Production of anti-tumour antibodies |
| Mast cell | Innate immune response | Tumour promoting inflammation, promotion of tumour angiogenesis | Secretion of anti-tumour cytokines and chemokines |
| Macrophage/ Monocyte | Innate immune response | Immunosuppression, promotion of tumour metastasis and chemoresistance | Tumour cell phagocytosis, secretion of anti-tumour cytokines and chemokines |
| Dendritic cell | Adaptive immune response | Inhibition of other immune cells | Mediation of an adaptive anti-tumour response |
| Neutrophil | Innate immune response | Inhibition of other immune cells, and enhancement of tumour metastasis | Direct tumour cell killing |
| Endothelial Cell | Tissue vascularization | Tumour vascularization, increased metastatic potential | Accessibility of anti-tumour immune cells or therapeutic agents to tumour core |
| Extracellular Matrix (ECM) | Tissue structure | Immunosuppression, induction of therapeutic resistance | Physical restraint of tumour growth |
| Fibroblast | Tissue structure | Facilitation of tumour metastasis, immunosuppression | Suppression of tumour growth, recruitment of anti-tumour immune cells |
| Cytokines/ Chemokines | Communication between different cells | Promotion of tumour cell survival and angiogenesis, maintenance of tumour stem cells | Induction of anti-tumour immune cell activity, restoration of anti-tumour immune function |

Large scale attempts to create DLBCL TME subtypes have taken advantage of the abundance of available DLBCL transcriptomic data using a technique called CIBERSORT. With CIBERSORT, single cell RNA sequencing (scRNAseq) data is collected from a subset of representative tissues, then cell types within the dataset are identified and annotated. This data is used to create a matrix with “barcode genes” that can discriminate between each cell type within the tissue. The matrix can be applied to

bulk RNAseq data, to infer cell type proportions (99). Thus, CIBERSORT allows researchers to measure the abundance of different cell types within dissociated and bulk processed tumour samples, representing the powerful potential to use publicly available datasets to answer novel questions related to the DLBCL TME. In one of the first uses of CIBERSORT to profile the DLBCL TME, Ciavarella et al. identified the presence of CD4 T cells, dendritic cells, and myofibroblasts from gene expression profiling data obtained from sequenced FFPE tumour specimens (100). The presence of these three cell types correlated with favourable patient prognosis, independently of COO classification.

In a more ambitious attempt, Steen et al. used an offshoot of CIBERSORT, called EcoTyper, to create a reference map of 45 normal and malignant lymphoid tissues, from scRNAseq data, and then applied this reference map to bulk transcriptomic data from 1577 DLBCL patients. Thirteen cell types which typically constitute the majority of the cellular compartment of DLBCL could be identified: B cells, plasma cells, CD8 T cells, CD4 T cells, regulatory T cells (Tregs), Tfh cells, natural killer (NK) cells, monocytes and macrophages, dendritic cells (DCs), neutrophils, mast cells, endothelial cells, and fibroblasts (101). Moreover, Steen et al. used their methodology to characterize the cell states of the B cells within the DLBCL tumours, identifying 5 different B cell states (S1 through S5), which are representative of the differentiation state of the B cell, but do not closely map back to LymphGen classification. By integrating DLBCL cell state with non-tumour TME composition, Steen et al. identified nine different lymphoma ecotypes (LEs), 8/9 of which were prognostic.

LE1 – LE4 were associated with poor patient prognosis, with LE1 and LE2 showing the highest abundance of tumour cells, with additional infiltration of DCs and

macrophages in LE1, and plasma cell infiltration in LE2. LE3 tumours were characterized by the presence of DCs and CD4 T cells but were also often double-hit lymphomas. LE4 tumours had a complex tumour ecosystem of CD4 and CD8 T cells, Tregs, macrophages, fibroblasts, and neutrophils. LE5 was not associated with patient prognosis and consisted largely of lymphoid cells – CD4 T cells, CD8 T cells, Tfh cells, and NK cells – and endothelial cells. LE6 – LE9 were associated with favourable patient prognosis. LE6 tumours had DCs, endothelial cells, mast cells, Tregs, Tfh cells, fibroblasts and plasma cells. LE7 tumours had NK cells, endothelial cells, DCs, Tfh cells, and mast cells. LE8 tumours had plasma cells, Tregs, and fibroblasts. LE9 tumours had fibroblasts, macrophages, Tregs, neutrophils, CD4 T cells, and CD8 T cells. The authors posit that these different lymphoma ecotypes are a unique perspective on lymphoma heterogeneity, expanding beyond COO and LymphGen classifications, and may be able to identify opportunities for therapeutic targeting.

In a similar study, Kotlov et al. also used CIBERSORT on 4655 DLBCLs from independent cohorts to identify components of the TME and describe 4 different lymphoma microenvironments (LMEs). The four LMEs were termed “germinal center-like”, due to the presence of cell types commonly found in germinal centers, “mesenchymal”, due to the abundance of stromal cells and enrichment of ECM pathways, “inflammatory”, due to the presence of inflammatory cells and cytokines, and “depleted”, due to the overall reduced presence of many microenvironmental components (102). Each of these DLBCL LMEs consisted of both ABC and GCB tumour types and were distributed between the different LymphGen classifications. Critically, LME classification was associated with clinical outcome, with the germinal center LME having the most

favourable response to R-CHOP, and the depleted LME having the worst response, particularly enriched for patients who experience disease relapse. Moreover, Kotlov et al. demonstrated that when ECM components are derived from cancer-associated fibroblasts, there is a favourable prognosis compared to when ECM components are derived from macrophages, concordant with findings by Ciavarella et al, which show that myofibroblasts are associated with favourable prognosis, and findings by Steen et al, which show enrichment of fibroblasts in their most positively prognostic LE9 subtype. Indeed, the results of these studies suggest that clinical trials for novel therapeutic agents should not only consider DLBCL COO and LymphGen subtypes but should also consider the composition of the TME as a predictive and prognostic factor. However, to date there is no unified method for classifying the DLBCL TME.

### *1.5.3 Techniques to Study the TME*

While CIBERSORT has been a powerful tool for the assessment of the DLBCL TME, using widely available transcriptomic data, it is not a direct measure of cell type abundance in the TME, but rather an *in-silico* approximation. To directly measure the abundance of components of the TME, flow cytometry has been classically used, due to its wide application in clinical hematology. With flow cytometry, samples from dissociated tissues or peripheral blood are stained with a panel of fluorescently conjugated antibodies marking cell lineage or cell status. The samples are then run through a flow cytometer, which can read the fluorescent signal on each individual cell (103), allowing for their classification and quantification.

Flow cytometry has been used extensively in DLBCL. Largely, studies have focused on tumour-infiltrating T cells (TILs). It has been found that CD4+ T cells, and

particularly CD45RO+ CD4 T cells, are associated with favourable prognosis (104-106). However, PD-1 expression on CD4 and CD8 T cells in DLBCL is associated with inferior prognosis (107). In a recent study, other immune cell subsets were also assessed in diagnostic DLBCL. With a cohort of 102 biopsy samples, Yu et al. measured the presence of normal B cells, T cells, NK cells, plasma cells, monocytes, and granulocytes (108). This study validated the positive prognostic impact of T cells, but further showed that increased proportions of NK cells correlate with improved survival, and the increased presence of granulocytes correlated with poor survival. Additional correlation analysis demonstrated that normal B cells are positively correlated with T cells, and granulocytes are positively correlated with monocytes.

However, flow cytometry and CIBERSORT both use blood or dissociated tissue to surmise information about the DLBCL TME composition. Therefore, these techniques do not have the ability to take into consideration how different cell types spatially cluster together in neighbourhoods that impact their overall function. For instance, a CD8 T cell may express an anti-tumour cytotoxic protein like IFN-γ or GZMB, but it must be in close physical proximity to a tumour cell for those cytotoxic granules to be tumoricidal. Thus, spatial tumour profiling techniques have been rapidly applied to DLBCL biology to better understand how cellular interactions impact disease biology (**Table 1.3**).

**Table 1.3 Comparison of Techniques to Study the TME of DLBCL**

| Technique | Sample Input | Maximum Number of Markers | Label | Data Acquisition | Spatial Resolution |
|---|---|---|---|---|---|
| CIBERSORT | Bulk RNAseq | Whole transcriptome | N/A | Bioinformatic | No |
| Flow Cytometry | Dissociated Tissue | 40+* | Fluorescently conjugated antibody | Flow cytometer | No |
| Spatial Transcriptomics | Histological section | Whole transcriptome | Barcoded microbeads | RNAseq | 1-10 cells |
| Multiplexed IF | Histological section | Up to 7** | Antibody | Fluorescence microscope | Single cell |
| MIBI | Histological section | 40+ | Metal conjugated antibody | Mass cytometer | Single cell |
| IMC | Histological section | 40+ | Metal conjugated antibody | Mass cytometer | Single cell |
| PhenoCycler | Histological section | 100+ | Oligonucleotide conjugated antibody | Fluorescence microscope | Single cell |

*40 colour flow cytometry is only possible when using a spectral flow cytometer. Most common flow cytometers are equipped to detect up to 18 colours.
** 7 colour multiplexed IF is only possible with the use of extensive experimental controls, or with the use of cyclic staining techniques, such as Opal.

Spatial technologies take advantage of histological specimens to map tumour composition. For instance, newly developed technologies can perform whole transcriptome sequencing on fresh frozen or FFPE samples mounted to glass slides, by using mRNA capture probes that are associated with spatially defined barcode sequences. In DLBCL, spatial transcriptomics have been used to probe the association between tumour cell phenotypes and immune cell phenotypes, in the context of their physical localization. For instance, spatial transcriptomics has shown that macrophages from reactive lymph nodes have different gene expression profiles, depending on their

localization in the dark zone, light zone, or interfollicular zone. In DLBCL, where normal lymph node spatial organization is lost, macrophages have a different and distinct gene expression profile, which correlates with COO and overall patient survival (109). Moreover, spatial transcriptomics have been used by Dai et al. to show that DLBCL tumour cells with high glycolysis activity are often in an immunosuppressive TME, characterized by CD8 T cell exclusion and macrophage abundance (110). However, due to the high cost per sample, spatial transcriptomics is often applied to a small subset of samples, and results are then validated with a larger cohort using more classical methods, such as IHC or multiplexed immunofluorescence (IF). Indeed, Dai et al. validated their DLBCL glycolytic signature by using IHC staining for four different glycolysis proteins.

IHC, multiplexed IF, and other antibody-based tissue imaging paradigms have the additional advantage of single cell resolution, while spatial transcriptomics is limited by a 1 – 10 cell resolution. With classical IHC, staining is often not performed for more than two markers per tissue, which severely limits its capability to interrogate the complex TME. IF, on the other hand, provides the opportunity to multiplex antibodies, by using a wider variety of fluorophores for visualization of staining or by using cyclic staining techniques. Autio et al. used a series of 4-plex IF staining panels, to evaluate CD4 T cell regulation, CD8 T cell regulation, CD8 T cell cytotoxicity, and Th1 T cells in a cohort of 188 DLBCL patients. They found that the expression of immune checkpoints on T cells in the TME, particularly TIM3, were associated with poor outcome for R-CHOP treated patients (111). In a similar study, Xu-Monette et al. performed cyclic IF on tissues from 405 patients. Their focus was also the DLBCL T cell compartment, but with additional markers included for NK cells, macrophages, and DLBCL cells (112). In their study, high

PD1 expression on CD8 T cells and high PD-L1 expression on macrophages were found to predict poor response to R-CHOP, while PD-L1 expression on tumour cells was predictive on superior patient survival, particularly when PD-L1+ DLBCL cells were in close proximity to PD1+ CD8 T cells. Thus, multiplexed IF not only increases the number of markers that can be analyzed as compared to traditional IHC, but also allows for spatial analysis of cell types, making it possible to study the physical interaction between immune and tumour cells within the TME.

However, multiplexed IF has distinct limitations. Some tissues and cell types may have considerable autofluorescence, which interferes with the discrimination between true positive and false positive signal. Additionally, fluorophores are prone to photobleaching, which can be problematic in scenarios requiring prolonged or repeated imaging. Multiplexed IF is also limited by the number of markers that can be stained in a single tissue, with a typical maximum of 7 markers per tissue. Both imaging mass cytometry (IMC) and Multiplexed Ion Beam Imaging (MIBI) overcome these limitations. These techniques are capable of imaging more than 40 markers in a single tissue, by using unique metal isotope conjugated antibodies. Tissues are stained with a panel of antibodies, and then either laser ablation (IMC) or an ion beam (MIBI) are used to release the isotopes from the tissue, where they are then measured by a mass spectrometer. Since marker detection with these methods is based on mass spectrometry of metal isotypes, data quality is not affected by autofluorescence. Moreover, the use of metal-tagged antibodies allows for multiplexing that does not need to take into consideration spectral overlap between fluorophores.

In DLBCL, IMC was used by Colombo et al. to profile 33 cases of DLBCL, with the aim of characterizing DLBCL immune cell spatial architecture and correlating their findings with DLBCL molecular subtype and responsiveness to R-CHOP. It was found that in tumours with low immune cell infiltration, macrophages were the predominant TME cell type, whereas CD4 T cells were the predominant TME cell type in tumours with greater immune infiltration. CD4 T cells were also found to have 2.88 times greater expression in C4 DLBCL tumours, as compared to the other Chapuy subtypes, indicating that the C4/ MCD tumour type is enriched for this TME cell type. In terms of responsiveness to R-CHOP, patients who were refractory to treatment were found to have increased expression of PD-L1/2, ICOS, VISTA, and pSTAT3. IMC profiling of DLBCL was also used to study fibroblastic reticular cells (FRCs) and their interactions with CD8 T cells (113). It was found that GZMB+ (cytotoxic) CD8 T cells had increased interactions with FRCs in patients with the best prognosis. In patients with the worst prognosis, CD8 T cells expressed markers of terminal exhaustion, including TIM3, LAG3, and PD1, and had decreased interactions with FRC cells. These results implicate the fibroblastic compartment as a contributor to DLBCL T cell immunostimulatory activity, further highlighting the diverse cellular interactions in DLCBL that impact patient outcomes.

In similar studies, MIBI has been used to profile the DLBCL TME. Using a 27-plex staining panel, Wright et al. found three different TME types in DLBCL: immune-deficient, dendritic cell (DC)-enriched, and macrophage-enriched (114). Upon correlation of DLBCL TME subtype with Chapuy et al. DLBCL clusters, macrophage-enriched DLBCLs were exclusively found to be in DLBCL clusters C1, C4, and C5, which are associated with immune evasion, while DC-enriched and immune-deficient TMEs were found within all

clusters (C1—C5). However, no correlation with clinical outcome was presented. Reiss et al. performed a similar study with MIBI, and identified 9 different immune cell types, plus tumour cells, in 85 DLBCL tumour samples (115). They found that tumour cells express significantly higher levels of the immune suppressive markers PD-L1 and IDO1 when they are in immune-enriched environments, suggesting that immune suppression in tumour cells might be induced when they are near certain immune cells.

Overall, these studies, using a variety of techniques to study the DLBCL TME, have had diverse findings. Despite the differences in methodology and sample size, several trends in data have manifested. Typically, the presence of CD4 T cells was associated with favourable prognosis. Similarly, the presence of fibroblasts or ECM-related signatures tended to predict moderately improved survival. Macrophages were usually found to be associated with immune depletion or immune escape, and the expression of exhaustion markers, such as PD1, TIM3, and LAG3 on CD4 and CD8 T cells correlated with poor prognosis. While many more studies will emerge which utilize CIBERSORT, flow cytometry, spatial transcriptomics, multiplexed IF, IMC, and MIBI, to interrogate the DLBCL TME, recent studies have also taken advantage of a new multiplexed imaging platform that has a much higher capability for multiplexing: PhenoCycler.

### *1.5.4 PhenoCycler Highly Multiplexed Immunofluorescence Imaging*

PhenoCycler, previously known as CODEX, takes advantage of the strengths of multiplexed IF and the strengths of IMC/ MIBI, while allowing for increased multiplexing relative to both technologies. Rather than metal conjugated antibodies, PhenoCycler uses antibodies that are conjugated to unique DNA oligonucleotide “barcodes”. Due to the

numerous potential combinations of unique DNA sequences, PhenoCycler allows for the staining of a single tissue with up to 100 different antibodies, which will be visualized with fluorescence. While fluorescence imaging is typically limited by spectral overlap of fluorophores, PhenoCycler bypasses this restriction via the iterative imaging of antibodies in the staining panel. Complementary oligonucleotide "reporters" are conjugated to either ATTO550, AF647, or AF750 fluorophores, which are washed onto the tissue using a robotic fluidics system. Thus, with PhenoCycler, three antibodies will be imaged at time, then the reporters will be stripped from their barcodes, and three new fluorescent reporters will be washed onto the tissue and imaged. The experiment will proceed in this cyclic fashion, until all markers in the staining panel are visualized (**Figure 1.4**).

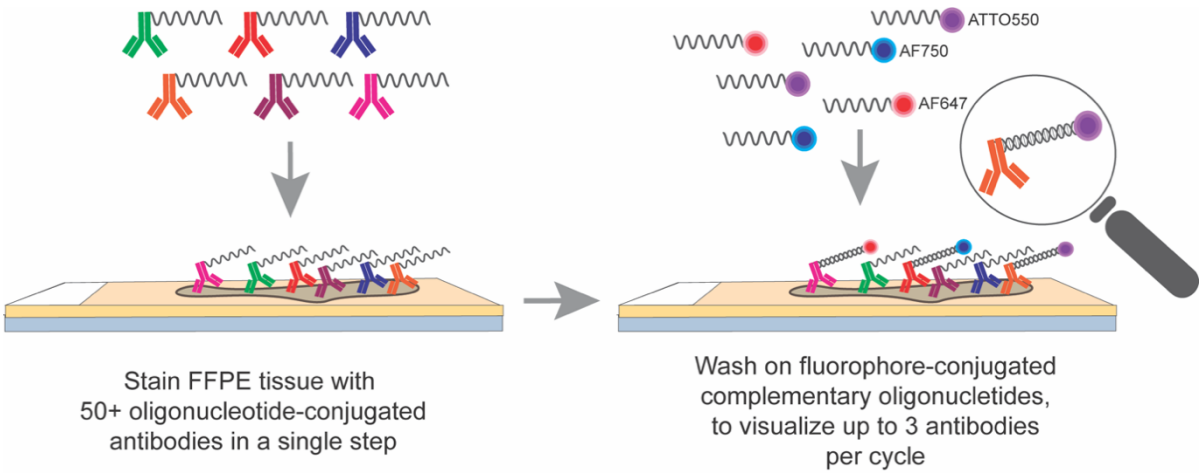


**Figure 1.4 Schematic of PhenoCycler Tissue Staining.** With PhenoCycler, tissues are stained with a panel of up to 100 different oligonucleotide conjugated antibodies in a single step. Then tissue staining is iteratively imaged, by washing on fluorescently tagged reporters which bind to their complementary barcode.

PhenoCycler has been recently used to characterize the DLBCL TME, with a particular focus on the subtyping of infiltrating T cells. Unsurprisingly, DLBCL tissues were

found to have disrupted structure as compared to normal lymph nodes. Neighbourhood analysis demonstrated that DLBCL tumours were lacking naïve and memory T cells, and cytotoxic T cells. Instead, PD1+ TIM3+ T cells were found to strongly co-localize with tumour cells and macrophages in DLBCL, thereby enhancing T cell exhaustion (116). In a smaller study, PhenoCycler was also used to identify the presence of TIGIT+ T cells in DLBCL tissues. When T cells were TIGIT+, they tended to create close contacts with tumour cells, and mouse modelling demonstrated that therapeutically targeting TIGIT induced durable tumour remission (117).

### *1.5.5 Tumour Cell Modulation of the TME*

As discussed above, the majority of studies which have used spatial technologies to study the DLBCL TME have taken “discovery” approaches, rather than hypothesis-driven approaches. The overarching goal of these studies has been to describe and classify the DLBCL TME to better understand the cellular components of the TME, and how their organization may predict therapeutic responses. Now that an abundance of experimental data is available regarding genomic/ transcriptomic and TME subtypes of DLBCL, more specific experimental questions can be posed.

For instance, studies that have integrated tumour cell mutations and phenotypes with microenvironmental characteristics are in short supply. In one such study, *TMEM30A* LOF mutations in DLBCL were examined in the context of DLBCL therapeutic sensitivity and immune cell infiltration. When *TMEM30A* was lost in B cells, antigen-dependent BCR signaling was enhanced, which conferred a survival advantage to *TMEM30A* mutant clones during malignant transformation. Critically, *TMEM30A* KO tumours had increased macrophage invasion, and were thereby uniquely sensitive to anti-CD47 therapy, which

functions to induce macrophage phagocytosis of tumour cells (118). This study serves to highlight that many of the gene mutations that are enriched in DLBCL are involved in signaling pathways that are activated when DLBCL cells are in contact with different immune cell types within the SLO, and many other mutations in DLBCL cause evasion of immune destruction. Indeed, targeted studies which investigate how specific gene mutations impact the DLBCL TME are warranted.

## 1.6 STAT6 in DLBCL

### *1.6.1 STAT6 Structure and Function*

Signal Transducer and Activator of Transcription 6 (STAT6) belongs to the STAT family of related proteins, which all function to transmit cytokine signals at the plasma membrane into gene expression changes in the nucleus. While a variety of cytokines and growth factors are known to activate STAT-family signaling, activation of STAT6 specifically depends on IL-4 or IL-13 stimulation, which signal through heterodimers composed of three possible subunits. IL-4 signals through both IL-4Rα complexed with the common gamma chain (γC), and through IL-4Rα complexed with IL-13Rα1 (119). IL-13 is also able to signal through the former but is additionally known to bind to with high affinity to IL-13Rα2, which is a non-signaling subunit, functioning as a “cytokine sink” (120, 121). Upon cytokine binding, the two receptor subunits will dimerize, allowing for downstream signaling through JAK proteins: IL-4Rα associates with JAK1, γC associates with JAK3, and IL-13Rα1 associates with JAK2/ TYK2 (121). IL-4/ IL-13 binding leads to phosphorylation of JAK1, which in turn will phosphorylate tyrosines in the IL-4Rα cytoplasmic domain (122), creating docking sites for STAT6. JAK1 can then

phosphorylate STAT6 at Tyrosine 641 (Y641), which promotes STAT6 homodimerization and nuclear translocation (**Figure 1.5**). In the nucleus, STAT6 acts as a transcriptional activator or transcriptional repressor.

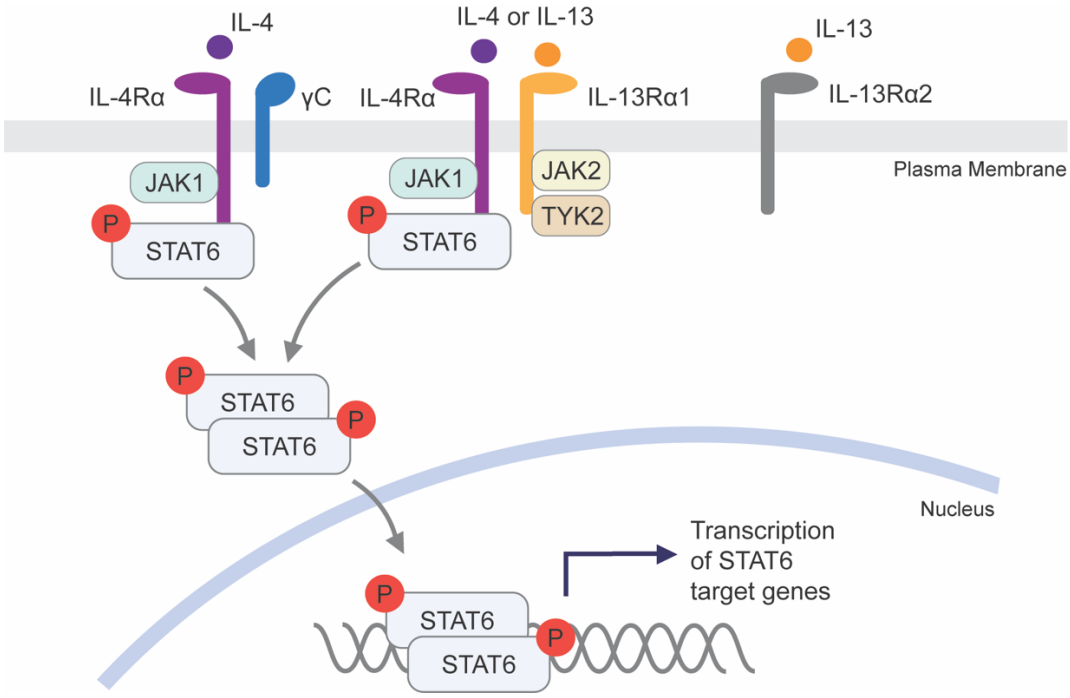


**Figure 1.5 Schematic of IL-4/ IL-13 Signaling.** Upon IL-4/ IL-13 binding to their receptors, phosphorylation of the IL-4Ra intracellular domain will induce STAT6 recruitment, where it will then be phosphorylated by JAK proteins on Tyrosine 641. Following STAT6 phosphorylation, the protein will homodimerize, and the translocate to the nucleus, where it can bind to DNA and regulate transcription of target genes.

Indeed, the protein sequence of STAT6 reflects the domains required for these functions, with five distinct modules: the coiled coil domain, the DNA-binding domain, the linker domain, the SH2 domain, and the transactivation (TAD) domain (**Figure 1.6**). The SH2 domain is responsible for STAT6 recruitment to IL-4Rα phospho-tyrosine residues and has been a focus of therapeutic targeting to reduce STAT6 phosphorylation (123, 124). STAT6 dimerization also occurs through the SH2 domain, and dimerization is

stabilized upon Y641 phosphorylation (125). Within the coiled coil domain, amino acids 136-140 are critical for STAT6 nuclear import through importin-α3 (126). While STAT6 can be imported into the nucleus independently of phosphorylation and dimerization (126), dimerization is required for STAT6 to interact with DNA through the DNA binding domain (125). Moreover, transcriptional activity of STAT6 can be modulated through other protein partners like CREBBP, p300 and NCoA-1, which interact with the STAT6 TAD domain (127, 128).

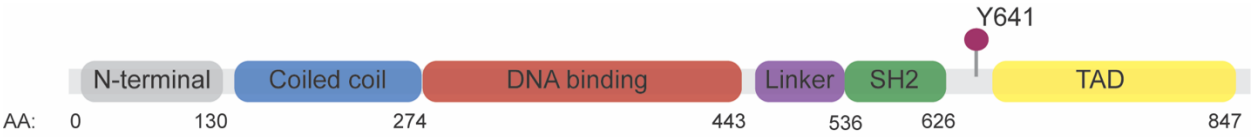


**Figure 1.6 Functional Domains within the STAT6 Protein Sequence.** (Adapted from Li et al. (125)) Schematic representation of the STAT6 protein, with functional domains annotated. Phosphorylation at Tyrosine 641 (Y641) is central to STAT6 activation and nuclear translocation.

STAT6 regulates the expression of various transcriptional targets across different cell types, including B cells, T cells, myeloid cells, and non-immune cells (129). In B cells, STAT6 controls key genes involved in proliferation, survival, and immune function, such as CD23 (*FCER2*), BCL-XL (*BCL2L1*), and IL-4Rα (*IL4Ra*) (130-133). STAT6 is similarly important for T cell and myeloid cell function, particularly in the context of Th2 and alternative macrophage activation (ie “M2”-differentiation). STAT6 directly controls transcription of GATA3 (134), which is the master transcription factor for Th2 differentiation. In myeloid cells, STAT6 promotes the expression of Arginase 1 (*ARG1*) and the Mannose Receptor C Type 1 (*MRC1*), which are both “M2”-Marcophage markers

(135, 136). In non-immune cells, STAT6 activation plays a significant role in regulating processes such as tissue remodeling and fibrosis, by regulating genes like *MUC5AC* in epithelial cells *COL1A1* and *COL1A2* in fibroblasts (137, 138).

### *1.6.2 STAT6 in Hematological Malignancies*

STAT6 is frequently overactivated or mutated in several hematological malignancies, including DLBCL, cHL, follicular lymphoma (FL), primary mediastinal B-cell lymphoma (PMBCL), and cutaneous T-cell lymphoma (CTCL). In these cancers, STAT6 has been demonstrated to play a role in promoting tumor cell survival and proliferation. It also regulates key cellular processes, including intercellular signaling, cell cycle progression, and genomic stability, as demonstrated in CTCL, where STAT6 controls the production of Th2 cytokines. Indeed, STAT6 inhibition was found to induce to cell cycle arrest and downregulation of cytokine production (136).

In PMBCL, STAT6 exhibits a complex relationship with BCL6. Studies have shown that STAT6 is a transcriptional repressor of BCL6, and the two proteins are not co-expressed within the same cell (139). Interestingly, paired knockdown of *STAT6* and *BCL6* in PMBCL cells sensitizes tumors to R-CHOP, indicating that intratumoral heterogeneity is a mechanism of drug resistance, and it is in part driven by STAT6 expression (140). Genomic analyses in PMBCL have identified *STAT6* mutations in 36-43% of patients, particularly in the DNA-binding domain (141, 142). Further reinforcing the role of STAT6 signaling in PMBCL, 24-30% of PMBCL cases harbor mutations in *IL4R*, with evidence suggesting that the I242N mutation in *IL4R* represents a GOF alteration that drives oncogenic STAT6 signaling (143).

In FL, around 10-13% of cases exhibit *STAT6* mutations, most commonly in the DNA binding domain, leading to heightened IL-4-induced expression of target genes such as *CCL17*, *FCER*, and *CISH*, due to increased nuclear residency of STAT6 (144, 145). Mechanistically, the STAT6 mutant protein in FL has been found to bind to the *PARP14* promoter, which is a co-activator of STAT6, creating a self-reinforcing regulatory circuit that amplifies STAT6-mediated transcription (130).

In cHL, constitutive phosphorylation of STAT6 has been observed in Hodgkin Reed-Sternberg (HRS) cells in 78% of cases and in multiple cell lines. This has been attributed to IL-13 production by HRS cells, leading to STAT6 activation. Indicating a role of STAT6 in HRS cell survival, antibody-mediated neutralization of IL-13 significantly reduced STAT6 phosphorylation and cellular proliferation (146). In support of these findings, knockdown of *STAT6* in cHL cell lines was found to induce apoptosis (147). A recent study which performed profiling of ctDNA from cHL patients found that *STAT6* was mutated in 34% of patients, and *IL4R* was mutated in 10% of patients. In particular, *IL4R* mutations were classified as GOF, as IL-13-induced STAT6 phosphorylation was increased when the mutation was present (148).

Collectively, these findings highlight STAT6 as a key oncogenic driver in a range of lymphomas, with diverse roles in regulating tumor cell proliferation and survival. Targeting STAT6 and its downstream pathways offer a promising therapeutic strategy, particularly in malignancies where *STAT6* mutations or dysregulated activity are prevalent.

### *1.6.3 STAT6 D419 Mutation*

*STAT6* mutations in hematological malignancies have been found in all regions of the gene. However, mutations in the D419 hotspot, which is in the DNA binding motif, seem to be of particular significance. Germline $STAT6^{D419}$ mutations are associated with severe immune dysregulation. Sharma et al. identified the $STAT6^{D419}$ variant in 16 patients from 10 families, all presenting with early-onset allergic disorders. These patients exhibited a range of immune abnormalities, including atopic dermatitis, eosinophilic gastrointestinal disease, asthma, food allergies, and anaphylaxis (149). Indeed, the mutation confers a GOF phenotype, characterized by sustained STAT6 phosphorylation and increased expression of STAT6 target genes, leading to a skewing towards a Th2 immune response. Similarly, Minskaia et al. described a germline $STAT6^{D419H}$ mutation in a family affected by early-onset atopic dermatitis, food allergies, eosinophilic asthma, and anaphylaxis (150). In functional studies on patient fibroblasts and PBMCs, the mutation was found to lead to heightened IL-4-induced STAT6 signaling, with higher levels of total and phosphorylated STAT6 compared to wild-type controls. Critically, Minskaia also found that one patient in their family cohort also developed follicular lymphoma. Thus, $STAT6^{D419}$ mutations may play a role in lymphoma development.

At DLBCL diagnosis, *STAT6* mutations are present, but are found all over the gene. However, at relapse, *STAT6* mutations are enriched at the D419 hotspot (45), suggesting that there is functional significance for STAT6 GOF in R-CHOP resistance. Given the enrichment of $STAT6^{D419}$ mutations at DLBCL relapse, our group undertook a research study aimed at understanding the functional significance of this mutation in

DLBCL growth and resistance to therapy, with the underlying hypothesis that *STAT6$^{D419}$* mutations would confer a selective survival advantage (52).

We found that STAT6$^{D419}$ tumour cells had increased expression of phospho-STAT6 in the nucleus of DLBCL cell lines upon IL-4/ IL-13 stimulation, consistent with studies by other groups (130, 144, 150). Moreover, we found that the increased phospho-STAT6 nuclear residency was associated with increased transcription of target genes. However, DLBCL cells lines expressing a *STAT6$^{D419}$* mutation did not have increased proliferation in the presence or absence of IL-4 stimulation, nor did STAT6$^{D419}$ tumour cells have increased resistance to the individual components of R-CHOP. Thus, our results assert that the expression of *STAT6$^{D419}$* does not inherently confer resistance of DLBCL cells to chemotherapy.

### *1.6.4 The TME and STAT6*

Our findings that STAT6$^{D419}$ tumour cells were not less sensitive to R-CHOP could potentially be explained by the experimental procedures used. DLBCL cell lines grown in culture lack many of the features of tumours *in vivo*. For instance, DLBCL cells in culture lack 3D architecture and spatial heterogeneity and have homogenous access to nutrients and growth factors. They are also lacking an intact microenvironment, which would normally consist of numerous cell types that influence growth and resistance to therapy. This is of particular significance in the context of STAT6$^{D419}$ tumours, as many of the genes that are upregulated in STAT6$^{D419}$ tumour cells relative to STAT6$^{WT}$ tumour cells encode proteins that control intercellular interactions, including the chemokine CCL17 (**Figure 1.7**).

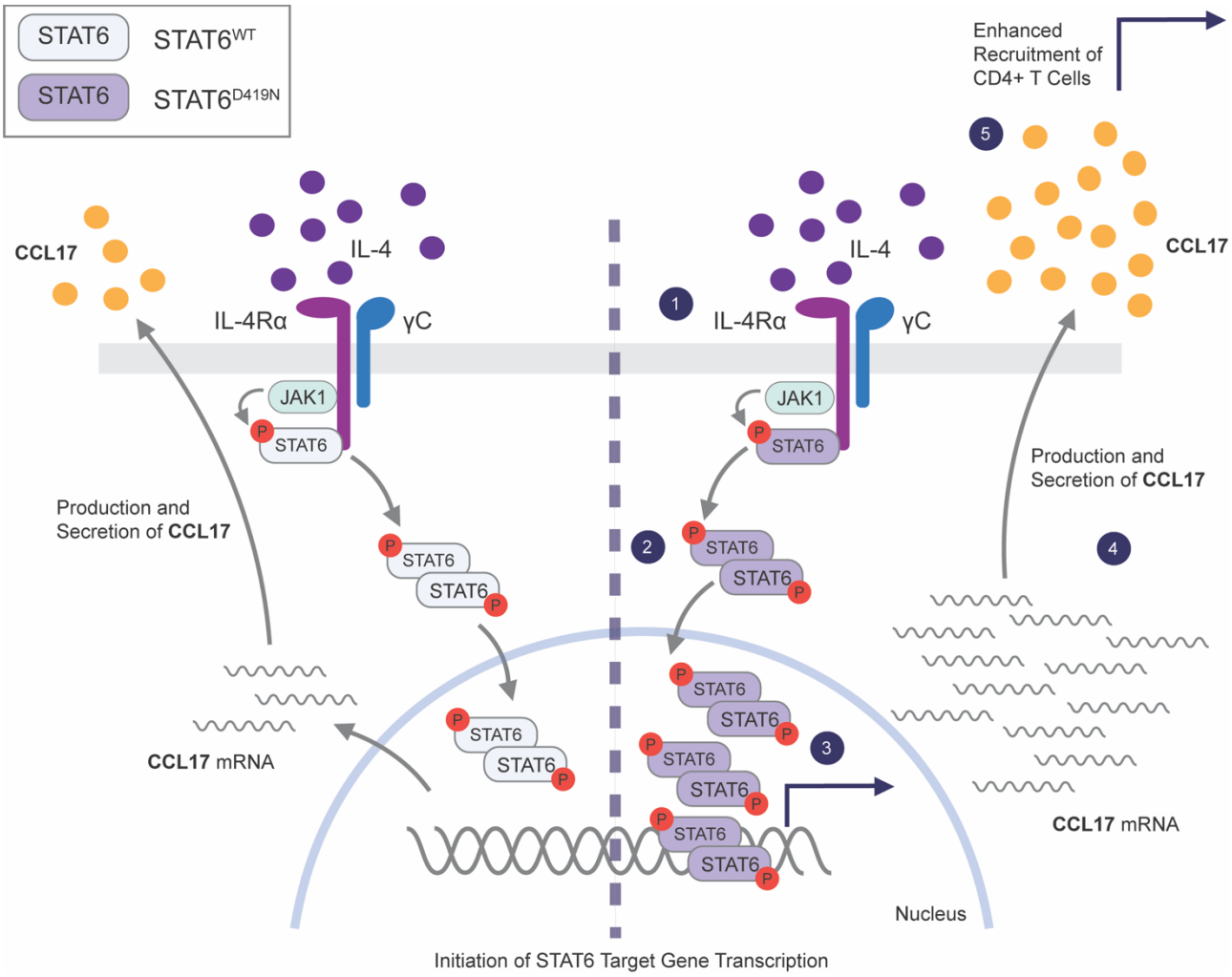


**Figure 1.7: STAT6 D419N Mutation in Lymphoma Cells.** (Adapted from Benoit & **Abraham** et al. (52)) 1. In *STAT6*$^{WT}$ and *STAT6*$^{D419N}$ lymphoma cells, IL-4 is required for STAT6 phosphorylation. 2. Following phosphorylation, both STAT6$^{WT}$ and STAT6$^{D419N}$ will dimerize and translocate to the nucleus. 3. However, STAT6$^{D419N}$ has increased nuclear retention as compared to STAT6$^{WT}$. 4. STAT6$^{D419N}$ promotes increased transcription of select gene targets, such as *CCL17.* 5. Increased transcription of *CCL17* by STAT6$^{D419N}$ leads to increased production and secretion of CCL17, which functions to recruit CD4$^{+}$ T-cells.

CCL17 is involved in the recruitment of CCR4-expressing immune cells to the TME, including CD4+ T cells (151). Indeed, when IHC staining was performed on rrDLBCL patient biopsies, the samples that were positive for phospho-STAT6 had significantly increased CD4+ T cells. The role of these CD4+ T cells in therapeutic

resistance or clonal expansion following the selective pressure of R-CHOP was not determined.

Beyond T cells in DLBCL, it has also been shown that inhibition of STAT6 in CTCL skin explants leads to a decrease in CCL17 expression, and a concomitant decrease in expression of anti-inflammatory (so-called “M2-like”) macrophage markers (136). Given the extensive crosstalk between different cell types in the TME, especially in the context of differential responsiveness to cytokine/ chemokine signaling, it is probable that STAT6 GOF has the potential to remodel many different elements the TME to promote resistance to therapy.

## 1.7 Rationale and Objectives

We hypothesize that *STAT6*$^{D419}$ GOF mutations in DLBCL contribute to remodelling of the TME leading to therapeutic resistance. Specifically, we predict that increased chemokine expression by STAT6$^{D419}$ tumour cells attracts immune cells that confer a survival advantage to DLBCL cells. Moreover, we aim to test if STAT6$^{D419}$-induced microenvironmental remodelling presents novel therapeutic vulnerabilities which can be exploited to restore sensitivity to chemotherapy.

In order to study STAT6$^{D419}$ modulation of the TME, a lymphoma model with an intact immune system is required. Thus, this study used mouse modelling to determine how STAT6$^{D419}$ impacts TME composition and spatial organization, and if this correlates with response to therapy. However, prior to studying STAT6$^{D419}$-mediated microenvironmental remodelling, we aimed to thoroughly define the spatial organization and intercellular interactions within the TME of two different murine models of lymphoma,

using PhenoCycler imaging. Critically, prior to the work described in this thesis, PhenoCycler imaging had not been described for murine FFPE tissues.

The detailed objectives of this thesis are as follows:

1. To develop tools and analytical techniques to study the TME of both murine and human lymphoma.
2. To determine how different mouse models of lymphoma differ in their microenvironmental composition and spatial organization.
3. To determine if mouse-modelling of STAT6$^{D419}$-mutant lymphoma faithfully recapitulates critical features of human disease.
4. To investigate mechanisms of STAT6$^{D419}$-mediated microenvironmental remodelling.
5. To identify novel therapeutic strategies for STAT6$^{D419}$ mutant rrDLBCL.
6. To define the microenvironmental composition and spatial organization of rrDLBCL, with a specific focus on STAT6$^{D419}$-mutant patients.

# Chapter 2: Tunable PhenoCycler imaging of the murine pre-clinical tumour microenvironments.

This chapter was published as an original research article (open access):

**MJ Abraham**, C Goncalves, P McCallum, V Gupta, H Chou, N Gagnon, SEJ Preston, F Huang, NA Johnson, WH Miller, KK Mann, & SV del Rincon. Tunable PhenoCycler Imaging of the Murine Pre-Clinical Tumour Microenvironments. **Cell and Bioscience. 2024.** doi: 10.1186/s13578-024-01199-4; PubMed PMID 38311785.

The online version of this article, and all supplementary material associated with it, can be found at: https://cellandbioscience.biomedcentral.com/articles/10.1186/s13578-024-01199-4

## 2.1 Abstract

**Background:** The tumour microenvironment (TME) consists of tumour-supportive immune cells, endothelial cells, and fibroblasts. PhenoCycler, a high-plex single cell spatial biology imaging platform, is used to characterize the complexity of the TME. Researchers worldwide harvest and bank tissues from mouse models which are employed to model a plethora of human disease. With the explosion of interest in spatial biology, these panoplies of archival tissues provide a valuable resource to answer new questions. Here, we describe our protocols for developing tunable PhenoCycler multiplexed imaging panels and describe our open-source data analysis pipeline. Using these protocols, we used PhenoCycler to spatially resolve the TME of 8 routinely employed pre-clinical models of lymphoma, breast cancer, and melanoma preserved as FFPE.

**Results:** Our data reveal distinct TMEs in the different cancer models that were imaged and show that cell-cell contacts differ depending on the tumour type examined. For

instance, we found that the immune infiltration in a murine model of melanoma is altered in cellular organization in melanomas that become resistant to αPD-1 therapy, with depletions in a number of cell-cell interactions.

**Conclusions:** This work presents a valuable resource study seamlessly adaptable to any field of research involving murine models. The methodology described allows researchers to address newly formed hypotheses using archival materials, bypassing the new to perform new mouse studies.

## 2.2 Introduction

Over the past two decades, there has been growing appreciation for the role of the tumour microenvironment (TME) in cancer biology (1, 2). As such, the central dogma of tumour progression has evolved to assert that oncogenic mutations underlie the transformation of normal cells to malignant cells, and subsequently, non-transformed cells are recruited via secretion of soluble factors, such as cytokines, chemokines, and extracellular vesicles, to support further cancer cell survival and propagation (3-6). The non-transformed cellular elements of the TME, including immune cells, fibroblasts, and endothelial cells, interact with tumour cells, and both cellular composition and intercellular interactions within the TME are critical influencers of cancer cell growth, metastasis, and response to therapy. Many emerging therapeutics, most notably immune checkpoint inhibitors (ICIs), specifically target components of the TME to elicit tumour control.

Phenotyping of the murine TME has helped to understand the response to novel combinatorial therapies and to track changes in tumour progression from initiation to metastatic disease (7, 8), with multi-parameter flow cytometry being the most widely used

technique to study the composition of the TME (9). In this method, malignant tissues are dissociated into single cell suspensions, stained with a panel of antibodies, and run through a flow cytometer, allowing for the identification of cells within the TME. However, a recent body of work has highlighted that TME composition alone is only part of a much bigger picture, and spatial information (e.g. cell-cell interactions) is crucial to further understand tumour progression and response to treatment. Immunofluorescence (IF) imaging of tumour sections, on the other hand, can preserve tissue architecture but is usually restricted to detection of 1 or 2 markers. To overcome these limitations, a surge of highly multiplexed tissue imaging technologies has emerged in the last 10 years (10-13), aimed at providing single cell spatial phenotyping of the TME and other complex tissue types.

PhenoCycler, formerly known as CODEX (CO-Detection by indexing (13)), has shown immense promise in the highly multiplexed imaging space. In brief, antibodies targeting desired proteins are conjugated to unique oligonucleotide “barcodes” and are then used to stain fresh frozen or formalin-fixed paraffin-embedded (FFPE) tissues. The PhenoCycler instrument is then used to automate the cyclic process of tissue washing, hybridizing up to three fluorescent “reporters” to primary antibodies oligonucleotide “barcodes”, imaging the tissue, then removing the fluorescent reporters before starting a new cycle process. This iterative process is repeated until all antibodies in a staining panel have been visualized (14). Reporters are complementary oligonucleotides to the unique barcodes, and are tagged with either fluorophores ATTO550 AF647, or AF750. As of this writing, PhenoCycler has been used to image up to 101 different markers in single tissue (15, 16), and has been used to spatially profile human cancers such as

cutaneous T cell lymphoma (17), follicular lymphoma (18), diffuse large B cell lymphoma (19), Hodgkin's lymphoma (20), bladder cancer (21), colorectal cancer (22), basal cell carcinoma (23), glioblastoma (24), breast cancer (25), and head and neck squamous cell carcinoma (26), and human non-cancerous conditions such as ulcerative colitis (27), diabetic nephropathy (28), functional dyspepsia (29), vitiligo (30), and Alzheimer's disease (31).

Comparatively fewer publications have used PhenoCycler technology to image murine tissues, and all have reported staining for fresh-frozen samples (13, 32-36). However, many research groups maintain archives of FFPE murine tissues. FFPE tissue blocks can be successfully sectioned and imaged with minimal evidence of degradation for up to 30 years (37), and FFPE tissues from multiple cohorts or experimental conditions can be easily combined into a single tissue microarray (TMA). Thus, we aimed to develop a tunable murine PhenoCycler antibody panel optimized for FFPE staining, thereby enabling researchers to utilize their archival materials to test newly developed hypotheses with existing material and bypassing the need to perform new mouse studies.

Herein we describe our protocol for the conjugation of antibodies that are optimized for IF staining of murine tissues preserved as FFPE and provide our protocols for PhenoCycler staining and open-source data analysis, which enables visualization of staining, cell segmentation, cell classification, and neighbourhood/proximity analysis. The protocols described below are tunable and offer flexibility to researchers who wish to use their own antibodies of interest for highly multiplexed staining. Furthermore, we demonstrate the feasibility of this approach with TME data obtained using 16-plex

PhenoCycler staining on FFPE tissues from pre-clinical mouse models of lymphoma, breast cancer, and melanoma.

## 2.3 Materials and Methods

Our tunable PhenoCycler workflow has four major components: 1) antibody selection; 2) antibody conjugation and optimization; 3) tissue staining and imaging; and 4) data analysis (**Figure 2.1**).

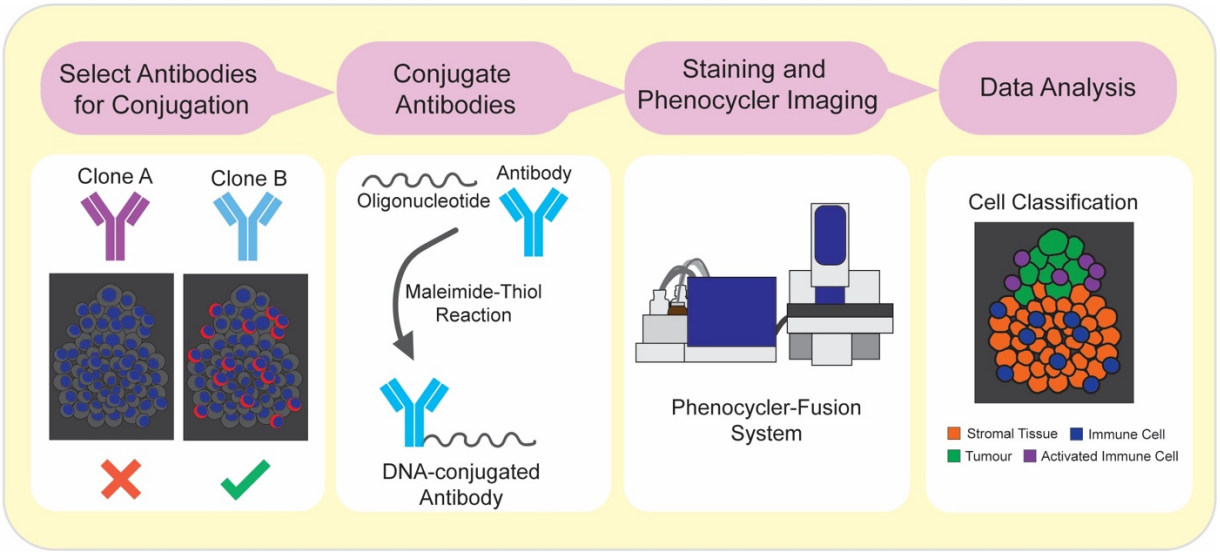


**Figure 2.1: Workflow for selection of antibodies, antibody conjugation, and PhenoCycler staining**
Schematic showing the workflow outlined in this Research Resource.

### *2.3.1 Selection and Validation of Antibodies for Conjugation, and Quality Control of Staining*

Due to epitope masking associated with FFPE preservation (38), the careful selection of antibodies is critical to successful PhenoCycler staining. Below, we describe our IF staining protocol for the selection of antibody clones which can prioritized for

barcode conjugation. All antibodies should be tested on the tissue they are ultimately meant to stain.

*Deparaffinization and Antigen Retrieval*

1. Mount 4 µm microtome tissue sections onto SuperFrost Plus slides (Fisherbrand).
2. Deparaffinize slides using the following solutions, for 5 minutes each: Xylene (1), Xylene (2), 100% EtOH (1), 100% EtOH (2), 95% EtOH, 70% EtOH, 50% EtOH, and running tap water.
3. Transfer slides to a PT Link Pre-treatment machine filled with 1X Tris-EDTA antigen retrieval buffer (pH 9.0) and cook at 90°C for 20 minutes. After depressurization, cool slides for 1 hour.
    i. Note: Less toxic alternatives, such as HistoChoice, can be used in place of Xylene.
    ii. Note: Recipes for all solutions used in these protocols can be found in **Table 2.1**. Recipes listed below will be underlined.

*Blocking*

4. Rinse slides in tap water and dry the glass around the tissue with a Kimwipe. Circle tissue with a hydrophobic PAP pen, and rinse with 2 changes of IF Wash Buffer.
5. Block slides for 30 minutes at room temperature with Primary Blocking Buffer, then rinse with 2 changes of IF Wash Buffer.
6. Block slides for another 30 minutes at room temperature with FC Blocking Buffer, then rinse with 2 changes of IF Wash Buffer.

**Table 2.1. Recipes for IF Staining, Antibody Conjugation, and PhenoCycler Staining Solutions.**

| Solution Name | Composition |
|---|---|
| 10X Tris-EDTA Antigen Retrieval Buffer, pH 9.0 | 6.05 g Tris<br>1.85 g EDTA<br>400 mL $ddH_2O$<br>• Adjust to pH 9.0<br>• Complete to 500 mL with $ddH_2O$<br>Store at 4°C for up to 30 Days |
| 1X Tris-EDTA Antigen Retrieval Buffer, pH 9.0 | 50 mL 10X Tris/EDTA Buffer pH 9.0<br>450 mL $ddH_2O$<br>250 µL Tween20<br>• Mix well and make fresh. |
| 10X Tris Buffered Saline (TBS) | 80 g NaCl<br>2 g KCl<br>30 g Tris<br>• Adjust pH to 7.4<br>• Complete to 1000 mL with $ddH_20$ |
| IF Wash Buffer | 200 mL 10X TBS<br>800 mL $ddH_2O$<br>250 uL Tween20 |
| Primary Blocking Buffer | 1000 µL IF Wash Buffer<br>20 µL Goat or Donkey Serum<br>• Vortex to mix. |
| FC Blocking Buffer | 500 µL FC Block<br>5 µL Anti-Mouse HRP<br>• Vortex to mix. |
| Antibody Buffer | 1000 µL IF Wash Buffer<br>1 µL Goat or Donkey Serum<br>• Vortex to mix. |
| Prepared DAPI | 500 µL PBS<br>1 µL 1mg/mL DAPI<br>• Vortex to mix. |
| Antibody Reduction Master Mix (*A*)<br>(for 1 conjugation) | 6.6 µL Reduction Solution 1 (*A*)<br>275 µL Reduction Solution 2 (*A*)<br>• Thawed aliquots of Reduction Solution 1 (*A*) should not be re-used |
| Bleaching Solution | 0.8 mL 10M NaOH<br>2.7mL 50% $H_2O_2$<br>26.5 mL 1X PBS |
| Staining Buffer with Blockers (*A*)<br>(for 2 samples) | 362 µL Staining Buffer<br>9.5 µL N Blocker (*A*)<br>9.5 µL G2 Blocker (*A*)<br>9.5 µL J Blocker (*A*)<br>9.5 µL S Blocker (*A*) |
| Post-Staining Fixation (*A*) | 1 mL 16% PFA<br>9 mL Storage Buffer (*A*) |
| Final Fixative Solution (*A*) | 1000 µL 1X PBS |

| | |
|---|---|
| | 20 µL Fixative Reagent (*A*)<br>• Thawed aliquots of Fixative Reagent (*A*) should not be re-used |
| Screening Buffer (*A*) | 3.5 mL 10X PhenoCycler Buffer (*A*)<br>24.5 mL Nuclease-Free Water<br>7 mL DMSO<br>• Allow the Screening Buffer to equilibrate to room temperature prior to use |
| Reporter Stock Solution (*A*)<br>(for 5 cycles) | 1220 uL Nuclease Free Water<br>150 uL 10X PhenoCycler Buffer (*A*)<br>125 uL Assay Reagent (*A*)<br>5 uL Nuclear Stain (*A*) |

*Primary and Secondary Antibody Incubation*

7. Dilute primary antibody in Antibody Buffer and incubate slides in primary antibody at 4°C overnight in a humidity chamber.
   i. Note: For initial optimization, we try 10 ug/ml antibody dilution (approximatively 1 in 100).
   ii. Note: Staining specificity can be improved for some antibodies by incubating with a higher antibody concentration (eg. 20 ug/ml), for 30 minutes at 37°C.
8. Rinse slides with 3 changes of IF Wash Buffer.
9. Incubate slides for 1 hour at room temperature with secondary antibody conjugated to AlexaFluor647, diluted 1 in 500 in Antibody Buffer.
10. Rinse slides with 3 changes of IF Wash Buffer.

*Counterstaining, Mounting, and Imaging*

11. Stain tissue with prepared DAPI for 15 minutes, then rinse slides 3 times with IF Wash Buffer.
12. Mount coverslips onto slides with Flouromount-G, and then allow to dry for 15 minutes.

13. Image slides with the same microscope that will be used for PhenoCycler image acquisition.

i. Note: Acquiring on the same microscope used for the Phenocycler image acquisition will give a better representation of the final staining. In this study we used the Fusion microscope from Akoya Biosciences.

ii. Note: The results from optimization staining will help in the subsequent steps in assessing the efficacy of the antibody conjugation by comparing both stains.

*Assessing IF Staining*

Assessing staining quality is challenging. Appropriate negative and positive tissue controls are required. If possible, staining assessment by a pathologist can guide selection of the most appropriate antibody clones. Ideally, a TMA comprising an array of different tissues and pathologies will provide the opportunity for robust assessment of antibody specificity and sensitivity, but whole-tissue slides can be used if a TMA is not available. Critical parameters to consider include:

a. if staining pattern within the tissue consistent with reported literature. Multiple online resources can be used, such as ProteinAtlas.

b. Signal to Noise Ratio (SNR): this parameter will guide the user to which fluorescent reporter to use. For example, if the SNR is very high, the dim AF750 reporter should but used, while the bright AF647 can be used for markers with low SNR.

### *2.3.2 Antibody Conjugation to an Oligonucleotide Barcode*

Once an antibody has shown strong and specific signal by IF, it can proceed to conjugation. Antibodies can be conjugated to barcodes which have complementary

reporters in ATTO550, AF647, or AF750 fluorophores. IF screening will inform which fluorophore will give optimal results. In general, antibodies which show very strong and specific staining should be conjugated to barcodes that have complementary reporters in AF750, antibodies which have weaker signal and lower abundance should be conjugated with barcodes that have complementary reporters in AF647, and antibodies which have medium abundance and weak to medium signal strength should be conjugated with barcodes that have complementary reporters in ATTO550.

Antibody conjugation requires reagents from Akoya Biosciences, and thus follows their recommended protocol. A more detailed protocol can be found here: https://www.akoyabio.com/wp-content/uploads/2021/01/CODEX-User-Manual.pdf

*Pre-experiment Notes*

- Antibodies to be conjugated must be carrier-free. The presence of BSA or other stabilizing agents will interfere with conjugation.
- If conjugating more than one antibody, carefully label all MWCO columns prior to starting. We recommend conjugating no more than 3 antibodies at a time, to reduce the risk of cross-contamination.
- Reagents which are purchased from Akoya and used “as-is” will be annotated as (*A*). Reagents that are purchased from Akoya but need preparation prior to use will be underlined and annotated as (*A*).

*Conjugation Reaction*

1. For each antibody to be conjugated, add 450 µL of Filter Blocking Solution (*A*) to a labelled 50 kDa MWCO column, then spin at 12,000g for 2 minutes. Following

centrifugation, discard flowthrough and aspirate any remaining liquid out of the filter unit.

i. Note: This is the only step where the liquid should be aspirated out of the filter unit. In all subsequent steps, the remaining liquid contains the unconjugated/conjugated antibody.

2. Add 50 µg of each antibody to be conjugated to their respective filter units, at an adjusted volume of 100 µL. Spin down tubes at 12,000 g for 8 minutes and discard the flowthrough.

3. Add 260 µL of Antibody Reduction Master Mix (*A*) to the top of each filter unit, close this lid, vortex for 3 seconds, then allow to sit at room temperature for 30 minutes.

i. Note: do not allow this reaction to exceed 30 minutes, as it can result in irreversible antibody damage.

4. Spin down tubes at 12,000 g for 8 minutes, then discard the flowthrough.

5. Add 450 µL of Conjugation Solution (*A*). Spin down again at 12,000 g for 8 minutes, then discard the flowthrough.

6. During the second centrifugation, prepare each assigned Barcode (*A*) by adding 10 µL of molecular biology grade nuclease free water, then add 210 µL of Conjugation Solution (*A*) to the resuspended barcodes.

7. Add the barcode solution to the filter. Close the lid and vortex for 3 seconds. Incubate the antibody conjugation reaction at room temperature for 2 hours.

8. Spin down tubes at 12,000 g for 8 minutes, then discard the flowthrough.

9. Add 450 µL of Purification Solution (*A*) to each filter, and spin down tubes at 12,000 g for 8 minutes, then discard the flowthrough.

10. Repeat Step 9 for a total of 3 purifications. At the end of the third purification, the filter will contain the conjugated antibody.

11. For each antibody, label a fresh tube with the antibody name and the barcode ID. Add 100 µL of Antibody Storage Solution (*A*) to each filter. Then, invert the filter unit into the new collection tube, and spin down at 3,000 g for 2 minutes.

i. Note: The final volume of the antibody will be around 120 µL

ii. Note: For long term storage, transfer antibodies to autoclaved screw top tubes, to reduce evaporation.

*Validation of Conjugation to an Oligonucleotide Barcode*

12. Cast a 10% SDS-PAGE gel, with 2 wells for each antibody whose conjugation is being validated, plus an additional well for the protein ladder (ie. if validating 4 antibodies, you would need a total of 9 wells, so a 10-well gel will suffice). Set up gel running apparatus, as you would for a typical western blot.

i. Note: Details on SDS-PAGE gel casting can be found here: https://www.bio-rad.com/webroot/web/pdf/lsr/literature/Bulletin_6201.pdf

13. Add 1 µL of unconjugated antibody to a tube with 9 µL of 1X lammeli loading dye. Add 0.5 µL of conjugated antibody to a different tube with 9.5 µL of 1X lammeli.

14. Boil samples for 5 minutes on a heating block at 95 °C.

15. Load samples and protein ladder into the gel and run until resolved.

i. Note: We typically run our gels at 90 V for 1.5 hours.

16. Following running, carefully remove the gel from the cassette, and place in a glass container. Fill the glass container with GelCode Blue Reagent.

17. Allow the gel to incubate in the GelCode reagent with gentle rocking, until the solution changes from pale brown to blue.

18. Carefully discard the GelCode reagent and replace with distilled water. Allow the gel to rinse with gentle rocking for 20 minutes. Wash 3 times with distilled water in the same fashion for 20 minutes each.

19. Following washing, blue antibody bands should resolve around 50 kDa. Image the bands with any gel imaging apparatus, such as a ChemiDoc.

20. Conjugation occurred successfully if there is an upward shift in weight from the unconjugated antibody to the conjugated antibody.

### *2.3.3 Optimization of Conjugated Antibodies*

Prior to performing a complete PhenoCycler experiment, conjugated antibodies must be further quality controlled and titrated. To do this, tissues are stained with the conjugated antibody of interest, and PhenoCycler reporters are manually applied and imaged. Staining fidelity is then assessed, and proper staining conditions are noted for larger multiplexed staining experiments.

*Tissue Staining and Fixation*

1. Follow steps 1 – 3 for *Deparaffinization and Antigen Retrieval*, described above.

2. To quench auto-fluorescence, place the slide in glass container and cover with Bleaching Solution. Sandwich the glass container between two LED lamps for 45 minutes at room temperature.

3. Replace the Bleaching Solution with fresh Bleaching Solution and repeat LED photobleaching for 45 minutes at room temperature (39).

   i. Note: we find that this extended LED photobleaching step helps decrease auto-fluorescence associated with FFPE tissue staining.

   ii. Note: The amount of $H_2O_2$ can be increased to 10% in tissue which demonstrate high levels of autofluorescence, such as heart or liver.

4. Wash the tissue 4 times in 1X PBS for 5 minutes per wash.

5. Dry the glass around the tissue with a Kimwipe, and circle tissue with a PAP pen.

6. Cover the tissue with Staining Buffer (*A*) and allow the tissue to equilibrate at room temperature for 30 minutes.

7. While the tissue is equilibrating, prepare the antibody solution. Antibodies are diluted in Staining Buffer, completed with N Blocker, G2 Blocker, J Blocker, and S Blocker (*A*).

8. Stain tissue by adding prepared antibody onto the tissue.

   i. Note: Staining time and temperature need to be optimized for each antibody. Common staining conditions include 3 hours at room temperature, or overnight at 4 °C.

9. Following antibody incubation, wash tissue 3 times in fresh Staining Buffer.

   i. Note: For highly multiplexed experiments where antibody staining conditions differ, staining can be done sequentially. For instance, 3 antibodies can be

applied for 30 minutes at 37 °C, then tissue can be washed in buffer and the remaining antibodies in the staining panel can be applied overnight at 4 °C.

10. Perform first tissue fixation, by incubating tissue in Post-Staining Fixation Solution (*A*) for 10 minutes at room temperature. Rinse tissue 3 times with PBS.

11. For the second fixation, transfer slides to a Coplin jar on ice filled with pre-chilled methanol. Allow to incubate for 5 minutes, then quickly transfer back to PBS. Rinse 3 times with PBS.

12. For the third and final fixation, add Final Fixative Solution (*A*) to slides, and incubate in a humidity chamber at room temperature for 20 minutes. Rinse tissue 3 times with PBS.

13. Transfer slide to Coplin jar with Storage Buffer (*A*).

i. Note: Slides can remain in Storage Buffer (*A*) at this step for up to 5 days at 4 °C.

*Manual Application of PhenoCycler Reporters and Tissue Imaging*

14. Prepare Screening Buffer (*A*) and allow to equilibrate to room temperature for 20 minutes before use.

15. Rinse slides in 3 changes of Screening Buffer (*A*) for 1 minute each, to allow the tissue to equilibrate to the new buffer.

16. Prepare the Reporter Stock Solution (*A*) and add 2.5 µL of each reporter to be tested to 97.5 µL of Reporter Stock Solution (*A*).

i. Note: More than one antibody/reporter can be tested at a time, provided the reporters are conjugated to different fluorophores. For instance, if tissue is stained with CD4-BX001 and CD19-BX002, 2.5 µL of both RX001-AF750 and

RX002-ATTO550 can be diluted into 95 µL of Reporter Stock Solution (*A*) for marker visualization in a single step.

17. Pipette the prepared Reporter Stock Solution (*A*) onto the tissue and incubate protected from light for 5 minutes.
18. Rinse slides in 3 changes of Screening Buffer (*A*), for 1 minute each.
19. Rinse slides with 1 change of 1X PhenoCycler Buffer (*A*).
20. Mount coverslips onto slides with Flouromount-G, and then allow to dry for 15 minutes.
21. Image slides with the same microscope that will be used for PhenoCycler image acquisition.

*Assessing PhenoCycler Staining*

When assessing the quality of a conjugated antibody, it is important to keep in mind the SNR from the previous step, as it will be used as a reference to compare for quality control. At this stage, multiple antibody concentrations should be tested as well as multiple incubation times and temperatures in order to get the best SNR. We also recommend performing one final staining with two extra markers: one that should co-localize and one that should not with the conjugated antibody being tested. This step will allow you to assess any non-specific binding of conjugated antibody and adjust staining and acquisition parameters for best SNR. Staining intensity and pattern should match the one obtained by standard IF staining.

### *2.3.4 PhenoCycler Multiplexed Imaging*

Once all antibodies have been conjugated and optimized, you may proceed to a full PhenoCycler staining experiment. Prior to beginning, all antibodies must be assigned to a cycle, a step that requires some thoughtful consideration. Each cycle will consist of up to 3 different antibodies, conjugated to barcodes that have reporters with different fluorophores. For instance, cycle 2 may consist of imaging CD4-BX001, CD19-BX002, and CD11b-BX003, which have RX001-AF750, RX002-ATTO550, and RX003-AF647 complementary reporters. When designing cycles, we try to include markers that are not likely to be present on the same cell type (ie, CD4, a marker of helper T cells, may be put in cycle 2, while CD3, a pan-lymphocyte marker, may be put in cycle 3). The first and last cycle of each staining experiment will consist of only DAPI ("Blank" cycle).

*Tissue Staining and Reporter Plate Preparation*

1. Follow steps 1 – 13 for *Tissue Staining and Fixation*, using all conjugated antibodies in the staining panel. Leave slide in Storage Buffer (*A*) until prepared to proceed to a full PhenoCycler Image Acquisition run.
    i. Note: For full PhenoCycler staining experiments, antibodies should not exceed 40% of the total Complete Staining Buffer solution, or insufficient blocking will occur.
2. Prepare enough Reporter Stock Solution (*A*) for the number of cycles in the experiment (each cycle requires a maximum of 250 µL of Reporter Stock Solution (*A*)).

3. For each cycle, label an amber 1.5 mL Eppendorf tube, and add 5 µL of each reporter for the assigned cycle. Complete to a volume of 250 µL using Reporter Stock Solution (*A*). Mix the contents gently by pipetting up and down.

i. Note: keep reporters on ice until use, and spin down prior to pipetting to collect any accumulated liquid in the cap.

ii. Note: the first cycle and the final cycle will consist of Reporter Stock Solution (*A*), with no florescent reporters added (ie. “Blank” cycles)

4. For each assigned cycle, pipette the reporter solution into a black-walled 96-well plate. Cover the wells with adhesive foil.

5. The reporter plate can be stored at 4 °C for up to two weeks or can be used immediately for the PhenoCycler experiment.

*PhenoCycler Image Acquisition*

Images are acquired using the default PhenoCycler protocol. In this study, we used the Phenocycler-Fusion system combining Phenocycler instrument with the Fusion microscope to streamline acquisition. We used acquisition parameters of the different antibodies defined during the titration step to acquire the fully stained tissue.

### *2.3.5 Open-Source Data Analysis*

Following a complete PhenoCycler staining experiment, PhenoCycler software will process images for downstream analysis. Imaging processing includes tile stitching and background correction. The final multiplexed image will be in QPTIFF format, which can be imported and visualized by many image analysis programs.

In this pipeline, we use the open source QuPath software, v3.2, which can be found here:

https://github.com/qupath/qupath/releases/

Cell segmentation is achieved using StarDist, which can be found here:

https://github.com/qupath/qupath-extension-stardist/releases

The pre-trained model we used for StarDist Segmentation can be found here:

https://github.com/qupath/models/tree/main/stardist

The StarDist .groovy file used in this study and sample Classifier data can be found here:

https://github.com/MMdR-lab/mouseCODEX-paper

*Setup*

1. Create directory including StarDist segmentation extension (qupath-extension-stardist-0.5.0.jar), the pre-trained StarDist model (dsb2018_heavy_augment.pb), and stardist_segmentation_0.5px.groovy file.
2. To install the StarDist extension into QuPath, open QuPath and drag and drop the segmentation extension (qupath-extension-stardist-0.5.0.jar) directly into the open QuPath window.
3. Create a list of the channel names in the order of acquisition in a .txt file with a separate line for each name.

*QuPath Image Import*

1. Create a new project in QuPath and add the PhenoCycler QPTIFF as a new image. Double click to open the image, and a pop-up will prompt you to select the image type. Set the image type as Fluorescence and keep “Auto-generate pyramids” selected.

i. Note: QPTIFF files are generated by the Phenocycler-Fusion system. For researchers using the Phenocycler combined to standard microscope, single channel OME-TIFF files can be combined into multiple channel OME-TIFF in ImageJ prior to proceeding.

2. Once the QPTIFF image is opened, all markers (i.e. αSMA, CD3, CD4, CD8, CD11b, CD11c, CD19. CD31, CD45, c-Myc, F4/80, FoxP3, Ki67, MelanA, MPO, and NaKATPase) will be simultaneously visible on the tissue, labeled as the fluorophore they were conjugated to in the order of cycle acquisition.

3. To set channel names, copy the list of channel names to the clipboard and then select the corresponding channels in the “Brightness/Contrast” dialog from the “View” dropdown menu and paste. Click apply to confirm.

4. In the “Brightness/Contrast” dialog box, you can toggle markers on and off, change their pseudo-colouring, and adjust their min/max display.

5. Make the channel names available as classifications in the “Annotations” tab by right-clicking or selecting the vertical ellipsis next to “Auto set” and choosing “Populate from image channels”.

*QuPath Cell Classification and Cell Segmentation*

6. To classify cells into phenotypes, a training image is used. The training image will contain 5 or 6 representation regions of interest, pooled into a single image.

i. To create a training image, select “Training images” from the “Classify” dropdown menu, and select “Create region annotations”.

ii. Using the default settings of: Width- 500; Height- 500; Size units- μm; Classification- Region*; and Location- Viewer Centre, create regions throughout the tissue which contain the cell phenotypes you wish to annotate.

iii. Save the image.

iv. From the “Classify” dropdown menu, select “Training images”, and select “Create training image”.

v. From the popup menu, select “Region*” as the Classification, type “50,000” px as Preferred image width, and toggle “Rectangles only”, then click OK.

vi. A training image will appear in the Project Image List dropdown menu.

vii. Open the training image, and save the project.

7. To segment the training image into cells, StarDist is used. Using the rectangle annotation tool, select the entire region.

8. To segment the annotated region into cells, drag and drop the stardist_segmentation_0.5px.groovy file into the open QuPath window. When the script editor appears, select “Run”.

i. Note: If an annotation is not selected, the error “Please select a parent object!” will appear.

9. A dialog box will appear, prompting the selection of the segmentation file. Choose the dsb2018_heavy_augment.pb file located in the directory you created in step 1.

10. Once segmentation is complete, you will be able to see cell detections in red overlay on the image. You can toggle the visibility of the cell detections using the overlay capacity slider bar at the top of the image window.

11. To proceed with cell classification, from the “Classify” dropdown menu, select “Training images” and select “Create duplicate channel training images”. From the popup window, select the markers that you wish to use to enable cell classification. Check the “Initialize Points annotations” box then select “OK”. There will now be duplicate training images in the Project Image List dropdown menu for each marker in the staining panel. These duplicate channels will be used for manual annotation of cell phenotypes.

i. Note: cell classification should be done in a single duplicate training image for phenotypes that are characterized by mutually exclusive markers (ie. lineage markers). For instance, if CD8+ T cells are classified as CD3+ CD8+, macrophages are classified as CD11b+ F4/80+, and fibroblasts are classified as CD45- αSMA+, they can be used in a classifier together.

ii. Note: in this project, we trained two classifiers to detect a total of 10 cell types. The first classifier was trained to detect CD8, FoxP3, CD31, F4/80, and CD11c. The second classifier was trained to detect CD4, CD19, MPO, αSMA, and Ki67+ tumour cells.

12. Open the duplicate image for the first cell type(s) you wish to classify.

13. Open the points annotation tool, add an annotation, and right click to set the annotation class (ex. if you are classifying helper T cells, set the class to CD4). Add a second annotation and set the class to “Ignore*”.

i. Note: an “Ignore” class is necessary for cell classification. This cannot be skipped.

14. Using point annotation, annotate 30-60 cells of your class of interest, and annotate another 30-60 cells as “Ignore*”. The “Ignore*” cells should be mutually exclusive from the cell you are classifying. For instance, if you are classifying CD4+ T cells, you could select CD8+ T cells, B cells, or tumour cells for the “Ignore*” class. This helps train the classifier to better detect your cells of interest.

15. From the “Classify” dropdown menu, select “Train object classifier”.

i. Set Object filter to “Cells”

ii. Set Classifier to “Artificial neural network (ANN_MLP)

iii. Set Feature to “All measurements”

iv. Set Classes to “Selected classes”

v. Set Training to “Unlocked annotations”

16. Click “Live update”. The cell mask on the training image should update to show where your cell phenotype has been detected.

17. Manually assess if the cell classifier is accurately detecting your cell phenotype of interest. If there are many false positive detections, continue to add annotations for “Ignore*”. If there are many false negative detections, continue to add annotations for your cell type of interest.

18. Once you are content with the cell classifier, enter the object classifier name, and click “Save”.

19. Repeat steps 12 – 18 for all cell phenotype classes you wish to annotate in your tissues.

20. Open the main image from the Project Image List.

21. Using the rectangle or polygon annotation tool, select the regions you wish to analyze. Following steps 7 – 9, use StarDist to segment the annotation region into cells.

22. Classify cells into phenotypes by opening the “Classify” dropdown menu, selecting “Object classification”, then selecting “Load object classification”. Select the classifiers you wish to apply to the tissue, then select “Apply classifiers sequentially”.

i. Note: If more than one classifier is used to detect cell types, there may be redundancy in classification (ie, some cells will be annotated as more than one class). For instance, in this study, our first classifier detected FoxP3+ cells, and our second classifier detected CD4+ cells. Thus, when the classifiers were applied together, regulatory T cells were classified as FoxP3+ CD4+.

ii. Note: Due to cell segmentation noise, sometimes dual classifiers may not make biological sense. It is up to the researcher to manually assess each cell class, and collapse classes as necessary.

23. Now, each cell will be annotated as a Phenotype. To export this data for spatial analysis with CytoMAP:

i. Save the QuPath project.

ii. From the “Measure” dropdown menu, select “Export Measurements.”

iii. Select the image you wish to export measurements from, and choose “cells” as the export type. Change separator type to “Comma (.csv)”.

iv. Click “Populate”, then select the columns to include from the dropdown list: Image Name, Image, Class, Centroid X, Centroid Y, and Cell Mean for each marker. The resulting .csv file will contain the fluorescence intensity of each marker for

each cell within the image, plus all cells will be annotated for their cellular phenotypes.

*CytoMAP Spatial Analysis*

24. In MATLAB, install the CytoMAP plugin in the “Add-Ons” drop down menu.
    i. For desktop use without MATLAB downloaded, an installer for the compiled version of CytoMAP is available at https://gitlab.com/gernerlab/cytomap/-/tree/master/. Follow the installation prompts
25. Open CytoMAP. From the “File” dropdown menu, select “Load Table of Cells”, then select the .csv file generated in step 23.
    i. Be mindful of .csv formatting when uploading. CytoMAP may not recognize certain symbols, such as ampersands or slashes.
26. A popup dialog box will prompt you to select the X axis. Click “Ch_Centroid_X_m” and click “Okay”.
27. A popup dialog box will prompt you to select the Y axis. Click “Ch_Centroid_Y_m” and click “Okay”.
28. A popup dialog box will prompt you to select the Z axis. Click “There is no Z (make a fake one)” and click “Okay”.
29. A “File Import Options” box will pop up. Select “Load”.
30. Select “Annotate Clusters”, and from the Select Classification Chanel dialog box, select “Ch_Class”. From the Annotate Class popup box, select “Save Annotations”. Close the Save Annotations box.

31. To make a heatmap showing the cellular mean intensity of the markers in the staining panel within the different cell phenotypes, click the “Extensions” dropdown menu, and select “cell_heatmaps.m”

i. Choose the cell phenotypes you wish to include.
ii. Choose the Channel MFIs you wish to include.
iii. Normalize per Sample.
iv. Select “MFI normalized to mean MFI of all cells”.
v. Select “Phenotype” for what to compare.
vi. Select “Individual Heatmap for each Sample”
vii. Select “linear” for scale.
viii. Click “Okay”.
    i. Note: If multiple .csv files are imported and annotated, you may choose to generate a combined heatmap.

32. To cluster cells into neighborhoods, select “Define Neighborhoods”.

i. Choose “Raster Scanned Neighborhood” for Neighborhood Type.
ii. Type “50” for Neighborhood Radius.
iii. Select “Fast Way”
iv. Click “Okay”

33. Once the loading bar for Defining Neighborhoods has finished, click “Cluster Neighborhoods into Regions”.

i. Select all Phenotypes for sorting.
ii. Use setting “Composition: Number of Cells/ Number of Cells in Neighborhood”

iii. Use setting “MFI normalized to mean MFI per neighborhood” and Normalize per Sample.
iv. For Colour scheme, select “sum(y,2)
v. For Number of Regions, select “Davies Bouldin (default)”
vi. For Model name, select “Create New Model”
vii. For Data Input Type, select “Raster Scanned Neighborhood”.
viii. For Algorithm, select “NN Self Organizing Map”.
ix. Click “Okay”
x. Enter a unique name for the Model.

34. Two figures will popup, one showing the Number of Clusters and the Davies Bouldin values, and the other showing the newly defined regions superimposed on the tissue image.

i. Note: In tumour tissues, overall cellular disorganization leads to fewer definitive regions.

35. To generate a heatmap showing the spatial relationships between cells in the tissues, select “Cell-Cell Correlation”.

i. Select the Phenotypes you wish to include.
ii. For Neighborhood Type, select your unique Model name.
iii. For data preparation, select “Cellularity: Number of Cells / Neighborhood”.
iv. Normalize per Sample.
v. Select “Individual Heatmap for each Sample”.
vi. For Colour Scale, select “linear”.
vii. For Calculation, select “Pearson Correlation Coefficient”.

viii. For Transform, select “None”.

ix. For Confidence Interval, select “1”.

36. CytoMAP can be used for other types of spatial analysis, and details can be found here:

https://cstoltzfus.com/posts/2021/06/CytoMAP%20Demo/

## 2.4 Results

### *2.4.1 Development of a Tunable PhenoCycler Antibody Panel for Staining Murine FFPE Tissue*

Using the protocols described above, we selected 16 antibodies which could be used to phenotype most common cells found in the murine TME (**Figure 2.2A**). Each of these antibodies were conjugated to Akoya PhenoCycler barcodes (**Table 2.2**) and were optimized for PhenoCycler staining. Each barcode has a complementary reporter conjugated to either ATTO550, AF647, or AF750, and barcodes were selected for each antibody with this in mind. In general, antibodies that showed very strong SNR were conjugated to barcodes with AF750-tagged complementary reporters, whereas antibodies that corresponded to antigens of lower abundance and lower expression were conjugated to barcodes with AF647-tagged complementary reporters, and antibodies that marked antigens of medium abundance and weak to medium SNR were conjugated to barcodes with ATTO550-tagged complementary reporters. With this staining panel, we were able to quantify tumour cells, endothelial cells, fibroblasts, myeloid cells (macrophages, neutrophils, and dendritic cells) and lymphoid cells (helper T cells, cytotoxic T cells, regulatory T cells, and B cells) in the murine TME (**Figure 2.2B**). We found that the highly multiplexed PhenoCycler staining had similar fidelity to single-plex

IF stains for each antibody included in the staining panel (**Supplemental Figure 2.1**). Furthermore, the protocols for analysis described above were used to examine how the spatial relationships between these cell types change across tumour models and experimental conditions.

**A**

| Antibody | Cell Type |
|---|---|
| aSMA | Fibroblast |
| CD3 | General T Cell |
| CD4 | Helper T Cell |
| CD8 | Cytotoxic T Cell |
| CD11b | Myeloid Cell |
| CD11c | Dendritic Cell |
| CD19 | B Cell |
| CD31 | Endothelial Cell |
| CD45 | Hematopoeitc Cell |
| c-Myc | Tumor Cell |
| F4/80 | Macrophage |
| FoxP3 | Regulatory T Cell |
| Ki67 | Tumor Cell |
| MelanA | Tumor Cell |
| MPO | Neutrophil |
| NaK-ATPase | Membrane Marker |

**B**

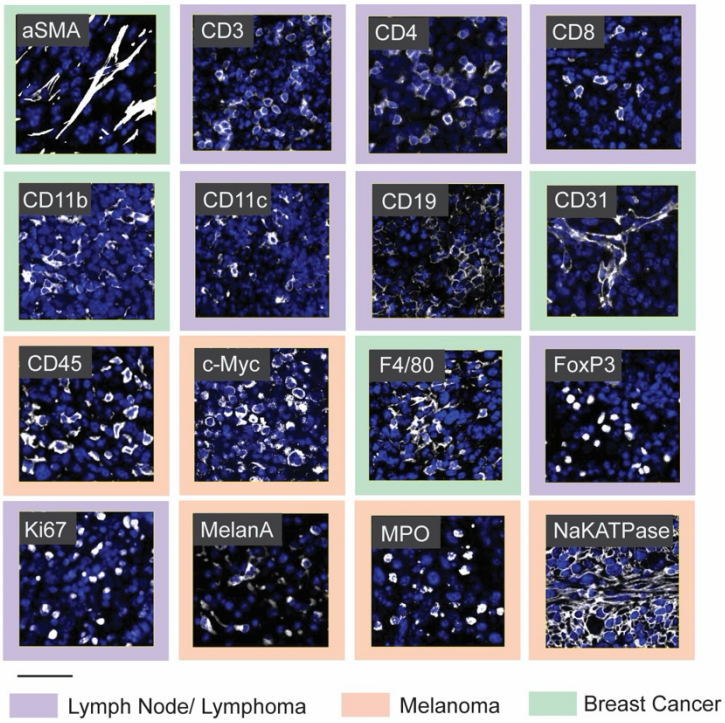


**Figure 2.2: 16-plex PhenoCycler staining of murine FFPE tissues**
**A.** Table showing the antibodies included in our Murine FFPE PhenoCycler staining panel, and the cell type they are used to identify. **B.** Images showing successful PhenoCycler staining of each antibody in the staining panel. In each image, DAPI is blue, and each individual marker is white. The colour of the outer border indicates the tissue type in the image. Scale bar is 50 μM.

**Table 2.2. Primary Antibody Table.**

| Antibody | Company | Clone | Catalog No. | Barcode | Reporter |
|---|---|---|---|---|---|
| αSMA | Abcam | 1A4 | ab240654 | BX014 | RX014-ATTO550 |
| CD3 | Abcam | CD3-12 | ab255972 | BX017 | RX017-ATT0550 |
| CD4 | Invitrogen | 4SM95 | 14-9766-82 | BX002 | RX002-ATTO550 |
| CD8 | Invitrogen | 4SM15 | 14-0808-82 | BX005 | RX005-ATTO550 |
| CD11b | Abcam | EPR1344 | ab209970 | BX003 | RX003-AF647 |
| CD11c | Cell Signaling | D1V9Y | 39143SF | BX015 | RX015-AF647 |
| CD19 | Cell Signaling | D4V4B | 86916SF | BX027 | RX027-AF647 |
| CD31 | Dianova | SZ31 | DIA-310-BA-2 | BX026 | RX026-ATT0550 |
| CD45 | R&D Systems | Polyclonal | AF114-SP | BX007 | RX007-AF750 |
| c-Myc | Abcam | Y69 | ab168727 | BX001 | RX001-AF750 |
| F4/80 | Cell Signaling | D2S9R | 25514SF | BX020 | RX020-ATTO550 |
| FoxP3 | Cell Signaling | D6O8R | 72338SF | BX019 | RX019-AF750 |
| Ki67 | Akoya | B56 | PN 232179 | BX047 | RX047-ATTO550 |
| MelanA | Abcam | EPR20380 | ab222483 | BX004 | RX004-AF750 |
| MPO | R&D Systems | Polyclonal | AF3667-SP | BX013 | RX013-AF750 |
| NaK-ATPase | Abcam | EP1845Y | ab167390 | BX023 | RX023-ATTO550 |

### *2.4.2 Generation of a Multi-Cancer TMA for PhenoCycler Staining*

Given that there is conservation amongst the cell types found in the TME across a number of tumour types (40), we generated a TMA with tumour cores banked from widely used pre-clinical mouse models of lymphoma, breast cancer, and melanoma, and matched normal tissues, with the goal of performing spatial phenotyping of the murine TME. To achieve this, archival FFPE tissue blocks were sectioned and stained with H&E and an anti-CD45 antibody to facilitate selection of immune-rich regions within the tumours for core-punching (**Figure 2.3A**). From each tissue block, two to three 1 mm cores were included, for a total of 84 cores (**Figure 2.3B**).

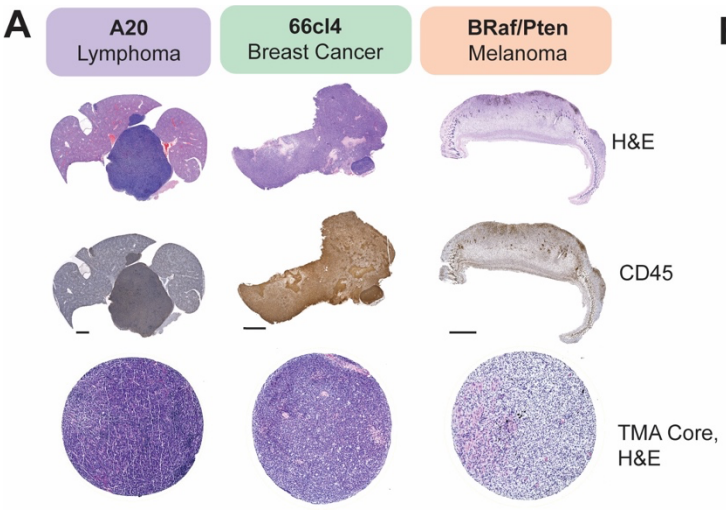


**B**

| Lymphoma | | | |
|---|---|---|---|
| Tissue | Samples | Cores/Sample | Total |
| Lymph Node | 3 | 2 | 6 |
| Eu-Myc | 3 | 3 | 9 |
| Liver | 3 | 2 | 6 |
| A20 | 3 | 2 | 6 |

| Breast Cancer | | | |
|---|---|---|---|
| Tissue | Samples | Cores/Sample | Total |
| Normal MFP | 3 | 2 | 6 |
| 66cl4 | 3 | 3 | 9 |
| 4T1 | 3 | 2 | 6 |
| 4T1 Liver Met | 3 | 1 | 3 |
| Adjacent Liver | 3 | 2 | 6 |

| Melanoma | | | |
|---|---|---|---|
| Tissue | Samples | Cores/Sample | Total |
| Normal Skin | 3 | 2 | 6 |
| BRaf/Pten | 3 | 2 | 6 |
| YUMMER1.7 + IgG | 3 | 2 | 6 |
| YUMMER1.7 + aPD1 | 3 | 3 | 9 |

Total Cores: **84**

**Figure 2.3: Generation of a murine tissue microarray (TMA) for PhenoCycler Staining**
**A.** Representative H&E and CD45 staining from murine tumour tissues. H&E and CD45 staining was used to select regions of interest for TMA core punching. Scale bars represent 100 µm. Bottom row shows H&E staining of the tissue cores, following TMA generation. Each TMA core is 1mm in size. **B.** Table indicating the types and numbers of cores included in our multi-cancer murine TMA.

For the lymphoma portion of the TMA, cores from A20 and Eµ-Myc tumours were included. A20 is a commonly used mouse model of B Cell Non-Hodgkin's Lymphoma (B-NHL), syngeneic to BALB/C mice (41). Upon tail vein injection, A20 cells will home to the liver to form an aggressive extranodal lymphoma, and samples from day-27 post-A20 tail vein injection were included in the TMA, with matched adjacent non-tumour bearing liver tissue (ie, tissue from a non-tumour bearing liver lobe). Eµ-Myc is a B-NHL model syngeneic to C57BL/6J mice, which forms tumours primarily in the spleen and cervical and inguinal lymph nodes. Samples from the lymph nodes of non-tumour bearing mice and from the cervical lymph nodes of mice at day-14 post-Eµ-Myc injection were included in the TMA.

Tumour samples grown from the 66cl4 and 4T1 murine triple-negative breast cancer cell lines were included in the multi-cancer TMA. Both cell lines are capable of forming

primary tumours following inoculation into the mammary fat pads of syngeneic BALB/c mice (42). However, they differ in their metastatic potential and route of dissemination (43). 66cl4 cells are weakly metastatic and tend to travel via the lymphatic system to the lung (43). Samples from our previously published (44) cohort of 66cl4 tumours from day-33 post-injection (roughly 1750 $mm^3$ in size) were included. The highly aggressive 4T1 model is metastatic to the bone, lung and liver and predominantly does so via the vasculature (43) (45). We included samples from primary 4T1 tumours harvested day-10 post-injection when they are 600 $mm^3$. Additionally, to define differences between the TME of primary and metastatic 4T1 tumours, samples were included from mice with 4T1 liver metastases, generated using the intrasplenic injection model of experimental metastasis (46).

Finally, to enable comparison of ICI-resistant and ICI-susceptible murine melanoma models, melanomas from the *Tyr::CreER*/*BRaf*$^{CA/+}$/*Pten*$^{lox/lox}$ conditional melanoma model (47) and the YUMMER1.7 syngeneic melanoma model (48) were included. The *Tyr::CreER*/*BRaf*$^{CA/+}$/*Pten*$^{lox/lox}$ transgenic mouse is a well-described murine model of melanoma, which allows 4-hydroxytamoxifen-inducible melanocyte-targeted *BRAF*$^{V600E}$ expression and simultaneous *PTEN* inactivation (referred to hereafter as *BRAF*$^{V600E}$/*PTEN*$^{-/-}$). Murine *BRAF*$^{V600E}$/*PTEN*$^{-/-}$ melanomas are characterized by low immune cell infiltration and are therefore known to be “immune cold” and resistant to ICI-therapy (49, 50). YUMMER1.7 cells were derived from a *BRAF*$^{V600E}$/*PTEN*$^{-/-}$ melanoma following subsequent exposure to ultraviolet radiation to increase mutational burden, making YUMMER1.7 melanomas sensitive to ICI treatment (48). We included samples

harvested at 2000 $mm^3$ from YUMMER1.7 melanomas treated with either αPD-1 immunotherapy or IgG control.

### *2.4.3 Comparing the TME of Nodal and Extranodal Murine B Cell Non-Hodgkin's Lymphoma*

B-NHL is the most commonly diagnosed lymphoid malignancy, arising from the abnormal proliferation of B lymphocytes. B-NHL frequently arises in secondary lymphoid organs, such as the lymph nodes or spleen, but extranodal involvement is common and has been shown to correlate with adverse outcomes (51). Studies have demonstrated that B-NHL has distinct biological features between different extranodal sites (52-54), and mouse modelling provides the opportunity to functionally examine how varied TMEs can impact the B-NHL immune cell infiltration, specifically as A20 tumours develop in the murine liver (**Figure 2.4A**), while Eμ-Myc tumours develop in the lymph nodes (**Figure 2.4B**).

Following PhenoCycler staining, DAPI-based segmentation (StarDist) of images was performed to extract single-cell marker expression, and cells were classified into phenotypes based on marker expression (**Figure 2.4C**; see protocols below). In A20 and Eμ-Myc tumours, we were able to detect dendritic cells, B cells, endothelial cells, CD4+ T cells, CD8+ T cells, macrophages, regulatory T cells (Tregs), tumour cells, neutrophils, and fibroblasts. Of note, in these tissues and in the tissues derived from other tumour types, CD31+ endothelial cells formed close contacts with αSMA+ fibroblasts, leading to fluorescence spillover of CD31 and αSMA lineage markers following cell segmentation. We classified these cells as "EndoFib", representing close contacts between endothelial cells and fibroblasts. This was similarly observed with tightly packed CD4+ and CD8+ T

cells in lymphoma tissues only, and we termed these cells “T Cells” in downstream analyses. Despite these challenges in cell segmentation, the proportions of immune cell types found in the A20 TME by PhenoCycler correlated closely with archival flow cytometry immunophenotyping of dissociated A20 tumours, showing that these two methodologies can similarly identify cells in the TME (**Figure 2.4D**).

The A20 B-NHL TME was characterized by high infiltration of immune cells (55.12%), relative to adjacent non-tumour bearing liver (16.27%) (**Figure 2.4E**). The A20 immune infiltration was comprised of dendritic cells (defined as CD11b+ CD11c+), macrophages (defined as CD11b+ F4/80+), CD8+ T cells (defined as CD3+ CD8+ FoxP3-), and Tregs (defined as CD3+ CD4+ FoxP3+), while immune cells in the adjacent liver were almost exclusively macrophages (likely Kupffer cells), consistent with what is expected in normal liver. We analyzed spatial interactions between the different cell phenotypes in A20 tumours using CytoMAP to calculate the probability of different cell types being within 50 μM of each other (55) (see methods). We found that Tregs were in close proximity to T cells (correlation coefficient = 0.695) and CD8+ T cells (correlation coefficient = 0.6011). Furthermore, tumour cells were spatially segregated from immune cells such as CD8 T cells (correlation coefficient = -0.1289), macrophages (correlation coefficient = -0.1287), and Tregs (correlation coefficient = -0.1942; **Figure 2.4F-G**). These results suggest that tumour cells tend to localize together within the extranodal B-NHL tumour mass while immune cells localize together at the tumour periphery and highlight that Tregs are a critical mediator of CD8+ T cell immunosuppression in A20 tumours.

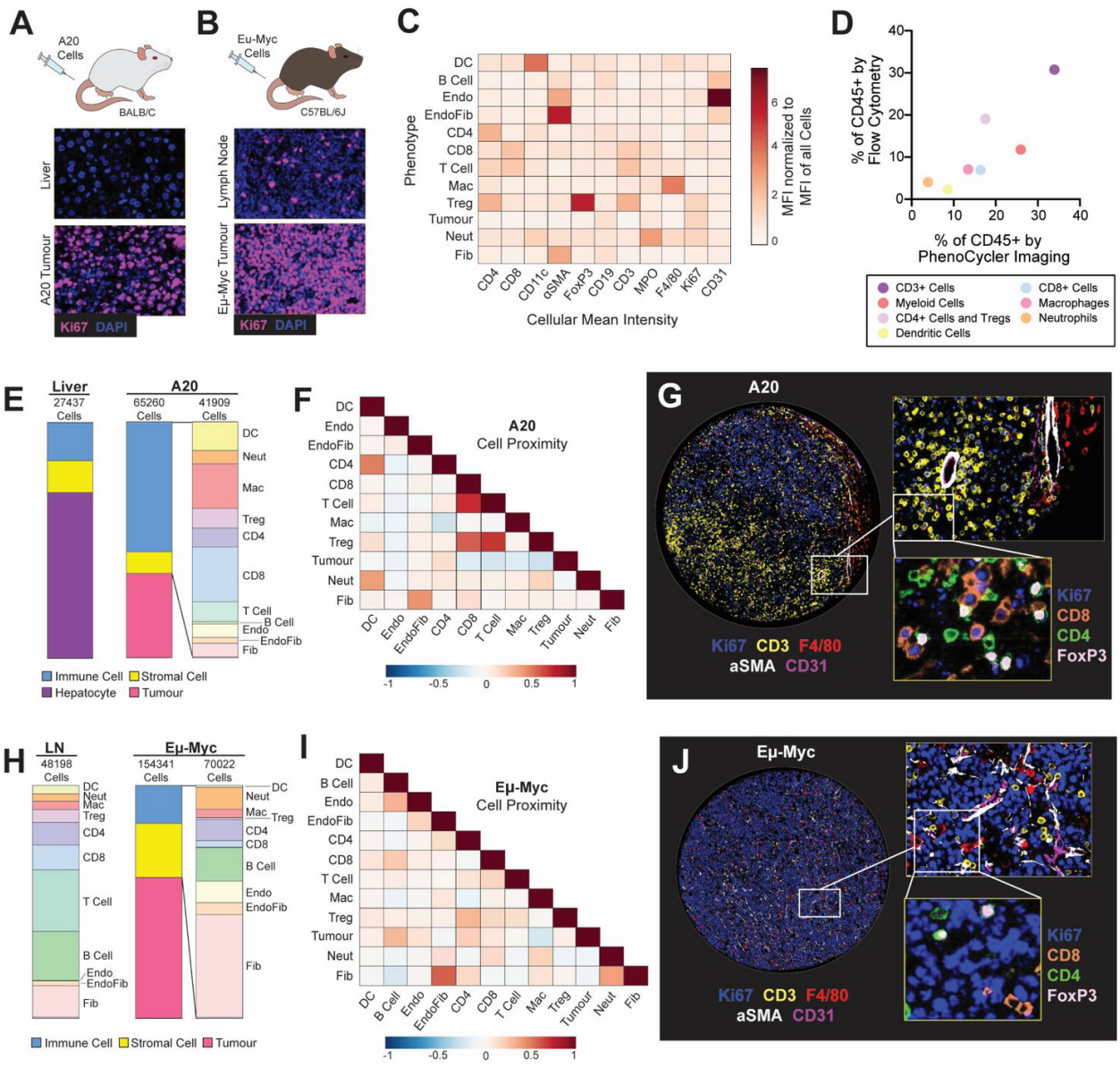


**Figure 2.4: PhenoCycler imaging of the murine nodal and extra-nodal B-cell lymphoma tumour microenvironment**

**A.** Schematic of the A20 model of extranodal B-NHL, and representative images of Ki67 staining in healthy liver and A20 tumour-bearing liver. **B.** Schematic of the Eμ-Myc model of nodal B-NHL, and representative images of Ki67 staining in healthy lymph node and an Eμ-Myc tumour-bearing lymph node. **C.** Heatmap showing the normalized cellular mean intensity of markers within the PhenoCycler staining panel, in different phenotypes of cells in A20 and Eμ-Myc tumours. **D.** Scatter plot comparing the proportions of different cell phenotypes as determined by PhenoCycler staining versus archival flow cytometry data, for A20 tumours. Pearson r = 0.8551, p = 0.0142. **E**. Proportions of different cell types in adjacent healthy liver and A20 tumour-bearing liver. **F.** Heatmap showing neighborhood analysis of A20 tumours, as Pearson correlation coefficient between cells. Blue hue indicates cells are likely to be in further proximity, while red hue indicates that

cells are likely to be in closer proximity. **G.** Representative image of an A20 tumour core. **H.** Proportions of different cell types in healthy lymph nodes and Eμ-Myc tumour-bearing lymph nodes. **I.** Heatmap showing neighborhood analysis of A20 tumours, as Pearson correlation coefficient between cells. **J.** Representative image of an Eμ-Myc tumour core.

As expected, non-tumour bearing murine cervical lymph nodes consisted almost entirely of immune cells (84.04%); however, the presence of Eμ-Myc tumours drastically decreased this proportion (16.41%). In Eμ-Myc tumours, the overall immune composition was altered relative to healthy lymph nodes, with an increase in neutrophils (defined as CD11b+ MPO+), and a decrease in Tregs, dendritic cells, and CD8+ T cells (**Figure 2.4H**). Eμ-Myc tumours also had an increased proportion of stromal cells, including fibroblasts and endothelial cells (23.09% in Eμ-Myc tumours, compared to 15.96% in healthy lymph node). Spatial analysis further demonstrated that Eμ-Myc tumours are relatively disorganized (**Figure 2.4I**), and different cell types seem to be randomly distributed throughout the tumour. For instance, while CD8+ T cells and Tregs can be detected (**Figure 2.4J**), they are spatially segregated and are likely not functionally interacting (correlation coefficient = 0.2058).

Our data shows that the presence of A20 extranodal tumours induces the recruitment of immune cells to the liver, while the presence of Eμ-Myc nodal tumours leads to immune cell displacement from the lymph nodes. Furthermore, as it has been previously suggested (56), our data suggest that A20 tumours rely on Tregs to induce immunosuppression and achieve immune evasion, while Eμ-Myc tumours are immune-depleted, and therefore do not require inhibitory immune cell interactions to achieve immunosuppression. Thus, these two models of B-NHL employ drastically different strategies to avoid immune destruction.

### *2.4.4 Defining Differences in the TME of Primary and Metastatic Murine Breast Cancer*

Breast cancer is a heterogeneous disease, comprised of different molecular subtypes. Patients with triple-negative breast cancer (TNBC) have the worst prognosis, largely due to aggressive tumour behaviour, increased risk of metastasis, and resistance to conventional anti-cancer therapies (57). Treatments which target the TME in TNBC have gained increased attention in recent years, spurred on by data demonstrating the strong immunogenicity of this tumour type (58) and success of combined chemotherapy and immunotherapy in clinical trials (59, 60). Understanding the cellular landscape of TNBC tumours will undoubtedly be beneficial for the continued development of successful TME-targeting therapies.

Towards this goal, we used PhenoCycler to image primary tumours from the commonly used pre-clinical murine 66cl4 and 4T1 TNBC models, as well as 4T1 liver metastases (**Figure 2.5A-B**). Using the protocols described below, we performed cell-segmentation and cell-clustering to identify cell phenotypes (**Figure 2.5C**). In these tumours, we could identify the same immune and stromal cell types as were found in lymphoma tumours. However, while lymphoma tumour cells were characterized by Ki67 positivity, we found that tumour cells in breast cancer models could be stratified based on Ki67 expression (**Figure 2.5D**), and both Ki67+ and Ki67- tumour cells were numerous enough to merit individual classification. Interestingly, the percentage of Ki67+ tumour cells was higher in the more aggressive 4T1 samples compared to 66cl4 (**Figure 2.5E**; percentage of Ki67+ tumour cells among total tumour cells: 66cl4: 41.13%; 4T1: 80.65%; 4T1-liver: 63.47%). The proportion of CD45+ immune cells was similar in all tumour

sample types (**Figure 2.5E**; 66cl4: 45.39%; 4T1-primary: 52.52%; 4T1-liver: 49.84%), with macrophages representing the dominant immune cell type (**Figure 2.5E-F**: 66cl4: 39.35%; 4T1-primary: 40%; 4T1-liver: 38.59%) in line with previously published reports (61).

In addition to the composition of the immune cell landscape, cell neighbourhood analyses highlighted further differences between tumour types. Immune cells in 66cl4 tumours were largely localized together in restricted regions, but were found to be intermingling with other cell types throughout 4T1 tumours (**Figure 2.5G-I**). In particular, 4T1 tumours were observed to have strong spatial interactions between CD8+ T cells and endothelial cells (correlation coefficient = 0.6198), and $Ki67^{+}$ tumour cells and macrophages (correlation coefficient = 0.5448; **Figure 2.5H**). In contrast, the interaction between endothelial cells and CD8+ T cells is lost in 4T1 liver metastases (correlation coefficient = -0.1667) compared to the primary tumour, with a concomitant increase in interactions between endothelial cells and neutrophils (correlation coefficient = 0.4064) and total neutrophil abundance (**Figure 2.5J-K**; 4T1: 0.19%; 4T1-liver: 0.88%). These data corroborate observations that formation of 4T1 liver metastases is heavily reliant on the infiltration of neutrophils into the TME (62), suggesting that proximity to the vascular endothelium may be indicative of immune cell influx patterns.

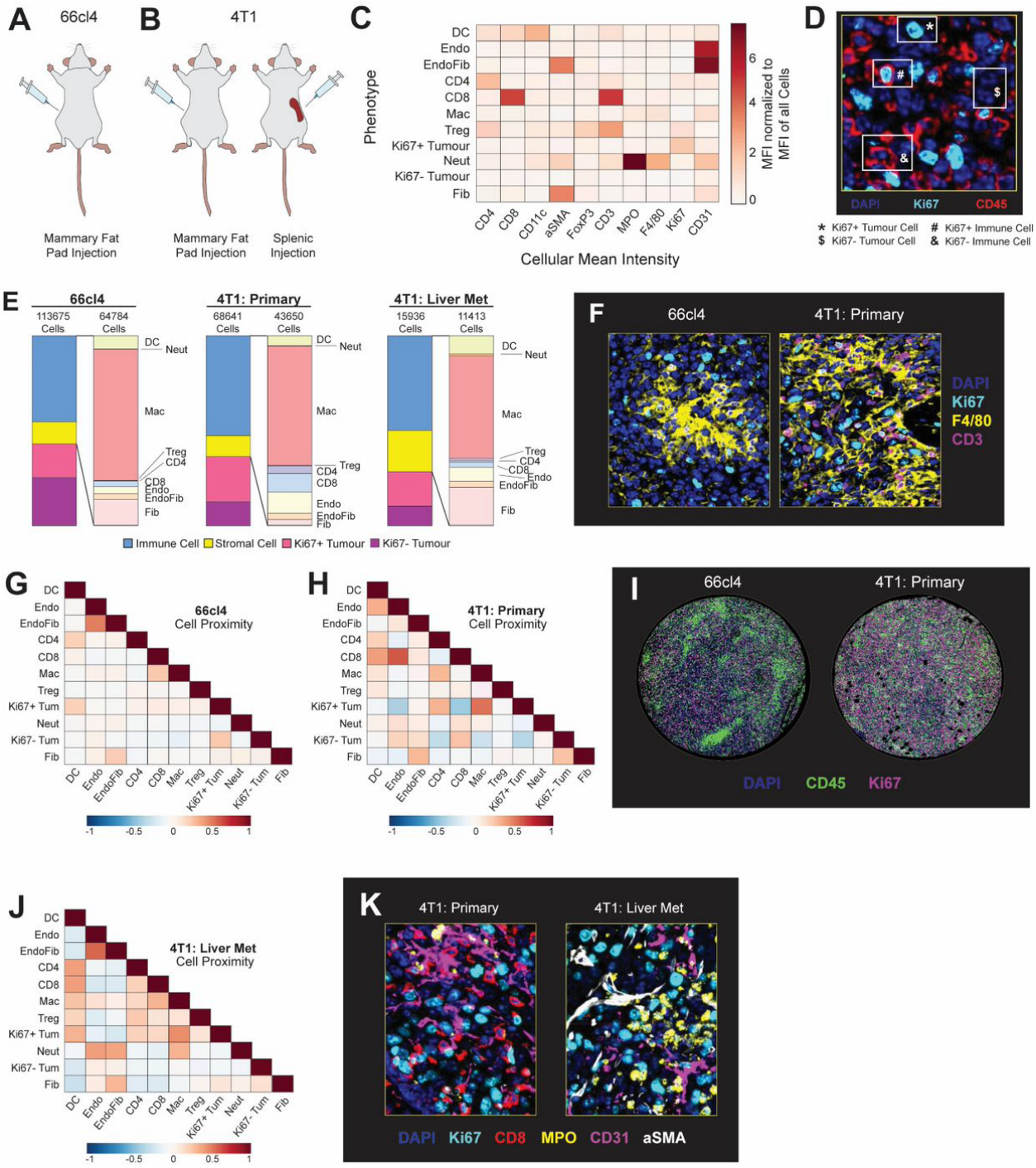


**Figure 2.5: PhenoCycler imaging of the murine breast cancer tumour microenvironment**

**A.** Schematic of the 66cl4 murine model of breast cancer. **B.** Schematics of the 4T1 murine models of breast cancer and breast cancer liver metastasis. **C.** Heatmap showing the normalized cellular mean intensity of markers within the PhenoCycler staining panel, in different phenotypes of cells in 66cl4 and 4T1 tumours**. D.** Representative image showing Ki67+ and Ki67- tumour cells. **E.** Proportions of different cell types in 66cl4 and

4T1 tumours. **F.** Representative images of macrophages and T cells in 66cl4 and 4T1 primary tumours. **G.** Heatmap showing neighborhood analysis of 66cl4 tumours. as Pearson correlation coefficient between cells. **H.** Heatmap showing neighborhood analysis of 4T1 primary tumours, as Pearson correlation coefficient between cells. **I.** Representative images showing immune cell infiltration patterns in 66cl4 and 4T1 tumours. **J.** Heatmap showing neighborhood analysis of 4T1 liver metastases, as Pearson correlation coefficient between cells. **K.** Representative images comparing immune and stromal cell types in 4T1 primary and 4T1 liver metastases.

These data illustrate the utility of PhenoCycler technology to profile the immune landscape of murine TNBC tumours, as we characterized immune cell composition of FFPE-processed murine tumour types while layering on top cellular distributions in space. We propose that future applications of PhenoCycler technology, using in-depth antibody panels which assess immune cell function or polarization, may aid in uncovering therapeutic options to augment anti-tumour immunity in TNBC patients.

### *2.4.5 Characterizing the TME of ICI-Resistant and ICI-Susceptible Murine Melanoma*

Melanoma is one of the most immunogenic cancer types, due to its high mutational burden, which leads to the production of neoantigens that are recognized by patrolling immune cells. To this end, ICI therapies have revolutionized the treatment of melanoma, but innate and acquired resistance remain as clinical challenges. Furthermore, clinical studies have shown that ICI resistance is associated with changes in TME composition (63, 64).

We used two immune competent murine models of melanoma for PhenoCycler staining: the *BRAF*$^{V600E}$/*PTEN*$^{-/-}$ model and the YUMMER1.7 model (**Figure 2.6A**). *BRAF*$^{V600E}$/*PTEN*$^{-/-}$ melanomas exhibit high intratumoural heterogeneity and melanoma cell plasticity, are known to be immune “cold”, and are insensitive to ICI treatment. Conversely, YUMMER1.7-derived tumours are highly immunogenic and are susceptible

to ICI-mediated tumour inhibition (48). In our previous work, we have shown that αPD-1 immunotherapy reduced the growth of YUMMER1.7 tumours and improved the overall survival of mice, but most tumours failed to go into complete remission (50), mimicking the human clinical scenario where more than half of patients experience disease progression following αPD-1 treatment (65). Thus, we aimed to determine if tumour regrowth following αPD-1 treatment is associated with TME remodeling by comparing isotype control (IgG)-treated tumours with αPD-1-treated tumours (αPD-1-relapsed), harvested when tumours were 2000 $mm^3$. Additionally, samples from *BRAF*$^{V600E}$/*PTEN*$^{-/-}$ tumours facilitated further comparison between an ICI-resistant and an ICI-sensitive murine model of melanoma.

PhenoCycler images from these murine melanomas were cell-segmented and classified based on marker expression (**Figure 2.6B**). Similarly to breast cancer, we found that two distinct populations of tumour cells were present: Ki67+ and Ki67- (**Figure 2.6C**). *BRAF*$^{V600E}$/*PTEN*$^{-/-}$ tumours were composed of 79.98% Ki67- tumour cells, and 2.88% Ki67+ proliferating tumour cells (**Figure 2.6D**). These data are consistent with our previous work demonstrating that *BRAF*$^{V600E}$/*PTEN*$^{-/-}$ melanoma cells typically undergo phenotype switching from a more proliferative to a more invasive state, that is characterized by slower proliferation. The remaining 17.12% of cells within *BRAF*$^{V600E}$/*PTEN*$^{-/-}$ tumours were stromal cells (5.29%) and immune cells (11.83%). The majority of the immune cells were found to be macrophages, with minimal T cell infiltration. Consistent with the fact that *BRAF*$^{V600E}$/*PTEN*$^{-/-}$ tumours are immune “cold”, spatial analysis demonstrated that cells within these tumours did not have preferential

interactions with each other (**Figure 2.6E**) and appeared randomly distributed within the tissues (**Figure 2.6F**).

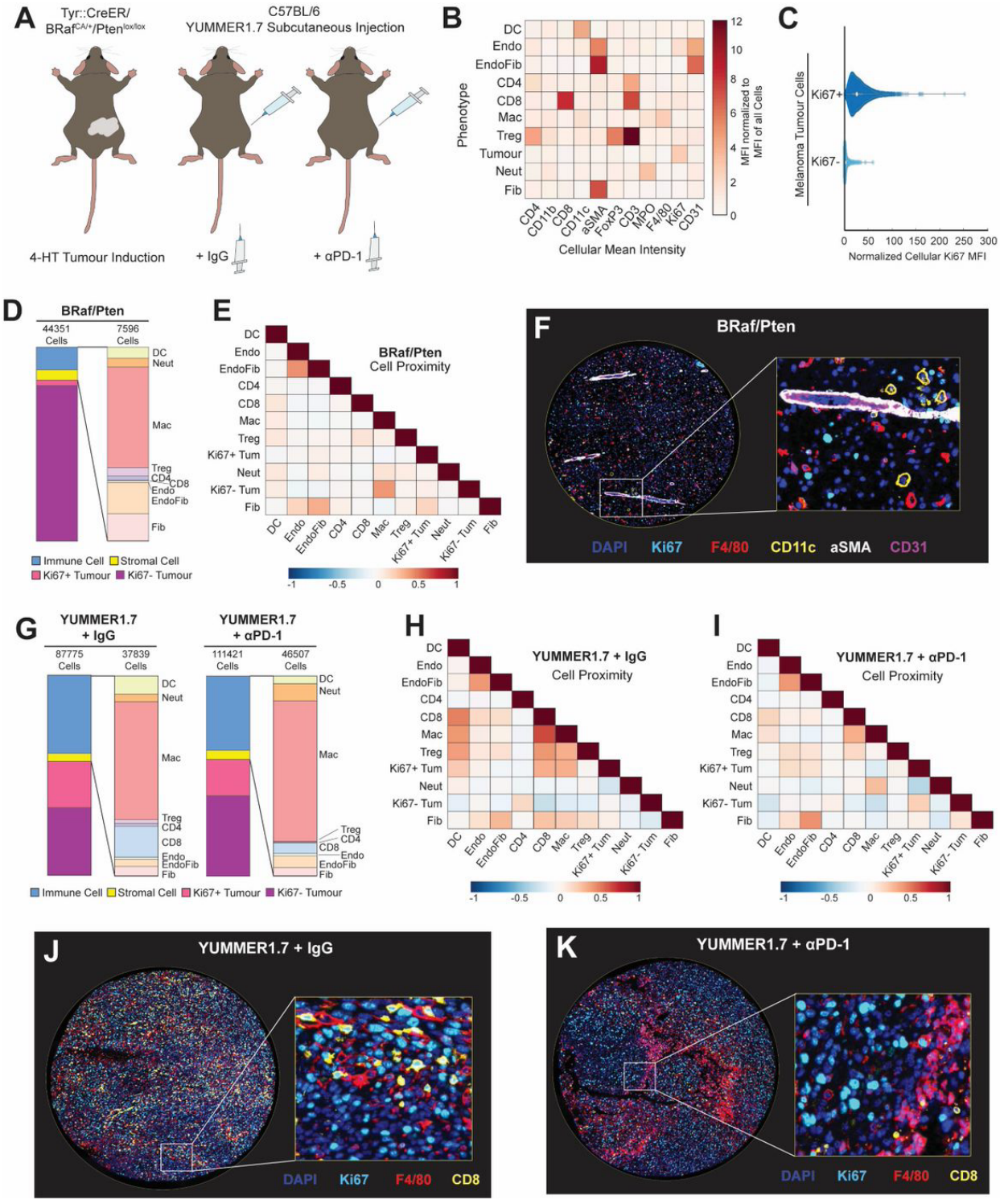

**Figure 2.6: PhenoCycler imaging of the murine melanoma tumour microenvironment**
**A.** Schematics of the BRaf/Pten and YUMMER1.7 murine models of melanoma. **B.** Heatmap showing the normalized cellular mean intensity of markers within the PhenoCycler staining panel, in different phenotypes of cells in BRaf/Pten and YUMMER1.7 tumours. **C.** Normalized Ki67 mean fluorescence intensity in Ki67+ tumour cells and Ki67- tumour cells. **D.** Proportions of different cell types in BRaf/Pten tumours. **E.** Heatmap showing neighborhood analysis of BRaf/Pten tumours, as Pearson correlation coefficient between cells. **F.** Representative image of BRaf/Pten tumour core. **G.** Proportions of different cell types in YUMMER1.7 tumours, treated with IgG control or αPD-1. **H-I.** Heatmap showing neighborhood analysis of YUMMER1.7 tumours treated with IgG control (**H**) or αPD-1 (**I**), as Pearson correlation coefficient between cells. **J.** Representative image of YUMMER1.7-IgG tumour core. **K.** Representative image of YUMMER1.7-αPD-1 tumour core.

As compared to *BRAF*$^{V600E}$/*PTEN*$^{-/-}$ tumours, YUMMER1.7 tumours had a significantly higher proportion of proliferative (Ki67+) tumour cells, which was slightly decreased upon resistance to αPD-1 treatment (**Figure 2.6G**; 23.23% in IgG-treated samples versus 18.22% in αPD-1-relapsed samples). Furthermore, both IgG-treated and αPD-1-relapsed YUMMER1.7 tumours were more immunogenically “hot” with increased immune cell abundance as compared to *BRAF*$^{V600E}$/*PTEN*$^{-/-}$ tumours (IgG-treated: 39.11% immune cells; αPD-1-relapsed: 37.1% immune cells). Whie IgG-treated and αPD-1 relapsed YUMMER1.7 tumours had similar immune cell invasion, there were distinct differences in cellular organization. Spatial analysis of YUMMER1.7-IgG tumours showed strong interactions between CD8+ T cells and macrophages (correlation coefficient = 0.6482), and CD8+ T cells and dendritic cells (correlation coefficient = 0.4957; **Figure 2.6H**). YUMMER1.7-IgG Ki67+ tumour cells were in close proximity to these immune cells (CD8+ T cell/ Ki67+ tumour cell correlation coefficient = 0.3529; macrophage/ Ki67+ tumour cell correlation coefficient = 0.3535; dendritic cell/ Ki67+ tumour cell correlation coefficient = 0.2486), as compared to Ki67- tumour cells (CD8+ T cell/ Ki67- tumour cell

correlation coefficient = -0.2316; macrophage/ Ki67- tumour cell correlation coefficient = -0.1342; dendritic cell/ Ki67- tumour cell correlation coefficient = -0.1013). However, Ki67- tumour cells were in closer contact with CD4+ T cells (Ki67+ tumour cell/ CD4+ T cell correlation coefficient = -0.0339, Ki67- tumour cell/ CD4+ T cell correlation coefficient = 0.1932). In αPD-1-relapsed tumours, all of these cellular contacts were reduced (**Figure 2.6I-K**), supporting reduced tumour-immune cell interaction as a mechanism of acquired ICI resistance in melanoma.

All together, these results support that Ki67+ proliferative melanoma cells have higher immunogenicity. In agreement with this, *BRAF*$^{V600E}$/*PTEN*$^{-/-}$ tumours have a substantially increased proportion of Ki67- tumour cells, correlating with a decreased proportion of infiltrating immune cells. Moreover, in YUMMER1.7-IgG tumours, Ki67+ tumour cells maintain close contacts with immune cells. In αPD-1-replapsed YUMMER1.7 tumours, there is no preferential interaction of Ki67+ or Ki67- tumour cells with immune cells, indicating immune dysfunction upon the emergence of ICI-resistance. To this end, our data supports the notion that ICI-resistance is associated with decreased interactions between immune cells and tumour cells (66), as αPD-1-relapsed YUMMER1.7 tumours have similar macrophage infiltration as compared to IgG controls, yet the tissue organization is altered such that there are limited cellular contacts between macrophages and tumour cells.

## 2.5 Discussion

### *2.5.1 PhenoCycler Imaging of Murine FFPE Tumour Tissues*

The TME is a central player in many of the biological challenges associated with cancer treatment, such as immune escape, disease metastasis, and drug resistance. Thus, it is critically important to assess both the composition and the spatial dynamics of the TME in mouse models that are commonly used in pre-clinical cancer research. Previously, PhenoCycler imaging of murine tissues had been limited to fresh frozen tissues. Here, we detail imaging FFPE murine tissues and provide our protocols for the optimization and conjugation of antibodies for this purpose. To illustrate the feasibility of this approach, we provide data showing successful staining of murine lymphoma, melanoma, and breast cancer tissues.

Immunofluorescence imaging of FFPE tissues is not without challenges. FFPE tissues tend to have high auto-fluorescence, which can distort true positive staining. Additionally, formalin-fixation induces protein cross-linking, leading to epitope masking and difficulties in primary antibody binding (38). However, many research groups archive tissues from previous pre-clinical studies in FFPE format; thus, it is a worthwhile endeavor to optimize antibodies for highly multiplexed imaging of murine FFPE tissues, to allow for the utilization of archival materials. To this end, the selection of antibody clones with an ideal SNR was a critical first step towards this goal. Following clone selection, antibodies were carefully optimized, for parameters such as concentration, incubation time and temperature, and imaging exposure time.

In this dataset, we first showed that the TME of murine B-NHL is altered between the A20 and Eμ-Myc models of B-NHL, suggesting two different mechanisms of immune

evasion. Then, we demonstrated that the distribution of the immune microenvironment differs between models of murine TNBC, and showed how measurement of interactions between endothelial and immune cells may relate to TME infiltration. Finally, using samples from murine melanoma, we examined how the TME is altered in the context of ICI-resistance, and found that ICI-susceptible tumours have increased spatial interactions between immune cells and tumour cells. Our data asserts that the careful selection of a mouse model is critical when designing experiments to study the TME. For instance, Eμ-Myc or *BRAF*$^{V600E}$/*PTEN*$^{-/-}$ models may be appropriate to study therapeutics that are predicted to increase immune cell trafficking or retention in the TME; while A20, 66cl4, 4T1, or YUMMER1.7 models could be useful to study therapeutics that re-activate immune cells already present in the TME. Furthermore, we demonstrate that PhenoCycler imaging of murine tumours can be employed both to test and to generate hypotheses. As an example of this, we hypothesized that the TME would be altered in different models of B-NHL, and our data found close cellular contacts between CD8+ T cells and Tregs in A20 B-NHL tumours, but not in Eμ-Myc tumours. Thus, one may hypothesize that Tregs in A20 function via direct inhibitory interactions with CD8+ T cells to suppress anti-tumour immunity (67), and to further investigate this, *ex vivo* functional assays could be employed. Throughout this study, there are numerous examples where our findings via PhenoCycler imaging have been hypothesis generating and could be further explored with i*n vitro* or *in vivo* experimentation.

### *2.5.2 Analysis of Highly Multiplexed Immunofluorescence Staining Data*

While many labs may be eager to begin highly multiplexed imaging of their experimental tissues, data analysis can appear to be a daunting task. Above, we provide

our workflows for open-source analysis of PhenoCycler imaging data. In our analysis pipeline, we primarily use QuPath software for cell classification (68), and CytoMAP for spatial analysis (55). In QuPath, images are segmented into single cells using a StarDist plugin (69, 70). In some cases, cell segmentation failed to discriminate individual cells when close contacts resulted in fluorescence spillover. This was particularly true in the case of intact blood vessels, where αSMA+ fibroblasts formed close contacts with CD31+ endothelial cells. In our dataset, we referred to these as “EndoFib” cells, and considered them to be a distinct entity. We also note that alternate segmentation methods that incorporate a cell membrane marker to define cellular boundaries may need to be utilized when the primary cell type of study is irregularly shaped or multinucleated, such as a fibroblast or a neuron (71).

To classify cells into phenotypes, we manually annotated a small number of cells based on their marker expression and used object-based classification methods in QuPath to extend this cell classification to the whole tissue. While this method of analysis proved to be highly successful in our hands, other analysis pipelines may allow more cursory or in-depth higher-plex image analysis. For instance, following cell segmentation, cellular mean intensity of all markers can be exported to a comma-separated values (CSV) file, which can be analyzed with FlowJo or other programs (so-called “hand-gating”). However, the success of hand-gating is limited by cell segmentation noise (72). Another alternative is to perform unsupervised clustering analysis, using pipelines such as Seurat, but we note that over-clustering has the potential to identify false phenotypes, and therefore must be used with caution. Overall, the analysis pipeline described above is an excellent starting point for novices in multiplexed immunofluorescence image

analysis and can be built upon to allow for more sophisticated analyses which answer increasingly complex experimental questions.

### *2.5.3 Limitations of the Technology*

While the PhenoCycler system for highly multiplexed fluorescent imaging has distinct advantages over other highly multiplexed imaging platforms, such as non-destructive tissue imaging, limited spectral overlap in fluorescence due to iterative cycles of imaging, and the use of robotic automation to increase throughput, there are also limitations to this technology. For instance, it is expensive and time consuming to identify antibody clones that are suitable for PhenoCycler immunofluorescence imaging. Additionally, the conjugation of an antibody to a DNA barcode can occasionally result in antibody dysfunction, and it is costly to research labs to correct problems of this nature. The process of identifying antibody clones suitable for PhenoCycler imaging represents a significant bottleneck in the PhenoCycler workflow, especially when generating custom antibody panels.

Furthermore, while PhenoCycler has been proven to image up to 100 markers, there is limited opportunity for signal amplification to aid in the visualization of targets of low abundance. To this point, there have been attempts to integrate tyramide-based signal amplification into the PhenoCycler workflow (20), but the proposed strategy requires iterative staining and stripping cycles, thereby increasing the risk of tissue damage and decreasing automation.

### *2.4.5 Concluding Remarks*

As new technologies in highly multiplexed imaging continue to emerge, we predict that many labs will require refined protocols for image acquisition and data analysis. Highly

multiplexed imaging provides the opportunity to visualize many diverse cell types in their native environments, and the insights provided from these types of experiments are instrumental in advancing the field of cancer research. Thus, we predict that the number of publications which employ highly multiplexed imaging will explode over the next decade. To this end, data must be appropriately collected and analyzed, and we hope to empower research groups to begin working towards this goal with the protocols provided above.

## 2.6 References for Chapter 2


1. Quail DF, Joyce JA. Microenvironmental regulation of tumor progression and metastasis. Nat Med. 2013;19(11):1423-37.
2. Hanahan D, Weinberg RA. Hallmarks of cancer: the next generation. Cell. 2011;144(5):646-74.
3. Kartikasari AER, Huertas CS, Mitchell A, Plebanski M. Tumor-Induced Inflammatory Cytokines and the Emerging Diagnostic Devices for Cancer Detection and Prognosis. Front Oncol. 2021;11:692142.
4. Bule P, Aguiar SI, Aires-Da-Silva F, Dias JNR. Chemokine-Directed Tumor Microenvironment Modulation in Cancer Immunotherapy. Int J Mol Sci. 2021;22(18).
5. Tao S-C, Guo S-C. Role of extracellular vesicles in tumour microenvironment. Cell Communication and Signaling. 2020;18(1):163.
6. Jin M-Z, Jin W-L. The updated landscape of tumor microenvironment and drug repurposing. Signal Transduction and Targeted Therapy. 2020;5(1):166.
7. Joyce JA, Pollard JW. Microenvironmental regulation of metastasis. Nature Reviews Cancer. 2009;9(4):239-52.
8. Zitvogel L, Pitt JM, Daillère R, Smyth MJ, Kroemer G. Mouse models in oncoimmunology. Nature Reviews Cancer. 2016;16(12):759-73.
9. McKinnon KM. Flow Cytometry: An Overview. Curr Protoc Immunol. 2018;120:5.1.-5.1.11.
10. Keren L, Bosse M, Marquez D, Angoshtari R, Jain S, Varma S, et al. A Structured Tumor-Immune Microenvironment in Triple Negative Breast Cancer Revealed by Multiplexed Ion Beam Imaging. Cell. 2018;174(6):1373-87.e19.
11. Jackson HW, Fischer JR, Zanotelli VRT, Ali HR, Mechera R, Soysal SD, et al. The single-cell pathology landscape of breast cancer. Nature. 2020;578(7796):615-20.
12. Radtke AJ, Chu CJ, Yaniv Z, Yao L, Marr J, Beuschel RT, et al. IBEX: an iterative immunolabeling and chemical bleaching method for high-content imaging of diverse tissues. Nature Protocols. 2022;17(2):378-401.
13. Goltsev Y, Samusik N, Kennedy-Darling J, Bhate S, Hale M, Vazquez G, et al. Deep Profiling of Mouse Splenic Architecture with CODEX Multiplexed Imaging. Cell. 2018;174(4):968-81.e15.

14. Black S, Phillips D, Hickey JW, Kennedy-Darling J, Venkataraaman VG, Samusik N, et al. CODEX multiplexed tissue imaging with DNA-conjugated antibodies. Nat Protoc. 2021;16(8):3802-35.
15. Jhaveri N, Nikulina N, Zong H, Ma N, Cheikh BB, Pratapa A, et al. Abstract 3877: Deep ultrahigh-plex spatial phenotyping of human cancer tissues. Cancer Research. 2022;82(12_Supplement):3877-.
16. Niyati J, Bassem Ben C, Nadezhda N, Ning M, Dmytro K, James D, et al. Single-cell Spatial Metabolic and Immune Phenotyping of Head and Neck Cancer Tissues Identifies Tissue Signatures of Response and Resistance to Immunotherapy. bioRxiv. 2023:2023.05.30.540859.
17. Phillips D, Matusiak M, Gutierrez BR, Bhate SS, Barlow GL, Jiang S, et al. Immune cell topography predicts response to PD-1 blockade in cutaneous T cell lymphoma. Nature Communications. 2021;12(1):6726.
18. Mondello P, Fama A, Larson MC, Feldman AL, Villasboas JC, Yang Z-Z, et al. Lack of intrafollicular memory CD4 + T cells is predictive of early clinical failure in newly diagnosed follicular lymphoma. Blood Cancer Journal. 2021;11(7):130.
19. Roider T, Baertsch MA, Fitzgerald D, Voehringer H, Brinkmann BJ, Czernilofsky F, et al. Multimodal and spatially resolved profiling identifies distinct patterns of T-cell infiltration in nodal B-cell lymphoma entities. bioRxiv. 2022:2022.11.04.514366.
20. Simonson PD, Valencia I, Patel SS. Tyramide-conjugated DNA barcodes enable signal amplification for multiparametric CODEX imaging. Commun Biol. 2022;5(1):627.
21. Gouin KH, Ing N, Plummer JT, Rosser CJ, Ben Cheikh B, Oh C, et al. An N-Cadherin 2 expressing epithelial cell subpopulation predicts response to surgery, chemotherapy and immunotherapy in bladder cancer. Nature Communications. 2021;12(1):4906.
22. Schürch CM, Bhate SS, Barlow GL, Phillips DJ, Noti L, Zlobec I, et al. Coordinated Cellular Neighborhoods Orchestrate Antitumoral Immunity at the Colorectal Cancer Invasive Front. Cell. 2020;182(5):1341-59.e19.
23. Haensel D, Daniel B, Gaddam S, Pan C, Fabo T, Bjelajac J, et al. Skin basal cell carcinomas assemble a pro-tumorigenic spatially organized and self-propagating Trem2+ myeloid niche. Nat Commun. 2023;14(1):2685.
24. Shekarian T, Zinner CP, Bartoszek EM, Duchemin W, Wachnowicz AT, Hogan S, et al. Immunotherapy of glioblastoma explants induces interferon-γ responses and spatial immune cell rearrangements in tumor center, but not periphery. Sci Adv. 2022;8(26):eabn9440.
25. Kumar T, Nee K, Wei R, He S, Nguyen QH, Bai S, et al. A spatially resolved single-cell genomic atlas of the adult human breast. Nature. 2023.
26. Sadeghirad H, Liu N, Monkman J, Ma N, Cheikh BB, Jhaveri N, et al. Compartmentalized spatial profiling of the tumor microenvironment in head and neck squamous cell carcinoma identifies immune checkpoint molecules and tumor necrosis factor receptor superfamily members as biomarkers of response to immunotherapy. Frontiers in Immunology. 2023;14.
27. Mayer AT, Holman DR, Sood A, Tandon U, Bhate SS, Bodapati S, et al. A tissue atlas of ulcerative colitis revealing evidence of sex-dependent differences in disease-driving inflammatory cell types and resistance to TNF inhibitor therapy. Science Advances. 2023;9(3):eadd1166.
28. Neumann EK, Patterson NH, Rivera ES, Allen JL, Brewer M, deCaestecker MP, et al. Highly multiplexed immunofluorescence of the human kidney using co-detection by indexing. Kidney Int. 2022;101(1):137-43.
29. Burns GL, Bruce JK, Minahan K, Mathe A, Fairlie T, Cameron R, et al. Type 2 and type 17 effector cells are increased in the duodenal mucosa but not peripheral blood of patients with functional dyspepsia. Front Immunol. 2022;13:1051632.

30. Kano S, Nakamura M, Nojiri Y, Magara T, Yoshimitsu M, Kato H, et al. Differences in the immune microenvironment between improved and non-improved cases of vitiligo after halo nevus excision. J Dermatol Sci. 2023;109(3):136-42.
31. Sanchez-Molina P, Pratapa A, Nikulina N, Cheikh B, Singh J, Dhawan A, et al. Single-cell spatial proteomic analysis by multiplexed imaging enables identification of microglial heterogeneity in Alzheimer's disease human brain. Research Square; 2023.
32. Melo Ferreira R, Sabo AR, Winfree S, Collins KS, Janosevic D, Gulbronson CJ, et al. Integration of spatial and single-cell transcriptomics localizes epithelial cell-immune cross-talk in kidney injury. JCI Insight. 2021;6(12).
33. Foster DS, Januszyk M, Delitto D, Yost KE, Griffin M, Guo J, et al. Multiomic analysis reveals conservation of cancer-associated fibroblast phenotypes across species and tissue of origin. Cancer Cell. 2022;40(11):1392-406.e7.
34. Yu Xin W, Colin AH, James NH, Jasmin G, Mohsen A, Shiqi S, et al. A single cell spatial temporal atlas of skeletal muscle reveals cellular neighborhoods that orchestrate regeneration and become disrupted in aging. bioRxiv. 2022:2022.06.10.494732.
35. Frede A, Czarnewski P, Monasterio G, Tripathi KP, Bejarano DA, Ramirez Flores RO, et al. B cell expansion hinders the stroma-epithelium regenerative cross talk during mucosal healing. Immunity. 2022;55(12):2336-51.e12.
36. Bejarano DA, Schlitzer A. Unveiling Macrophage Heterogeneity and Their Spatial Distribution Using Multiplexed Tissue Imaging. Methods Mol Biol. 2024;2713:281-96.
37. Ono Y, Sato H, Miyazaki T, Fujiki K, Kume E, Tanaka M. Quality assessment of long-term stored formalin-fixed paraffin embedded tissues for histopathological evaluation. J Toxicol Pathol. 2018;31(1):61-4.
38. Scalia CR, Boi G, Bolognesi MM, Riva L, Manzoni M, DeSmedt L, et al. Antigen Masking During Fixation and Embedding, Dissected. J Histochem Cytochem. 2017;65(1):5-20.
39. Du Z, Lin JR, Rashid R, Maliga Z, Wang S, Aster JC, et al. Qualifying antibodies for image-based immune profiling and multiplexed tissue imaging. Nat Protoc. 2019;14(10):2900-30.
40. Bagaev A, Kotlov N, Nomie K, Svekolkin V, Gafurov A, Isaeva O, et al. Conserved pan-cancer microenvironment subtypes predict response to immunotherapy. Cancer Cell. 2021;39(6):845-65.e7.
41. Kim KJ, Kanellopoulos-Langevin C, Merwin RM, Sachs DH, Asofsky R. Establishment and characterization of BALB/c lymphoma lines with B cell properties. J Immunol. 1979;122(2):549-54.
42. Dexter DL, Kowalski HM, Blazar BA, Fligiel Z, Vogel R, Heppner GH. Heterogeneity of tumor cells from a single mouse mammary tumor. Cancer Res. 1978;38(10):3174-81.
43. Aslakson CJ, Miller FR. Selective events in the metastatic process defined by analysis of the sequential dissemination of subpopulations of a mouse mammary tumor. Cancer Res. 1992;52(6):1399-405.
44. Guo Q, Bartish M, Gonçalves C, Huang F, Smith-Voudouris J, Krisna SS, et al. The MNK1/2-eIF4E Axis Supports Immune Suppression and Metastasis in Postpartum Breast Cancer. Cancer Res. 2021;81(14):3876-89.
45. Pulaski BA, Ostrand-Rosenberg S. Mouse 4T1 breast tumor model. Curr Protoc Immunol. 2001;Chapter 20:Unit 20.2.
46. Dafflon C, Santamaría-Martínez A, Ordóñez-Morán P. An Intrasplenic Injection Model for the Study of Cancer Stem Cell Seeding Capacity. Methods Mol Biol. 2020;2171:293-302.
47. Dankort D, Curley DP, Cartlidge RA, Nelson B, Karnezis AN, Damsky WE, Jr., et al. Braf(V600E) cooperates with Pten loss to induce metastatic melanoma. Nat Genet. 2009;41(5):544-52.

48. Wang J, Perry CJ, Meeth K, Thakral D, Damsky W, Micevic G, et al. UV-induced somatic mutations elicit a functional T cell response in the YUMMER1.7 mouse melanoma model. Pigment Cell Melanoma Res. 2017;30(4):428-35.
49. Peng W, Chen JQ, Liu C, Malu S, Creasy C, Tetzlaff MT, et al. Loss of PTEN Promotes Resistance to T Cell-Mediated Immunotherapy. Cancer Discov. 2016;6(2):202-16.
50. Huang F, Gonçalves C, Bartish M, Rémy-Sarrazin J, Issa ME, Cordeiro B, et al. Inhibiting the MNK1/2-eIF4E axis impairs melanoma phenotype switching and potentiates antitumor immune responses. J Clin Invest. 2021;131(8).
51. Castillo JJ, Winer ES, Olszewski AJ. Sites of extranodal involvement are prognostic in patients with diffuse large B-cell lymphoma in the rituximab era: an analysis of the Surveillance, Epidemiology and End Results database. Am J Hematol. 2014;89(3):310-4.
52. Ben Abdelwahed R, Cosette J, Donnou S, Crozet L, Ouakrim H, Fridman WH, et al. Lymphoma B-cell responsiveness to CpG-DNA depends on the tumor microenvironment. J Exp Clin Cancer Res. 2013;32(1):18.
53. Donnou S, Galand C, Daussy C, Crozet L, Fridman WH, Sautès-Fridman C, et al. Immune adaptive microenvironment profiles in intracerebral and intrasplenic lymphomas share common characteristics. Clinical and Experimental Immunology. 2011;165(3):329-37.
54. Galand C, Donnou S, Molina TJ, Fridman WH, Fisson S, Sautes-fridman C. Influence of Tumor Location on the Composition of Immune Infiltrate and Its Impact on Patient Survival. Lessons from DCBCL and Animal Models. Frontiers in Immunology. 2012;3.
55. Stoltzfus CR, Filipek J, Gern BH, Olin BE, Leal JM, Wu Y, et al. CytoMAP: A Spatial Analysis Toolbox Reveals Features of Myeloid Cell Organization in Lymphoid Tissues. Cell Reports. 2020;31(3):107523.
56. Marabelle A, Kohrt H, Sagiv-Barfi I, Ajami B, Axtell RC, Zhou G, et al. Depleting tumor-specific Tregs at a single site eradicates disseminated tumors. J Clin Invest. 2013;123(6):2447-63.
57. Valencia GA, Rioja P, Morante Z, Ruiz R, Fuentes H, Castaneda CA, et al. Immunotherapy in triple-negative breast cancer: A literature review and new advances. World J Clin Oncol. 2022;13(3):219-36.
58. Liu Z, Li M, Jiang Z, Wang X. A Comprehensive Immunologic Portrait of Triple-Negative Breast Cancer. Transl Oncol. 2018;11(2):311-29.
59. Cortes J, Cescon DW, Rugo HS, Nowecki Z, Im SA, Yusof MM, et al. Pembrolizumab plus chemotherapy versus placebo plus chemotherapy for previously untreated locally recurrent inoperable or metastatic triple-negative breast cancer (KEYNOTE-355): a randomised, placebo-controlled, double-blind, phase 3 clinical trial. Lancet. 2020;396(10265):1817-28.
60. Schmid P, Cortes J, Dent R, Pusztai L, McArthur H, Kümmel S, et al. VP7-2021: KEYNOTE-522: Phase III study of neoadjuvant pembrolizumab + chemotherapy vs. placebo + chemotherapy, followed by adjuvant pembrolizumab vs. placebo for early-stage TNBC. Annals of Oncology. 2021;32(9):1198-200.
61. DuPré SA, Redelman D, Hunter KW, Jr. The mouse mammary carcinoma 4T1: characterization of the cellular landscape of primary tumours and metastatic tumour foci. Int J Exp Pathol. 2007;88(5):351-60.
62. Tabariès S, Ouellet V, Hsu BE, Annis MG, Rose AA, Meunier L, et al. Granulocytic immune infiltrates are essential for the efficient formation of breast cancer liver metastases. Breast Cancer Res. 2015;17(1):45.
63. Gide TN, Quek C, Menzies AM, Tasker AT, Shang P, Holst J, et al. Distinct Immune Cell Populations Define Response to Anti-PD-1 Monotherapy and Anti-PD-1/Anti-CTLA-4 Combined Therapy. Cancer Cell. 2019;35(2):238-55.e6.
64. Hossain SM, Gimenez G, Stockwell PA, Tsai P, Print CG, Rys J, et al. Innate immune checkpoint inhibitor resistance is associated with melanoma sub-types exhibiting invasive and de-differentiated gene expression signatures. Frontiers in Immunology. 2022;13.

65. Patrinely JR, Jr., Baker LX, Davis EJ, Song H, Ye F, Johnson DB. Outcomes after progression of disease with anti-PD-1/PD-L1 therapy for patients with advanced melanoma. Cancer. 2020;126(15):3448-55.
66. Moldoveanu D, Ramsay L, Lajoie M, Anderson-Trocme L, Lingrand M, Berry D, et al. Spatially mapping the immune landscape of melanoma using imaging mass cytometry. Sci Immunol. 2022;7(70):eabi5072.
67. Sojka DK, Huang YH, Fowell DJ. Mechanisms of regulatory T-cell suppression - a diverse arsenal for a moving target. Immunology. 2008;124(1):13-22.
68. Bankhead P, Loughrey MB, Fernández JA, Dombrowski Y, McArt DG, Dunne PD, et al. QuPath: Open source software for digital pathology image analysis. Scientific Reports. 2017;7(1):16878.
69. Schmidt U, Weigert M, Broaddus C, Myers G, editors. Cell Detection with Star-Convex Polygons. Medical Image Computing and Computer Assisted Intervention – MICCAI 2018; 2018 2018//; Cham: Springer International Publishing.
70. Weigert M, Schmidt U, Haase R, Sugawara K, Myers G, editors. Star-convex Polyhedra for 3D Object Detection and Segmentation in Microscopy. 2020 IEEE Winter Conference on Applications of Computer Vision (WACV); 2020 1-5 March 2020.
71. Dayao MT, Brusko M, Wasserfall C, Bar-Joseph Z. Membrane marker selection for segmenting single cell spatial proteomics data. Nature Communications. 2022;13(1):1999.
72. Hickey JW, Tan Y, Nolan GP, Goltsev Y. Strategies for Accurate Cell Type Identification in CODEX Multiplexed Imaging Data. Front Immunol. 2021;12:727626.

## 2.7 Supplementary Materials for Chapter 2

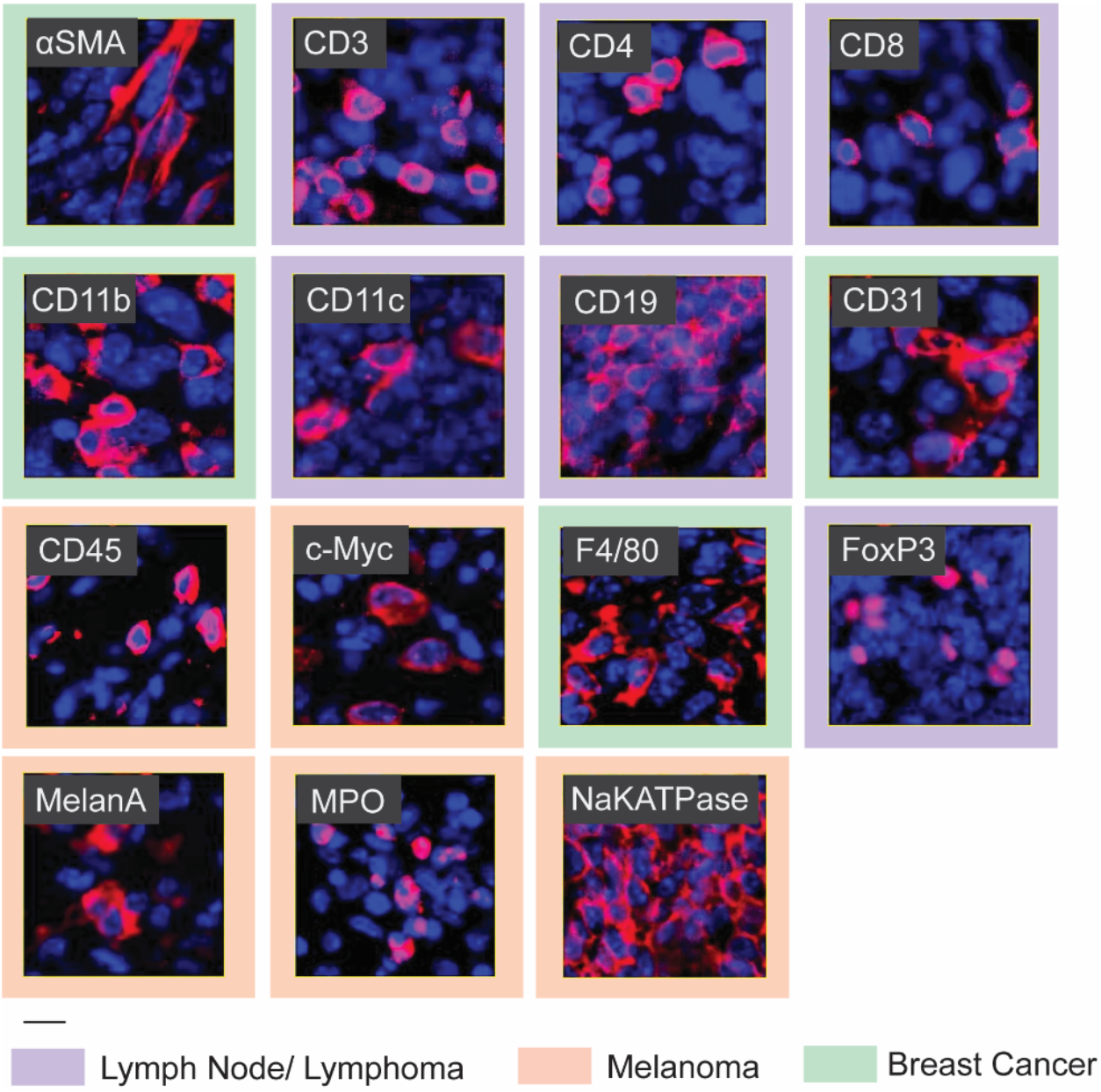


**Supplemental Figure 2.1: Immunofluorescence optimization of antibodies for murine FFPE staining**
Images showing successful immunofluorescence staining of each antibody that was optimized for PhenoCycler oligonucleotide barcode conjugation. In each image, DAPI is blue, and each individual marker is red. In each case, AF647-tagged secondary antibodies were used. The colour of the outer border indicates the tissue type in the image. Scale bar is 15 μM.

**Supplemental Table 2.1: Reagents and Tools Table**

| Reagent or Resource | Reference or Source | Identifier or Catalog No. |
|---|---|---|
| ***Experimental Models*** | | |
| BALB/C Mice | Charles River | BALB/cAnNCrl |
| C57BL/6J Mice | The Jackson Laboratory | Strain #:000664 |
| Braf/PTEN Mice | The Jackson Laboratory | Strain #:013590 |
| A20 | ATCC | TIB-208 |
| Eμ-Myc | Lab of Dr. Jerry Pelletier | N/A |
| 66cl4 | Lab of Dr. Josie Ursini-Siegel | N/A |
| 4T1 | ATCC | CRL-2539 |
| YUMMER1.7 | Lab of Dr. Marcus Bosenberg | N/A |
| ***Drugs and Treatments*** | | |
| 4-Hydroxytamoxifen | Sigma-Aldrich | H6278 |
| IgG Control | Bio X Cell | 2A3, BE0089 |
| aPD-1 | Bio X Cell | RMP1-14, BE0146 |
| ***Chemicals and Reagents*** | | |
| Tris | Bio Basic | TB0195 |
| EDTA | Bio Basic | EB0185 |
| Sodium Chloride | Bio Basic | SB0476 |
| Potassium Chloride | Bio Basic | PB0440 |
| Sodium Hydroxide 10N | VWR | BDH7247-1 |
| 50% $H_2O_2$ | Sigma-Aldrich | 516813-500ML |
| Paraformaldehyde 16% | Electron Microscopy Sciences | 15710 |
| Tween20 | VWR | 0777-1L |
| ***IHC and IF Reagents and Tools*** | | |
| SuperFrost Plus Slides | Fisher | 22-037-246 |
| Xylenes | Fisher | X5-4 |
| Ethanol | Commercial Alcohols | P016EAAN |
| Hydrophobic Barrier PAP Pen | Thermo Scientific | R3777 |
| Harris' Hematoxylin | Sigma-Aldrich | 638A-85 |
| Eosin Y Solution | Sigma-Aldrich | HT110116 |
| Donkey Serum | Jackson ImmunoResearch | 017-000-121 |
| FC Blocking Reagent | Made in house | |
| ECL Anti-mouse IgG, Horseradish peroxidase linked whole antibody from sheep | Cytiva | NA931V |
| Mouse CD45 Antibody | R&D Systems | AF114 |
| Dnk pAb to Goat IgG (HRP polymer) | Abcam | Ab214881 |
| ImmPACT DAB Substrate Kit, Peroxidase | Vector Laboratories | SK-4105 |

| | | |
|---|---|---|
| AF647 donkey anti-rabbit IgG | Invitrogen | A31573 |
| Donkey anti-Rat IgG DyLight 650 | Invitrogen | SA5-10029 |
| AF647 donkey anti-goat IgG | Invitrogen | A21447 |
| DAPI (1 mg/mL) | Thermo Scientific | 62248 |
| Flouromount-G | Invitrogen | 00-4958-02 |
| 24x55mm No. 1.5 Thickness Cover Slips | Epredia | 152455 |
| ***PhenoCycler Antibody Conjugation and Tissue Staining*** | | |
| Lammeli Loading Dye | Bio-Rad | #1610737EDU |
| GelCode Blue Stain Reagent | Thermo Scientific | 24590 |
| 1X D-PBS | Wisent | 311-425-CL |
| Methanol | Commercial Alcohols | P016MEOH |
| ***Akoya Reagents*** | | |
| 10X PhenoCycler Buffer | Akoya | 7000001 |
| Staining Kit | Akoya | 7000008 |
| Conjugation Kit | Akoya | 7000009 |
| Black-walled 96-well plate | Akoya | 7000006 |
| Adhesive foil | Akoya | 7000007 |
| Assay Reagent | Akoya | 7000002 |
| Nuclear Stain | Akoya | 7000003 |
| Flow Cell | Akoya | 240204 |
| ***Software*** | | |
| QuPath | Bankhead et al. (68) | |
| StarDist | Schmidt et al. (69) | |
| MatLab | MathWorks | |
| CytoMAP | Stoltzfus et al. (55)<br><br>Weigert et al. (70) | |
| GraphPad Prism | Dotmatics | |
| ***Other*** | | |
| Microtome | Leica | RM2125 RTS |
| PT Link for Pre-Treatment | Agilent | |
| LED Lamps | | 20000 Lux Intensity |
| AxioScan 7 | Zeiss | |
| PhenoCycler-Fusion | Akoya | |

## Bridging Text

In Chapter 2, we developed experimental and analytical tools to study the murine TME. We were the first research team to develop a PhenoCycler antibody panel for murine FFPE tissue, and we reported our methodology for selecting and screening antibody clones which show high fidelity staining in a variety of murine FFPE tissues. These antibodies were conjugated to DNA-oligonucleotides and were used in a PhenoCycler staining experiment. To this end, highly multiplexed PhenoCycler imaging was performed on tissues derived from 8 different murine models of cancer, and matched normal tissues. We also reported our pipeline for PhenoCycler image analysis, using open-source software that requires minimal knowledge of coding languages. The analysis pipeline described how to visualize PhenoCycler images in QuPath, perform cell segmentation, classify cells into phenotypes, and perform spatial analyses.

Regarding the specific aims of this thesis, we described how the TME differed between two different models of syngeneic murine lymphoma: A20 and Eu-Myc. A20 was found to be richer in lymphoid infiltration, with increased cellular contacts between different cell types, while Eu-Myc tumours had increased prevalence of tumour cells and stromal components, with decreased cellular contacts between different cell types. We therefore propose that A20 is an ideal model to study therapeutic interventions where the function of cells already present in the TME is modulated, and Eu-Myc is an ideal model to study how an “immune cold” TME impacts disease progression. Eu-Myc could be further used identify therapeutic interventions that may increase immune cell trafficking to the TME.

Indeed, in Chapter 3, the Eu-Myc model was used to study how STAT6$^{D419N}$ mutation impacts CD4+ T cell invasion into the TME. Moreover, PhenoCycler imaging of both murine and human tissues was employed to answer specific questions related to STAT6$^{D419}$-mutant-mediated modulation of the TME. Therefore, the techniques and mouse models that were developed in Chapter 3 created a foundation for the research in Chapter 3, that aimed to ask experimental questions with direct clinical relevance to the human rrDLBCL population.

# Chapter 3: The CCL17-CCR4 Axis is Critical for Mutant STAT6-Mediated Microenvironmental Remodeling and Therapeutic Resistance in Relapsed and Refractory Diffuse Large B Cell Lymphoma

This chapter has been published as a pre-print:

**MJ Abraham**, C Guilbert, N Gagnon, C Goncalves, A Benoit, R Rys, SEJ Preston, RD Morin, WH Miller Jr., NA Johnson, SV del Rincon, & KK Mann. The CCL17-CCR4 Axis is Critical for Mutant STAT6-Mediated Microenvironmental Remodelling and Therapeutic Resistance in Relapsed and Refractory Diffuse Large B Cell Lymphoma. **BioRxiv. 2024.** doi: 10.1101/2024.12.13.628396.

The online version of this article, and all supplementary material associated with it, can be found at: https://www.biorxiv.org/lookup/doi/10.1101/2024.12.13.628396

## 3.1 Abstract

Relapsed and refractory Diffuse Large B Cell Lymphoma (rrDLBCL) presents a significant challenge in hematology-oncology, with approximately 30-40% of DLBCL patients experiencing relapse or resistance to treatment. This underscores the urgent need to better understand the molecular mechanisms governing therapeutic resistance. Signal Transducer and Activator of Transcription 6 (STAT6) has been previously identified as a gene with recurrent D419 gain-of-function mutations in rrDLCBL. When $STAT6^{D419}$ mutations are present in DLBCL tumour cells, we have demonstrated that transcription of the chemokine CCL17 (aka TARC) is increased, and tumours have increased infiltration of CD4+ T cells. However, the significance of increased T cell infiltration had not been determined. In the present study, we developed a mouse model of $STAT6^{D419N}$ mutant

DLBCL, that recapitulates the critical features of human STAT6$^{D419}$ mutant DLBCL, including increased expression of phospho-STAT6, increased CD4+ T cell invasion, and resistance to doxorubicin treatment. With this model, we found CD4+ T cells in STAT6$^{D419N}$ tumours have higher expression of the receptor for CCL17, CCR4. Using *ex vivo* functional assays we demonstrate that STAT6$^{D419N}$ tumour cells are directly chemoattractive to CCR4+ CD4+ T cells, and when CCR4 is inhibited using a small molecule antagonist, CD4+ T cells in STAT6$^{D419N}$ tumours are reduced and STAT6$^{D419N}$ tumours regain therapeutic sensitivity to doxorubicin. Using PhenoCycler imaging of human rrDLBCL samples, we find that STAT6$^{D419}$ tumours indeed have increased expression of phospho-STAT6+ and increased cellular interactions between phospho-STAT6+ tumour cells and CD4+/ CCR4+ CD4+ T cells. Thus, our data identifies CCR4 as an attractive therapeutic target in STAT6$^{D419}$ mutant rrDLBCL.

## 3.2 Introduction

Diffuse Large B Cell Lymphoma (DLBCL) is the most commonly diagnosed lymphoid malignancy in adults. The first-line treatment for DLBCL is the poly-chemoimmunotherapy R-CHOP, which leads to complete remission for most patients. However, approximately 30-40% of patients will be refractory to R-CHOP or will relapse following treatment (relapsed/refractory DLBCL: rrDLBCL). Thus, it is critically important to better understand mechanisms of therapeutic resistance, with the overall goal of identifying treatment modalities with increased efficacy for rrDLBCL patients.

One interesting target in rrDLBCL is Signal Transducer and Activator of Transcription 6 (STAT6). STAT6 is mutated or overactivated in several hematological

malignancies, including cutaneous T cell lymphoma (CTCL) (1), primary mediastinal B cell lymphoma (PMBCL) (2-5), follicular lymphoma (FL) (6-9), and classical Hodgkin's lymphoma (cHL) (10-12). In these cancer types, STAT6 signaling promotes tumour cell survival, proliferation, and resistance to apoptosis, leading to the classification of STAT6 as a potential therapeutic target in lymphoma. In DLBCL, STAT6 is not frequently overactivated, except in the case of relapsed/refractory disease, where our group has previously reported that mutations at the D419 gain-of-function hotspot are enriched (13). Indeed, we have shown that the presence of *STAT6*$^{D419}$ mutation in DLBCL cell lines leads to increased IL-4/13-dependent phospho-STAT6 nuclear residency. This correlates with increased expression of STAT6 transcriptional targets, including the chemokine *CCL17* (aka TARC), which is chemoattractive to CCR4+ immune cells, including CD4+ T cells. Concordantly, in human rrDLBCL, we found that increased tumour-cell derived *CCL17* is associated with increased CD4+ T cell invasion, specifically in STAT6-mutant samples (14).

Overall, research from our group and others has demonstrated that hyperactivation of STAT6, whether resulting from increased levels of IL-4/13 in the tumour microenvironment (TME) or due to gene mutation, can lead to tumour cell autonomous and microenvironmental changes. However, the clinical significance of these findings in rrDLBCL remains unclear. For instance, it is unknown if the CD4+ T cell infiltrate in *STAT6*$^{D419}$-mutant tumours is skewed towards a specific polarization state or if these T cells contribute to disease progression and therapeutic resistance. Moreover, while we hypothesize that CCL17 is the main chemoattractant driving CD4+ T cell recruitment, this has not been experimentally proven. Recent publications have asserted that the spatial

organization of tumours is just as important as their cellular constitution (15), but it is unknown if or how *STAT6$^{D419}$* mutation induces tumour restructuring, and if CCL17-CCR4 plays a role. Finally, STAT6$^{D419}$ mutations are enriched in rrDLBCL, but *in vitro* data indicates that STAT6$^{D419}$ mutant tumour cells do not have increased resistance to any of the individual components of R-CHOP (14). It is still unknown if *STAT6$^{D419}$*-mutations might contribute to therapeutic resistance due to changes in the TME.

In this study, we aimed to develop a mouse model that could recapitulate critical features of *STAT6$^{D419}$*-mutant DLBCL, including increased phospho-STAT6 positivity in tumour tissue and increased CD4+ T cell invasion. With this model, we could address the outstanding questions related to *STAT6$^{D419}$*-driven microenvironmental modification. Using flow cytometry, *ex vivo* functional assays, and highly-multiplexed immunofluorescent PhenoCycler imaging, we demonstrate that *STAT6$^{D419N}$*-mutant tumour cells are more chemoattractive to CCR4+ CD4+ T cells. Additionally, we show that STAT6$^{D419N}$ tumours are indeed resistant to doxorubicin. Importantly, we demonstrate that blocking CCL17-induced CD4+ T cell recruitment to the STAT6$^{D419N}$ TME, using a small molecule inhibitor of CCR4, re-sensitizes tumours to doxorubicin treatment. In human STAT6$^{D419}$-mutant DLBCL biopsy tissues, we show that tumour cells have increased expression of phospho-STAT6 and CCL17. Moreover, STAT6$^{D419}$-mutant tissues have increased interactions between phospho-STAT6+ tumour cells and CD4+/ CCR4+ CD4+ T cells as compared to STAT6$^{WT}$ rrDLBCL samples. Thus, our data identifies CCR4 as an attractive therapeutic target for rrDLBCL patients with overactivated STAT6 signaling.

## 3.3 Results

### *3.3.1 The Immunocompetent mSTAT6$^{D419N}$-Eμ-Myc Lymphoma Closely Recapitulates Critical Features of STAT6$^{D419}$ Mutant rrDLBCL.*

Using *in vitro* models, we have previously demonstrated that STAT6$^{D419}$ lymphoma cells have a similar proliferative rate and therapeutic sensitivity as STAT6$^{WT}$ lymphoma cells (14). However, our previous data also indicated that *STAT6$^{D419}$* mutation may function to induce therapeutic resistance via modulation of the TME. Thus, we developed an immunocompetent mouse model of STAT6$^{D419N}$ lymphoma, to study how mutated *STAT6* impacts microenvironmental dynamics. To do this, we generated Eμ-Myc lymphoma cell lines overexpressing either murine (m) *STAT6$^{WT}$* or *STAT6$^{D419N}$*. These lymphoma cells can be injected into C57BL/6 mice via tail vein, where they home to the lymph nodes and spleen, and produce an orthotopic model of B cell lymphoma (**Figure 3.1A**). Disease burden can be followed via ultrasound (**Figure 3.1B**), and mice reach endpoint at 14-days post-injection, when cervical lymph node (cLN) size has exceeded 100 mm$^3$. Critically, both Eμ-Myc-mSTAT6$^{WT}$ tumours and Eμ-Myc-mSTAT6$^{D419N}$ tumours grow at the same rate (**Figure 3.1C**), and neither genotype provides a survival advantage in the context of primary disease.

To characterize these tumours over their development, lymph nodes were harvested at early-, mid-, and late-disease (days 8, 11, and 14 post-injection, respectively). At early and late disease, Eμ-Myc-mSTAT6$^{WT}$ and Eμ-Myc-mSTAT6$^{D419N}$ tumours had a similar percentage of Ki67+ cells within the lymph nodes (**Figure 3.1D-E**).

However, at mid-disease, Eμ-Myc-mSTAT6$^{D419N}$ tumours had significantly less Ki67+ tumour cells, despite no difference in tumour weight (**Figure 3.1F**). To characterize this discrepancy, we performed IHC co-staining for CD4 and phospho-STAT6 (**Figure 3.1G**). Consistent with patient samples, we found that Eμ-Myc-mSTAT6$^{D419N}$ tumours had increased CD4 and phospho-STAT6 positivity (**Figure 3.1H**), and these two metrics were positively correlated (**Figure 3.1I**). This could be further recapitulated with flow cytometry (antibodies used for flow cytometry found in **Sup. Table 3.1**), where we found that Eμ-Myc-mSTAT6$^{D419N}$ tumours were composed of an increased proportion of CD4+ T cells (represented as % of CD45+ cells within the tumour mass) and had a significantly increased total abundance of CD4+ T cells (**Figure 3.1J**). These differences were not observed at early or late disease (**Sup. Figure 3.1A-B**). No differences in proportion or abundance of CD8+ T cells were observed at any timepoint (**Figure 3.1K, Sup. Figure 3.1C-D**). Thus, our mouse model of STAT6$^{D419N}$-mutant lymphoma closely replicates the human disease it is designed to model.

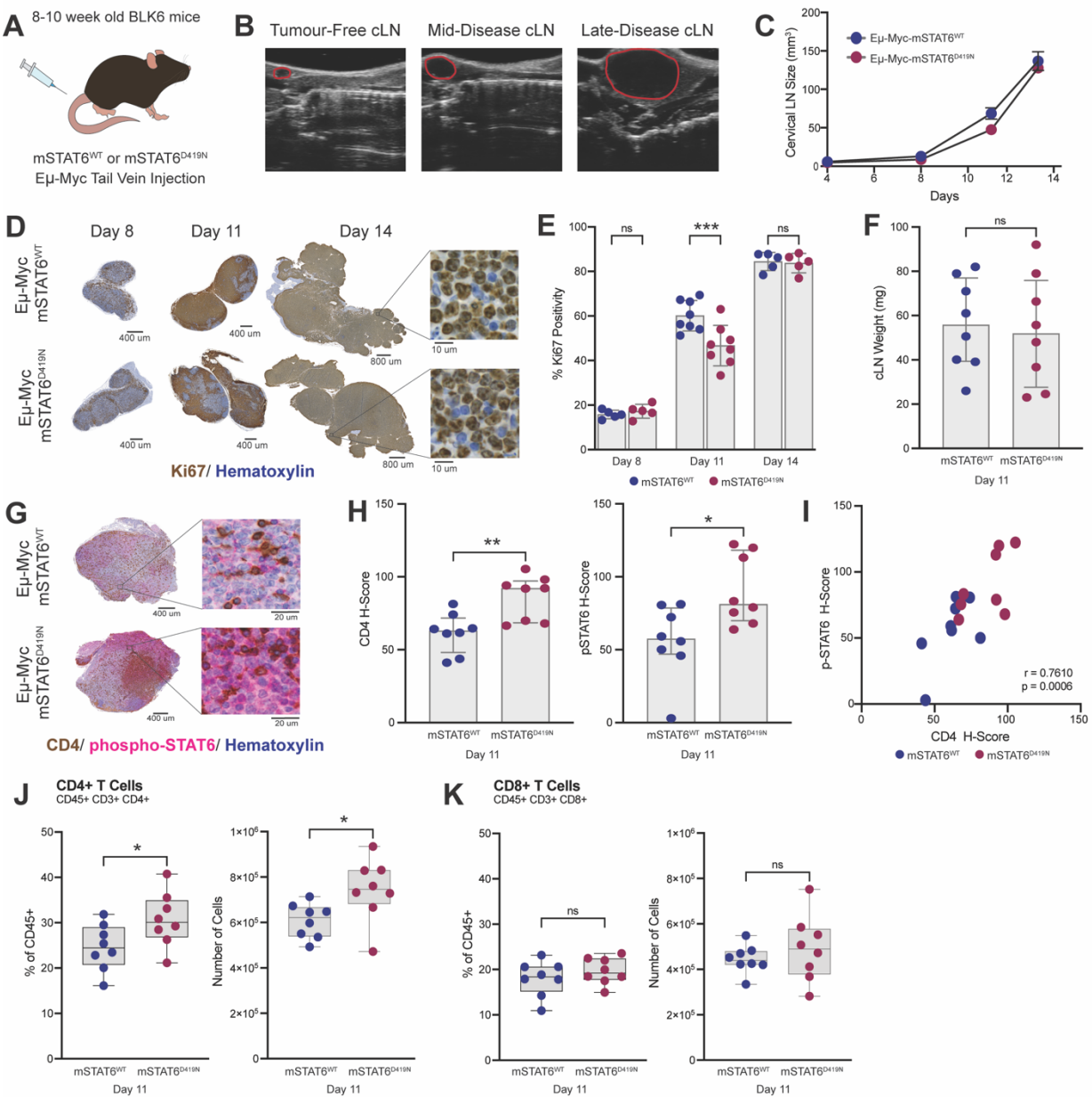


**Figure 3.1: STAT6$^{D419N}$-Eμ-Myc murine lymphoma tumours recapitulate critical features of human STAT6$^{D419}$ lymphoma**

**A.** To study the impact of STAT6$^{D419}$ mutation on the lymphoma TME, 8-10 week old female C57BL/6 mice were injected via tail vein with mSTAT6$^{WT}$ or mSTAT6$^{D419N}$ Eμ-Myc tumour cells. **B.** Ultrasound images of tumour-free, mid-disease (day 11 post-injection), and late disease (day 14 post-injection) Eμ-Myc tumours, in the cLN. The anatomical structure that looks like a hatched line is the trachea. In all images, the cLN/tumour is outlined in red. **C.** cLN volume, quantified by ultrasound imaging, over time in mSTAT6$^{WT}$ or mSTAT6$^{D419N}$ Eμ-Myc tumour bearing mice. **D.** Representative Ki67 staining of early-, mid-, and late-disease mSTAT6$^{WT}$ and mSTAT6$^{D419N}$ Eμ-Myc tumours (day 8, day 11, and day 14, respectively). **E.** Quantification of Ki67 positive

cells in mSTAT6$^{WT}$ and mSTAT6$^{D419N}$ Eμ-Myc tumours. At day 11, mSTAT6$^{D419N}$ Eμ-Myc tumours have significantly fewer Ki67+ cells. **F.** Weights of mSTAT6$^{WT}$ and mSTAT6$^{D419N}$ Eμ-Myc tumours at day 11. Concordant with ultrasound data, mSTAT6$^{WT}$ and mSTAT6$^{D419N}$ cLN tumours are the same weight at this this time point. **G.** Representative images of CD4 (brown) and phospho-STAT6 (pink) IHC co-staining in day 11 mSTAT6$^{WT}$ and mSTAT6$^{D419N}$ Eμ-Myc tumours. CD4 staining is consistently membranous, while phospho-STAT6 is expressed in both the cell cytoplasm and nucleus. **H.** Quantification of CD4 and phospho-STAT6 H-scores (see methods) in day 11 mSTAT6$^{WT}$ and mSTAT6$^{D419N}$ Eμ-Myc tumours. mSTAT6$^{D419N}$ Eμ-Myc tumours have significantly increased CD4 and phospho-STAT6 expression. **I.** Correlation of CD4 and phospho-STAT6 expression in each tissue. Pearson correlation r = 0.7610. **J.** Quantification of CD4+ T cells in day 11 mSTAT6$^{WT}$ and mSTAT6$^{D419N}$ Eμ-Myc tumours. CD4+ T cells are live, single cells, that are CD45+, CD3+, and CD4+. Data is expressed as a percentage of CD45+ cells in each tissue, and as the total number of CD4+ T cells in each tissue. **K.** Quantification of CD8+ T cells in day 11 mSTAT6$^{WT}$ and mSTAT6$^{D419N}$ Eμ-Myc tumours. CD8+ T cells are live, single cells, that are CD45+, CD3+, and CD8+. Data is expressed as a percentage of CD45+ cells in each tissue, and as the total number of CD8+ T cells in each tissue. Detailed statistics and n for each figure can be found in **Sup. Table 3.5**.

### *3.3.2 mSTAT6$^{D419N}$-Eμ-Myc Tumours have Increased CCR4+ Th1 Cells and Increased Hallmarks of Inflammation*

We next questioned how CD4+ T cells are being enhanced in the Eμ-Myc-STAT6$^{D419N}$ TME. It is well-established that the STAT6 transcriptional target CCL17 is overexpressed by *STAT6$^{D419}$*-mutant lymphoma cells in response to IL-4 stimulation (6, 7, 14), and CCL17 can drive recruitment of CCR4+ immune cells, including CD4+ T cells. We first examined the expression of CCR4 on CD4+ T cells in Eμ-Myc-mSTAT6$^{WT}$ and mSTAT6$^{D419N}$ day 11 tumours. Flow cytometry analysis revealed a significant increase in the total number of CCR4+ CD4+ T cells in mSTAT6$^{D419N}$ tumors compared to mSTAT6$^{WT}$ tumors (**Figure 3.2A**). This suggests that mSTAT6$^{D419N}$ tumors more effectively recruit or retain CCR4+ CD4+ T cells, consistent with the previously described increase in CCL17 in *STAT6$^{D419}$* tumours (7, 14).

We further compared the polarization states of CD4+ T cells in mSTAT6$^{WT}$ and mSTAT6$^{D419N}$ tumours by quantifying regulatory T cells (Tregs), T follicular helper cells (Tfh), inflammatory T helper cells (Th1), and anti-inflammatory T helper cells (Th2) using flow cytometry (**Figure 3.2B**). Among these subsets, only Th1 cells were significantly increased in mSTAT6$^{D419N}$ tumors, indicating a skewed immune profile favoring Th1 cell recruitment or expansion. Indeed, a higher percentage of Th1 cells in mSTAT6$^{D419N}$ tumors were CCR4-positive compared to those in mSTAT6$^{WT}$ tumors. Additionally, Th1 cells in mSTAT6$^{D419N}$ tumors exhibited a significantly higher mean fluorescence intensity (MFI) of CCR4 expression (**Figure 3.2C**).

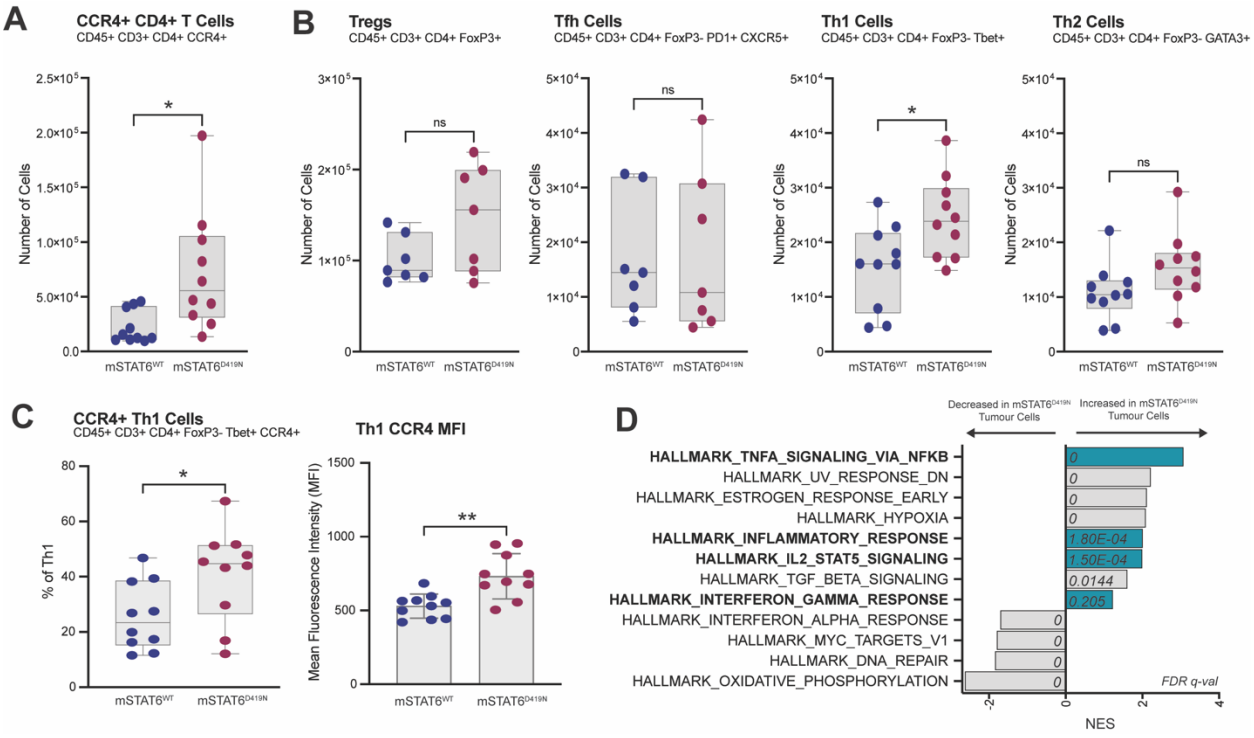


**Figure 3.2: STAT6$^{D419N}$-Eμ-Myc tumours have increased prevalence of CCR4+ Th1 cells**

**A.** Quantification of CCR4+ CD4+ T cells in day 11 mSTAT6$^{WT}$ and mSTAT6$^{D419N}$ Eμ-Myc tumours. CCR4+ CD4+ T cells are live, single cells, that are CD45+, CD3+, CD4+, and CCR4+. Data is expressed as a total number of CCR4+ CD4+ T cells in each

tissue. **B.** Quantification of Tregs (CD45+ CD3+ CD4+ FoxP3+), Tfh cells (CD45+ CD3+ CD4+ FoxP3- PD1+ CXCR5+), Th1 cells (CD45+ CD3+ CD4+ FoxP3- Tbet+), and Th2 (CD45+ CD3+ CD4+ FoxP3- GATA3+) in in day 11 mSTAT6$^{WT}$ and mSTAT6$^{D419N}$ Eμ-Myc tumours. Data is expressed as a total number of cells in each tissue. **C.** Expression of CCR4 on Th1 cells in day 11 mSTAT6$^{WT}$ and mSTAT6$^{D419N}$ Eμ-Myc tumours, expressed as total percentage of Th1 cells that are CCR4+ (CD45+ CD3+ CD4+ FoxP3- Tbet+ CCR4+), and as the mean fluorescence intensity (MFI) of CCR4 expression on Th1 cells. **D.** Gene set enrichment analysis (GSEA) obtained from RNAseq of isolated tumour cells (ie. CD19+ cells) from day 11 mSTAT6$^{WT}$ and mSTAT6$^{D419N}$ Eμ-Myc tumours. Teal colouring indicates enrichment of pathways associated with inflammation and inflammatory signaling. NES = Normalized Enrichment Score.

To explore the broader impact of immune changes on the tumour compartment, we isolated Eμ-Myc cells from mSTAT6$^{WT}$ and mSTAT6$^{D419N}$ mid-disease tumours, using CD19 microbeads, and performed bulk RNA sequencing. Gene set enrichment analysis (GSEA) indicated that mSTAT6$^{D419N}$ tumour cells had increased hallmarks of inflammation (**Figure 3.2D**), consistent with the elevated presence of Th1 cells. Of note, Th1 cells in mSTAT6$^{WT}$ and mSTAT6$^{D419N}$ tumours did not express more interferon-gamma (IFNγ), nor did they show increased expression of activation or degranulation markers (CD69 and CD107a, respectively; **Sup. Figure 3.2A-C**). Additionally, the expression of these markers was not changed on CD8+ T cells (**Sup. Figure 3.2D-F**). These findings demonstrate that mSTAT6$^{D419N}$ mutation leads to the increased presence of CCR4+ Th1 cells, that may contribute to an enhanced inflammatory response signature in mSTAT6$^{D419N}$ tumour cells.

### *3.3.3 mSTAT6$^{D419N}$ Tumours are Chemoattractive to CCR4+ CD4+ T Cells.*

To experimentally validate that STAT6$^{D419N}$ tumor cells attract CCR4+ immune cells, we conducted a series of *ex vivo* assays designed to assess the chemoattractive properties of Eμ-Myc-mSTAT6$^{WT}$ and mSTAT6$^{D419N}$ tumor cells. We first tested the ability

of Eμ-Myc tumour cells in culture to attract various CCR4+ immune cells, including CD4+ T cells, eosinophils, dendritic cells, macrophages, NK cells, and CD8+ T cells. In this experiment, mSTAT6$^{WT}$ and mSTAT6$^{D419N}$ Eμ-Myc cells were plated in a 6-well dish and were stimulated with IL-4. One hour following stimulation, bulk splenocytes from non-tumour bearing mice were plated overtop the Eμ-Myc tumour cells, using a 5 μm pore membrane. Splenocytes were allowed to migrate towards the tumour cells for 16 hours, then migrated cells were collected and characterized by flow cytometry (**Figure 3.3A**). Concordant with our previous studies, qPCR confirmed that mSTAT6$^{D419N}$ tumour cells indeed produced significantly more *CCL17* in response to IL-4 stimulation than mSTAT6$^{WT}$ tumour cells (**Figure 3.3B**). Indeed, IL-4-stimulated tumour cells induced significant migration of CCR4+ splenocytes, predominantly compared of CD4+ T cells (**Figure 3.3C**). As predicted, STAT6$^{D419N}$ cells induced significantly greater migration of CCR4+ CD4+ T cells as compared to STAT6$^{WT}$ cells. This migration was blocked by pre-treating splenocytes with the CCR4 inhibitor AZD2098 (16). These findings demonstrate that STAT6$^{D419N}$ tumor cells are more effective at attracting CCR4+ CD4+ T cells, highlighting the functional impact of increased CCL17 production by mSTAT6$^{D419N}$ tumour cells.

*In vivo*, there is extensive crosstalk between tumour cells, immune cells, and stroma, that is not recapitulated with splenocytes from tumour-naïve mice migrating towards tumour cells stimulated with a single cytokine. Thus, we next attempted to more closely model the complexity of an intact TME *ex vivo*, to better characterize CD4+ T cell migration. To do this, mice were injected with either mSTAT6$^{WT}$ or mSTAT6$^{D419N}$ tumor cells, and at mid-disease, tumors and spleens were harvested and dissociated. CD4+ T

cells were enriched from the tumour-bearing spleens, and tumor supernatants were collected from lymph nodes (**Figure 3.3D**). Thus, with this model, CD4+ T cells have been polarized due to tumour exposure, and tumour supernatants represent the secretome of an intact TME. Chemokine/cytokine profiling of tumour supernatants demonstrated that mSTAT6$^{D419N}$ tumours tended to express higher levels of many cytokines/chemokines, including Th1-associated cytokines IFNγ, IL-2, TNFα, and IL-12, and the CCR4-ligands and STAT6 transcriptional targets CCL17 and CCL22 (**Figure 3.3E**). Supernatants from either mSTAT6$^{WT}$ or mSTAT6$^{D419N}$ tumours were then used as chemoattractants to CD4+ T cells derived from tumour-bearing spleens (**Figure 3.3F**).

We found that significantly more CCR4+ CD4+ T cells migrated towards STAT6$^{D419N}$ supernatant compared to STAT6$^{WT}$ supernatant, regardless of whether the CD4+ T cells were derived from STAT6$^{WT}$ or STAT6$^{D419N}$ tumour-bearing mice (**Figure 3.3G**). This migration was markedly reduced when CD4+ T cells were pretreated with AZD2098, indicating the role of CCR4-CCL17 interaction in transmigration of CD4+ T cells towards tumour supernatant. We further phenotyped the migrated T cells, and found that similar proportions of Treg, Tfh, Th1, Th2, and naive/unclassified CD4+ T cells migrated towards both STAT6$^{WT}$ and STAT6$^{D419N}$ supernatants (**Figure 3.3H**), suggesting that the chemoattractive effect of STAT6$^{D419N}$ supernatant is not specific to any CD4+ T cell subset. These experiments collectively demonstrate that STAT6$^{D419N}$ tumors possess a heightened ability to attract CCR4+ CD4+ T cells through increased production of CCL17, thereby enhancing the CD4-rich microenvironmental characteristics of STAT6$^{D419N}$ tumours.

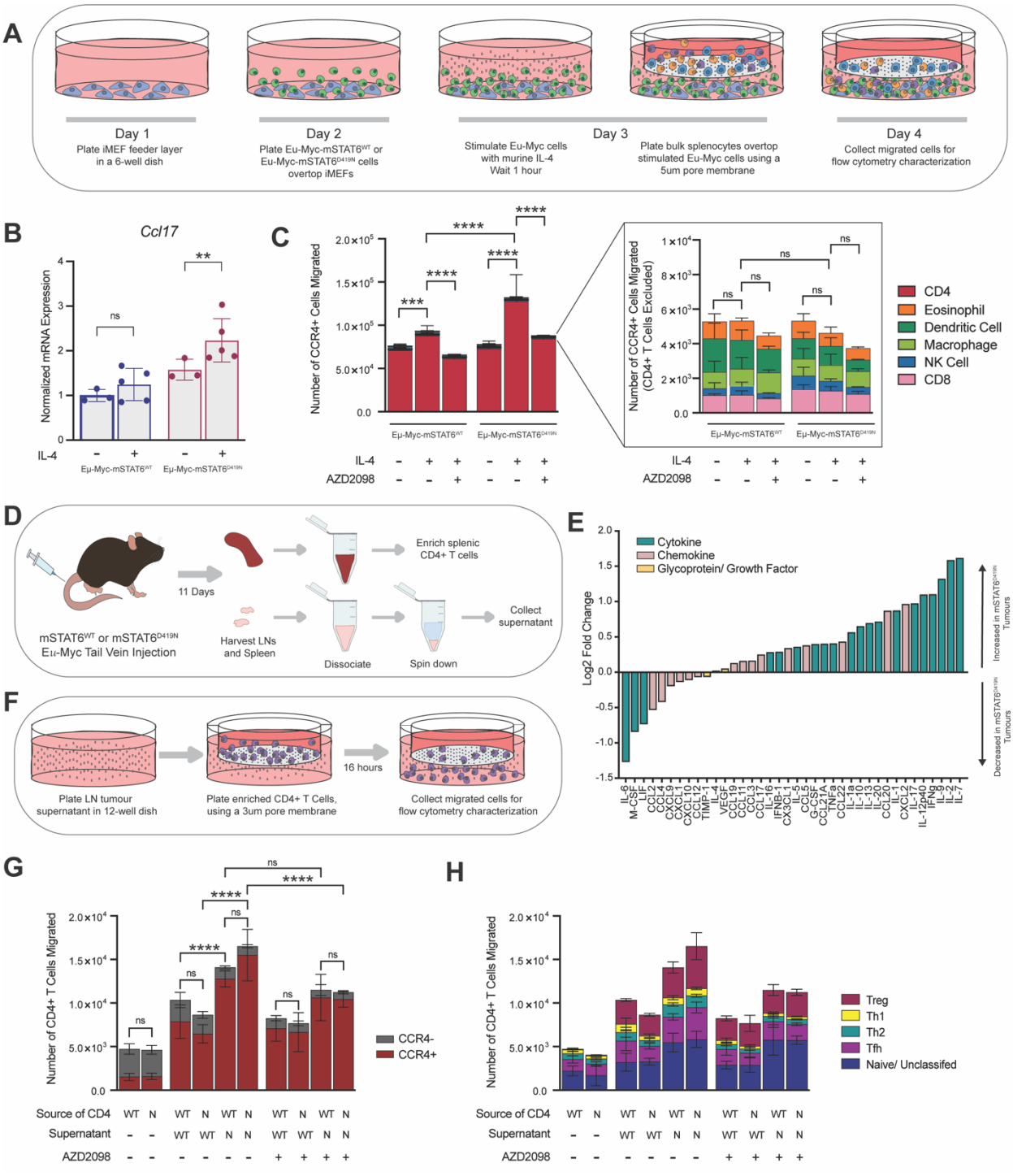


**Figure 3.3: STAT6$^{D419N}$-Eμ-Myc tumours are directly chemoattractive to CCR4+ CD4+ T cells.**

**A.** Schematic demonstrating the workflow for determining the ability of mSTAT6$^{WT}$ and mSTAT6$^{D419N}$ Eμ-Myc tumour cells, +/- mIL-4 to attract different cell types from tumour-

naïve spleen, +/- AZD2098. **B.** Quantification of *Ccl17* expression in mSTAT6$^{WT}$ and mSTAT6$^{D419N}$ Eμ-Myc tumour cells, following 1 hour of mIL-4 or vehicle stimulation. **C.** Quantification of CCR4+ splenocytes that migrated towards mSTAT6$^{WT}$ or mSTAT6$^{D419N}$ Eμ-Myc tumour cells, as determined by flow cytometry. (**C$_i$**) shows all migrated cells. (**C$_{ii}$**) is the same data but excluding CD4+ T cells for better visualization of other migrated cellular subsets. **D.** Schematic demonstrating the workflow for collecting tumour-exposed CD4+ T cells from spleen and day 11 mSTAT6$^{WT}$ and mSTAT6$^{D419N}$ Eμ-Myc day 11 tumour supernatants. **E.** Waterfall plot showing the log2 fold change in expression of cytokines and chemokines between mSTAT6$^{WT}$ and mSTAT6$^{D419N}$ Eμ-Myc day 11 tumour supernatants. **F.** Schematic demonstrating the workflow for determining the ability of mSTAT6$^{WT}$ and mSTAT6$^{D419N}$ Eμ-Myc day 11 tumour supernatants to attract CD4+ T cells from tumour-exposed spleen. **G.** Quantification of CCR4+ CD4+ T cells enriched from either STAT6$^{WT}$ or STAT6$^{D419N}$ Eμ-Myc day 11 tumour bearing mice that migrated towards STAT6$^{WT}$ or STAT6$^{D419N}$ Eμ-Myc day 11 tumour supernatants. **H.** Data from (**G**), expressed as CD4+ T cell polarization state (ie. Treg, Th1, Th2, Tfh, or Naïve/ Unclassified).

### *3.3.4 mSTAT6$^{D419N}$ Eμ-Myc Tumours are Resistant to Doxorubicin Treatment*

*In vitro,* mSTAT6$^{D419N}$ Eμ-Myc tumour cells do not have altered sensitivity to any of the individual components of R-CHOP (17). However, our data indicate that *mSTAT6$^{D419N}$* mutation drives increased frequency of CCR4+ CD4+ T cells, leading to evidence of enhanced tumour cell inflammatory signaling, which is known to correlate with doxorubicin resistance in human DLBCL patients (18-20). Thus, we hypothesized that an intact tumour microenvironment is required to truly realize the impact of *STAT6$^{D419}$* mutation on therapeutic response, and that our mouse model of *STAT6$^{D419}$*-mutant lymphoma may not recapitulate the results previously obtained *in vitro*.

To investigate this, mice were injected with Eμ-Myc mSTAT6$^{WT}$ or mSTAT6$^{D419N}$ tumour cells on Day 1, then were given 3 mg/kg of doxorubicin at day 11, day 13, and day 15 post-injection (**Figure 3.4A**). Over the course of disease, tumours were monitored via ultrasound. We found that mSTAT6$^{WT}$ tumours returned to baseline size by day 15 post-injection, indicating the efficacy of doxorubicin treatment. However, mSTAT6$^{D419N}$

tumour volume stabilized during doxorubicin treatment, but tumours continued to grow immediately upon the cessation of treatment (**Figure 3.4B**). Additionally, ultrasound monitoring of the secondary tumour site, the inguinal lymph node (iLN), revealed that 100% of mice with mSTAT6$^{WT}$ tumours had sustained disease clearance in the iLN, whereas 40% of mice with mSTAT6$^{D419N}$ tumours had bilateral iLN relapse (**Figure 3.4C**). While not achieving statistical significance (Gehan-Breslow-Wilcoxon test p = 0.0764), this led to decreased overall survival of mSTAT6$^{D419N}$ tumour bearing mice treated with doxorubicin (**Figure 3.4D**).

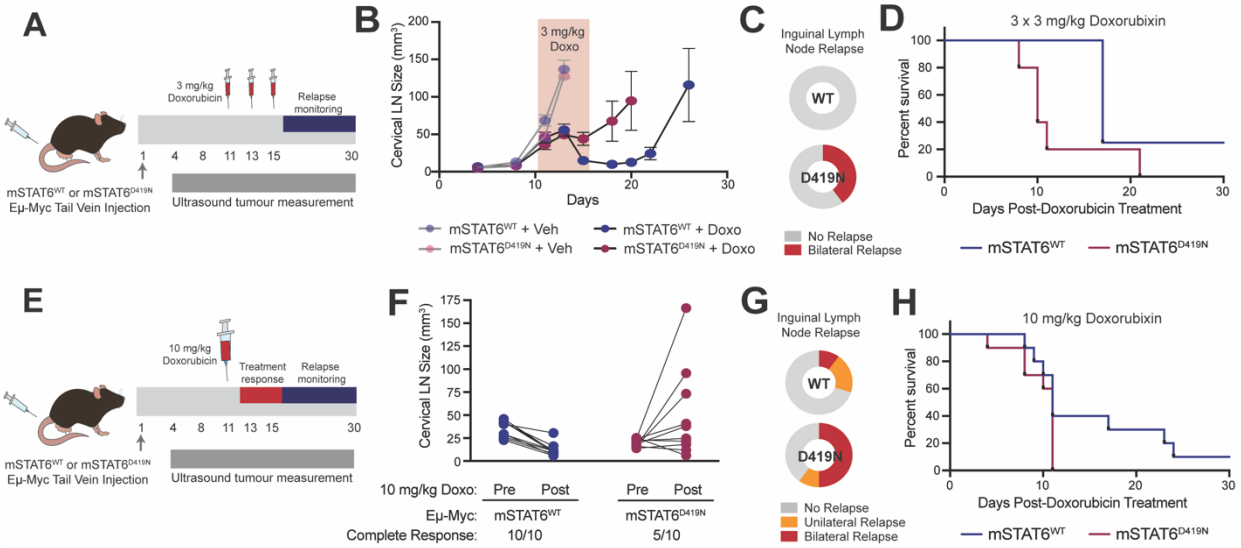


**Figure 3.4: mSTAT6$^{D419N}$-Eμ-Myc tumours are resistant to doxorubicin treatment.** **A.** Schematic demonstrating the timeline for 3 x 3 mg/kg doxorubicin treatment and relapse monitoring for mSTAT6$^{WT}$ and mSTAT6$^{D419N}$ Eμ-Myc tumour bearing mice. **B.** Growth curve of mSTAT6$^{WT}$ and mSTAT6$^{D419N}$ Eμ-Myc tumours, treated with either 3 x 3 mg/kg doxorubicin or vehicle control. Red shaded area indicates the days where doxorubicin treatment was given. **C.** Pie charts showing the proportion of mice with secondary tumour site (ie. the iLN) relapse following 3 x 3 mg/kg doxorubicin treatment. **D.** Kaplan-Meier survival curve of mSTAT6$^{WT}$ and mSTAT6$^{D419N}$ Eμ-Myc tumour bearing mice following 3 x 3 mg/kg doxorubicin treatment. **E.** Schematic demonstrating the timeline for 10 mg/kg doxorubicin treatment and relapse monitoring for mSTAT6$^{WT}$ and mSTAT6$^{D419N}$ Eμ-Myc tumour bearing mice. **F.** Treatment response of mSTAT6$^{WT}$ and mSTAT6$^{D419N}$ Eμ-Myc tumour bearing mice following 10 mg/kg doxorubicin. Connecting lines show the pre- and post-treatment cLN volumes in individual mice. If the slope of the connecting line is negative, mice are considered to have had a complete response

to doxorubicin. Pre-treatment is day 11 post-Eμ-Myc injection, and post-treatment is day 15 post-Eμ-Myc injection. **G.** Pie charts showing the proportion of mice with iLN relapse following 10 mg/kg doxorubicin treatment. **H.** Kaplan-Meier survival curve of $mSTAT6^{WT}$ and $mSTAT6^{D419N}$ Eμ-Myc tumour bearing mice following 10 mg/kg doxorubicin treatment.

We next changed our treatment paradigm, to more closely model primary-refractory disease, by giving each mouse a single high-dose doxorubicin treatment of 10 mg/kg at day 11 post-injection, which represents a timepoint where tumours have established, and our data indicates that $mSTAT6^{D419N}$ tumours have CCR4+ CD4+ T cell invasion **(Figure 3.4E**). Similar to our findings with 3 x 3 mg/kg doxorubicin, we found that 100% of mice bearing $mSTAT6^{WT}$ tumours decreased to baseline size, while only 50% of mice bearing $mSTAT6^{D419N}$ tumours decreased in size (**Figure 3.4F**). This was recapitulated in the iLN, where 100% of mice bearing $mSTAT6^{WT}$ tumours had durable disease clearance in the iLN, while 50% of mice bearing $mSTAT6^{D419N}$ tumours had bilateral iLN relapse, and another 10% had unilateral iLN relapse (**Figure 3.4G**). Accordingly, $mSTAT6^{WT}$ tumour bearing mice had a trend towards improved overall survival (Gehan-Breslow-Wilcoxon test $p = 0.1211$; **Figure 3.4H**).

Tumours collected at disease endpoint showed no difference in tumour burden or skewing in the proportions of CD4+ T cells, and CD8+ T cells between $mSTAT6^{WT}$ and $mSTAT6^{D419N}$ tumours (**Sup. Figure 3.3A-D**). These results indicate that the $mSTAT6^{D419N}$-driven changes in the TME at day 11 are sufficient to engender resistance to doxorubicin, but that changes in the TME are not retained or exaggerated at disease relapse in this mouse model.

### *3.3.5 PhenoCycler Imaging Reveals Preferential Spatial Interactions between phospho-STAT6+ Tumour Cells and CCR4+ CD4+ T cells in Eμ-Myc Tumours*

Recent publications have demonstrated that the spatial organization of tumours at a single cell level is an additional layer of disease heterogeneity that must be understood to make conclusions about the contribution of the TME to disease progression (21, 22). Moreover, the cellular interactions within a tumour can be predictive of therapeutic responses (15, 23-25). To interrogate how cellular interactions are altered in the context of mSTAT6$^{D419N}$ lymphoma, we developed a custom highly multiplexed PhenoCycler spatial imaging antibody panel (**Sup. Table 3.2**), specifically optimized for murine FFPE imaging. Using this imaging panel, we were able to visualize tumour structure and myeloid/ lymphoid infiltration. Moreover, we included markers for the intercellular STAT6 signaling axis, including phospho-STAT6, IL4R, CCL17, CCL22, and CCR4. To examine the spatiotemporal dynamics involved in Eμ-Myc tumour development, we generated a tissue microarray (TMA) with cores collected from Eμ-Myc mSTAT6$^{WT}$ and mSTAT6$^{D419N}$ tumours at early-, mid-, and late-disease, and disease relapse (**Figure 3.5A, Sup. Figure 3.4A-B**). This TMA was imaged with PhenoCycler (**Figure 3.5B**), and analysis was performed to classify the different cell types found within each core and to characterize their spatial interactions.

With PhenoCycler, we identified cellular clusters corresponding to tumor cells, B cells, CD8+ T cells, CD4+ T cells, Tregs, macrophages, dendritic cells (DCs), neutrophils, fibroblasts, and endothelial cells (**Figure 3.5C**). Fewer than 5% of cells remained "unclassified", due to overlapping marker expression and cell segmentation noise. When

these classifications were overlaid onto multiplexed tumor images in a Voronoi diagram, the accuracy in distinguishing different cell types within the TME was clear (**Figure 3.5D**).

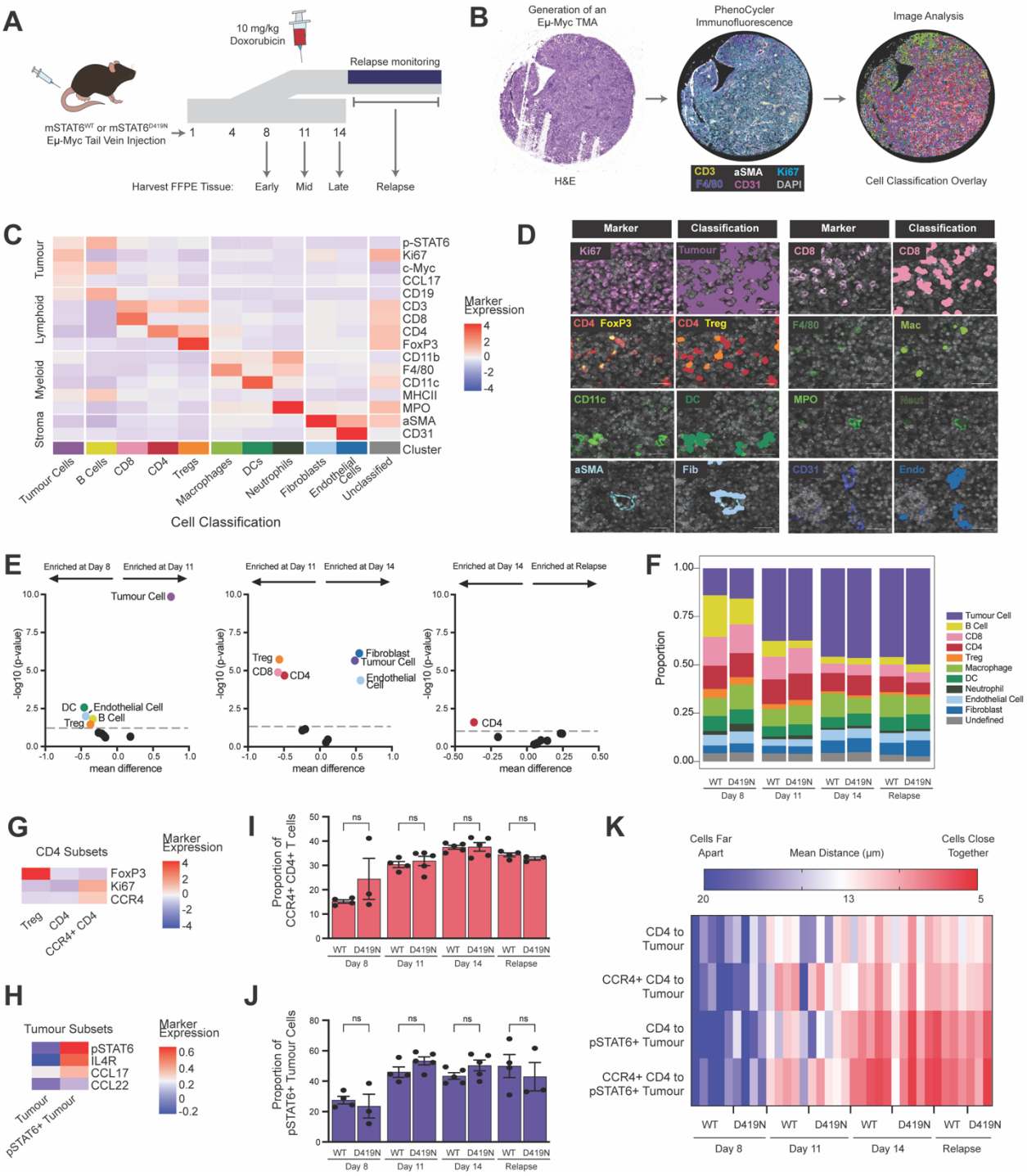


**Figure 3.5: PhenoCycler imaging reveals that phospho-STAT6+ tumour cells are in close proximity to CCR4+ CD4+ T cells.**

**A.** Schematic showing the timeline for collection of FFPE samples from mSTAT6$^{WT}$ and mSTAT6$^{D419N}$ Eμ-Myc tumours for PhenoCycler staining. **B.** For this experiment, an Eμ-Myc TMA was generated for PhenoCycler staining with a 35-plex custom antibody panel optimized for murine FFPE staining. With PhenoCycler, antibodies marking tumour cells, immune cells, and stromal cells can be used to stain tissue in a single step. Immunofluorescent images are acquired with the PhenoCycler-Fusion system. Images are analyzed and different cell types within each tissue are classified. **C.** Heatmap showing the mean expression of different markers with cell classifications. **D.** Voronoi overlay showing accurate classification of different cell types within Eμ-Myc tumour tissues. **E.** Volcano plots showing the change in abundance of different cell types over the course of Eμ-Myc tumour evolution. Coloured dots above the grey dashed lines indicate cell types that have significantly changed in abundance between the indicated time points. **F.** Proportions of different cell types in mSTAT6$^{WT}$ and mSTAT6$^{D419N}$ Eμ-Myc tumours at early-, mid-, late-disease, and relapse. **G.** Heatmap showing the mean expression of FoxP3, Ki67, and CCR4 in different CD4+ T Cell subsets (ie. Treg, CD4, and CCR4+ CD4). **H.** Heatmap showing the mean expression of phospho-STAT6, IL4R, CCL17, and CCL22 in tumour cells and phospho-STAT6+ tumour cells. **I**. Proportion of CCR4+ CD4 T cells among total CD4+ T cells in mSTAT6$^{WT}$ and mSTAT6$^{D419N}$ Eμ-Myc tumours at early-, mid-, late-disease, and relapse. **J.** Proportion of phospho-STAT6+ tumour cells among total tumour cells in mSTAT6$^{WT}$ and mSTAT6$^{D419N}$ Eμ-Myc tumours at early-, mid-, late-disease, and relapse. **K.** Spatial distance calculations between the annotated cell types. Blue hue indicates that cells are found further apart, while red hue indicates that cells are found closer together.

Using these classifications, we first sought to characterize how the TME of Eμ-Myc tumours evolve over the course of disease progression (**Figure 3.5E**). As expected, from early- to mid-disease, Eμ-Myc tumours showed significant expansion the tumour cell compartment, and a decrease in endothelial cells, Tregs, DCs, and non-transformed B cells. As tumours progressed to late disease, the tumour cell compartment increased even further, with additional expansion of stromal components, including endothelial cells and fibroblasts. At the late disease timepoint, there was also a relative decrease in all T cell subsets, concordant with human data that suggests that exclusion of T cells from lymphoma tumours is an indicator of aggressive disease (26). Tumours collected at disease relapse were almost indistinguishable from late-disease treatment-naïve tumours, apart from a small decrease in CD4+ T cells at relapse compared to untreated

late-disease tumours. Thus, our PhenoCycler data are consistent with a loss in cellular heterogeneity with disease progression where tumour cells continue to expand and TME constituents are lost.

We next compared how the proportions of different cell types varied between mSTAT6$^{WT}$ and mSTAT6$^{D419N}$ tumours in early-disease, mid-disease, late-disease, and relapsed tumours. Although we saw an increase in CD4+ T cells in mSTAT6$^{D419N}$ tumours at mid-disease by flow cytometry, we found no significant differences in the proportions of any of the different cell types in mSTAT6$^{WT}$ and mSTAT6$^{D419N}$ tumour at any time point (**Figure 3.5F**). Therefore, we next aimed to further segment cells into more specific subtypes and polarization states, to see if any differences would emerge. We were able to identify M1-like, M2-like, M0-like, and PD-L1+ macrophages within our macrophage subclassification (**Sup. Figure 3.5A-B**), TCF1+, PD1+, Ki67+, and GZMB+ CD8+ T cells within our CD8 subclassification (**Sup. Figure 3.5C-D**), CCR4+ CD4+ T cells within our CD4+ T cell subclassification (**Figure 3.5G**), and phospho-STAT6+ tumour cells within our tumour cell subclassification (**Figure 3.5H**). When the proportions of these different cell types were compared over time, we found both pSTAT6+ tumour cells and CCR4+ CD4+ T cells significantly increased in prevalence from early to mid-disease **(**Sup. **Figure 3.5E**).

Given our interest in the chemoattraction of phospho-STAT6+ tumour cells to CCR4+ CD4+ T cells, we next examined the proportions of these cell types within their parent population across time. We found that CCR4+ CD4+ T cells were increased in proportion in mid-, late- and relapsed-disease as compared to early-disease, but that there were no significant differences between mSTAT6$^{WT}$ and mSTAT6$^{D419N}$ at any time

point (**Figure 3.5I**). The proportion of phospho-STAT6+ tumour cells showed a similar trend (**Figure 3.5J**). Thus, we next examined how phospho-STAT6 expression impacted the immediate environment of the tumour cell. When we measured the mean distance between CD4+ T cells and tumour cells, CCR4+ CD4+ T cells and tumour cells, CD4+ T cells and phospho-STAT6+ tumour cells, and CCR4+ CD4+ T cells and phospho-STAT6+ tumour cells we found that in mid-, late-, and relapsed-disease, the cells with the closest proximity were phospho-STAT6+ tumour cells and CCR4+ CD4+ T cells (**Figure 3.5K**). Interestingly, at early disease, regardless of CCR4 and phospho-STAT6 expression status, CD4+ T cells were the furthest distance away from tumour cells, indicating that the physical proximity of CD4 T cells and tumour cells is gained as the tumours evolve. The observed increase in proximity at later disease timepoints is independent of tumour genotype, indicating that activation of STAT6 signaling is sufficient to induce the interaction of tumour cells with CD4+ and CCR4+ CD4+ T cells. Thus, our results support the notion that expression of phospho-STAT6 in Eμ-Myc tumour cells leads to the recruitment of CCR4+ CD4+ T cells.

### *3.3.6 Treatment of mSTAT6$^{D419N}$ Eμ-Myc Tumours with the CCR4 Inhibitor AZD2098 Re-Sensitizes them to Doxorubicin*

We aimed to investigate how inhibiting CCR4 would affect the growth of Eμ-Myc tumors, following our discovery that phospho-STAT6 expression in tumor cells enhances the recruitment of CCR4+ CD4+ T cells. To do this, we treated Eμ-Myc tumor-bearing mice with AZD2098 and monitored tumor growth and changes in the TME over time (**Figure 3.6A**). AZD2098 was administered via oral gavage twice weekly, and we found that it successfully blocked the mid-disease invasion of CD4+ T cells into mSTAT6$^{D419N}$

tumors (**Figure 3.6B**). Further analysis showed that AZD2098 did not affect the numbers of Tregs or Tfh cells in either mSTAT6$^{WT}$ or mSTAT6$^{D419N}$ tumors. However, as previously noted, Th1 cells were more abundant in mSTAT6$^{D419N}$ tumors compared to mSTAT6$^{WT}$, and treatment with AZD2098 resulted in a modest decrease in Th1 cells in mSTAT6$^{D419N}$ tumors. Consistent with CCR4's role in Th2 cells (27, 28), AZD2098 treatment reduced Th2 cells in both mSTAT6$^{WT}$ and mSTAT6$^{D419N}$ tumors (**Figure 3.6C**). Despite these shifts in TME composition, AZD2098 treatment did not significantly alter the growth rate of either mSTAT6$^{WT}$ or mSTAT6$^{D419N}$ tumors (**Figure 3.6D**).

Encouraged by AZD2098's ability to reduce CD4+ T cell infiltration in mSTAT6$^{D419N}$ tumors to levels comparable to mSTAT6$^{WT}$, we hypothesized that the addition of AZD2098 could restore doxorubicin sensitivity in mSTAT6$^{D419N}$ tumors (**Figure 3.6E**). As in previous experiments, 100% of mSTAT6$^{WT}$ tumors responded completely to doxorubicin alone, whereas only 20% of mSTAT6$^{D419N}$ tumors responded (**Figure 3.6F**). Remarkably, combining AZD2098 with doxorubicin resulted in a complete response of 100% of mSTAT6$^{WT}$ tumors and 80% of mSTAT6$^{D419N}$ tumors. While mSTAT6$^{D419N}$ tumors treated with doxorubicin alone resumed growth immediately after treatment cessation, tumors treated with the combination of doxorubicin and AZD2098 did not regrow until approximately one-week post-treatment (**Figure 3.6G**). Additionally, 80% of mSTAT6$^{D419N}$ tumors treated with doxorubicin alone showed bilateral inguinal lymph node relapse, whereas those treated with the combination showed only unilateral relapse, indicating a minor reduction in systemic disease (**Figure 3.6H**). Overall, the combination treatment significantly improved survival in mice bearing mSTAT6$^{D419N}$ tumors, but not in those with mSTAT6$^{WT}$ tumors (**Figure 3.6I**). These findings demonstrate that inhibiting

the CCL17-CCR4 signaling axis re-sensitizes mSTAT6$^{D419N}$ Eμ-Myc tumors to doxorubicin treatment.

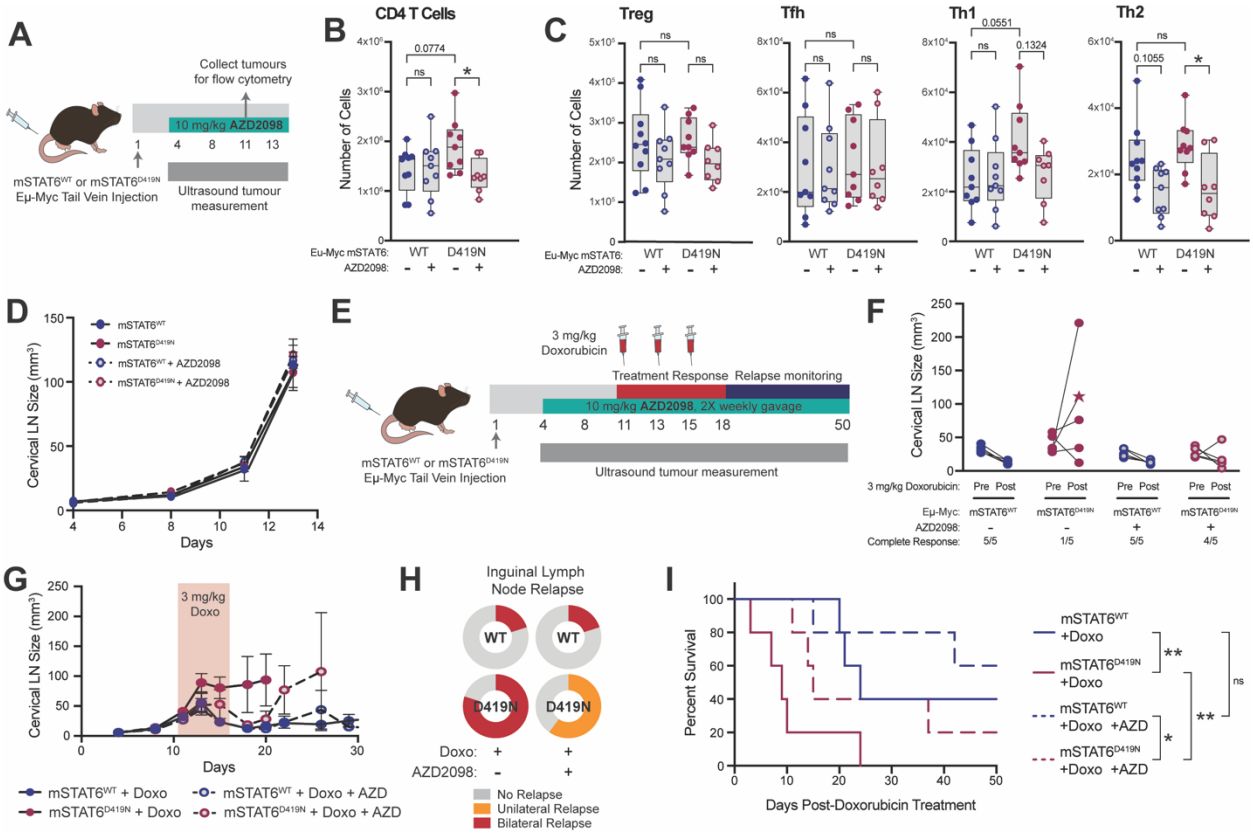


**Figure 3.6: CCR4 inhibition resensitizes mSTAT6$^{D419N}$-Eμ-Myc tumours to doxorubicin treatment.**

**A.** Schematic demonstrating the timeline for determining the impact of AZD2098 treatment on mSTAT6$^{WT}$ and mSTAT6$^{D419N}$ Eμ-Myc TME composition and tumour growth. **B.** Quantification of CD4+ T cells in mSTAT6$^{WT}$ and mSTAT6$^{D419N}$ day 11 Eμ-Myc tumours, following treatment with AZD2098 or vehicle control. **C.** Quantification of Tregs (CD45+ CD3+ CD4+ FoxP3+), Tfh cells (CD45+ CD3+ CD4+ FoxP3- PD1+ CXCR5+), Th1 cells (CD45+ CD3+ CD4+ FoxP3- Tbet+), and Th2 (CD45+ CD3+ CD4+ FoxP3- GATA3+) in mSTAT6$^{WT}$ and mSTAT6$^{D419N}$ day 11 Eμ-Myc tumours, following treatment with AZD2098 or vehicle control. **D.** Growth curve of mSTAT6$^{WT}$ and mSTAT6$^{D419N}$ Eμ-Myc tumours, treated with either 2 times weekly 10 mg/kg AZD2098 or vehicle control. **E.** Schematic demonstrating the timeline for 3 x 3 mg/kg doxorubicin and 10 mg/kg AZD treatment and relapse monitoring for mSTAT6$^{WT}$ and mSTAT6$^{D419N}$ Eμ-Myc tumour bearing mice. **F.** Treatment response of mSTAT6$^{WT}$ and mSTAT6$^{D419N}$ Eμ-Myc tumour bearing mice following 3 x 3 mg/kg doxorubicin and 10 mg/kg AZD2098. Connecting lines show the pre- and post-treatment cLN volumes in individual mice. Pre-treatment is day 11 post-Eμ-Myc injection, and post-treatment is day 18 post-Eμ-Myc injection. Star indicates the cLN volume is from day 15 post-Eμ-Myc injection, and the

mouse did not survive until day 18 post-Eμ-Myc injection. **G.** Growth curve of mSTAT6$^{WT}$ and mSTAT6$^{D419N}$ Eμ-Myc tumours, treated with 3 x 3 mg/kg doxorubicin and 10 mg/kg AZD2098, or vehicle controls. Red shaded area indicates the days where doxorubicin treatment was given**. H.** Pie charts showing the proportion of mice with secondary tumour site (ie. the iLN) relapse following 3 x 3 mg/kg doxorubicin and 10 mg/kg AZD2098 treatment. **I.** Kaplan-Meier survival curve of mSTAT6$^{WT}$ and mSTAT6$^{D419N}$ Eμ-Myc tumour bearing mice following combination treatment with 3 x 3 mg/kg doxorubicin with 10 mg/kg AZD2098.

### *3.3.7 PhenoCycler Imaging of STAT6$^{D419}$-Mutant rrDLBCL Patient Samples Shows Increased Expression of phospho-STAT6, CCL17, and CCR4*

To validate our results in human samples, we performed PhenoCycler imaging on a DLBCL TMA with biopsy tissues collected at disease relapse. We additionally included slides with full biopsy specimens from 6 patients with STAT6$^{D419}$-mutant DLBCL, to compare how the presence of STAT6 mutation impacts the CCL17-CCR4 signaling axis (**Figure 3.7A-B**). Of these STAT6$^{D419}$-mutant tissue biopsies, three were relapse biopsies from DLBCL patients, one was a diagnostic DLBCL biopsy from a patient who proceeded to relapse, one was a diagnostic primary mediastinal B cell lymphoma (PMBCL) biopsy, and one was a diagnostic follicular lymphoma biopsy, that proceeded to transform into DLBCL (GCB) involving the central nervous system (DLBCL-CNS).

Using PhenoCycler, we were clearly able to visualize tumour cells, T cells, myeloid cells, fibroblasts, and endothelial cells within human DLBCL tissues (**Figure 3.7C, Sup. Figure 3.6**). Similarly to the Eμ-Myc TMA, samples were analyzed by segmenting images into cells, then performing unsupervised clustering based on cellular expression of the lineage markers CD11b, CD11c, CD14, CD15, CD20, CD21, CD31, CD3, CD4, CD8, CD68, FoxP3, Ki67, MPO, PAX5, pan-CK, and αSMA (**Figure 3.7D**). We then compared the proportion of these different cell types in rrDLBCL and STAT6$^{D419}$-mutant samples

(**Figure 3.7E**). Concordant with our previous observations (14), STAT6$^{D419}$-mutant rrDLBCL samples were among the highest expressors of CD4+ T cells. Intriguingly, the STAT6$^{D419}$-mutant sample from diagnostic DLBCL, FL, and PMBCL had relatively fewer CD4+ T cells.

We next examined phospho-STAT6 and CCL17 expression in tumour cells, and CCR4 expression in CD4+ T cells (**Figure 3.7F**). In tumour cells in STAT6$^{D419}$-mutant samples, phospho-STAT6 and CCL17 expression was significantly increased, as measured by mean fluorescence intensity (MFI) of each marker (**Figure 3.7G**). Additionally, the expression of CCL17 and phospho-STAT6 were significantly positively correlated (**Figure 3.7H**). CCR4 showed a similar increase in expression in CD4 T cells from STAT6$^{D419}$-mutant patients, and this was also significantly positively correlated with phospho-STAT6 expression (**Figure 3.7I-J**).

Finally, we asked if CD4+ and CCR4+ CD4+ T cells have increased proximity to phospho-STAT6+ tumour cells in STAT6$^{D419}$-mutant samples. To do this, we measured the proportion of total tumour cells versus phospho-STAT6+ tumour cells that have direct cellular contact with CD4+/ CCR4+ CD4+ T cells (**Figure 3.7K**). When these measurements were performed, we found that the proportion of total tumour cells interacting with CD4+ T cells or CCR4+ CD4+ T cells was unchanged between STAT6$^{WT}$ and STAT6$^{D419}$-mutant tissues. However, we found that proportion of CD4+ T cells interacting with phospho-STAT6+ tumour cells was significantly increased in STAT6$^{D419}$-mutant biopsies, and the proportion of CCR4+ CD4+ T cells interacting with phospho-STAT6+ tumour cells trended towards increased in STAT6$^{D419}$-mutant biopsies. Thus, these results strongly imply that the CCL17-CCR4 axis is over-activated in STAT6$^{D419}$

rrDLCBL tissues, leading to alterations in TME organization, and favouring interactions between CD4+ T cells and phospho-STAT6+ tumour cells.

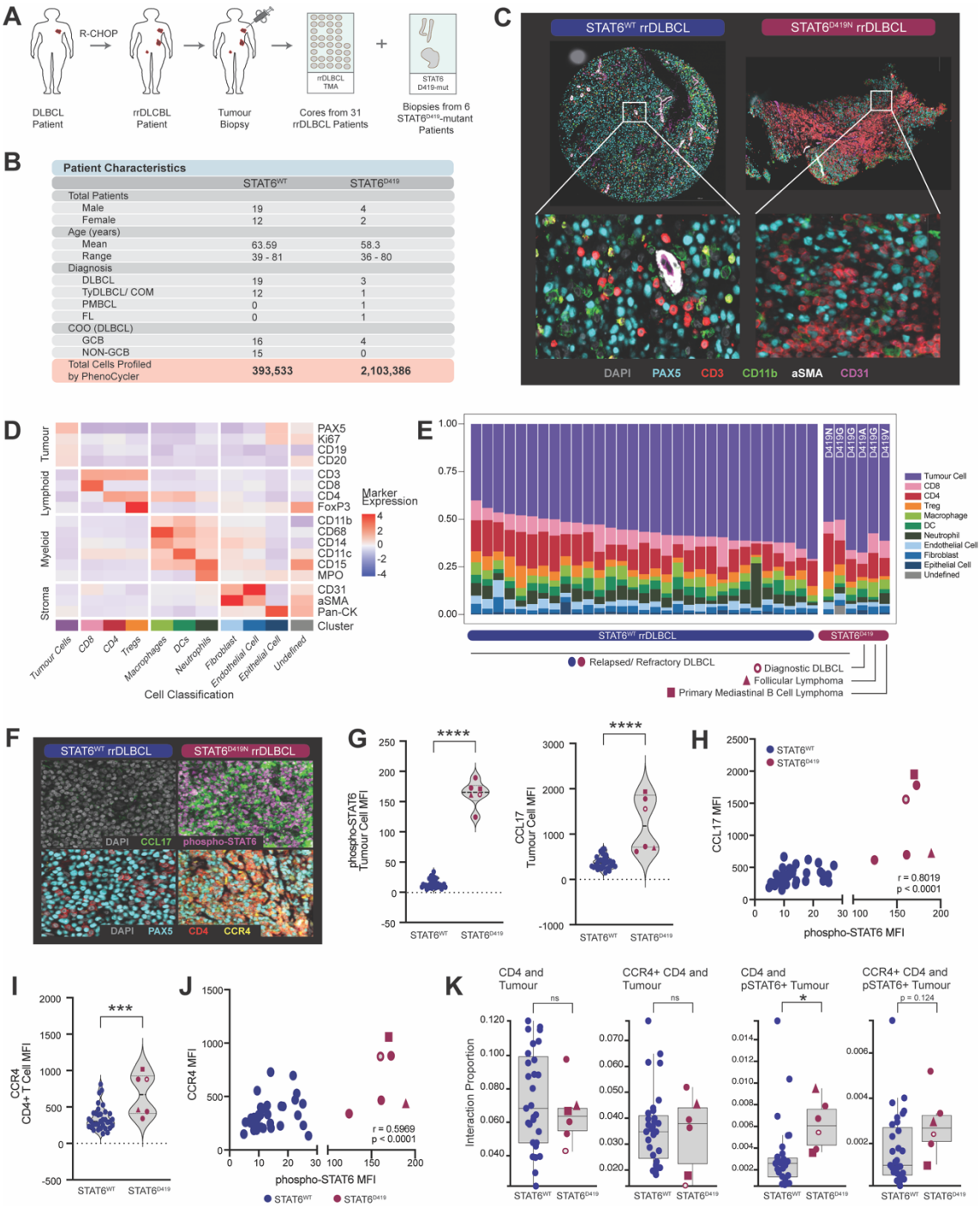


**Figure 3.7: PhenoCycler Imaging of human rrDLBCL biopsies reveals increased phospho-STAT6, CCL17, and CCR4 in STAT6$^{D419}$-mutant tumors**

**A.** Schematic depicting the human DLBCL samples used in this study for PhenoCycler imaging. A TMA was constructed with cores from rrDLBCL tissues. Additionally, whole biopsies from $STAT6^{D419}$-mutant patients were imaged. **B.** Patient characteristics for the biopsies included in this study. **C.** Representative images of a $STAT6^{WT}$ rrDLBCL TMA core, and a $STAT6^{D419N}$ rrDLBCL biopsy. **D.** Heatmap showing the mean expression of different markers with cell classifications. **E.** Proportions of different cell types in $STAT6^{WT}$ rrDLBCL and $STAT6^{D419}$-mutant lymphoma biopsies. $STAT6^{D419}$ biopsies included a diagnostic biopsy (open circle), a follicular lymphoma biopsy (triangle), and a primary mediastinal B cell lymphoma (square). **F.** Representative images of pSTAT6, CCL17, and CCR4 in a $STAT6^{WT}$ and $STAT6^{D419N}$ rrDLBCL biopsy. **G.** Mean fluorescence intensity (MFI) of phospho-STAT6 and CCL17 in tumour cells in $STAT6^{WT}$ and $STAT6^{D419}$-mutant biopsies. **H.** Correlation of phospho-STAT6 and CCL17 in each biopsy. Pearson correlation r = 0.8019. **I.** MFI of CCR4 in CD4+ T cells in $STAT6^{WT}$ and $STAT6^{D419}$-mutant biopsies. **J.** Correlation of phospho-STAT6 and CCR4 in each biopsy. Pearson correlation r = 0.5969. **K.** Interaction proportion between CD4+ T cells and tumour cells, CCR4+ CD4+ T cells and tumour cells, CD4+ T cells and phospho-STAT6+ tumour cells, and CCR4+ CD4+ T cells and phospho-STAT6+ T cells.

## 3.4 Discussion

In the present study, we directly demonstrate that mutation of STAT6 at residue D419 is sufficient to drive microenvironmental remodelling, largely via the CCL17-CCR4 axis. Using an immunocompetent mouse model, we showed that $STAT6^{D419N}$ mutant tumours have increased invasion of CCR4+ CD4+ T cells, coupled with resistance to doxorubicin treatment. Moreover, *ex vivo* functional assays demonstrated that $STAT6^{D419N}$ tumour cells are directly chemoattractive to CCR4+ CD4+ T cells. When Eμ-Myc-m$STAT6^{D419N}$ tumour bearing mice were treated with the small molecule CCR4 inhibitor AZD2098, we observed that CD4+ T cell infiltration was reduced, and mice were re-sensitized to doxorubicin treatment. In human $STAT^{D419}$ tumour samples, we confirm that expression of phospho-STAT6 in tumour cells is increased relative to $STAT6^{WT}$ rrDLBCL samples. Similarly to our mouse model, we observed increased tumour cell expression of CCL17 and increased cellular interactions of phospho-STAT6+ tumour cells

with CD4+ T cells. Thus, our findings via mouse modelling are highly relevant to the human rrDLBCL population.

Given the increase in phospho-STAT6 expression observed in human and murine STAT6$^{D419}$ DLBCL tumours (13), we initially hypothesized that STAT6$^{D419}$-mutant tumour cells might be more chemoattractive to IL-4-producing CD4+ T cells, such as Th2 or Tfh cells, that may then function to maintain STAT6 phosphorylation. However, our data indicates that STAT6-mutant lymphoma tumour cells actually have increased abundance of CCR4+ Th1-polarized CD4+ T cells, and not Th2 or Tfh cells. This is a surprising finding, especially given that CCR4 expression is typically associated with Th2 cells and Tregs; but we note that we are not the first to describe CCR4 expression on Th1 cells (27, 29, 30). Indeed, the m*STAT6*-mutant TME has increased Th1 associated cytokines, and m*STAT6* mutant tumour cells display evidence of an inflammatory gene signature. Concordant with previously published literature (18-20, 31, 32), this inflammatory TME is associated with therapeutic resistance to doxorubicin. Upon treatment of STAT6 mutant tumours with the CCR4 inhibitor AZD2098, CD4+ T cell invasion is reduced, and therapeutic sensitivity to doxorubicin is restored. Thus, our data show that the inflammatory TME induced by *STAT6$^{D419N}$* mutation contributes to therapeutic resistance.

Our study utilized the power of multiplex imaging to define tumour/ TME cellular heterogeneity within the context of spatial information. In both mouse and human tumors, phospho-STAT6+ tumor cells were closely associated with CD4+/CCR4+ T cells, an interaction which when inhibited reversed doxorubicin-resistance. This emphasizes the importance of understanding not only what cell types are present in the TME, but also their association with each other. While flow cytometry allows screening of larger number

of cells comprising the TME, the PhenoCycler adds information regarding location. Of note, a current limitation of this study is the dependence upon region selection for the TMA and a single 2D section per tumor. Thus, if differences in proportions of cells are subtley modified or tumor-region specific, PhenoCycler imaging of TMA cores may not have the power to discriminate the changes. We additionally note that both murine tumour types have the same Eμ-Myc parent, with the only difference being overexpression of either m*STAT6*$^{WT}$ or m*STAT6*$^{D419N}$; hence, subtle differences are expected. In human STAT6$^{D419}$ mutant tumours, co-mutation with other genes of the EZB DLBCL subtype, such as BCL6, CREBBP, and p300, are always observed (13, 14, 33). We propose that the interplay between EZB gene mutations and STAT6$^{D419}$ mutation may be central to STAT6-mediated modifications to the TME. This might explain why our PhenoCycler results in human were much more exaggerated as compared to mouse.

In rrDLBCL patient samples, we found that phospho-STAT6 and CCL17 are more highly expressed in tumour cells of STAT6$^{D419}$-mutant patients, and expression of phospho-STAT6 was positively correlated with tumour cell expression of CCL17 and CD4+ T cell expression of CCR4. Additionally, we found that phospho-STAT6+ tumour cells in STAT6$^{D419}$ tumours have increased interactions with CD4+ T cells and CCR4+ CD4+ T cells, as compared to STAT6$^{WT}$ rrDLBCL tumours. These results expand our previous findings (14), to assert that phospho-STAT6 expression in rrDLBCL tumours contributes to TME remodelling via favouring interactions of tumour cells with the CD4 T cell compartment, largely due to the CCL17-CCR4 axis.

CCR4 has been established as a therapeutic target in Mycosis fungoides (MF) and Sezary syndrome (SS), due to tumour cell upregulation of CCR4. Indeed, the CCR4-

targeted monoclonal antibody Mogamulizumab was FDA approved for the treatment of relapsed and refractory MF and SS in 2018 (34, 35). CCR4 has also been previously described as a potential therapeutic target in DLBCL. In a study using imaging mass cytometry (IMC), it was reported that CCR4 is expressed on PD1+ Tregs in the DLBCL and cHL TME. In DLBCL, CCR4+ Tregs are in close proximity to PD1+ CD4+ T cells and PD1+ CD8+ T cells, while these interactions are not present in cHL tumours (22). The authors suggest that these cellular interactions may be a mechanism of immune evasion in DLBCL relative to cHL and may be one factor that underlies the lack of therapeutic susceptibility of DLBCL tumours to immune checkpoint inhibitors. Accordingly, in a Phase I clinical trial (NCT03309878) Mogamulizumab was tested in combination with the anti-PD1 antibody Pembrolizumab for the treatment of rrDLBCL (36); however, due to the presence of serious adverse events, the trial was discontinued prior to Phase II. If Mogamulizumab was to be revisited for the treatment of rrDLBCL, future clinical studies could have phospho-STAT6 tumour cell positivity by IHC or IF as inclusion criteria, to select for patients who may have clinical benefits that outweighs the chance of adverse events.

While our results indicate a critical role for the CCL17-CCR4 axis in STAT6$^{D419}$-mediated microenvironmental remodelling, they do not preclude the potential for other mechanisms of action underlying STAT6$^{D419}$-mediated doxorubicin resistance. For instance, STAT6 is a transcription factor that controls expression of genes such as CD23, CISH, IL2RA, BCL-6, BCL-XL, CDK2 (4, 6, 37) . These proteins play roles in B cell activation, resistance to apoptosis, cell cycling. Thus, future studies may investigate the cellular and molecular responses of STAT6$^{D419}$ tumour cells to doxorubicin, with a specific

focus on how altered regulation of these genes impacts tumour cell survival in an intact TME. As such, our study did not address specifically why CCR4+ CD4+ T cells engender therapeutic resistance in STAT6$^{D419N}$ mutant tumours. In future studies, single cell transcriptomic approaches will be used to determine the specific phenotype of CCR4+ CD4+ T cells, and how they might drive tumour growth and chemoresistance.

In summary, our findings highlight the importance of investigations focused on the intricate interplay between DLBCL tumour cells and the TME. Indeed, the full functional impact of STAT6$^{D419}$ mutations could only be realized by utilizing an immunocompetent mouse model. Given that many of the gene mutations that are enriched in DLBCL are predicted to modify the interaction of the tumour cell with the TME, we emphasize that future studies should take a TME-centric approach to better understand the efficacy of immunomodulatory agents in DLBCL, especially given the rise of CAR-T therapy for rrDLBCL treatment. Overall, a better understanding of the mechanisms of therapeutic resistance and immune escape in DLBCL could improve clinical outcomes, particularly for those with relapsed and refractory disease.

## 3.5 Materials and Methods

All reagents and tools can be found in **Supplementary Table 3.4**.

### *3.5.1 Cell Culture*

MEF$^{ARF-/-}$ and Phoenix-AMPHO cells were grown in DMEM media supplemented with 10% fetal bovine serum (FBS) and 0.5% penicillin-streptomycin (P/S). To generate mitotically inactive MEFs for co-culture, MEF$^{ARF-/-}$ cells were given 40 Gy accumulated irradiation using a MultiRad225 (Faxitron) with a 0.5mm Cu filter and set to 225.0 kV and

17.8 mA. Following irradiation, cells were frozen in FBS supplemented with 10% DMSO. Eμ-Myc cells were co-cultured with irradiated $MEF^{ARF-/-}$ (iMEF) cells in 50% DMEM/ 50% Iscove's media, supplemented with FBS (10%), P/S (0.5%), and β-mercaptoethanol (50 nM).

To produce murine $STAT6^{WT}$ and $STAT6^{D419N}$ lymphoma cell lines, Phoenix-AMPHO packaging cells were transfected with pMIG plasmids containing WT or D419N mutant m*STAT6* and a GFP reporter. Retrovirus supernatant was used to transduce Eμ-Myc cells by spinoculation (centrifugation at 800 x g for 30 minutes at room temperature with 6 μg/mL polybrene, every 12 hours for 2 consecutive days). Successfully transduced GFP+ cells were sorted with a BD FACSAria Fusion Cell Sorter at the Lady Davis Institute Flow Cytometry Facility and were maintained in cell culture.

### *3.5.2 Mouse Modelling*

All mouse experiments were performed in accordance with an Animal Use Protocol approved by the McGill University Animal Care Committee. Mice were housed in the animal facility of the Lady Davis Institute for Medical Research.

$1x10^6$ $mSTAT6^{WT}$ or $mSTAT6^{D419N}$ Eμ-Myc cells in 0.1mL of sterile PBS were injected into 8–10-week-old female C57BL/6 mice via tail vein on Day 1. Tumour cells homed to lymph nodes, and disease burden was monitored using a VEVO-3100 Ultrasound machine, with Vevo LAB software used for tumour volume calculation. Mice were sacrificed if tumour volume in the cLN exceeded 100 $mm^3$, or if they showed signs of weight loss and hind-leg paralysis.

Where indicated, mice were treated with doxorubicin (2 mg/mL; Jewish General Hospital Oncology Pharmacy) or AZD2098 (MedChemExpress). Doxorubicin was given

as three doses of 3 mg/kg or one dose of 10 mg/kg, via intraperitoneal injection using a sterile 28-gauge needle. AZD2098 was purchased as powder, prepared at 2 mg/mL, in 10% DMSO and 90% corn oil, and mice were gavaged twice weekly at a dose of 10 mg/kg.

At the indicated time points, mice were humanely sacrificed using isoflurane anesthesia, $CO_2$, and cervical dislocation. Tumours were harvested and processed for flow cytometry, or were saved in FFPE blocks.

*3.5.3 Immunohistochemistry*

For Ki67 staining, FFPE tumor and lymph node sections were deparaffinized using three changes of xylene and were hydrated through graded alcohols. Antigen-retrieval was performed for 20 minutes at 95 °C, using a PT Link Antigen Retrieval machine (Agilent) with Tris-EDTA pH 9.0 buffer. Endogenous peroxidases were quenched with 4.5% $H_2O_2$ for 15 minutes, and slides were blocked with 2% donkey serum for 30 minutes. They were then stained with Ki67 antibody (1:400; Cell Signaling Technology) for 30 minutes at 37°C and incubated in anti-rabbit secondary antibody for one hour at room temperature, followed by 1 minute DAB exposure. Slides were counterstained with hematoxylin, blued with blueing buffer, and were mounted with coverslips and Permount. For pSTAT6-CD4 co-staining, slides were prepared with the same deparaffinization, antigen retrieval, and quenching/blocking steps. Then slides were incubated with CD4 antibody (1:50; Invitrogen) for 30 minutes at 37°C and incubated in anti-rat secondary antibody for one hour at room temperature, followed by 2 minutes DAB exposure. Following DAB exposure, slides were again quenched and blocked. They were then incubated overnight at 4°C with pSTAT6 antibody (1:250; Cell Signaling Technology), and

then were incubated in anti-rabbit secondary antibody for one hour, followed by a Magenta Red (Agilent) detection protocol. Slides were then counterstained with hematoxylin, blued with blueing buffer, and mounted. For all slides, images were acquired in brightfield with an AxioScan 7 (Zeiss) and were analyzed using QuPath 0.5.1-x64 software (38). Where applicable, staining was quantified based on percent positivity for a given marker, based on an intensity cut-off, or was quantified as H-Score. H-Score is calculated by indexing each cell within the tissue as having negative, weak, moderate, or strong staining for the given marker, based on three different intensity cut-offs. Then, the following formula was used to score the tissues, out of a maximum of 300:

H-Score = (0* (% of negative cells)) + (1* (% of weak staining cells)) + (2* (% of moderate staining cells)) + (3* (% of strong staining cells))

*3.5.4 Flow Cytometry*

cLN tumours were harvested at the indicated time points, and were gently crushed in a 1mL Eppendorf tube using a pestle. Following crushing, cells were passed through a 70 µm cell strainer. Single cells obtained from tumour dissociation were counted and $2x10^6$ cells per sample were plated in a 96-well V-bottom plate. Cells were incubated with fixable aqua live/dead stain (30 minutes; Invitrogen), Fc block (30 minutes), and then were incubated with fluorescently conjugated antibodies (30 minutes). For intracellular staining of transcription factors, cells were fixed and permeabilized (eBioscience), then were incubated in fluorescently conjugated intracellular staining antibodies diluted in permeabilization buffer. The flow antibodies used in this study can be found in **Supplementary Table 3.1**. Data was acquired on an LSRFortessa (BD; Lady Davis Institute Flow Cytometry Core), and FlowJo (BD) was used for all flow cytometry data

analysis. Following analysis, the number of each cell type of interest was normalized to total tumour cell count, and data was presented as total number of each cell type found within each tumour.

### *3.5.5 RNA Sequencing and qPCR*

For RNA sequencing, CD19+ cells were purified from 3 biological replicates each of mSTAT6$^{WT}$ and mSTAT6$^{D419N}$ Eμ-Myc Day 11 cLN tumours, using CD19 microbeads (Miltenyi), as per manufacturer protocol. RNA was extracted from purified B cells using the Absolutely Total RNA Purification Kit (Agilent Technologies), as per manufacturer protocol. RNA sequencing was performed at Genome Quebec. Paired read 100 bp sequencing runs were performed on an Illumina NovaSeq 6000 S2 PE100.

For qPCR, RNA was extracted from tumour cells using the E.Z.N.A. total RNA isolation kit (OMEGA Bio-Tek). cDNA was synthesized from 1 mg of total RNA, using the iScript cDNA Synthesis Kit (Bio-Rad). mRNA expression was quantified using the QuantStudio 7 Flex PCR System with SYBR Green.

### *3.5.6 Ex Vivo Chemoattraction*

For experiments with chemoattraction towards tumour cells *in vitro*, Eμ-Myc-mSTAT6$^{WT}$ or Eμ-Myc-mSTAT6$^{D419N}$ cells were plated at a confluence of 3x10$^5$ cells/mL, overtop of iMEF cells. After 24 hours, tumour cells were stimulated with 5 ng/mL of murine (m) IL-4 (PeproTech) or vehicle control. After 1 hour, cells from a duplicate plate were collected for RNA isolation and qPCR analysis, to confirm CCL17 upregulation in mIL-4 stimulated Eμ-Myc-mSTAT6$^{D419N}$ tumour cells. In tandem, spleens from female tumour naïve C57BL/6 mice were harvested and dissociated. Red blood cells (RBCs) were lysed for 10 minutes on ice (eBioscience). Splenocytes were treated with either 10 μM AZD2098

(MedChemExpress) or vehicle control for 1 hour at room temperature. Following tumour cell incubation in mIL-4 and splenocyte incubation in AZD2098, $1x10^6$ bulk splenocytes were plated overtop the stimulated or non-stimulated Eμ-Myc tumour cells, using a 5 μm pore transparent membrane. Splenocytes were allowed to migrate towards Eμ-Myc tumour cells for 16 hours. Migrated splenocytes were collected and stained with fixable aqua live/dead stain. They were then incubated with Fc block (30 minutes), then were stained with fluorescently conjugated antibodies to detect B cells, CD4+ T cells, CD8+ T cells, DCs, macrophages, NK cells, and eosinophils. Cells were not fixed, in order to preserve tumour cell endogenous GFP expression. The entire sample was acquired on an LSRFortessa, and FlowJo was used for analysis. The plated tumour cells were distinguished from migrated cells via expression of GFP and CD19, and tumour cells were excluded from the migrated cell counts.

For chemoattraction towards tumour supernatants, cLN tumours and spleens were harvested at day 11 post- Eμ-Myc-mSTAT6$^{WT}$ and Eμ-Myc-mSTAT6$^{D419N}$ tumour cell injection. cLNs were crushed in a 1mL Eppendorf tube with 500uL total volume of PBS and were incubated on ice for 20 minutes. Following incubation, tubes were spun down at 300 x g for 10 minutes, and tumour supernatants were collected (see below). Spleens were also dissociated, with 10-minute RBC lysis. Following dissociation, CD4+ T cells were purified from splenocytes (Miltenyi), as per manufacturer protocol. Following purification, CD4+ T cells were treated for 1 hour at room temperature with either 10 μM AZD2098 or vehicle control. While CD4+ T cells were incubating in AZD2098, equal volumes of tumour supernatants or PBS control were plated in a 12-well plate. $5x10^5$ CD4+ T cells were plated overtop the Eμ-Myc-mSTAT6$^{WT}$ and Eμ-Myc-mSTAT6$^{D419N}$

tumour supernatants, using a 3 μm pore transparent membrane. CD4+ T cells were allowed to migrate towards tumour supernatants for 16 hours, then were collected for CD4+ T cell quantification and phenotyping by flow cytometry.

### *3.5.7 Chemokine/Cytokine Profiling*

At day 11 post-Eμ-Myc injection, Eμ-Myc-mSTAT6$^{WT}$ and Eμ-Myc-mSTAT6$^{D419N}$ tumours were dissociated, as described above. Tumour samples were allowed to incubate on ice on 20 minutes, then were spun down at 300 x g for 10 minutes. The supernatant was collected and was either used fresh for chemoattraction experiments or stored at -80 °C for cytokine profiling. The cell pellet was counted. To determine the cytokine/chemokine constitution of tumour supernatants, 44-Plex Mouse Cytokine/Chemokine profiling was performed with Eve Technologies (Calgary, AB, Canada), and cytokine/chemokine expression was normalized to total cell number in each tumour.

### *3.5.8 Generation of an Eμ-Myc TMA*

FFPE tissue blocks containing Eμ-Myc cLN tumours from early-, mid-, late-, and relapsed-disease were sectioned and stained with H&E, to facilitate region selection for core punching. Fatty regions or regions that showed evidence of necrosis were avoided. The TMA was generated with the Jewish General Hospital Research Pathology Core. From each tissue block, one to three 1 mm cores were included (**Sup. Figure 3.4**).

### *3.5.9 PhenoCycler Staining*

PhenoCycler staining was performed as described previously (39-41). FFPE murine and human lymphoma tissue sections were baked for 1 hour at 60 °C, deparaffinized using xylene, and were hydrated through graded alcohols. Antigen-

retrieval was performed for 20 minutes at 95 °C, with Tris-EDTA pH 9.0 buffer. Tissue autofluorescence was quenched by bathing slides in a solution of 4.5% $H_2O_2$ and 20 mM NaOH prepared in PBS, sandwiched between LED lights at 25000 lux, for 45 minutes at room temperature. Slides were then washed with PBS (3 x 5 minutes) and hydration buffer (Akoya Biosciences; 2 x 5 minutes). Slides were equilibrated in staining buffer (Akoya Biosciences; 30 minutes) while the antibody staining cocktail was prepared in staining buffer supplemented with N, G, J, and S blockers (Akoya Biosciences) and oligonucleotide-conjugated antibodies diluted at the concentrations indicated in **Supplementary Table 3.2** and **Supplementary Table 3.3**. Antibody staining occurred in two steps. The first step used antibodies optimized for 30-minute incubation at 37 °C (indicated in **Sup. Table 3.2** and **Sup. Table 3.3**). After the first staining step, slides were washed in three changes of staining buffer before proceeding. The second step used antibodies optimized for overnight (ON) incubation at 4 °C. After overnight staining, slides were washed in three changes of staining buffer, and were fixed with 1.6% PFA for 10 minutes, ice-cold methanol for 5 minutes, and fixative solution (Akoya Biosciences) for 20 minutes. Slides were then stored until imaging with a PhenoCycler-Fusion instrument (up to 2 days).

The slides were mounted with a flow cell (Akoya Biosciences), to allow for automated fluidics that wash on and off fluorescently conjugated oligonucleotides that are complementary to the oligonucleotides that are conjugated to each antibody (aka “reporters”), while allowing the slide to stay mounted to a fluorescent microscope. To image slides, a reporter plate was prepared that included solutions containing PhenoCycler-Fusion buffer, DAPI, salmon sperm DNA, and up to three different reporters.

The reporter plate solutions were washed onto the tissue cyclically, using the PhenoCycler-Fusion instrument, until all antibodies in the staining panel were visualized. The final outcome was qptiff files with highly multiplexed immunofluorescent images.

Following staining, the flow cell was removed using 24-hour incubation in Citrisolv. The Citrisolv was washed off, using grading alcohols, then H&E staining was performed. Slides were then mounted and imaged with an AxioScan 7 (Zeiss).

### *3.5.10 PhenoCycler Data Analysis*

Multiplexed qptiff images were uploaded to Enable Medicine, where cell segmentation was performed using DeepCell, with DRAQ5 as a nuclear marker and NaK-ATPase (mouse) or B-actin (human) as membrane markers. Quality control, within the Enable Medicine platform, was used to exclude tumour cores of poor quality or individual cells that showed evidence of staining artifacts (ie. increased signal sum, decreased signal variation, and abnormalities in cell size or nuclear signal). Unsupervised clustering was then performed to identify major cell types, using Leiden clustering, set to detect 50 neighbours, with a UMAP minimum distance of 0.1 and a clustering resolution of 0.5. The accuracy of clustering was visually confirmed using Voronoi diagrams, and Leiden sub-clustering was used to further refine clusters to ensure accurate cell classification. Sub-clustering was also used to subclassify cells based on the expression of markers of interest. Spatial neighbour calculations were performed in Enable, by calculating the mean distance between cell types of interest within samples.

### *3.5.11 Patient Data*

The patient cohort used for PhenoCycler imaging consisted of FFPE preserved samples obtained prospectively from patients treated in Montreal QC, at the Jewish

General Hospital. The biobanking of this project was approved by the research ethics board at the Jewish General Hospital, in accordance with the declaration of Helsinki. Patients were all treated with curative intent R-CHOP-like regimens. At disease relapse, tissue biopsies were collected for biobanking. Using banked specimens, one-millimeter cores of rrDLCBL FFPE tissue were used to construct a TMA, with the Jewish General Hospital Research Pathology Core. 4uM TMA sections were mounted onto SuperFrost slides and were stained with a 52-plex PhenoCycler antibody cocktail, following the protocol described above. For $STAT6^{D419}$ mutant samples, whole sections were mounted onto SuperFrost slides, with two sections from two different patients per slide. Patient metadata included age, sex, cell-of-origin (COO), and STAT6 mutational status.

### *3.5.12 Statistical Analysis*

A detailed list of statistics used, including test used, same size, and p-value, for each figure can be found in **Supplementary Table 3.5**.

### *3.5.13 Data Availability Statement*

All raw data will be made available upon reasonable request to the corresponding author.

## 3.6 References for Chapter 3


1. Gaydosik AM, Queen DS, Trager MH, Akilov OE, Geskin LJ, Fuschiotti P. Genome-wide transcriptome analysis of the STAT6-regulated genes in advanced-stage cutaneous T-cell lymphoma. Blood. 2020;136(15):1748-59.
2. Häberle MT, Kelsch E, Dorsch K, Möller P, Ritz O. Knock-down of BCL6 / STAT6 sensitizes primary B cell lymphoma cells for treatment with current therapeutic agents. Oncoscience. 2014;1(4):283-6.
3. Ritz O, Guiter C, Castellano F, Dorsch K, Melzner J, Jais JP, et al. Recurrent mutations of the STAT6 DNA binding domain in primary mediastinal B-cell lymphoma. Blood. 2009;114(6):1236-42.
4. Ritz O, Rommel K, Dorsch K, Kelsch E, Melzner J, Buck M, et al. STAT6-mediated BCL6 repression in primary mediastinal B-cell lymphoma (PMBL). Oncotarget. 2013;4(7):1093-102.
5. Chapuy B, Stewart C, Dunford AJ, Kim J, Wienand K, Kamburov A, et al. Genomic analyses of PMBL reveal new drivers and mechanisms of sensitivity to PD-1 blockade. Blood. 2019;134(26):2369-82.
6. Yildiz M, Li H, Bernard D, Amin NA, Ouillette P, Jones S, et al. Activating STAT6 mutations in follicular lymphoma. Blood. 2015;125(4):668-79.
7. Mentz M, Keay W, Strobl CD, Antoniolli M, Adolph L, Heide M, et al. PARP14 is a novel target in STAT6 mutant follicular lymphoma. Leukemia. 2022;36(9):2281-92.
8. Okosun J, Bödör C, Wang J, Araf S, Yang CY, Pan C, et al. Integrated genomic analysis identifies recurrent mutations and evolution patterns driving the initiation and progression of follicular lymphoma. Nat Genet. 2014;46(2):176-81.
9. Xian RR, Xie Y, Haley LM, Yonescu R, Pallavajjala A, Pittaluga S, et al. CREBBP and STAT6 co-mutation and 16p13 and 1p36 loss define the t(14;18)-negative diffuse variant of follicular lymphoma. Blood Cancer Journal. 2020;10(6):69.
10. Skinnider BF, Elia AJ, Gascoyne RD, Patterson B, Trumper L, Kapp U, Mak TW. Signal transducer and activator of transcription 6 is frequently activated in Hodgkin and Reed-Sternberg cells of Hodgkin lymphoma. Blood. 2002;99(2):618-26.
11. Baus D, Nonnenmacher F, Jankowski S, Döring C, Bräutigam C, Frank M, et al. STAT6 and STAT1 are essential antagonistic regulators of cell survival in classical Hodgkin lymphoma cell line. Leukemia. 2009;23(10):1885-93.
12. Alig SK, Shahrokh Esfahani M, Garofalo A, Li MY, Rossi C, Flerlage T, et al. Distinct Hodgkin lymphoma subtypes defined by noninvasive genomic profiling. Nature. 2024;625(7996):778-87.
13. Morin RD, Assouline S, Alcaide M, Mohajeri A, Johnston RL, Chong L, et al. Genetic Landscapes of Relapsed and Refractory Diffuse Large B-Cell Lymphomas. Clin Cancer Res. 2016;22(9):2290-300.
14. Benoit A, Abraham MJ, Li S, Kim J, Estrada-Tejedor R, Bakadlag R, et al. STAT6 mutations enriched at diffuse large B-cell lymphoma relapse reshape the tumor microenvironment. International Journal of Hematology. 2024;119(3):275-90.
15. Phillips D, Matusiak M, Gutierrez BR, Bhate SS, Barlow GL, Jiang S, et al. Immune cell topography predicts response to PD-1 blockade in cutaneous T cell lymphoma. Nature Communications. 2021;12(1):6726.

16. Kindon N, Andrews G, Baxter A, Cheshire D, Hemsley P, Johnson T, et al. Discovery of AZD-2098 and AZD-1678, Two Potent and Bioavailable CCR4 Receptor Antagonists. ACS Med Chem Lett. 2017;8(9):981-6.
17. Benoit A, Abraham MJ, Li S, Kim J, Estrada-Tejedor R, Bakadlag R, et al. STAT6 mutations enriched at diffuse large B-cell lymphoma relapse reshape the tumor microenvironment. International Journal of Hematology. 2024.
18. Hartert KT, Wenzl K, Krull JE, Manske M, Sarangi V, Asmann Y, et al. Targeting of inflammatory pathways with R2CHOP in high-risk DLBCL. Leukemia. 2021;35(2):522-33.
19. Monti S, Savage KJ, Kutok JL, Feuerhake F, Kurtin P, Mihm M, et al. Molecular profiling of diffuse large B-cell lymphoma identifies robust subtypes including one characterized by host inflammatory response. Blood. 2005;105(5):1851-61.
20. Yu J, Fu L, Zhang Z, Ding L, Hong L, Gao F, et al. Causal relationships between circulating inflammatory cytokines and diffuse large B cell lymphoma: a bidirectional Mendelian randomization study. Clinical and Experimental Medicine. 2023;23(8):4585-95.
21. Wright KT, Weirather JL, Jiang S, Kao KZ, Sigal Y, Giobbie-Hurder A, et al. Diffuse large B-cell lymphomas have spatially defined, tumor immune microenvironments revealed by high-parameter imaging. Blood Advances. 2023;7(16):4633-46.
22. Colombo AR, Hav M, Singh M, Xu A, Gamboa A, Lemos T, et al. Single-cell spatial analysis of tumor immune architecture in diffuse large B-cell lymphoma. Blood Adv. 2022;6(16):4675-90.
23. Blise KE, Sivagnanam S, Banik GL, Coussens LM, Goecks J. Single-cell spatial architectures associated with clinical outcome in head and neck squamous cell carcinoma. npj Precision Oncology. 2022;6(1):10.
24. Yeh CY, Aguirre K, Laveroni O, Kim S, Wang A, Liang B, et al. Mapping spatial organization and genetic cell-state regulators to target immune evasion in ovarian cancer. Nature Immunology. 2024;25(10):1943-58.
25. Reiss DJ, Nakayama Y, Weng AP, Stokes ME, Sehn L, Steidl C, et al. High-plex imaging and cellular neighborhood spatial analysis reveals multiple immune escape and suppression patterns in diffuse large B-cell lymphoma. Leukemia. 2024;38(5):1164-8.
26. Kotlov N, Bagaev A, Revuelta MV, Phillip JM, Cacciapuoti MT, Antysheva Z, et al. Clinical and Biological Subtypes of B-cell Lymphoma Revealed by Microenvironmental Signatures. Cancer Discovery. 2021;11(6):1468-89.
27. Kim CH, Rott L, Kunkel EJ, Genovese MC, Andrew DP, Wu L, Butcher EC. Rules of chemokine receptor association with T cell polarization in vivo. J Clin Invest. 2001;108(9):1331-9.
28. Anderson CA, Patel P, Viney JM, Phillips RM, Solari R, Pease JE. A degradatory fate for CCR4 suggests a primary role in Th2 inflammation. J Leukoc Biol. 2020;107(3):455-66.
29. Andrew DP, Ruffing N, Kim CH, Miao W, Heath H, Li Y, et al. C-C chemokine receptor 4 expression defines a major subset of circulating nonintestinal memory T cells of both Th1 and Th2 potential. J Immunol. 2001;166(1):103-11.

30. Freeman CM, Stolberg VR, Chiu BC, Lukacs NW, Kunkel SL, Chensue SW. CCR4 participation in Th type 1 (mycobacterial) and Th type 2 (schistosomal) anamnestic pulmonary granulomatous responses. J Immunol. 2006;177(6):4149-58.
31. Godfrey J, Tumuluru S, Bao R, Leukam M, Venkataraman G, Phillip J, et al. PD-L1 gene alterations identify a subset of diffuse large B-cell lymphoma harboring a T-cell-inflamed phenotype. Blood. 2019;133(21):2279-90.
32. Apollonio B, Spada F, Petrov N, Cozzetto D, Papazoglou D, Jarvis P, et al. Tumor-activated lymph node fibroblasts suppress T cell function in diffuse large B cell lymphoma. J Clin Invest. 2023;133(13).
33. Wright GW, Huang DW, Phelan JD, Coulibaly ZA, Roulland S, Young RM, et al. A Probabilistic Classification Tool for Genetic Subtypes of Diffuse Large B Cell Lymphoma with Therapeutic Implications. Cancer Cell. 2020;37(4):551-68.e14.
34. Kasamon YL, Chen H, de Claro RA, Nie L, Ye J, Blumenthal GM, et al. FDA Approval Summary: Mogamulizumab-kpkc for Mycosis Fungoides and Sézary Syndrome. Clinical Cancer Research. 2019;25(24):7275-80.
35. Kim YH, Bagot M, Pinter-Brown L, Rook AH, Porcu P, Horwitz SM, et al. Mogamulizumab versus vorinostat in previously treated cutaneous T-cell lymphoma (MAVORIC): an international, open-label, randomised, controlled phase 3 trial. The Lancet Oncology. 2018;19(9):1192-204.
36. Joffe E, Vardhana SA, Kumar A, Abedi M, Hoeg R, Sharon E, Younes A. A phase I and randomized phase II etctn study of KW-0761 (Mogamulizumab) and MK-3475 (Pembrolizumab) in relapsed and refractory diffuse large B-cell lymphoma. Journal of Clinical Oncology. 2020;38(15_suppl):TPS8072-TPS.
37. Ritz O, Guiter C, Dorsch K, Dusanter-Fourt I, Wegener S, Jouault H, et al. STAT6 activity is regulated by SOCS-1 and modulates BCL-XL expression in primary mediastinal B-Cell lymphoma. Leukemia. 2008;22(11):2106-10.
38. Bankhead P, Loughrey MB, Fernández JA, Dombrowski Y, McArt DG, Dunne PD, et al. QuPath: Open source software for digital pathology image analysis. Scientific Reports. 2017;7(1):16878.
39. Abraham MJ, Goncalves C, McCallum P, Gupta V, Preston SEJ, Huang F, et al. Tunable PhenoCycler imaging of the murine pre-clinical tumour microenvironments. Cell & Bioscience. 2024;14(1):19.
40. Donovan ML, Jhaveri N, Ma N, Cheikh BB, DeRosa J, Mihani R, et al. Protocol for high-plex, whole-slide imaging of human formalin-fixed paraffin-embedded tissue using PhenoCycler-Fusion. STAR Protocols. 2024;5(3):103226.
41. Black S, Phillips D, Hickey JW, Kennedy-Darling J, Venkataraaman VG, Samusik N, et al. CODEX multiplexed tissue imaging with DNA-conjugated antibodies. Nat Protoc. 2021;16(8):3802-35.

## 3.7 Supplementary Materials for Chapter 3

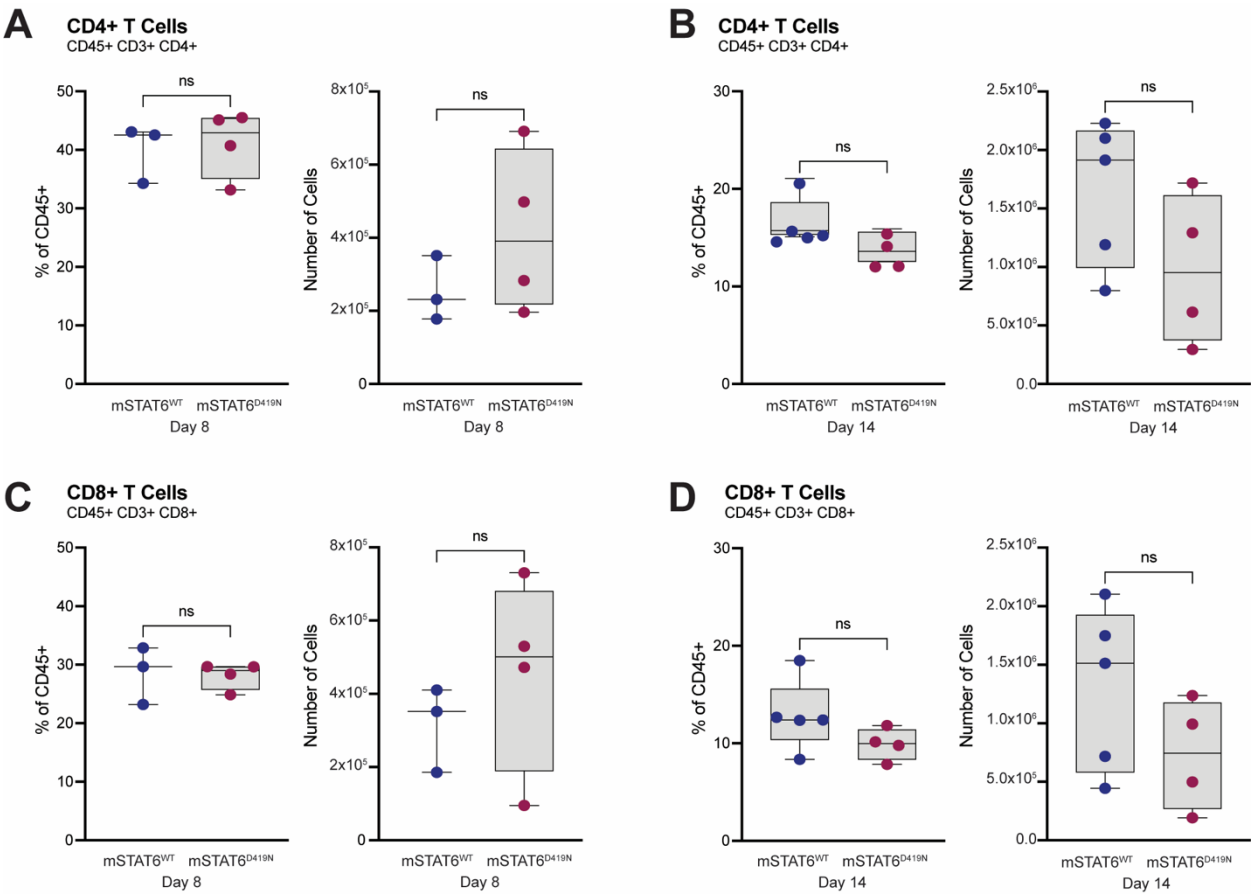


**Supplementary Figure 3.1: mSTAT6$^{D419N}$ Eμ-Myc tumours have no difference in number or proportion of CD4+ or CD8+ T cells at early and late disease as compared to mSTAT6$^{WT}$ Eμ-Myc tumours.**
**A.** Quantification of CD4+ T cells in day 8 mSTAT6$^{WT}$ and mSTAT6$^{D419N}$ Eμ-Myc tumours. CD4+ T cells are live, single cells, that are CD45+, CD3+, and CD4+. Data is expressed as a percentage of CD45+ cells in each tissue, and as the total number of CD4+ T cells in each tissue. **B.** Quantification of CD4+ T cells in day 14 mSTAT6$^{WT}$ and mSTAT6$^{D419N}$ Eμ-Myc tumours. **C.** Quantification of CD8+ T cells in day 8 mSTAT6$^{WT}$ and mSTAT6$^{D419N}$ Eμ-Myc tumours. CD8+ T cells are live, single cells, that are CD45+, CD3+, and CD8+. **D.** Quantification of CD8+ T cells in day 14 mSTAT6$^{WT}$ and mSTAT6$^{D419N}$ Eμ-Myc tumours.

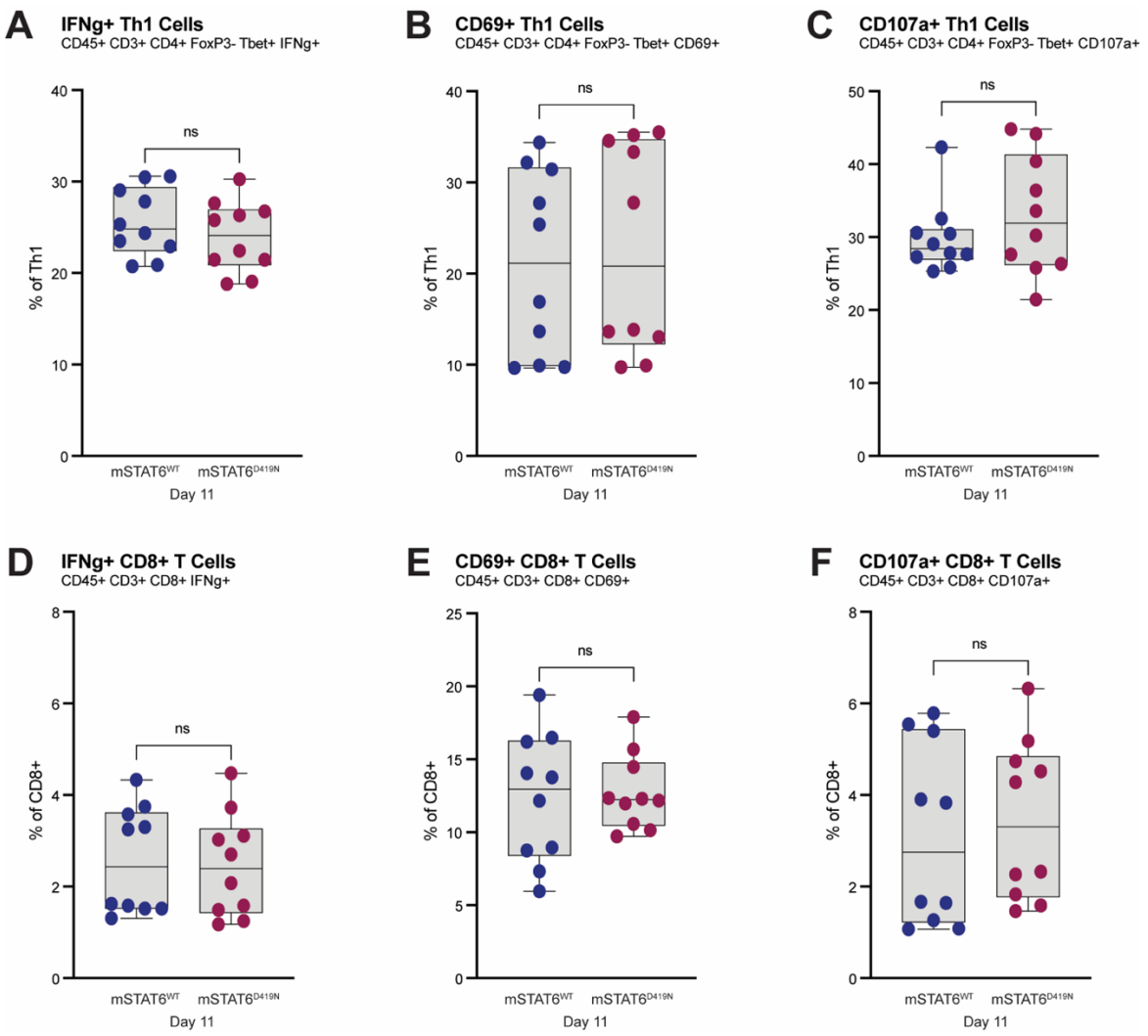


**Supplementary Figure 3.2: mSTAT6$^{D419N}$ Eμ-Myc tumours have no difference in expression of IFNγ, CD69, and CD107a in Th1 cells and CD8+ T cells as compared to mSTAT6$^{WT}$ Eμ-Myc tumours.**

**A.** Expression of IFNγ on Th1 cells in day 11 mSTAT6$^{WT}$ and mSTAT6$^{D419N}$ Eμ-Myc tumours, expressed as total percentage of Th1 cells that are IFNγ+ (CD45+ CD3+ CD4+ FoxP3- Tbet+ IFNγ+). **B.** Expression of CD69 on Th1 cells in day 11 mSTAT6$^{WT}$ and mSTAT6$^{D419N}$ Eμ-Myc tumours, expressed as total percentage of Th1 cells that are CD69+ (CD45+ CD3+ CD4+ FoxP3- Tbet+ CD69+). **C.** Expression of CD107a on Th1 cells in day 11 mSTAT6$^{WT}$ and mSTAT6$^{D419N}$ Eμ-Myc tumours, expressed as total percentage of Th1 cells that are CD107a+ (CD45+ CD3+ CD4+ FoxP3- Tbet+ CD107a+). **D.** Expression of IFNγ on CD8+ T cells in day 11 mSTAT6$^{WT}$ and mSTAT6$^{D419N}$ Eμ-Myc tumours, expressed as total percentage of CD8+ T cells that are IFNγ+ (CD45+ CD3+ CD8+ IFNγ+). **E.** Expression of CD69 on CD8+ T cells in day 11 mSTAT6$^{WT}$ and mSTAT6$^{D419N}$ Eμ-Myc tumours, expressed as total percentage of CD8+ T cells that are CD69+ (CD45+ CD3+ CD8+ CD69+). **F.** Expression of CD107a on CD8+ T cells in day 11 mSTAT6$^{WT}$ and mSTAT6$^{D419N}$ Eμ-Myc tumours, expressed as total percentage of CD8+ T cells that are CD107a+ (CD45+ CD3+ CD8+ CD107a+).

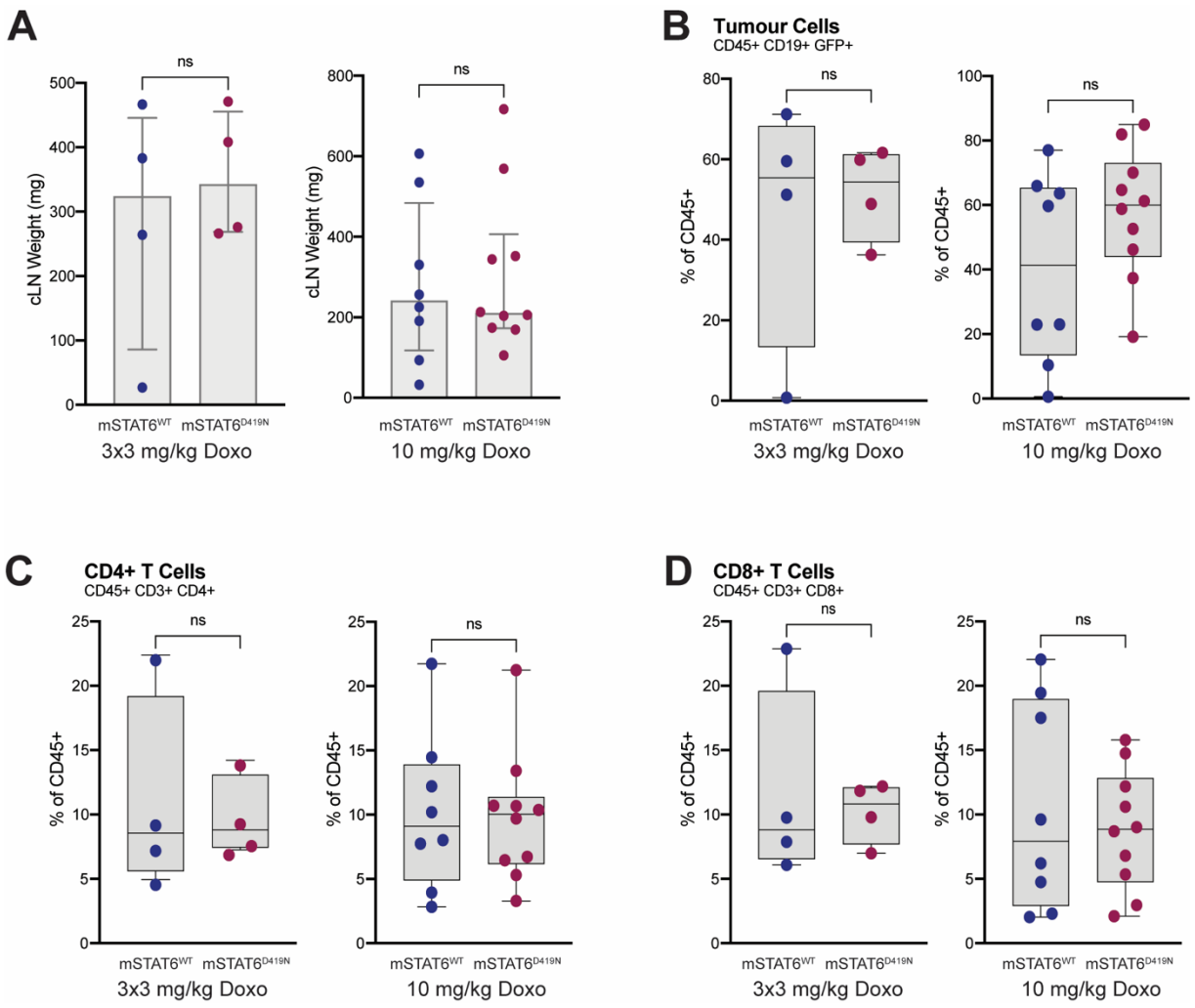


**Supplementary Figure 3.3: mSTAT6$^{WT}$ and mSTAT6$^{D419N}$ Eμ-Myc tumours have no difference in tumour burden or expression of CD4+ and CD8+ T cells, following relapse from doxorubicin treatment.**

**A.** Weights of mSTAT6$^{WT}$ and mSTAT6$^{D419N}$ relapsed Eμ-Myc tumours, following 3x3 mg/kg or 10mg/kg doxorubicin treatment. **B.** Quantification of tumour cells in relapsed mSTAT6$^{WT}$ and mSTAT6$^{D419N}$ Eμ-Myc tumours. Tumour cells are live, single cells, that are CD45+, CD19+, and GFP+. Data is expressed as a percentage of CD45+ cells in each tissue. **C.** Quantification of CD4+ T cells in relapsed mSTAT6$^{WT}$ and mSTAT6$^{D419N}$ Eμ-Myc tumours. CD4+ T cells are live, single cells, that are CD45+, CD3+, and CD4+. Data is expressed as a percentage of CD45+ cells in each tissue. **D.** Quantification of CD8+ T cells in relapsed mSTAT6$^{WT}$ and mSTAT6$^{D419N}$ Eμ-Myc tumours. CD8+ T cells are live, single cells, that are CD45+, CD3+, and CD8+. Data is expressed as a percentage of CD45+ cells in each tissue.

**A**

| Eμ-Myc Tissue Microarray | | | |
|---|---|---|---|
| | mSTAT6$^{WT}$ | mSTAT6$^{D419N}$ | Total |
| Day 8 | | | |
| Biological Replicates | 5 | 5 | 10 |
| Technical Replicates per Core | 1 | 1 | 1 |
| Cores Used for Analysis | 4 | 3 | 7 |
| Day 8 Total Cells | 89,050 | 73,360 | 162,410 |
| Day 11 | | | |
| Biological Replicates | 5 | 5 | 10 |
| Technical Replicates per Core | 2 | 2 | 2 |
| Cores Used for Analysis | 7 | 9 | 16 |
| Day 11 Total Cells | 200,820 | 308,186 | 509,006 |
| Day 14 | | | |
| Biological Replicates | 5 | 5 | 10 |
| Technical Replicates per Core | 3 | 3 | 3 |
| Cores Used for Analysis | 14 | 11 | 25 |
| Day 14 Total Cells | 604,504 | 452,366 | 1,056,870 |
| Relapse | | | |
| Biological Replicates | 4 | 3 | 7 |
| Technical Replicates per Core | 2 | 2 | 2 |
| Cores Used for Analysis | 8 | 6 | 14 |
| Relapse Total Cells | 355,194 | 249,106 | 604,300 |
| Total Cells Profiled by PhenoCycler | **1,249,568** | **1,083,018** | **2,332,586** |

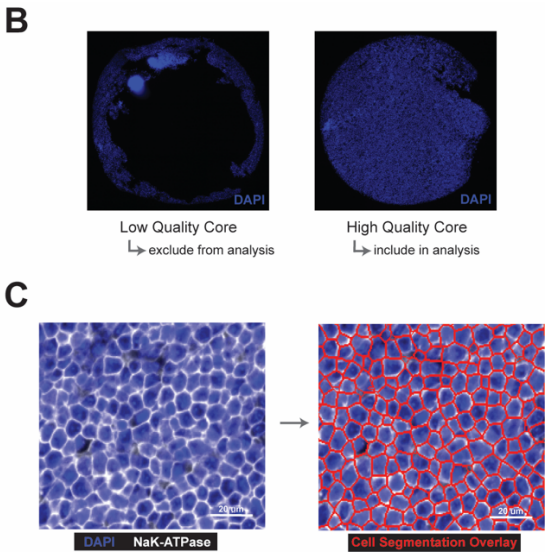


**Supplementary Figure 3.4: Construction and analysis of an Eμ-Myc TMA.**
**A.** Table showing the design of an Eμ-Myc TMA, with cores included from early- (day 8), mid- (day 11), late- (day 14), and relapsed-disease, from both Eμ-Myc mSTAT6$^{WT}$ and mSTAT6$^{D419N}$ tumour-bearing cLNs. Biological replicates indicate the number of mice that tissues were taken from, and technical replicates indicates the total number of core punches per tissue. If cores were of low quality, they were excluded from analysis, and this is reflected in the final number of cores used for analysis. **B.** Representative images of a low-quality and high-quality core on the Eμ-Myc TMA. Low quality cores were excluded from analysis. **C.** Sample image of DeepCell membrane-based cell segmentation. The first panel shows DAPI nuclear staining, and NaK-ATPase membranous staining. The second panel shows the cell segmentation mask, overlayed in red.

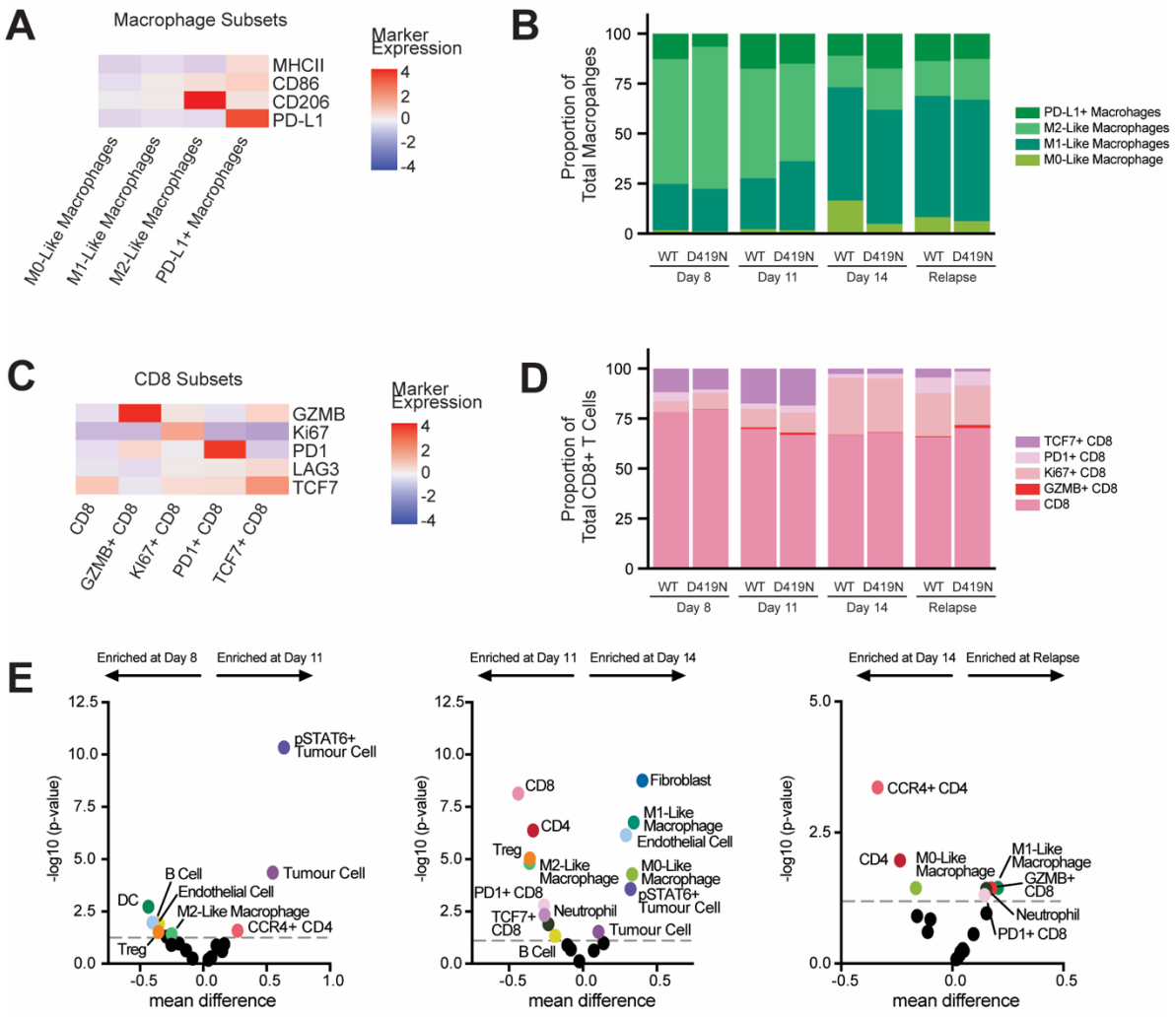


**Supplementary Figure 3.5: Analysis of expanded cell classifications from Eμ-Myc PhenoCycler imaging.**

**A.** Heatmap showing the mean expression of MHCII, CD86, CD206, and PDL1 in different Macrophage subsets (ie. M0-like, M1-like, M2-like, and PD-L1+). **B.** Proportion of different macrophage subsets among total macrophages in mSTAT6$^{WT}$ and mSTAT6$^{D419N}$ Eμ-Myc tumours at early-, mid-, late-disease, and relapse. **C.** Heatmap showing the mean expression of GZMB, Ki67, PD1, LAG3, and TCF7 in CD8+ T cell subsets (ie. CD8, GZMB+ CD8. Ki67+ CD8, PD1+ CD8, and TCF7+ CD8). **D.** Proportion of different CD8+ T cell subsets among total CD8+ T cells in mSTAT6$^{WT}$ and mSTAT6$^{D419N}$ Eμ-Myc tumours at early-, mid-, late-disease, and relapse. **E.** Volcano plots showing the change in abundance of different cell types over the course of Eμ-Myc tumour evolution. Coloured dots above the grey dashed lines indicate cell types that have significantly changed in abundance between the indicated time points.

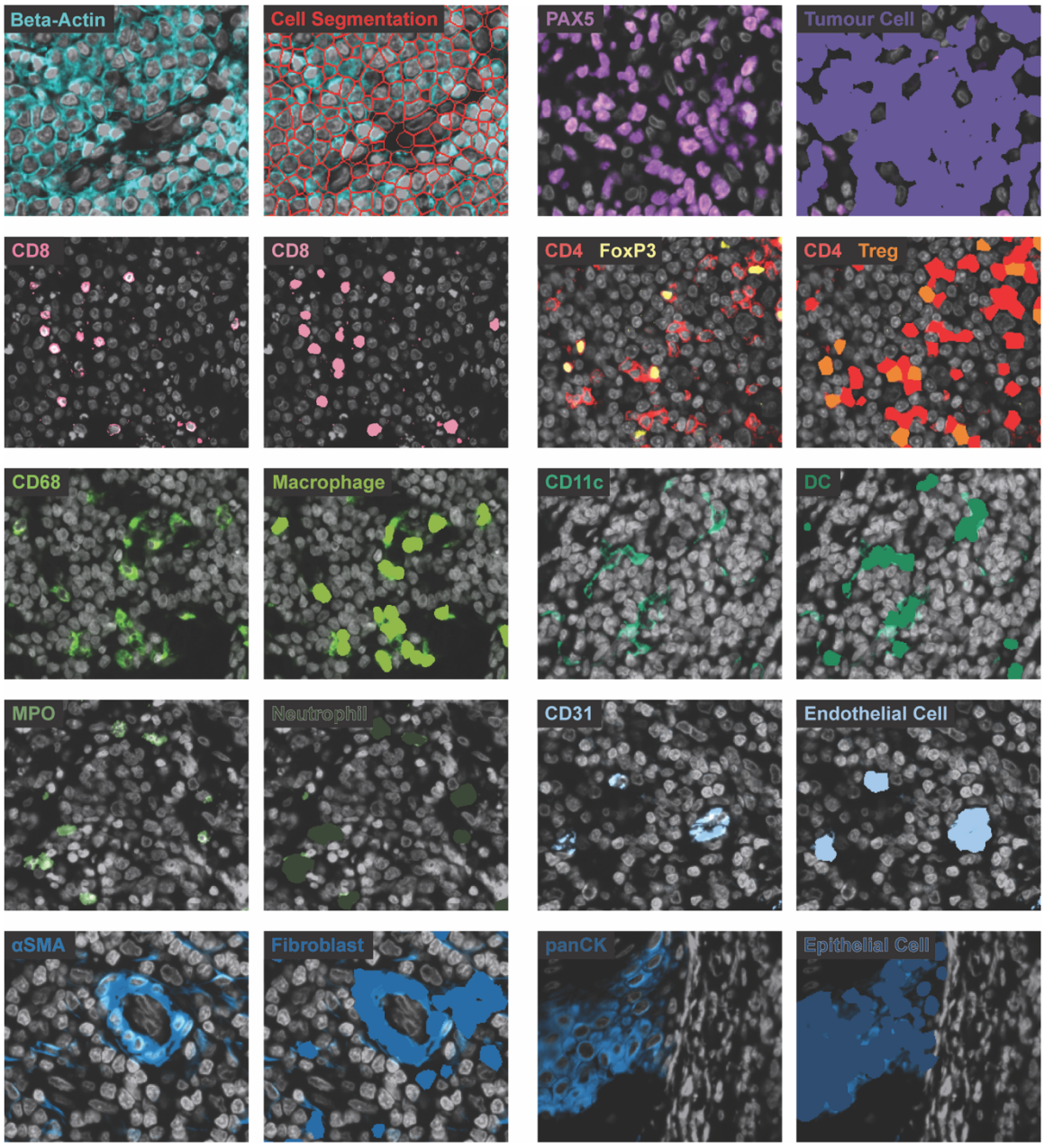


**Supplementary Figure 3.6: Cell segmentation and classification of human DLBCL PhenoCycler images.**
Cell segmentation overlay and Voronoi overlays showing accurate classification of different cell types within human tumour tissues.

**Supplementary Table 3.1. Antibodies for Flow Cytometry**

| Antibody | Clone | Fluorophore | Supplier | Catalog No. |
|---|---|---|---|---|
| CD45 | 30-F11 | BUV395 | eBioscience | 363-0451-82 |
| CD19 | 1D3 | AF700 | BD Pharmingen | 557958 |
| CD19 | 1D3 | PE-Cy7 | BD Pharmingen | 552854 |
| CD3 | 145-2C11 | BV650 | BD Horizon | 564378 |
| CD4 | RM4-5 | APC-Cy7 | BD Pharmingen | 565650 |
| CD8 | 53-6.7 | PerCP-Cy5.5 | BD Pharmingen | 551162 |
| PD-L1 | MIH5 | BUV737 | BD OptiBuild | 741877 |
| CXCR5 | L138D7 | PE/Dazzle594 | Biolegend | 145522 |
| PD-1 | J43 | BV421 | BD Horizon | 562584 |
| GATA3 | L50-823 | BV711 | BD Horizon | 565449 |
| FoxP3 | FJK-16s | FITC | Invitrogen | 11-5773-82 |
| Tbet | O4-46 | AF647 | BD Pharmingen | 561267 |
| CCR4 | 2G12 | PE-Cy7 | Biolegend | 131214 |
| IFNγ | XMG1.2 | PE | BD Pharmingen | 562020 |
| CD69 | H1.2F3 | PE-Cy5 | Biolegend | 104510 |
| CD107a | 1D4B | BV786 | BD Horizon | 564349 |
| CD11b | M1/70 | e450 | Invitrogen | 48-0112-82 |
| CD11c | HL3 | BV786 | BD Horizon | 563735 |
| F4/80 | BM8 | PE | Invitrogen | 12-4801-82 |
| NKp46 | 29A1.4 | APC | eBioscience | 11-3351-80 |
| SiglecF | E50-2440 | PE-CF594 | BD Horizon | 562757 |

**Supplementary Table 3.2. Antibodies for Mouse PhenoCycler Staining (35-plex)**

| Antibody | Barcode | Fluorophore | Staining Concentration |
|---|---|---|---|
| c-Myc | BX001 | AF750 | 1 in 25, ON |
| CD4 | BX002 | ATTO550 | 1 in 200, ON |
| CD11b | BX003 | AF647 | 1 in 200, ON |
| p-STAT6 | BX004 | AF750 | 1 in 25, ON |
| CD8 | BX005 | ATTO550 | 1 in 200, ON |
| MHCII | BX006 | AF647 | 1 in 50, ON |
| CD45 | BX007 | AF750 | 1 in 100, ON |
| MPO | BX013 | AF750 | 1 in 200, ON |
| αSMA | BX014 | ATTO550 | 1 in 200, ON |
| CD11c | BX015 | AF647 | 1 in 50, ON |
| CCL17 | BX016 | AF647 | 1 in 100, ON |
| CD3 | BX017 | ATTO550 | 1 in 100, ON |
| FoxP3 | BX019 | AF750 | 1 in 100, ON |
| F4/80 | BX020 | ATTO550 | 1 in 100, ON |
| LAG3 | BX021 | AF647 | 1 in 50, ON |
| CCL22 | BX022 | AF750 | 1 in 100, ON |
| NaK-ATPase | BX023 | ATTO550 | 1 in 200, ON |
| Ly6G | BX024 | AF647 | 1 in 100, ON |
| CD206 | BX025 | AF750 | 1 in 100, ON |
| CD31 | BX026 | ATTO550 | 1 in 50, ON |
| CD19 | BX027 | AF647 | 1 in 50, ON |
| Tbet | BX029 | ATTO550 | 1 in 50, ON |
| PD-L1 | BX030 | AF647 | 1 in 100, ON |
| CD86 | BX032 | ATTO550 | 1 in 50, ON |
| GATA3 | BX033 | AF647 | 1 in 50, ON |
| IFNγ | BX036 | AF647 | 1 in 50, ON |
| IL4R | BX037 | ATTO550 | 1 in 50, ON |
| CD44 | BX040 | ATTO550 | 1 in 50, ON |
| CD107a | BX042 | AF647 | 1 in 100, ON |
| GZMB | BX043 | AF750 | 1 in 50, ON |
| PD-1 | BX046 | AF647 | 1 in 100, ON |
| Ki67 | BX047 | ATTO550 | 1 in 200, ON |
| TCF7 | BX055 | ATTO550 | 1 in 100, ON |
| CitH3 | BX078 | ATTO550 | 1 in 100, ON |
| CCR4 | BX106 | AF647 | 1 in 100, ON |

**Supplementary Table 3.3: Antibodies for Human PhenoCycler Staining (52-plex)**

| Antibody | Barcode | Fluorophore | Staining Concentration |
|---|---|---|---|
| CD31 | BX001 | AF750 | 1 in 100, ON |
| TIGIT | BX002 | ATTO550 | 1 in 100, ON |
| CD4 | BX003 | AF647 | 1 in 200, ON |
| pSTAT6 | BX004 | AF750 | 1 in 25, ON |
| TIM3 | BX005 | ATTO550 | 1 in 200, ON |
| TCF1/7 | BX006 | AF647 | 1 in 100, ON |
| CD20 | BX007 | AF750 | 1 in 400, ON |
| CD15 | BX010 | AF647 | 1 in 100, ON |
| αSMA | BX013 | AF750 | 1 in 200, ON |
| PAX5 | BX014 | ATTO550 | 1 in 200, ON |
| CD68 | BX015 | AF647 | 1 in 200, ON |
| CCL17 | BX016 | AF647 | 1 in 100, ON |
| CD45RO | BX017 | ATTO550 | 1 in 200, ON |
| panCK | BX019 | AF750 | 1 in 200, ON |
| IFNγ | BX020 | AF647 | 1 in 200, ON |
| CD45 | BX021 | AF647 | 1 in 200, ON |
| CCL22 | BX022 | AF750 | 1 in 100, ON |
| NaK-ATPase | BX023 | ATTO550 | 1 in 100, ON |
| CD11c | BX024 | AF647 | 1 in 100, 30 min 37 °C |
| CD8 | BX026 | ATTO550 | 1 in 200, ON |
| CX3CR1 | BX027 | AF647 | 1 in 100, ON |
| CD56 | BX028 | ATTO550 | 1 in 200, ON |
| HLA-A | BX029 | ATTO550 | 1 in 200, ON |
| FoxP3 | BX031 | AF647 | 1 in 200, ON |
| CD21 | BX032 | ATTO550 | 1 in 200, ON |
| HLA-DR | BX033 | AF647 | 1 in 400, ON |
| CD11b | BX034 | ATTO550 | 1 in 200, ON |
| CD163 | BX035 | ATTO550 | 1 in 200, ON |
| CTLA4 | BX036 | AF647 | 1 in 100, ON |
| CD14 | BX037 | ATTO550 | 1 in 200, ON |
| VISTA | BX040 | ATTO550 | 1 in 100, ON |
| GZMB | BX041 | ATTO550 | 1 in 200, ON |
| CX3CL1 | BX042 | AF647 | 1 in 100, 30 min 37 °C |
| CD19 | BX043 | ATTO550 | 1 in 200, ON |
| MNK1 | BX045 | AF647 | 1 in 50, ON |
| PD-1 | BX046 | AF647 | 1 in 100, ON |
| Ki67 | BX047 | ATTO550 | 1 in 200, ON |
| GATA3 | BX049 | ATTO550 | 1 in 100, ON |
| CD86 | BX050 | AF647 | 1 in 100, ON |
| Tbet | BX052 | ATTO550 | 1 in 100, ON |
| p-eIF4E | BX054 | AF647 | 1 in 50, 30 min 37 °C |
| LAG3 | BX055 | AF647 | 1 in 100, ON |

| | | | |
|---|---|---|---|
| TOX | BX060 | ATTO550 | 1 in 200, ON |
| PD-L1 | BX067 | AF647 | 1 in 200, ON |
| CitH3 | BX078 | ATTO550 | 1 in 100, ON |
| CD3 | BX080 | AF647 | 1 in 200, ON |
| CD38 | BX089 | ATTO550 | 1 in 100, ON |
| MPO | BX098 | ATTO550 | 1 in 200, ON |
| CCR4 | BX106 | AF647 | 1 in 100, ON |
| CD45RA | BX113 | ATTO550 | 1 in 100, ON |
| B-Actin | BX117 | AF750 | 1 in 200, ON |
| eIF4E | BX518 | AF647 | 1 in 100, ON |

**Supplementary Table 3.4: Reagents and Tools**

| Reagent or resource | Reference or source | Identifier |
|---|---|---|
| **Cell lines** | | |
| Eμ-Myc Parental | Dr. Jerry Pelletier | NA |
| $MEF^{ARF-/-}$ | Dr. Jerry Pelletier | NA |
| Phoenix-AMPHO | ATCC | CRL-3212 |
| Eμ-Myc $mSTAT6^{WT}$ | This study | NA |
| Eμ-Myc $mSTAT6^{D419N}$ | This study | NA |
| **Antibodies for IHC** | | |
| Ki67 Rabbit mAb | Cell Signaling Technology | 12202S |
| CD4 Monoclonal Antibody | Invitrogen | 14-0042-82 |
| Phospho-STAT6 (Tyr641) Rabbit mAb | Cell Signaling Technology | 56554S |
| EnVision+ System- HRP Labellled Polymer Anti-Rabbit | Dako | K4003 |
| Goat Anti-Rat IgG H+L (HRP Polymer) | Abcam | ab214882 |
| **Dyes and Stains** | | |
| LIVE/DEAD Fixable Aqua Dead Cell Stain Kit | ThermoFisher | L34966 |
| DAPI | ThermoFisher | D1306 |
| DRAQ5 | Biolegend | 424101 |
| Harris' Alum Hematoxylin Mercury Free | Sigma-Aldrich | 638A-85 |
| Eosin Y Solution | Sigma-Aldrich | HT110116-500ML |
| ImmPACT DAB Substrate Kit, Peroxidase | Vector Laboratories | SK-4105 |
| EnVision FLEX HRP Magenta Substrate Chromogen System | Agilient Technologies | GV92511-2 |
| **Drugs, reagents, and other consumables** | | |
| Doxorubicin | Jewish General Hospital Oncology Pharmacy | 1201 |
| AZD2098 | MedChemExpress | HY-U00064 |
| Recombinant Murine IL-4 | PeproTech | 214-14 |
| FoxP3/ Transcription Factor Fixation/ Permeabilization Concentrate and Diluent | eBioscience | 00-5521-00 |
| CD19 MicroBeads, mouse | Miltenyi Biotec | 130-121-301 |
| CD4+ T Cell Isolation Kit, mouse | Miltenyi Biotec | 130-104-454 |
| LS Columns | Miltenyi Biotec | 130-042-401 |
| 5.0 um 6-well PET insert | Sarstedt | 83.3930.500 |
| 3.0 um 12-well PET insert | Sarstedt | 83.3931.300 |
| Sample Kit for PhenoCycler-Fusion | Akoya Biosciences | 7000017 |
| 10X Buffer Kit for PhenoCycler-Fusion | Akoya Biosciences | 7000019 |
| Antibody Conjugation Kit | Akoya Biosciences | 7000009 |

| | | |
|---|---|---|
| Salmon sperm DNA, sheared (10mg/mL) | Invitrogen | AM9680 |
| Permount Mounting Medium | Fisher Scientific | SP15-500 |
| Trypan Blue, 0.4% Solution | Wisent | 609-130-EL |
| RPMI | Wisent | 350-000-CL |
| ISCOVE | Wisent | 319-105-CL |
| DMEM | Wisent | 319-005-CL |
| Fetal bovine serum | Wisent | 080-450 |
| Penicillin-streptomycin | Wisent | 450-201-EL |
| β-mercaptoethanol | Sigma | M3148-100mL |
| **Software** | | |
| FlowJo v10.10 | BD Biosciences | |
| Prism (version 6.0) | GraphPad | |
| Illustrator 2024 | Adobe | |
| QuPath v0.5.1 | | |
| Enable Medicine Platform | Enable Medicine | |
| **Instruments** | | |
| BD LSRFortessa Flow Cytometer | BD Bioscience | |
| FACSAria Fusion Cell Sorter | BD Bioscience | |
| VEVO-3100 | FUJIFILM VisualSonics | |
| Mastercycler X50a | Eppendorf | |
| QuantStudio 7 Flex | Applied Biosystems by Life Technologies | |
| PT Link, Pre-Treatment Module for Tissue Specimens | Agilent Dako | |
| AxioScan 7 Microscope Slide Scanner | Zeiss | |
| Countess 3 Automated Cell Counter | ThermoFisher | AMQAX2000 |
| PhenoCycler-Fusion | Akoya Bioscience | |

**Supplementary Table 3.5: Statistics**

| Figure | Test Used | n | Comparisons and p-values |
|---|---|---|---|
| **Figure 1** | | | |
| 1C | 2way ANOVA, with Sidak's multiple comparison test | $mSTAT6^{WT}$ = 5<br>$mSTAT6^{D419N}$ = 5 | Day 4 $mSTAT6^{WT}$ vs Day 4 $mSTAT6^{D419N}$, p = 0.5284<br>Day 8 $mSTAT6^{WT}$ vs Day 8 $mSTAT6^{D419N}$, p = 2372<br>Day 11 $mSTAT6^{WT}$ vs Day 11 $mSTAT6^{D419N}$, p = 0.0217<br>Day 13 $mSTAT6^{WT}$ vs Day 13 $mSTAT6^{D419N}$, p = 0.5142 |
| 1E | 2way ANOVA, with uncorrected Fisher's LSD | D8 $mSTAT6^{WT}$ = 5<br>D8 $mSTAT6^{D419N}$ = 5<br>D11 $mSTAT6^{WT}$ = 8<br>D11 $mSTAT6^{D419N}$ = 8<br>D14 $mSTAT6^{WT}$ = 5<br>D14 $mSTAT6^{D419N}$ = 5 | Day 8 $mSTAT6^{WT}$ vs Day 8 $mSTAT6^{D419N}$, p = 0.7096<br>Day 11 $mSTAT6^{WT}$ vs Day 11 $mSTAT6^{D419N}$, p = 0.0001<br>Day 14 $mSTAT6^{WT}$ vs Day 14 $mSTAT6^{D419N}$, p = 0.8429 |
| 1F | Unpaired t test, two-tailed | D11 $mSTAT6^{WT}$ = 8<br>D11 $mSTAT6^{D419N}$ = 8 | Day 11 $mSTAT6^{WT}$ vs Day 11 $mSTAT6^{D419N}$, p = 0.8012 |
| 1H | Unpaired t test, two-tailed | D11 $mSTAT6^{WT}$ = 8<br>D11 $mSTAT6^{D419N}$ = 8 | CD4 H-score: Day 11 $mSTAT6^{WT}$ vs Day 11 $mSTAT6^{D419N}$, p = 0.0047<br>Phospho-STAT6 H-score: Day 11 $mSTAT6^{WT}$ vs Day 11 $mSTAT6^{D419N}$, p = 0.0138 |
| 1I | Pearson correlation | Number of pairs = 16<br>D11 $mSTAT6^{WT}$ = 8<br>D11 $mSTAT6^{D419N}$ = 8 | r = 0.7610<br>p = 0.0006 |
| 1J | Unpaired t test, two-tailed | D11 $mSTAT6^{WT}$ = 8<br>D11 $mSTAT6^{D419N}$ = 8 | % of CD45: Day 11 $mSTAT6^{WT}$ vs Day 11 $mSTAT6^{D419N}$, p = 0.0047<br>Number of cells: Day 11 $mSTAT6^{WT}$ vs Day 11 $mSTAT6^{D419N}$, p = 0.0267 |
| 1K | Unpaired t test, two-tailed | D11 $mSTAT6^{WT}$ = 8<br>D11 $mSTAT6^{D419N}$ = 8 | % of CD45: Day 11 $mSTAT6^{WT}$ vs Day 11 $mSTAT6^{D419N}$, p = 0.3459<br>Number of cells: Day 11 $mSTAT6^{WT}$ vs Day 11 $mSTAT6^{D419N}$, p = 0.4188 |
| **Figure 2** | | | |
| 2A | Unpaired t test, two-tailed | D11 $mSTAT6^{WT}$ = 10<br>D11 $mSTAT6^{D419N}$ = 10 | Day 11 $mSTAT6^{WT}$ vs Day 11 $mSTAT6^{D419N}$, p = 0.0122 |
| 2B | Unpaired t test, two-tailed | Tregs/ Tfh D11 $mSTAT6^{WT}$ = 7<br>Tregs/ Tfh D11 $mSTAT6^{D419N}$ = 7<br>Th1/ Th2 D11 $mSTAT6^{WT}$ = 10 | Tregs: $mSTAT6^{WT}$ vs $mSTAT6^{D419N}$, p = 0.0793<br>Tfh: $mSTAT6^{WT}$ vs $mSTAT6^{D419N}$, p = 0.9008<br>Th1: $mSTAT6^{WT}$ vs $mSTAT6^{D419N}$, p = 0.0153 |

| | | | |
|---|---|---|---|
| | | Th1/ Th2 D11 mSTAT6$^{D419N}$ = 10 | Th2: mSTAT6$^{WT}$ vs mSTAT6$^{D419N}$, p = 0.0943 |
| 2C | Unpaired t test, two-tailed | D11 mSTAT6$^{WT}$ = 10<br>D11 mSTAT6$^{D419N}$ = 10 | CCR4+ Th1: mSTAT6$^{WT}$ vs mSTAT6$^{D419N}$, p = 0.0317<br>CCR4+ MFI Th1: mSTAT6$^{WT}$ vs mSTAT6$^{D419N}$, p = 0.0017 |
| **Figure 3** | | | |
| 3B | 2way ANOVA, with Tukey's multiple comparison test | mSTAT6$^{WT}$ -IL-4 = 3<br>mSTAT6$^{WT}$ +IL-4 = 5<br>mSTAT6$^{D419N}$ -IL-4 = 3<br>mSTAT6$^{D419N}$ +IL-4 = 5 | mSTAT6$^{WT}$ -IL-4 vs mSTAT6$^{WT}$ +IL-4, p = 0.7936<br>mSTAT6$^{D419N}$ -IL-4 vs mSTAT6$^{D419N}$ +IL-4, p = 0.0053 |
| 3C | 2way ANOVA, with Tukey's multiple comparison test | mSTAT6$^{WT}$ -IL-4 = 5<br>mSTAT6$^{WT}$ +IL-4 = 5<br>mSTAT6$^{WT}$ +IL-4 +AZD2098 = 5<br>mSTAT6$^{D419N}$ -IL-4 = 5<br>mSTAT6$^{D419N}$ +IL-4 = 5<br>mSTAT6$^{D419N}$ +IL-4 +AZD2098 = 5 | CD4: mSTAT6$^{WT}$ -IL-4 vs mSTAT6$^{WT}$ +IL-4, p = 0.0008<br>CD4: mSTAT6$^{WT}$ +IL-4 vs mSTAT6$^{WT}$ +IL-4 +AZD2098, p < 0.0001<br>CD4: mSTAT6$^{WT}$ +IL-4 vs mSTAT6$^{D419N}$ +IL-4, p < 0.0001<br>CD4: mSTAT6$^{D419N}$ -IL-4 vs mSTAT6$^{D419N}$ +IL-4, p < 0.0001<br>CD4: mSTAT6$^{D419N}$ +IL-4 vs mSTAT6$^{D419N}$ +IL-4 +AZD2098, p < 0.0001<br>CD8, NK cell, macrophage, DC, eosinophil: mSTAT6$^{WT}$ -IL-4 vs mSTAT6$^{WT}$ +IL-4, p > 0.9999<br>CD8, NK cell, macrophage, DC, eosinophil: mSTAT6$^{WT}$ +IL-4 vs mSTAT6$^{WT}$ +IL-4 +AZD2098, p > 0.9999<br>CD8, NK cell, macrophage, DC, eosinophil: mSTAT6$^{WT}$ +IL-4 vs mSTAT6$^{D419N}$ +IL-4, p > 0.9999<br>CD8, NK cell, macrophage, DC, eosinophil: mSTAT6$^{D419N}$ -IL-4 vs mSTAT6$^{D419N}$ +IL-4, p > 0.9999<br>CD8, NK cell, macrophage, DC, eosinophil: mSTAT6$^{D419N}$ +IL-4 vs mSTAT6$^{D419N}$ +IL-4 +AZD2098, p > 0.9999 |
| **Figure 4** | | | |
| 4B | 2way ANOVA, with Sidak's multiple comparison test | mSTAT6$^{WT}$ +Veh = 5<br>mSTAT6$^{D419N}$+Veh = 5<br>mSTAT6$^{WT}$ + 3x3 mg/kg Doxo = 4<br>mSTAT6$^{D419N}$ + 3x3 mg/kg Doxo = 5 | mSTAT6$^{WT}$ +Veh vs mSTAT6$^{D419N}$+Veh, p = 0.8641<br>mSTAT6$^{WT}$ +Veh vs mSTAT6$^{WT}$ + 3x3 mg/kg Doxo, p = 0.0009<br>mSTAT6$^{D419N}$+Veh vs mSTAT6$^{D419N}$ + 3x3 mg/kg Doxo, p = 0.8151 |

| | | | |
|---|---|---|---|
| | | | mSTAT6$^{WT}$ + 3x3 mg/kg Doxo vs mSTAT6$^{D419N}$ + 3x3 mg/kg Doxo, p = 0.0511 |
| 4D | Gehan-Breslow-Wilcoxon test | mSTAT6$^{WT}$ + 3x3 mg/kg Doxo = 10<br>mSTAT6$^{D419N}$ + 3x3 mg/kg Doxo = 10 | mSTAT6$^{WT}$ + 3x3 mg/kg Doxo vs mSTAT6$^{D419N}$ + 3x3 mg/kg Doxo, p = 0.0764 |
| 4F | 2way ANOVA, with uncorrected Fisher's LSD | mSTAT6$^{WT}$ + 10 mg/kg Doxo = 10<br>mSTAT6$^{D419N}$ + 10 mg/kg Doxo = 10 | Pre: mSTAT6$^{WT}$ + 10 mg/kg Doxo vs mSTAT6$^{D419N}$ + 10 mg/kg Doxo, p = 0.2061<br>Post: mSTAT6$^{WT}$ + 10 mg/kg Doxo vs mSTAT6$^{D419N}$ + 10 mg/kg Doxo, p = 0.0023<br>mSTAT6$^{WT}$: Pre vs Post, p = 0.0615<br>mSTAT6$^{D419N}$: Pre vs Post, p = 0.0164 |
| 4H | Gehan-Breslow-Wilcoxon test | mSTAT6$^{WT}$ + 10 mg/kg Doxo = 10<br>mSTAT6$^{D419N}$ + 10 mg/kg Doxo = 10 | mSTAT6$^{WT}$ + 10 mg/kg Doxo vs mSTAT6$^{D419N}$ + 10 mg/kg Doxo, p = 0.1211 |
| **Figure 6** | | | |
| 6B | 2way ANOVA, with Tukey's multiple comparison test | mSTAT6$^{WT}$ + Veh= 9<br>mSTAT6$^{D419N}$ + Veh = 9<br>mSTAT6$^{WT}$ + 10 mg/kg AZD2098 = 9<br>mSTAT6$^{D419N}$ + 10 mg/kg AZD2098 = 8 | mSTAT6$^{WT}$ + Veh vs mSTAT6$^{D419N}$ + Veh, p = 0.0774<br>mSTAT6$^{WT}$ + Veh vs mSTAT6$^{WT}$ + 10 mg/kg AZD2098, p = 0.9613<br>mSTAT6$^{D419N}$ + Veh vs mSTAT6$^{D419N}$ + 10 mg/kg AZD2098, p = 0.0445 |
| 6C | 2way ANOVA, with Tukey's multiple comparison test | mSTAT6$^{WT}$ + Veh= 9<br>mSTAT6$^{D419N}$ + Veh = 9<br>mSTAT6$^{WT}$ + 10 mg/kg AZD2098 = 9<br>mSTAT6$^{D419N}$ + 10 mg/kg AZD2098 = 8 | Treg: mSTAT6$^{WT}$ + Veh vs mSTAT6$^{D419N}$ + Veh, p = 0.9940<br>Treg: mSTAT6$^{WT}$ + Veh vs mSTAT6$^{WT}$ + 10 mg/kg AZD2098, p = 0.6536<br>Treg: mSTAT6$^{D419N}$ + Veh vs mSTAT6$^{D419N}$ + 10 mg/kg AZD2098, p = 0.3958<br>Tfh: mSTAT6$^{WT}$ + Veh vs mSTAT6$^{D419N}$ + Veh, p = 0.7400<br>Tfh: mSTAT6$^{WT}$ + Veh vs mSTAT6$^{WT}$ + 10 mg/kg AZD2098, p = 0.9737<br>Tfh: mSTAT6$^{D419N}$ + Veh vs mSTAT6$^{D419N}$ + 10 mg/kg AZD2098, p = 0.9185<br>Th1: mSTAT6$^{WT}$ + Veh vs mSTAT6$^{D419N}$ + Veh, p = 0.0551 |

| | | | |
|---|---|---|---|
| | | | Th1: mSTAT6$^{WT}$ + Veh vs mSTAT6$^{WT}$ + 10 mg/kg AZD2098, p = 0.9970<br>Th1: mSTAT6$^{D419N}$ + Veh vs mSTAT6$^{D419N}$ + 10 mg/kg AZD2098, p = 0.1324<br>Th2: mSTAT6$^{WT}$ + Veh vs mSTAT6$^{D419N}$ + Veh, p = 0.7550<br>Th2: mSTAT6$^{WT}$ + Veh vs mSTAT6$^{WT}$ + 10 mg/kg AZD2098, p = 0.1055<br>Th2: mSTAT6$^{D419N}$ + Veh vs mSTAT6$^{D419N}$ + 10 mg/kg AZD2098, p = 0.0170 |
| 6D | 3way ANOVA | mSTAT6$^{WT}$ + Veh= 3<br>mSTAT6$^{D419N}$ + Veh =4<br>mSTAT6$^{WT}$ + 10 mg/kg AZD2098 = 3<br>mSTAT6$^{D419N}$ + 10 mg/kg AZD2098 = 5 | Time, p < 0.0001<br>mSTAT6$^{WT}$ vs mSTAT6$^{D419N}$, p = 0.8843<br>Veh vs AZD2098, p = 0.3360 |
| 6F | 2way ANOVA, with uncorrected Fisher's LSD | mSTAT6$^{WT}$ + Doxo = 5<br>mSTAT6$^{D419N}$ + Doxo = 5<br>mSTAT6$^{WT}$ + Doxo + AZD2098 = 5<br>mSTAT6$^{D419N}$ + Doxo + AZD2098 = 5 | Pre: mSTAT6$^{WT}$ + Doxo vs mSTAT6$^{D419N}$ + Doxo, p = 0.6611<br>Pre: mSTAT6$^{WT}$ + Doxo vs mSTAT6$^{WT}$ + Doxo + AZD2098, p = 0.7703<br>Pre: mSTAT6$^{D419N}$ + Doxo vs mSTAT6$^{D419N}$ + Doxo + AZD2098, p = 0.4867<br>Post: mSTAT6$^{WT}$ + Doxo vs mSTAT6$^{D419N}$ + Doxo, p = 0.0003<br>Post: mSTAT6$^{WT}$ + Doxo vs mSTAT6$^{WT}$ + Doxo + AZD2098, p = 0.9994<br>Post: mSTAT6$^{D419N}$ + Doxo vs mSTAT6$^{D419N}$ + Doxo + AZD2098, p = 0.0006<br>mSTAT6$^{WT}$ + Doxo: Pre vs Post, p = 0.3082<br>mSTAT6$^{D419N}$ + Doxo: Pre vs Post, p = 0.0135<br>mSTAT6$^{WT}$ + Doxo + AZD2098: Pre vs Post, p = 0.4645<br>mSTAT6$^{D419N}$ + Doxo + AZD2098: Pre vs Post, p = 0.6449 |
| 6I | Gehan-Breslow-Wilcoxon test, Bonferroni corrected | mSTAT6$^{WT}$ + Doxo = 5<br>mSTAT6$^{D419N}$ + Doxo = 5<br>mSTAT6$^{WT}$ + Doxo + AZD2098 = 5 | mSTAT6$^{WT}$ + Doxo vs mSTAT6$^{D419N}$ + Doxo, p = 0.0070 |

| | | | |
|---|---|---|---|
| | | mSTAT6$^{D419N}$ + Doxo + AZD2098 = 5 | mSTAT6$^{WT}$ + Doxo + AZD2098 vs mSTAT6$^{D419N}$ + Doxo + AZD2098, p = 0.0248<br>mSTAT6$^{WT}$ + Doxo vs mSTAT6$^{D419N}$ + Doxo + AZD2098, p = 0.1446<br>mSTAT6$^{D419N}$ + Doxo vs mSTAT6$^{D419N}$ + Doxo + AZD2098, p = 0.0095 |
| **Figure 7** | | | |
| 7G | Unpaired t test, two-tailed | STAT6$^{WT}$ = 31<br>STAT6$^{D419N}$ =6 | phospho-STAT6: STAT6$^{WT}$ vs STAT6$^{D419N}$, p < 0.0001<br>CCL17: STAT6$^{WT}$ vs STAT6$^{D419N}$, p < 0.0001 |
| 7H | Pearson correlation | Number of pairs = 37<br>STAT6$^{WT}$ = 31<br>STAT6$^{D419N}$ =6 | r = 0.8019<br>p < 0.0001 |
| 7I | Unpaired t test, two-tailed | STAT6$^{WT}$ = 31<br>STAT6$^{D419N}$ =6 | CCR4: STAT6$^{WT}$ vs STAT6$^{D419N}$, p = 0.0003 |
| 7J | Pearson correlation | Number of pairs = 37<br>STAT6$^{WT}$ = 31<br>STAT6$^{D419N}$ =6 | r = 0.5969<br>p < 0.0001 |
| 7K | Unpaired t test, two-tailed | STAT6$^{WT}$ = 31<br>STAT6$^{D419N}$ =6 | CD4 and Tumour: STAT6$^{WT}$ vs STAT6$^{D419N}$, p = 0.369<br>CCR4+ CD4 and Tumour: STAT6$^{WT}$ vs STAT6$^{D419N}$, p = 0.767<br>CD4 and pSTAT6+ Tumour: STAT6$^{WT}$ vs STAT6$^{D419N}$, p = 0.021<br>CCR4+ CD4 and pSTAT6+ Tumour: STAT6$^{WT}$ vs STAT6$^{D419N}$, p = 0.124 |
| **Figure S1** | | | |
| S1A | Unpaired t test, two-tailed | D8 mSTAT6$^{WT}$ = 3<br>D8 mSTAT6$^{D419N}$ = 4 | % of CD45: Day 8 mSTAT6$^{WT}$ vs Day 8 mSTAT6$^{D419N}$, p = 0.7900<br>Number of cells: Day 8 mSTAT6$^{WT}$ vs Day 8 mSTAT6$^{D419N}$, p = 0.2898 |
| S1B | Unpaired t test, two-tailed | D14 mSTAT6$^{WT}$ = 5<br>D14 mSTAT6$^{D419N}$ = 4 | % of CD45: Day 14 mSTAT6$^{WT}$ vs Day 14 mSTAT6$^{D419N}$, p = 0.0934<br>Number of cells: Day 14 mSTAT6$^{WT}$ vs Day 14 mSTAT6$^{D419N}$, p = 0.1598 |
| S1C | Unpaired t test, two-tailed | D8 mSTAT6$^{WT}$ = 3<br>D8 mSTAT6$^{D419N}$ = 4 | % of CD45: Day 8 mSTAT6$^{WT}$ vs Day 8 mSTAT6$^{D419N}$, p = 0.8780 |

| | | | |
|---|---|---|---|
| | | | Number of cells: Day 8 mSTAT6$^{WT}$ vs Day 8 mSTAT6$^{D419N}$, p = 0.4364 |
| S1D | Unpaired t test, two-tailed | D14 mSTAT6$^{WT}$ = 5<br>D14 mSTAT6$^{D419N}$ = 4 | % of CD45: Day 14 mSTAT6$^{WT}$ vs Day 14 mSTAT6$^{D419N}$, p = 0.1788<br>Number of cells: Day 14 mSTAT6$^{WT}$ vs Day 14 mSTAT6$^{D419N}$, p = 0.2048 |
| **Figure S2** | | | |
| S2A | Unpaired t test, two-tailed | D11 mSTAT6$^{WT}$ = 10<br>D11 mSTAT6$^{D419N}$ = 10 | Day 11 mSTAT6$^{WT}$ vs Day 11 mSTAT6$^{D419N}$, p = 0.3681 |
| S2B | Unpaired t test, two-tailed | D11 mSTAT6$^{WT}$ = 10<br>D11 mSTAT6$^{D419N}$ = 10 | Day 11 mSTAT6$^{WT}$ vs Day 11 mSTAT6$^{D419N}$, p = 0.7515 |
| S2C | Unpaired t test, two-tailed | D11 mSTAT6$^{WT}$ = 10<br>D11 mSTAT6$^{D419N}$ = 10 | Day 11 mSTAT6$^{WT}$ vs Day 11 mSTAT6$^{D419N}$, p = 0.3017 |
| S2D | Unpaired t test, two-tailed | D11 mSTAT6$^{WT}$ = 10<br>D11 mSTAT6$^{D419N}$ = 10 | Day 11 mSTAT6$^{WT}$ vs Day 11 mSTAT6$^{D419N}$, p = 0.8248 |
| S2E | Unpaired t test, two-tailed | D11 mSTAT6$^{WT}$ = 10<br>D11 mSTAT6$^{D419N}$ = 10 | Day 11 mSTAT6$^{WT}$ vs Day 11 mSTAT6$^{D419N}$, p = 0.7978 |
| S2F | Unpaired t test, two-tailed | D11 mSTAT6$^{WT}$ = 10<br>D11 mSTAT6$^{D419N}$ = 10 | Day 11 mSTAT6$^{WT}$ vs Day 11 mSTAT6$^{D419N}$, p = 0.6957 |
| **Figure S3** | | | |
| S3A | Unpaired t test, two-tailed | mSTAT6$^{WT}$ + 3x3 mg/kg Doxo = 4<br>mSTAT6$^{D419N}$ + 3x3 mg/kg Doxo = 4<br>mSTAT6$^{WT}$ + 10 mg/kg Doxo = 8<br>mSTAT6$^{D419N}$ + 10 mg/kg Doxo = 10 | 3x3 mg/kg Doxo: mSTAT6$^{WT}$ vs mSTAT6$^{D419N}$, p = 0.5393<br>10 mg/kg Doxo: mSTAT6$^{WT}$ vs mSTAT6$^{D419N}$, p = 0.8210 |
| S3B | Unpaired t test, two-tailed | mSTAT6$^{WT}$ + 3x3 mg/kg Doxo = 4<br>mSTAT6$^{D419N}$ + 3x3 mg/kg Doxo = 4<br>mSTAT6$^{WT}$ + 10 mg/kg Doxo = 8<br>mSTAT6$^{D419N}$ + 10 mg/kg Doxo = 10 | 3x3 mg/kg Doxo: mSTAT6$^{WT}$ vs mSTAT6$^{D419N}$, p = 0.7304<br>10 mg/kg Doxo: mSTAT6$^{WT}$ vs mSTAT6$^{D419N}$, p = 0.1555 |
| S3C | Unpaired t test, two-tailed | mSTAT6$^{WT}$ + 3x3 mg/kg Doxo = 4<br>mSTAT6$^{D419N}$ + 3x3 mg/kg Doxo = 4<br>mSTAT6$^{WT}$ + 10 mg/kg Doxo = 8<br>mSTAT6$^{D419N}$ + 10 mg/kg Doxo = 10 | 3x3 mg/kg Doxo: mSTAT6$^{WT}$ vs mSTAT6$^{D419N}$, p = 0.7585<br>10 mg/kg Doxo: mSTAT6$^{WT}$ vs mSTAT6$^{D419N}$, p = 0.8938 |
| S3D | Unpaired t test, two-tailed | mSTAT6$^{WT}$ + 3x3 mg/kg Doxo = 4 | 3x3 mg/kg Doxo: mSTAT6$^{WT}$ vs mSTAT6$^{D419N}$, p = 0.7290 |

| | | | |
|---|---|---|---|
| | | mSTAT6$^{D419N}$ + 3x3 mg/kg Doxo = 4<br>mSTAT6$^{WT}$ + 10 mg/kg Doxo = 8<br>mSTAT6$^{D419N}$ + 10 mg/kg Doxo = 10 | 10 mg/kg Doxo: mSTAT6$^{WT}$ vs mSTAT6$^{D419N}$, p = 0.5891 |

# Chapter 4: Discussion and Future Directions

## 4.1 Summary of Results and Study Limitations

In recent years, it has been increasingly appreciated that the TME is a crucial driver of therapeutic response and therapeutic resistance in many different cancer types. Therefore, in this thesis of work, we aimed to spatially study the TME of murine and human DLBCL to understand how tumour-cell driven TME remodelling impacts therapeutic resistance. To do this, mouse models of DLBCL were employed, and custom antibody panels for highly multiplexed PhenoCycler imaging were developed.

In Chapter 2, the use of PhenoCycler technology enabled in-depth, hypothesis-generating observations related to TME composition of various mouse models of cancer. This is crucial, as these studies revealed how immune cell abundance and spatial organization can vary in the TME across cancer types, enhancing our understanding of immune evasion, metastasis, and drug resistance mechanisms. PhenoCycler imaging of Eμ-Myc and A20 murine models of lymphoma demonstrated that Eμ-Myc tumours have relatively decreased lymphoid infiltration relative to A20 tumours. Indeed, Eμ-Myc tumours are “disorganized”, meaning that very few preferential interactions between different cell types were observed.

In Chapter 3, Eμ-Myc was used to model STAT6$^{D419}$-mutant rrDLBCL. This model was optimal for this study, as we were able to detect a relative increase in CD4+ T cell infiltration in mSTA6$^{D419N}$ tumours, coupled with increased tumour-cell expression of phospho-STAT6. Moreover, STAT6$^{D419N}$-Eμ-Myc tumours demonstrated resistance to doxorubicin, which could be reversed by blocking CD4+ T cell infiltration into the TME. The results from Chapter 3 emphasized the importance of focusing on TME dynamics in

the context of specific oncogenic mutations. The combination of PhenoCycler imaging of human and murine tissues with functional assays using cells derived from immunocompetent mouse models thus represents a powerful paradigm for screening TME-based therapeutic targets for DLBCL treatment.

However, there were distinct limitations associated with the experimental techniques and models used. While PhenoCycler allows for in-depth phenotyping of the murine and human TME, it is limited by the 2D region selected for imaging, especially in the context of a TMA. Moreover, the selection of antibodies that are included or excluded from the staining panel represents the bias of the experimenter, in contrast to techniques such as spatial transcriptomics, that capture the heterogeneity of the TME in an unbiased manner. Additionally, mouse models of human disease, especially syngeneic models, are inherently flawed, as they cannot fully capture the genetic heterogeneity and sequential clonal evolution of tumorigenesis that is characteristic of human disease.

The rationale for selection of PhenoCycler analysis techniques, mouse models of lymphoma, and the drug target for STAT6$^{D419}$-mutant lymphoma that were used in this thesis, and their limitations as they pertain to these studies, are discussed in further depth below.

## 4.2 Analysis of Highly Multiplexed Imaging Data

In Chapters 2 and 3, different approaches for cell segmentation and cell classification of PhenoCycler imaging data were used. The merits and drawbacks of these different methods are discussed below.

### *4.2.1 Cell Segmentation*

Cell segmentation is the process of isolating and creating borders around individual cells within a histological image, thereby allowing for the classification of single cells into phenotypes and enabling spatial analyses. Cell segmentation is a critical first step in PhenoCycler image analysis, as the fidelity of cell segmentation will define the cell boundaries that determine cellular expression of different markers in each cell for all downstream analysis steps.

In Chapter 2, cell segmentation was achieved using StarDist in QuPath software (152, 153). StarDist is a nuclear expansion-based cell segmentation algorithm (**Figure 4.1**). It works by identifying the nuclei of each cell, based on DAPI or DRAQ5 expression, then projecting radially from the nuclei to predict the cell boundary. StarDist was found to effectively segment tumour and immune cells but showed less effective cell segmentation for irregularly shaped cells, such as fibroblasts. Therefore, in Chapter 3, DeepCell, a membrane-based cell segmentation method, was employed (154). With DeepCell, nuclear expansion was used in combination with a membrane marker that delineated the cell boundary. For murine tissues, this marker was NaK-ATPase, and for human tissues, this marker was β-actin. As both membrane markers outlined each cell's outermost structure, DeepCell provided a more accurate representation of different cell shapes compared to StarDist's predicted cell boundary. However, to use DeepCell in this fashion, pre-planning is required, and a suitable membrane marker must be incorporated into the staining panel. With StarDist, only nuclear staining is required, thus it is more amenable to the segmentation of a wider variety of immunofluorescent images.

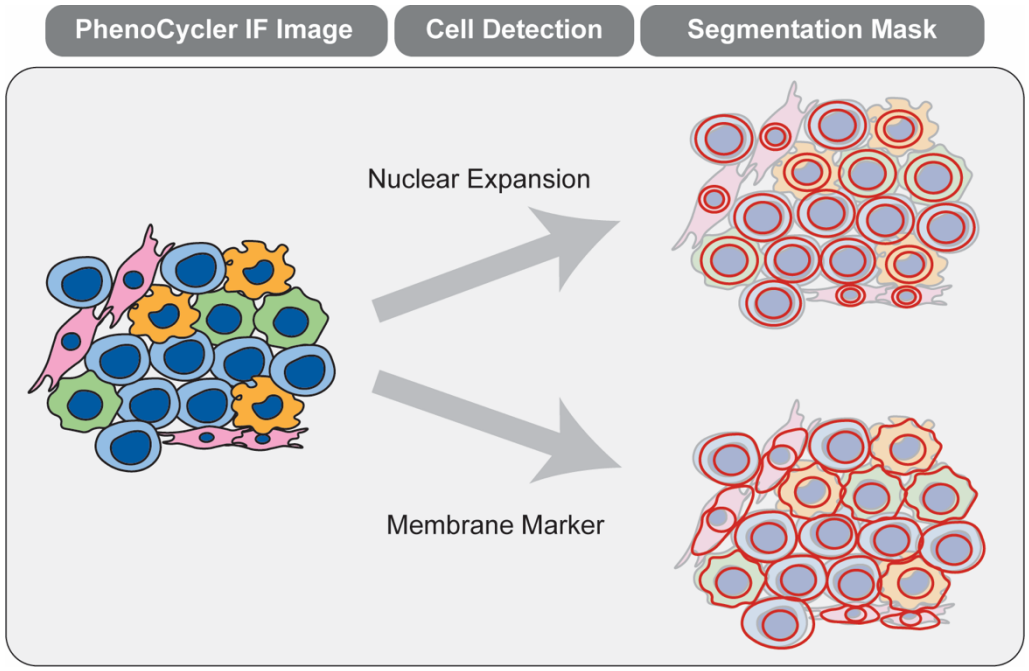


**Figure 4.1: Cell Segmentation by nuclear expansion versus membrane marker expression.**
Schematic demonstrating the different segmentation outcomes when nuclear expansion versus membrane marker-based segmentation is used on the same hypothetical image. Nuclear expansion fails to correctly delineate the borders of irregularly shaped cells.

To use membrane-based segmentation, the selection of a marker which uniformly stains the membranes of different cell types is a critical step. In unpublished data, we have observed drastically different staining patterns of the membrane markers NaK-ATPase, β-actin, and β-catenin in the different cell types within tissues such as liver, heart, colon, and skin. While this has not been a problem in DLBCL tissues that are primarily composed of immune cells, it is still an important consideration when designing PhenoCycler imaging panels. Different membrane markers must be screened to determine the one with the most uniform staining across the tissue. Alternatively, newer cell segmentation methods, such as RAMCES and InstanSeg, have demonstrated that

utilizing multiple different membrane markers within the same tissue can increase the fidelity of cell segmentation for different cell types within the same tissue (155, 156).

### *4.2.3 Cell Classification*

In Chapter 2, cells were classified by manually annotating the different cell types found within representative training images, then using an Artificial Neural Networks (ANN)-based machine learning algorithm to apply these cell classifications across entire tissue cores. In Chapter 3, cells were classified by using unsupervised clustering. In both cases, cells were identified with high accuracy.

The supervised learning approach requires knowledge of different cell types within the TME for accurate cell classification. However, as the user's existing knowledge is being leveraged to train the ANN model, classification tends to closely align with known biological cell types. Moreover, the approach described in Chapter 2 does not require the use of coding languages, such as Python or R, and is therefore accessible to scientists of different academic backgrounds. Despite these strengths, the accuracy of classification depends heavily on the breadth and quality of the manually annotated training set. If the annotated images do not include a wide range of cell types and tissue architectures, the model may not generalize well to an entire tissue. For instance, in Chapter 3, PhenoCycler imaging was performed on tissues from more than 30 different DLBCL patients. In this scenario, it is challenging to select representative regions from a subset of patients which will generalize well across the entire cohort. Moreover, manual annotation is subject to user bias and error. Mislabeling in the training set can misguide the algorithm, potentially leading to systematic errors in the classifications.

Unsupervised clustering, on the other hand, removes bias, as it is data driven. Cells are grouped into clusters based on similarities in marker expression profiles, and clusters are then manually annotated to identify different cell types. As cell types are discovered based exclusively on data patterns, unsupervised clustering can identify rare cell phenotypes within tissues. However, unsupervised clustering carries the risk of over-clustering or under-clustering, which can respectively result in the labelling of false cell types or can miss biologically relevant distinctions.

Ultimately, the choice between these methods depends on the research questions that are being asked. Critically, many research questions may be answered without the need for highly multiplexed spatial imaging, so the definition of a specific and narrow hypothesis should be an initial step in experimental design. The broad classification of different cell types within the TME of different tumour types in Chapter 2 benefited from a supervised, knowledge-based approach, while Chapter 3's higher-plex and more detailed subclassification of tumor and immune cells in multiple different patients was better suited to the granularity of unsupervised clustering. Whichever method is chosen, the classification results should closely align with visual inspection, ensuring that the results reflect the biological reality of the tissue. Together, these methods offer complementary approaches for understanding cellular diversity within the TME, enabling a contextually supported analysis of tumor biology, not only for DLBCL, but for other various cancer types.

## 4.3 Mouse Modelling to Study the DLBCL TME

### *4.3.1 Spatiotemporal TME Evolution*

In Chapter 2, the Eμ-Myc and A20 syngeneic murine models of lymphoma were employed, and PhenoCycler tumour imaging was performed on both these tissue types from a single time point in disease: at humane endpoint, when tumour volume is sufficient to induce distress in the mouse. However, in Chapter 3, Eμ-Myc mSTAT6$^{WT}$ and mSTAT6$^{D419N}$ tumours were spatially profiled over the course of disease development, with timepoints from early-, mid-, late- and relapsed-disease. The approach used in Chapter 3 demonstrated that the prevalence and spatial organization of the non-tumour cellular components of the TME evolve alongside the tumour.

We observed that lymphoid cells, including CD8+ T cells, CD4+ T cells and Tregs, are excluded from Eμ-Myc tumours at late disease, while the stromal compartment, including fibroblasts and endothelial cells, is expanded. Additionally, at disease relapse, we observed that CD4+ T cells were further decreased in prevalence as compared to treatment naïve endpoint tumours. The stromal compartment of solid tumours is known to provide structural support for the expanding tumor mass, but can further function to contribute to an immunosuppressive environment by creating physical and molecular barriers to immune cell infiltration (157). Thus, early in disease progression, the tumor may be relatively more accessible to immune cells, but as the tumor advances, it establishes a more fortified microenvironment that minimizes immune cell infiltration (113, 158, 159). Moreover, the progressive depletion of CD4+ T cells from mid-disease to disease relapse could be reflective of their physical exclusion from the TME but could further be a result of the selective pressure exerted by doxorubicin treatment, leading to

a depleted microenvironment that is even less responsive to immune surveillance. These results mimic early reports from human DLBCL data, which suggests that the TME becomes more “immune cold” at disease relapse (160).

These results emphasize the importance of selecting an appropriate endpoint for experiments that examine immune and stromal spatial dynamics in the TME. Our findings in Eμ-Myc show how the TME can shift from an “immune-responsive” to an “immune-evasive” state over time, in a way that single-timepoint analyses might miss. By capturing the TME at multiple timepoints, we can discern the sequential alterations in cellular composition and spatial interactions that influence disease progression and therapeutic response.

### *4.3.2 Immunocompetent Mouse Models and Genetic Diversity*

Immunocompetent mouse models are essential for studying the TME, as they retain a fully functional immune system, allowing for investigations centered around the interactions between immune cells and tumour cells, which are known to be vital to disease progression and therapeutic response. Indeed, in our previous *in vitro* work, we found that $STAT6^{D419}$-mutant tumour cells did not have altered sensitivity to any of the individual components of R-CHOP (52). Therefore, we predicted that if differences in therapeutic sensitivity were present between $STAT6^{WT}$ and $STAT^{D419N}$ tumours, an intact TME would be required in order for these differences to be apparent. This was indeed the case, as $mSTAT6^{D419N}$-Eμ-Myc tumours *in vivo* demonstrated significant resistance to doxorubicin treatment, which could be reversed using treatment with a small molecule inhibitor of CCR4, which functioned to reduce CD4+ T cell infiltration into the TME.

However, syngeneic immunocompetent mouse models lack genetic diversity, and do not demonstrate the stepwise accumulation of oncogenic mutations that are characteristic of human tumourigenesis. To this point, intratumoural heterogeneity in DLBCL is hypothesized to underlie intrinsic and acquired resistance to therapy, and the study of clonal rrDLBCL genetic alterations is how STAT6$^{D419}$ mutations were identified in the first place (45). Indeed, STAT6$^{D419}$-mutations in human DLBCL have thus far only been identified in GCB/EZB tumours, suggesting that STAT6-GOF may provide a selective survival advantage specifically in the context of this DLCBL tumour type. Therefore, to better understand microenvironmental dynamics in STAT6$^{D419}$-mutant rrDLBCL, alternate mouse models with increased genetic diversity could be explored.

Discussed below are mouse models that could be used to further study STAT6$^{D419}$-mutant DLBCL.

### *4.3.3 Other Mouse Models Not Employed in this Study*

In 2023, a GEMM with a whole-body STAT6$^{D419N}$ mutation was published (161). This mouse model was used to investigate the role of STAT6-GOF in dermatitis and eosinophilic inflammation, as germline heterozygous STAT6$^{D419}$-mutations have been recorded in families with early-onset allergic disease (149, 150). It was found that homo- and heterozygous STAT6$^{D419N}$ mice displayed phenotypes associated with heightened eosinophilic responses and skin inflammation, consistent with STAT6's role in amplifying immune signaling pathways. It has not yet been reported if these mice have developed spontaneous lymphoma-like malignancies. However, if these mice were to develop lymphoma, their tumour cells would present an attractive opportunity for the development a new model of syngeneic DLBCL. In this scenario, the STAT6$^{D419N}$ tumour cells would

demonstrate the accumulation of mutations that are required to result in malignant transformation. Therefore, these tumour cells would be a better representation of human DLBCL genetic diversity. Murine STAT6$^{D419N}$ tumour cells could be maintained ex vivo and could be re-implanted into WT mice, where they could be used to study tumour immune cell infiltration and therapeutic responses. The additional advantage of this model would be that the tumour cells contain the STAT6$^{D419N}$ mutation, while the host would express STAT6$^{WT}$, which is what is seen in most cases of STAT6$^{D419}$-mutant rrDLBCL.

Similarly, a tumour biopsy from a STAT6$^{D419}$-mutant DLBCL patient could be used to develop a novel PDX model. As with other PDX models, it would be predicted that a STAT6$^{D419}$-mutant PDX would maintain the genetic characteristics and therapeutic vulnerabilities of human STAT6$^{D419}$-mutant DLBCL (90, 91). However, as discussed in Chapter 1, PDX models are typically used with immunocompromised mice, thereby critically impeding the ability to study tumour-host interactions. Moreover, both the GEMM-derived tumor model discussed above and a STAT6$^{D419}$-mutant PDX model would rely on fresh tumor material, which may or may not engraft and propagate effectively in the host mouse. For these reasons, a STAT6$^{D419}$-mutant PDX model is likely unfeasible.

The most practical approach, albeit time-consuming, would be the development of a new GEMM of STAT6$^{D419N}$ lymphoma, by putting the STAT6$^{D419N}$ mutant allele under the control of a B cell specific promoter/ enhancer, such as Eu, Iu, or Vav. This strategy would restrict STAT6$^{D419N}$ expression to B cells but would still require the additional accumulation of mutations for malignant transformation. Moreover, this mouse could be crossed with other GEMMs of the EZB subtype, to potentially accelerate lymphomagenesis, but to also more faithfully model the genetic diversity in human

STAT6$^{D419-}$mutant DLBCL. Such a GEMM would facilitate investigations into the role of STAT6$^{D419N}$ in B cell transformation, tumor progression, and therapeutic resistance, offering a robust, immune-competent model for studying rrDLBCL in a controlled genetic and immunologic context.

## 4.4 CCR4 as a Therapeutic Target in STAT6-mutant rrDLBCL

### *4.4.1 CCR4 Inhibitors*

In Chapter 3, the small-molecule CCR4 inhibitor AZD2098 (162) was used to reverse STAT6$^{D419N}$-mediated doxorubicin resistance. CCR4 is a G protein-coupled receptor (GPCR) with CCL17 and CCL22 (aka TARC and MDC) acting as its major agonists. These two chemokines have different binding affinity for CCR4, with CCL17 showing lower binding affinity for CCR4 and the ability to interact with CCR4 in its major conformation, and CCL22 showing higher binding affinity and the ability to interact with both the major and minor conformation (163, 164). Upon binding of either chemokine, downstream β-arrestin signaling through p38 and rho-associated protein kinase (ROCK) is responsible for inducing T cell migration (165). Inhibiting CCR4 prevents various immune cells from undergoing CCL17/ 22 -dependent migration to sites of inflammation.

In previous studies, inhibition of the CCR4/ CCL17 axis has been suggested for the treatment of diseases driven by excessive Th2 responses, such as asthma and atopic dermatitis (166, 167). In cancer, CCL17 has been shown to promote tumour cell proliferation and metastasis (168-170). Moreover, CCL17 was demonstrated to induce the transformation of human keratinocytes into cutaneous squamous cell carcinoma (171). Beyond the effect of CCL17 on the tumour cell compartment, it has also been

shown to modulate the TME through recruitment of Tregs that inhibit CD8+ T cell cytotoxic responses (172, 173).

It has only been in recent years where CCR4 inhibition has been considered for the treatment of hematological malignancies. The use of the FDA-approved monoclonal antibody, Mogamulizumab, is discussed below.

*4.4.2 Mogamulizumab for CTCL and DLBCL*

Mogamulizumab (aka Poteligeo) is approved for the treatment of relapsed or refractory CTCL and certain adult T cell leukemias/lymphomas (ATLL), where malignant T cells overexpress CCR4. The mechanism of action is via the binding of Mogamulizumab to CCR4, facilitating antibody-dependent cellular cytotoxicity (ADCC) of CCR4-expressing tumour cells (174). Beyond direct cytotoxicity to tumour cells, depletion of CCR4-expressing Tregs also reduces immune suppression in the TME, potentially allowing for anti-tumor immune responses to become more effective (175). Indeed, in clinical trials, Mogamulizumab demonstrated a significant therapeutic benefit over standard therapies, leading to its approval as a second-line treatment for relapsed or refractory CTCL (174, 176).

In DLBCL, Mogamulizumab is still under investigation, particularly for NOS-DLBCLs, where the tumour cells themselves express higher levels of CCR4 (177). However, the main rationale of Mogamulizumab for DLBCL treatment is to disrupt the recruitment and accumulation of immunosuppressive and anti-inflammatory cells, such as Tregs and Th2 cells, in the TME, potentially sensitizing the tumour to ICI (178). As such, targeting the TME through T cell functional modulation represents a novel angle for treating R-CHOP resistant cases of DLBCL. In an early-phase clinical trial,

Mogamulizumab in combination with Pembrolizumab showed promise in improving immune activation and reducing tumour progression in DLBCL (179). However, adverse events were significant, and the trial was discontinued.

In our study, while we found that AZD2098 reduced Th2 infiltration in the Eμ-Myc TME, we also found that Th1 cells were reduced by AZD2098, specifically in Eμ-Myc mSTAT6$^{D419N}$ tumours. These findings highlight the complexity of targeting CCR4 as a TME-modulating agent, as our results show that the tumour genotype has a distinct impact of the outcome of CCR4-inhibitor treatment. While Th1 cells are typically considered to be central to anti-tumour immune responses, our results instead imply that CCR4+ Th1 cells in Eμ-Myc-mSTAT6$^{D419N}$ tumours support tumour-promoting inflammation, and that their depletion leads to improved sensitivity to doxorubicin. Future studies might further examine if CCR4+ Th1 cells are functionally distinct from CCR4- Th1 cells, and how they differentially impact tumour progression. If Mogamulizumab were to be tested for the treatment of STAT6$^{D419}$-mutant lymphoma, these studies would be critical for contextualizing the expected anti-tumour immune responses.

### *4.4.3 Other Therapeutic Targets for STAT6$^{D419}$-DLBCL*

In Chapter 3, AZD2098 was used to therapeutically target mSTAT6$^{D419N}$-Eμ-Myc tumours, as we aimed to investigate if the observed doxorubicin resistance was attributable to changes in the TME. Therefore, we chose to therapeutically target a protein that was present on cells of the TME, rather than a protein with enhanced expression in the STAT6$^{D419N}$ tumour cells themselves. To this end, various other strategies, which specifically target enhanced STAT6 signaling in the tumour cell, could be explored to treat STAT6$^{D419}$-mutant rrDLBCL (**Figure 4.2**).

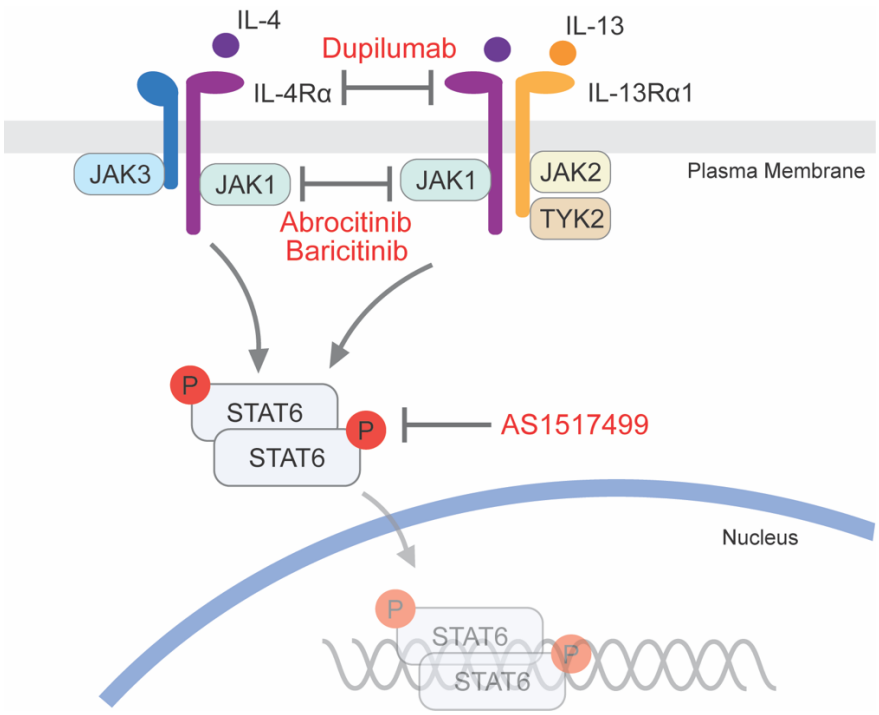


**Figure 4.2: Alternate therapeutic targets for STAT6$^{D419}$-mutant DLBCL.**
Schematic demonstrating the different therapeutic targets for STAT6$^{D419}$-mutant DLBCL. IL-4Ra and JAK inhibitors are both FDA approved for various disease. STAT6 inhibitors are currently in clinical testing.

The first potential therapeutic target is IL-4Ra, which is the IL-4 receptor subunit that is required for both IL-4- and IL-13-dependent STAT6 activation. In our previous study, we demonstrated that STAT6 phosphorylation in STAT6$^{D419}$-mutant tumour cells is dependent on IL-4 or IL-13 stimulation (52). Thus, inhibiting the signaling of IL-4/13 through their common receptor has the potential to block oncogenic STAT6 activation in STAT6$^{D419}$-mutant tumour cells. Dupilumab, an FDA-approved monoclonal antibody against IL-4Rα used in allergic diseases and asthma, could theoretically attenuate STAT6 signaling in DLBCL. This reduction in STAT6 activity may decrease proliferation and

survival signals within the tumour cells and potentially resensitize them to therapies like R-CHOP.

Similarly, JAK1 inhibitors could be used to the same effect. Following IL-4/13 binding to their receptors, JAK1 is the next downstream protein that is activated, which functions to induce STAT6 phosphorylation. Various JAK1 inhibitors have been developed and FDA approved, such as Abrocitinib and Baricitinib. Similarly, various other less specific JAK inhibitors function to inhibit JAK2 or JAK3 in addition to JAK1, such as Ruxolitinib and Tofacitinib. By inhibiting JAK1, JAK-inhibitors could effectively reduce STAT6 activation, potentially reversing the pathological effects of $STAT6^{D419}$ mutations in DLBCL.

While there are currently no FDA-approved therapeutics, the continued development of direct STAT6 inhibitors could offer another therapeutic option specifically designed to treat tumours harboring GOF mutations in STAT6. The small molecule STAT6 inhibitor AS1517499 has been used in *in vitro* and *in vivo* research to study diverse diseases such as asthma, renal and lung fibrosis, breast cancer, and colon cancer (180-184). In these studies, AS1517499 has proven to inhibit STAT6 phosphorylation, modulate immune responses, and ameliorate disease.

Finally, we have provided compelling evidence that $STAT6^{D419}$-mutations in rrDLBCL function to remodel the TME, favouring the expansion of the CD4+ T cell compartment. Thus, it is appealing to speculate that $STAT6^{D419}$-mutant rrDLBCL may be uniquely sensitive to therapeutics that reinvigorate T cell responses in the TME, such as ICIs. STAT6 GOF mutations are known to promote a pro-inflammatory, T cell-enriched TME, creating a potential context where immune modulation could effectively counter tumour immune evasion mechanisms. In support of this idea, evidence from other tumour models

suggests that blocking STAT6 signaling can reverse immunosuppressive conditions within the TME (185), further highlighting the potential efficacy of ICIs in STAT6$^{D419}$-mutant rrDLBCL.

## 4.5 Future Directions

### *4.5.1 Spatiotemporal Profiling of A20 Murine Lymphoma*

In Chapter 2, the A20 model of murine B cell lymphoma was introduced and utilized, but in Chapter 3, only Eμ-Myc was used to investigate STAT6$^{D419N}$-mediated TME remodelling. Therefore, STAT6 mutations could be introduced into A20 tumour cells, and the experiments in Chapter 3 could be repeated. This would provide an exciting opportunity confirm our previous results or identify alternate mechanisms of STAT6 GOF intrinsic tumour growth or impact on the TME.

However, the more exciting outstanding research questions surrounding the A20 tumour model relate to spatiotemporal and organotrophic growth. Specifically, a future experiment could perform PhenoCycler imaging of A20 tumours across different organs at different stages of disease development. In this experiment, we could map cellular composition and spatial organization of A20 tumours, including immune and stromal cell interactions, to capture organ-specific TME adaptations that may support or inhibit tumor growth.

This experiment would reveal how site-specific factors shape immune responses within the TME across disease stages, potentially identifying regional differences in immune cell recruitment, activation, and polarization. If such differences were found, novel opportunities for therapeutic targeting could be proposed. These results would be

highly translatable to the human DLBCL population, as 30% of DLBCL patients have extranodal disease.

### *4.5.2 Non-CD4 Components of the STAT6$^{D419N}$ TME*

Chapter 3 largely focused on CD4+ T cell expansion in the STAT6$^{D419N}$ TME. However, chemokine profiling showed that much is different in mSTAT6$^{D419N}$ tumours as compared to mSTAT6$^{WT}$ tumours. Future experiments could extend the focus on STAT6$^{D419N}$-driven changes within the TME to explore the roles of myeloid cells, which were largely underexamined in current studies. Given the influence of STAT6$^{D419N}$ on TME composition via CCL17-mediated CD4+ T cell recruitment, it is plausible that this signaling pathway also affects myeloid populations, either directly or through secondary interactions. Myeloid cells, such as macrophages, dendritic cells, and myeloid-derived suppressor cells (MDSCs), are integral to immune modulation in the TME, influencing tumour growth, immune cell recruitment, and therapeutic resistance. Profiling myeloid cell populations in the STAT6$^{D419N}$ TME, including their abundance, phenotypes, and spatial organization relative to CD4+ T cells, would provide insights into how STAT6$^{D419N}$ mutations reshape the broader immune landscape and uncover any compensatory or synergistic effects with T cell recruitment.

### *4.5.3 Mechanism of STAT6$^{D419}$-mutant-mediated Therapeutic Resistance*

One major outstanding question related to STAT6$^{D419N}$-mediated TME remodelling is the specific mechanism of action whereby CCR4+ Th1 cells engender doxorubicin resistance. While we demonstrate that mSTAT6$^{D419N}$ tumour cells isolated from the TME have increased evidence of inflammation, this does not directly show if and how CCR4+ Th1 cells play a role.

To explore the mechanisms by which CCR4+ Th1 cells contribute to doxorubicin resistance in STAT6$^{D419N}$ tumours, future experiments could focus on the functional properties of Th1 cells within the TME and their interactions with tumour cells. One approach would be to preform single cell RNA sequencing (scRNAseq) of the cells in the mSTAT6$^{WT}$ and mSTAT6$^{D419N}$ TME, to determine if the phenotypes of different CD4+ T cell types differ between these two tumour types. This experiment could potentially identify a TME-signature that is associated with doxorubicin resistance that could be validated in other publicly available human and murine scRNAseq datasets. Another approach would be to isolate CCR4+ Th1 cells from the TME of mSTAT6$^{D419N}$ and mSTAT6$^{WT}$ Eμ-Myc tumours and develop a co-culture with tumour cells *in vitro*. RNAseq could be performed to specifically determine whether these cells are responsible for inducing the inflammatory signature that was observed in mSTAT6$^{D419N}$ tumour cells *in vivo.* Moreover, the addition of doxorubicin to these co-cultures could reveal if interactions between Th1 cells and tumour cells confer resistance by enhancing survival signals or potentially by limiting doxorubicin uptake.

### *4.5.4 The TME of Diagnostic versus Relapsed DLBCL*

In Chapter 3, we are the first team to report spatial immunophenotyping of the human DLBCL TME using samples obtained at disease relapse. However, due to the focused research questions that were being addressed, the full characterization of this human PhenoCycler dataset is not fully realized. The acquired PhenoCycler dataset can be leveraged to gain further insight into the progression of DLBCL, by performing future experiments wherein PhenoCycler imaging of human DLBCL tissues at diagnosis could be done, to compare the spatial organization of the TME at diagnosis versus relapse.

By profiling immune and stromal cell populations at both diagnosis and relapse, it will be possible to describe novel changes in cell abundance, spatial distribution, and cellular interactions that emerge as disease advances. Spatial profiling of immune cell subsets, such as T cells, macrophages, and DCs, will identify any shifts in localization relative to tumour cells, stromal cells, and other immune cells that could influence their overall function. Tracking these alterations from initial diagnosis to relapse, in matched patient samples if possible, will provide a clear picture of how the TME evolves under therapeutic pressure and will identify cellular patterns associated with treatment resistance. These analyses would not only provide insights into the cellular dynamics driving rrDLBCL but could also help identify biomarkers predictive of relapse and position researchers to suggest potential therapeutic targets that pre-empt or counteract these changes.

## 4.6 Concluding Summary

The detailed objectives of this thesis were defined as follows:

1. To develop tools and analytical techniques to study the tumour microenvironment of both murine and human lymphoma.
2. To determine how different mouse models of lymphoma differ in their microenvironmental composition and spatial organization.
3. To determine if mouse-modelling of $STAT6^{D419}$-mutant lymphoma faithfully recapitulates critical features of human disease.
4. To investigate mechanisms of $STAT6^{D419}$-mediated microenvironmental remodelling.

5. To identify novel therapeutic strategies for STAT6$^{D419}$ mutant rrDLBCL.
6. To define the microenvironmental composition and spatial organization of rrDLBCL, with a specific focus on STAT6$^{D419}$-mutant patients.

The aims of this thesis were addressed as follows:

1. In Chapter 2, a custom 16-plex PhenoCycler panel was developed and utilized to study the TME of various murine cancers. In Chapter 3, this panel was extended to 35-plex, allowing for deeper analysis of cell state and activation status in the context of STAT6$^{D419N}$-mutation. Moreover, a 52-plex PhenoCycler panel was used to phenotype the TME of human rrDLBCL. Of note, we are the first to develop panels and report successful PhenoCycler imaging of murine FFPE tissues. We are also the first to perform PhenoCycler imaging on human rrDLBCL biopsies.
2. Chapter 2 demonstrated that the A20 and Eμ-Myc murine lymphoma tumour models have distinct differences in immune cell composition and spatial organization, with A20 having increased expression of lymphoid cells and increased interactions between immune cells of the TME, and Eμ-Myc tumours having a relatively expanded stromal compartment and depletions in a number of cell-cell interactions. These results highlight how these two models can be used to answer different research questions related to the DLBCL TME.
3. In Chapter 3, Eμ-Myc mSTAT6$^{D419N}$ tumours were found to faithfully recapitulate human STAT6$^{D419}$-mutant rrDLBCL tumours, with increased expression of phospho-STAT6, increased invasion of CD4+ T cells, and resistance to doxorubicin treatment. This mouse model represents a powerful tool to identify and

screen therapeutics that could specifically be used to treat STAT6$^{D419}$-mutant rrDLBCL patients.

4. Mechanistically, Chapter 3 demonstrated that STAT6$^{D419N}$ tumour cells remodel the TME via increased secretion of CCL17, leading to increased recruitment of CCR4 expressing CD4+ T cells. The CCR4+ CD4+ T cells are predominantly polarized towards a Th1-like state, leading to evidence of enhanced inflammation in the mSTAT6$^{D419N}$ TME. Tumour inflammation is associated with resistance to chemotherapy, thereby identifying a potential rationale for why STAT6$^{D419}$-mutant tumour cells are identified specifically at DLBCL relapse.
5. Chapter 3 demonstrated that STAT6$^{D419N}$ tumours can be resensitized to doxorubicin by blocking CCL17-mediated CD4+ T cell recruitment to the TME using a small molecule inhibitor of CCR4, AZD2098. Critically, the CCR4-targeted monoclonal antibody Mogamulizumab is FDA-approved for other hematological malignancies, demonstrating the direct clinical relevance of these findings.
6. The final figure of Chapter 3 demonstrated that human STAT6$^{D419}$-mutant rrDLBCL samples have increased tumour cell expression of phospho-STAT6 and CCL17, and that CD4+ T cells in STAT6$^{D419}$-mutant rrDLBCL also have increased expression of CCR4. Thus, our novel findings using a murine model of lymphoma are directly relevant to the human rrDLBCL population, and successfully identified a therapeutically actionable axis for the treatment of a subset of rrDLBCL patients.

## References for Chapters 1 and 4


1. Brenner DR, Gillis J, Demers AA, Ellison LF, Billette JM, Zhang SX, et al. Projected estimates of cancer in Canada in 2024. Cmaj. 2024;196(18):E615-e23.
2. Sung H, Ferlay J, Siegel RL, Laversanne M, Soerjomataram I, Jemal A, Bray F. Global Cancer Statistics 2020: GLOBOCAN Estimates of Incidence and Mortality Worldwide for 36 Cancers in 185 Countries. CA Cancer J Clin. 2021;71(3):209-49.
3. Hardy RR, Carmack CE, Shinton SA, Kemp JD, Hayakawa K. Resolution and characterization of pro-B and pre-pro-B cell stages in normal mouse bone marrow. J Exp Med. 1991;173(5):1213-25.
4. Hardy RR, Hayakawa K, Haaijman J, Herzenberg LA. B-cell subpopulations identified by two-colour fluorescence analysis. Nature. 1982;297(5867):589-91.
5. Bassing CH, Swat W, Alt FW. The mechanism and regulation of chromosomal V(D)J recombination. Cell. 2002;109 Suppl:S45-55.
6. Mårtensson IL, Keenan RA, Licence S. The pre-B-cell receptor. Curr Opin Immunol. 2007;19(2):137-42.
7. Lanzavecchia A. Antigen-specific interaction between T and B cells. Nature. 1985;314(6011):537-9.
8. Kerfoot SM, Yaari G, Patel JR, Johnson KL, Gonzalez DG, Kleinstein SH, Haberman AM. Germinal center B cell and T follicular helper cell development initiates in the interfollicular zone. Immunity. 2011;34(6):947-60.
9. Okada T, Miller MJ, Parker I, Krummel MF, Neighbors M, Hartley SB, et al. Antigen-engaged B cells undergo chemotaxis toward the T zone and form motile conjugates with helper T cells. PLoS Biol. 2005;3(6):e150.
10. Muramatsu M, Kinoshita K, Fagarasan S, Yamada S, Shinkai Y, Honjo T. Class switch recombination and hypermutation require activation-induced cytidine deaminase (AID), a potential RNA editing enzyme. Cell. 2000;102(5):553-63.
11. Victora GD, Schwickert TA, Fooksman DR, Kamphorst AO, Meyer-Hermann M, Dustin ML, Nussenzweig MC. Germinal center dynamics revealed by multiphoton microscopy with a photoactivatable fluorescent reporter. Cell. 2010;143(4):592-605.
12. Allen CD, Okada T, Tang HL, Cyster JG. Imaging of germinal center selection events during affinity maturation. Science. 2007;315(5811):528-31.
13. Nutt SL, Tarlinton DM. Germinal center B and follicular helper T cells: siblings, cousins or just good friends? Nature Immunology. 2011;12(6):472-7.
14. Tas JMJ, Mesin L, Pasqual G, Targ S, Jacobsen JT, Mano YM, et al. Visualizing antibody affinity maturation in germinal centers. Science. 2016;351(6277):1048-54.
15. Xu Z, Zan H, Pone EJ, Mai T, Casali P. Immunoglobulin class-switch DNA recombination: induction, targeting and beyond. Nat Rev Immunol. 2012;12(7):517-31.
16. Deenick EK, Hasbold J, Hodgkin PD. Decision criteria for resolving isotype switching conflicts by B cells. Eur J Immunol. 2005;35(10):2949-55.
17. Laidlaw BJ, Cyster JG. Transcriptional regulation of memory B cell differentiation. Nat Rev Immunol. 2021;21(4):209-20.
18. Srinivasan L, Sasaki Y, Calado DP, Zhang B, Paik JH, DePinho RA, et al. PI3 kinase signals BCR-dependent mature B cell survival. Cell. 2009;139(3):573-86.

19. Fornek JL, Tygrett LT, Waldschmidt TJ, Poli V, Rickert RC, Kansas GS. Critical role for Stat3 in T-dependent terminal differentiation of IgG B cells. Blood. 2006;107(3):1085-91.
20. Khiem D, Cyster JG, Schwarz JJ, Black BL. A p38 MAPK-MEF2C pathway regulates B-cell proliferation. Proceedings of the National Academy of Sciences. 2008;105(44):17067-72.
21. Hanahan D. Hallmarks of Cancer: New Dimensions. Cancer Discov. 2022;12(1):31-46.
22. Mlynarczyk C, Fontán L, Melnick A. Germinal center-derived lymphomas: The darkest side of humoral immunity. Immunol Rev. 2019;288(1):214-39.
23. De Silva NS, Klein U. Dynamics of B cells in germinal centres. Nature Reviews Immunology. 2015;15(3):137-48.
24. de Miranda NF, Peng R, Georgiou K, Wu C, Falk Sörqvist E, Berglund M, et al. DNA repair genes are selectively mutated in diffuse large B cell lymphomas. J Exp Med. 2013;210(9):1729-42.
25. Neuberger MS, Rada C. Somatic hypermutation: activation-induced deaminase for C/G followed by polymerase eta for A/T. J Exp Med. 2007;204(1):7-10.
26. Delbos F, De Smet A, Faili A, Aoufouchi S, Weill JC, Reynaud CA. Contribution of DNA polymerase eta to immunoglobulin gene hypermutation in the mouse. J Exp Med. 2005;201(8):1191-6.
27. Phan RT, Saito M, Basso K, Niu H, Dalla-Favera R. BCL6 interacts with the transcription factor Miz-1 to suppress the cyclin-dependent kinase inhibitor p21 and cell cycle arrest in germinal center B cells. Nat Immunol. 2005;6(10):1054-60.
28. Phan RT, Dalla-Favera R. The BCL6 proto-oncogene suppresses p53 expression in germinal-centre B cells. Nature. 2004;432(7017):635-9.
29. Phan RT, Saito M, Kitagawa Y, Means AR, Dalla-Favera R. Genotoxic stress regulates expression of the proto-oncogene Bcl6 in germinal center B cells. Nat Immunol. 2007;8(10):1132-9.
30. Chen ST, Oliveira TY, Gazumyan A, Cipolla M, Nussenzweig MC. B cell receptor signaling in germinal centers prolongs survival and primes B cells for selection. Immunity. 2023;56(3):547-61.e7.
31. Xie Y, Pittaluga S, Jaffe ES. The histological classification of diffuse large B-cell lymphomas. Semin Hematol. 2015;52(2):57-66.
32. Barrington SF, Mikhaeel NG, Kostakoglu L, Meignan M, Hutchings M, Müeller SP, et al. Role of imaging in the staging and response assessment of lymphoma: consensus of the International Conference on Malignant Lymphomas Imaging Working Group. J Clin Oncol. 2014;32(27):3048-58.
33. Tilly H, Gomes da Silva M, Vitolo U, Jack A, Meignan M, Lopez-Guillermo A, et al. Diffuse large B-cell lymphoma (DLBCL): ESMO Clinical Practice Guidelines for diagnosis, treatment and follow-up. Ann Oncol. 2015;26 Suppl 5:v116-25.
34. Sehn LH, Salles G. Diffuse Large B-Cell Lymphoma. N Engl J Med. 2021;384(9):842-58.
35. Schmitz N, Nickelsen M, Ziepert M, Haenel M, Borchmann P, Schmidt C, et al. Conventional chemotherapy (CHOEP-14) with rituximab or high-dose chemotherapy (MegaCHOEP) with rituximab for young, high-risk patients with aggressive B-cell

lymphoma: an open-label, randomised, phase 3 trial (DSHNHL 2002-1). Lancet Oncol. 2012;13(12):1250-9.
36. Cunningham D, Hawkes EA, Jack A, Qian W, Smith P, Mouncey P, et al. Rituximab plus cyclophosphamide, doxorubicin, vincristine, and prednisolone in patients with newly diagnosed diffuse large B-cell non-Hodgkin lymphoma: a phase 3 comparison of dose intensification with 14-day versus 21-day cycles. Lancet. 2013;381(9880):1817-26.
37. Tilly H, Morschhauser F, Sehn Laurie H, Friedberg Jonathan W, Trněný M, Sharman Jeff P, et al. Polatuzumab Vedotin in Previously Untreated Diffuse Large B-Cell Lymphoma. New England Journal of Medicine. 2022;386(4):351-63.
38. Younes A, Sehn LH, Johnson P, Zinzani PL, Hong X, Zhu J, et al. Randomized Phase III Trial of Ibrutinib and Rituximab Plus Cyclophosphamide, Doxorubicin, Vincristine, and Prednisone in Non-Germinal Center B-Cell Diffuse Large B-Cell Lymphoma. J Clin Oncol. 2019;37(15):1285-95.
39. Morschhauser F, Feugier P, Flinn IW, Gasiorowski R, Greil R, Illés Á, et al. A phase 2 study of venetoclax plus R-CHOP as first-line treatment for patients with diffuse large B-cell lymphoma. Blood. 2021;137(5):600-9.
40. Moccia AA, Hitz F, Hoskins P, Klasa R, Power MM, Savage KJ, et al. Gemcitabine, dexamethasone, and cisplatin (GDP) is an effective and well-tolerated salvage therapy for relapsed/refractory diffuse large B-cell lymphoma and Hodgkin lymphoma. Leuk Lymphoma. 2017;58(2):324-32.
41. Crump M, Neelapu SS, Farooq U, Van Den Neste E, Kuruvilla J, Westin J, et al. Outcomes in refractory diffuse large B-cell lymphoma: results from the international SCHOLAR-1 study. Blood. 2017;130(16):1800-8.
42. Al-Mansour M, Al-Foheidi M, Ibrahim E. Efficacy and safety of second-generation CAR T-cell therapy in diffuse large B-cell lymphoma: A meta-analysis. Mol Clin Oncol. 2020;13(4):33.
43. Westin Jason R, Oluwole Olalekan O, Kersten Marie J, Miklos David B, Perales M-A, Ghobadi A, et al. Survival with Axicabtagene Ciloleucel in Large B-Cell Lymphoma. New England Journal of Medicine. 2023;389(2):148-57.
44. Kamdar M, Solomon SR, Arnason J, Johnston PB, Glass B, Bachanova V, et al. Lisocabtagene maraleucel versus standard of care with salvage chemotherapy followed by autologous stem cell transplantation as second-line treatment in patients with relapsed or refractory large B-cell lymphoma (TRANSFORM): results from an interim analysis of an open-label, randomised, phase 3 trial. The Lancet. 2022;399(10343):2294-308.
45. Morin RD, Assouline S, Alcaide M, Mohajeri A, Johnston RL, Chong L, et al. Genetic Landscapes of Relapsed and Refractory Diffuse Large B-Cell Lymphomas. Clin Cancer Res. 2016;22(9):2290-300.
46. Mareschal S, Dubois S, Viailly P-J, Bertrand P, Bohers E, Maingonnat C, et al. Whole exome sequencing of relapsed/refractory patients expands the repertoire of somatic mutations in diffuse large B-cell lymphoma. Genes, Chromosomes and Cancer. 2016;55(3):251-67.
47. Park HY, Lee SB, Yoo HY, Kim SJ, Kim WS, Kim JI, Ko YH. Whole-exome and transcriptome sequencing of refractory diffuse large B-cell lymphoma. Oncotarget. 2016;7(52):86433-45.

48. Greenawalt DM, Liang WS, Saif S, Johnson J, Todorov P, Dulak A, et al. Comparative analysis of primary versus relapse/refractory DLBCL identifies shifts in mutation spectrum. Oncotarget. 2017;8(59):99237-44.
49. Zhang X, Wu Z, Hao Y, Yu T, Li X, Liang Y, et al. Aberrantly Activated APOBEC3B Is Associated With Mutant p53-Driven Refractory/Relapsed Diffuse Large B-Cell Lymphoma. Front Immunol. 2022;13:888250.
50. Trinh DL, Scott DW, Morin RD, Mendez-Lago M, An J, Jones SJ, et al. Analysis of FOXO1 mutations in diffuse large B-cell lymphoma. Blood. 2013;121(18):3666-74.
51. Arthur SE, Mottok A, Alcaide M, Rushton C, Grande BM, Ennishi D, et al. Functional Investigation of the Gene NFKBIZ and the Impact of 3'UTR Mutations in Diffuse Large B-Cell Lymphoma. Blood. 2017;130:1228.
52. Benoit A, Abraham MJ, Li S, Kim J, Estrada-Tejedor R, Bakadlag R, et al. STAT6 mutations enriched at diffuse large B-cell lymphoma relapse reshape the tumor microenvironment. International Journal of Hematology. 2024.
53. Chan HT, Chin YM, Low SK. Circulating Tumor DNA-Based Genomic Profiling Assays in Adult Solid Tumors for Precision Oncology: Recent Advancements and Future Challenges. Cancers (Basel). 2022;14(13).
54. Rushton CK, Arthur SE, Alcaide M, Cheung M, Jiang A, Coyle KM, et al. Genetic and evolutionary patterns of treatment resistance in relapsed B-cell lymphoma. Blood Adv. 2020;4(13):2886-98.
55. Reddy A, Zhang J, Davis NS, Moffitt AB, Love CL, Waldrop A, et al. Genetic and Functional Drivers of Diffuse Large B Cell Lymphoma. Cell. 2017;171(2):481-94.e15.
56. Alizadeh AA, Eisen MB, Davis RE, Ma C, Lossos IS, Rosenwald A, et al. Distinct types of diffuse large B-cell lymphoma identified by gene expression profiling. Nature. 2000;403(6769):503-11.
57. Hans CP, Weisenburger DD, Greiner TC, Gascoyne RD, Delabie J, Ott G, et al. Confirmation of the molecular classification of diffuse large B-cell lymphoma by immunohistochemistry using a tissue microarray. Blood. 2004;103(1):275-82.
58. Choi WW, Weisenburger DD, Greiner TC, Piris MA, Banham AH, Delabie J, et al. A new immunostain algorithm classifies diffuse large B-cell lymphoma into molecular subtypes with high accuracy. Clin Cancer Res. 2009;15(17):5494-502.
59. Chapuy B, Stewart C, Dunford AJ, Kim J, Kamburov A, Redd RA, et al. Molecular subtypes of diffuse large B cell lymphoma are associated with distinct pathogenic mechanisms and outcomes. Nat Med. 2018;24(5):679-90.
60. Schmitz R, Wright George W, Huang Da W, Johnson Calvin A, Phelan James D, Wang James Q, et al. Genetics and Pathogenesis of Diffuse Large B-Cell Lymphoma. New England Journal of Medicine. 2018;378(15):1396-407.
61. Ennishi D, Jiang A, Boyle M, Collinge B, Grande BM, Ben-Neriah S, et al. Double-Hit Gene Expression Signature Defines a Distinct Subgroup of Germinal Center B-Cell-Like Diffuse Large B-Cell Lymphoma. J Clin Oncol. 2019;37(3):190-201.
62. Wright GW, Huang DW, Phelan JD, Coulibaly ZA, Roulland S, Young RM, et al. A Probabilistic Classification Tool for Genetic Subtypes of Diffuse Large B Cell Lymphoma with Therapeutic Implications. Cancer Cell. 2020;37(4):551-68.e14.

63. Tabatabai A, Arora A, Höfmann S, Jauch M, von Tresckow B, Hansen J, et al. Mouse models of diffuse large B cell lymphoma. Front Immunol. 2023;14:1313371.
64. Egle A, Harris AW, Bath ML, O'Reilly L, Cory S. VavP-Bcl2 transgenic mice develop follicular lymphoma preceded by germinal center hyperplasia. Blood. 2004;103(6):2276-83.
65. Ennishi D, Takata K, Béguelin W, Duns G, Mottok A, Farinha P, et al. Molecular and Genetic Characterization of MHC Deficiency Identifies EZH2 as Therapeutic Target for Enhancing Immune Recognition. Cancer Discovery. 2019;9(4):546-63.
66. Zhang J, Dominguez-Sola D, Hussein S, Lee JE, Holmes AB, Bansal M, et al. Disruption of KMT2D perturbs germinal center B cell development and promotes lymphomagenesis. Nat Med. 2015;21(10):1190-8.
67. Zhang J, Vlasevska S, Wells VA, Nataraj S, Holmes AB, Duval R, et al. The CREBBP Acetyltransferase Is a Haploinsufficient Tumor Suppressor in B-cell Lymphoma. Cancer Discov. 2017;7(3):322-37.
68. Cattoretti G, Pasqualucci L, Ballon G, Tam W, Nandula SV, Shen Q, et al. Deregulated BCL6 expression recapitulates the pathogenesis of human diffuse large B cell lymphomas in mice. Cancer Cell. 2005;7(5):445-55.
69. Knittel G, Liedgens P, Korovkina D, Seeger JM, Al-Baldawi Y, Al-Maarri M, et al. B-cell-specific conditional expression of Myd88p.L252P leads to the development of diffuse large B-cell lymphoma in mice. Blood. 2016;127(22):2732-41.
70. Flümann R, Hansen J, Pelzer BW, Nieper P, Lohmann T, Kisis I, et al. Distinct Genetically Determined Origins of Myd88/BCL2-Driven Aggressive Lymphoma Rationalize Targeted Therapeutic Intervention Strategies. Blood Cancer Discov. 2023;4(1):78-97.
71. Kim KJ, Kanellopoulos-Langevin C, Merwin RM, Sachs DH, Asofsky R. Establishment and characterization of BALB/c lymphoma lines with B cell properties. J Immunol. 1979;122(2):549-54.
72. Kim KJ, Dejoy SQ. Con A induction of IgG secretion from a B-lymphoid tumour cell line, A20. Immunology. 1986;59(1):15-21.
73. Guja K, Liehr T, Rincic M, Kosyakova N, Hussein Azawi SS. Molecular Cytogenetic Characterization Identified the Murine B-Cell Lymphoma Cell Line A-20 as a Model for Sporadic Burkitt's Lymphoma. J Histochem Cytochem. 2017;65(11):669-77.
74. Bascuas T, Moreno M, Mónaco A, Reyes L, Paolino A, Oliver P, et al. A novel non-Hodgkin lymphoma murine model closer to the standard clinical scenario. Journal of Translational Medicine. 2016;14(1):323.
75. Del Rio ML, Perez-Simon JA, Rodriguez-Barbosa JI. Differential Engraftment of Parental A20 PD-L1 WT and PD-L1 KO Leukemia Cells in Semiallogeneic Recipients in the Context of PD-L1/PD-1 Interaction and NK Cell-Mediated Hybrid Resistance. Front Immunol. 2022;13:887348.
76. Gilman KE, Matiatos AP, Cracchiolo MJ, Moon AG, Davini DW, Simpson RJ, Katsanis E. Multiagent Intratumoral Immunotherapy Can Be Effective in A20 Lymphoma Clearance and Generation of Systemic T Cell Immunity. Cancers (Basel). 2023;15(7).
77. Kueberuwa G, Zheng W, Kalaitsidou M, Gilham DE, Hawkins RE. A Syngeneic Mouse B-Cell Lymphoma Model for Pre-Clinical Evaluation of CD19 CAR T Cells. J Vis Exp. 2018(140).

78. Donnou S, Galand C, Touitou V, Sautès-Fridman C, Fabry Z, Fisson S. Murine models of B-cell lymphomas: promising tools for designing cancer therapies. Adv Hematol. 2012;2012:701704.
79. Abraham MJ, Goncalves C, McCallum P, Gupta V, Preston SEJ, Huang F, et al. Tunable PhenoCycler imaging of the murine pre-clinical tumour microenvironments. Cell Biosci. 2024;14(1):19.
80. Donnou S, Galand C, Daussy C, Crozet L, Fridman WH, Sautès-Fridman C, Fisson S. Immune adaptive microenvironment profiles in intracerebral and intrasplenic lymphomas share common characteristics. Clin Exp Immunol. 2011;165(3):329-37.
81. Harris AW, Pinkert CA, Crawford M, Langdon WY, Brinster RL, Adams JM. The E mu-myc transgenic mouse. A model for high-incidence spontaneous lymphoma and leukemia of early B cells. J Exp Med. 1988;167(2):353-71.
82. Winkler R, Piskor EM, Kosan C. Lessons from Using Genetically Engineered Mouse Models of MYC-Induced Lymphoma. Cells. 2022;12(1).
83. Rempel RE, Jiang X, Fullerton P, Tan TZ, Ye J, Lau JA, et al. Utilization of the Eμ-Myc Mouse to Model Heterogeneity of Therapeutic Response. Molecular Cancer Therapeutics. 2014;13(12):3219-29.
84. Strasser A, Harris AW, Bath ML, Cory S. Novel primitive lymphoid tumours induced in transgenic mice by cooperation between myc and bcl-2. Nature. 1990;348(6299):331-3.
85. Lefebure M, Tothill RW, Kruse E, Hawkins ED, Shortt J, Matthews GM, et al. Genomic characterisation of Eμ-Myc mouse lymphomas identifies Bcor as a Myc co-operative tumour-suppressor gene. Nat Commun. 2017;8:14581.
86. Wendel HG, Silva RL, Malina A, Mills JR, Zhu H, Ueda T, et al. Dissecting eIF4E action in tumorigenesis. Genes Dev. 2007;21(24):3232-7.
87. Wall M, Poortinga G, Stanley KL, Lindemann RK, Bots M, Chan CJ, et al. The mTORC1 inhibitor everolimus prevents and treats Eμ-Myc lymphoma by restoring oncogene-induced senescence. Cancer Discov. 2013;3(1):82-95.
88. Oh DH, Ma X, Hogg SJ, He J, Kearney C, Brasacchio D, et al. Rationally designed chimeric PI3K-BET bromodomain inhibitors elicit curative responses in MYC-driven lymphoma. Proc Natl Acad Sci U S A. 2023;120(36):e2306414120.
89. Liu Y, Wu W, Cai C, Zhang H, Shen H, Han Y. Patient-derived xenograft models in cancer therapy: technologies and applications. Signal Transduction and Targeted Therapy. 2023;8(1):160.
90. Chapuy B, Cheng H, Watahiki A, Ducar MD, Tan Y, Chen L, et al. Diffuse large B-cell lymphoma patient-derived xenograft models capture the molecular and biological heterogeneity of the disease. Blood. 2016;127(18):2203-13.
91. Zhang L, Nomie K, Zhang H, Bell T, Pham L, Kadri S, et al. B-Cell Lymphoma Patient-Derived Xenograft Models Enable Drug Discovery and Are a Platform for Personalized Therapy. Clin Cancer Res. 2017;23(15):4212-23.
92. Quail DF, Joyce JA. Microenvironmental regulation of tumor progression and metastasis. Nat Med. 2013;19(11):1423-37.
93. Scott DW, Gascoyne RD. The tumour microenvironment in B cell lymphomas. Nature Reviews Cancer. 2014;14(8):517-34.

94. He X, Xu C. Immune checkpoint signaling and cancer immunotherapy. Cell Research. 2020;30(8):660-9.
95. Staudt LM. Oncogenic activation of NF-kappaB. Cold Spring Harb Perspect Biol. 2010;2(6):a000109.
96. Viganò E, Duns G, Ennishi D, Gascoyne RD, Morin RD, Scott DW, Steidl C. Recurrent IL4R Somatic Mutations in Diffuse Large B-Cell Lymphoma Lead to an Altered Gene Expression Profile and Changes in Tumor Microenvironment Composition. Blood. 2018;132:669.
97. Gupta M, Stenson M, Han JJ, Maurer MJ, Wellik L, Ziesmer SC, et al. Elevated Serum IL-10 Levels in Patients with Diffuse Large B Cell Lymphoma: A Mechanism of Aberrant JAK2 Kinase Activation. Blood. 2011;118(21):960-.
98. Li J-m, Xu Z-z, Wang A-h, Hu J. Activation of PI3K/Akt/mTOR Pathway in Diffuse Large B-Cell Lymphomas: Clinical Significance and Inhibitory Effect by Rituximab. Blood. 2009;114(22):1934.
99. Newman AM, Steen CB, Liu CL, Gentles AJ, Chaudhuri AA, Scherer F, et al. Determining cell type abundance and expression from bulk tissues with digital cytometry. Nature Biotechnology. 2019;37(7):773-82.
100. Ciavarella S, Vegliante MC, Fabbri M, De Summa S, Melle F, Motta G, et al. Dissection of DLBCL microenvironment provides a gene expression-based predictor of survival applicable to formalin-fixed paraffin-embedded tissue. Ann Oncol. 2018;29(12):2363-70.
101. Steen CB, Luca BA, Esfahani MS, Azizi A, Sworder BJ, Nabet BY, et al. The landscape of tumor cell states and ecosystems in diffuse large B cell lymphoma. Cancer Cell. 2021;39(10):1422-37.e10.
102. Kotlov N, Bagaev A, Revuelta MV, Phillip JM, Cacciapuoti MT, Antysheva Z, et al. Clinical and Biological Subtypes of B-cell Lymphoma Revealed by Microenvironmental Signatures. Cancer Discov. 2021;11(6):1468-89.
103. Santinon F, Young YK, Del Rincón SV, Mann KK. Analyzing the Tumor-Immune Microenvironment by Flow Cytometry. Methods Mol Biol. 2023;2614:17-36.
104. Xu Y, Kroft SH, McKenna RW, Aquino DB. Prognostic significance of tumour-infiltrating T lymphocytes and T-cell subsets in de novo diffuse large B-cell lymphoma: a multiparameter flow cytometry study. Br J Haematol. 2001;112(4):945-9.
105. Keane C, Gill D, Vari F, Cross D, Griffiths L, Gandhi M. CD4(+) tumor infiltrating lymphocytes are prognostic and independent of R-IPI in patients with DLBCL receiving R-CHOP chemo-immunotherapy. Am J Hematol. 2013;88(4):273-6.
106. Chen Z, Deng X, Ye Y, Gao L, Zhang W, Liu W, Zhao S. Novel risk stratification of de novo diffuse large B cell lymphoma based on tumour-infiltrating T lymphocytes evaluated by flow cytometry. Ann Hematol. 2019;98(2):391-9.
107. Chen Z, Deng X, Ye Y, Zhang W, Liu W, Zhao S. Flow Cytometry-Assessed PD1/PDL1 Status in Tumor-Infiltrating Lymphocytes: A Link With the Prognosis of Diffuse Large B-Cell Lymphoma. Front Oncol. 2021;11:687911.
108. Yu T, Xu-Monette ZY, Lagoo A, Shuai W, Wang B, Neff J, et al. Flow cytometry quantification of tumor-infiltrating lymphocytes to predict the survival of patients with diffuse large B-cell lymphoma. Front Immunol. 2024;15:1335689.

109. Liu M, Bertolazzi G, Sridhar S, Lee RX, Jaynes P, Mulder K, et al. Spatially-resolved transcriptomics reveal macrophage heterogeneity and prognostic significance in diffuse large B-cell lymphoma. Nature Communications. 2024;15(1):2113.
110. Dai L, Fan G, Xie T, Li L, Tang L, Chen H, et al. Single-cell and spatial transcriptomics reveal a high glycolysis B cell and tumor-associated macrophages cluster correlated with poor prognosis and exhausted immune microenvironment in diffuse large B-cell lymphoma. Biomarker Research. 2024;12(1):58.
111. Matias A, Suvi-Katri L, Oscar B, Satu M, Judit Mészáros J, Marja-Liisa K-L, et al. Immune cell constitution in the tumor microenvironment predicts the outcome in diffuse large B-cell lymphoma. Haematologica. 2021;106(3):718-29.
112. Xu-Monette ZY, Xiao M, Au Q, Padmanabhan R, Xu B, Hoe N, et al. Immune Profiling and Quantitative Analysis Decipher the Clinical Role of Immune-Checkpoint Expression in the Tumor Immune Microenvironment of DLBCL. Cancer Immunol Res. 2019;7(4):644-57.
113. Apollonio B, Spada F, Petrov N, Cozzetto D, Papazoglou D, Jarvis P, et al. Tumor-activated lymph node fibroblasts suppress T cell function in diffuse large B cell lymphoma. J Clin Invest. 2023;133(13).
114. Wright KT, Weirather JL, Jiang S, Kao KZ, Sigal Y, Giobbie-Hurder A, et al. Diffuse large B-cell lymphomas have spatially defined, tumor immune microenvironments revealed by high-parameter imaging. Blood Adv. 2023;7(16):4633-46.
115. Reiss DJ, Nakayama Y, Weng AP, Stokes ME, Sehn L, Steidl C, et al. High-plex imaging and cellular neighborhood spatial analysis reveals multiple immune escape and suppression patterns in diffuse large B-cell lymphoma. Leukemia. 2024;38(5):1164-8.
116. Roider T, Baertsch MA, Fitzgerald D, Vöhringer H, Brinkmann BJ, Czernilofsky F, et al. Multimodal and spatially resolved profiling identifies distinct patterns of T cell infiltration in nodal B cell lymphoma entities. Nature Cell Biology. 2024;26(3):478-89.
117. Godfrey J, Chen X, Sunseri N, Cooper A, Yu J, Varlamova A, et al. TIGIT is a key inhibitory checkpoint receptor in lymphoma. J Immunother Cancer. 2023;11(6).
118. Ennishi D, Healy S, Bashashati A, Saberi S, Hother C, Mottok A, et al. TMEM30A loss-of-function mutations drive lymphomagenesis and confer therapeutically exploitable vulnerability in B-cell lymphoma. Nature Medicine. 2020;26(4):577-88.
119. Nicola MH, Preeta D, Nicolas JD, Svetlana PC, Achsah DK. The Type I and Type II Receptor Complexes for IL-4 and IL-13 Differentially Regulate Allergic Lung Inflammation. In: Celso P, editor. Allergic Diseases. Rijeka: IntechOpen; 2012. p. Ch. 3.
120. Lupardus PJ, Birnbaum ME, Garcia KC. Molecular basis for shared cytokine recognition revealed in the structure of an unusually high affinity complex between IL-13 and IL-13Ralpha2. Structure. 2010;18(3):332-42.
121. McCormick SM, Heller NM. Commentary: IL-4 and IL-13 receptors and signaling. Cytokine. 2015;75(1):38-50.
122. Smerz-Bertling C, Duschl A. Both Interleukin 4 and Interleukin 13 Induce Tyrosine Phosphorylation of the 140-kDa Subunit of the Interleukin 4 Receptor (∗). Journal of Biological Chemistry. 1995;270(2):966-70.
123. Mandal PK, Morlacchi P, Knight JM, Link TM, Lee GRt, Nurieva R, et al. Targeting the Src Homology 2 (SH2) Domain of Signal Transducer and Activator of Transcription 6 (STAT6) with Cell-Permeable, Phosphatase-Stable Phosphopeptide Mimics Potently

Inhibits Tyr641 Phosphorylation and Transcriptional Activity. J Med Chem. 2015;58(22):8970-84.
124. Ryan JJ, McReynolds LJ, Huang H, Nelms K, Paul WE. Characterization of a mobile Stat6 activation motif in the human IL-4 receptor. J Immunol. 1998;161(4):1811-21.
125. Li J, Rodriguez JP, Niu F, Pu M, Wang J, Hung L-W, et al. Structural basis for DNA recognition by STAT6. Proceedings of the National Academy of Sciences. 2016;113(46):13015-20.
126. Chen HC, Reich NC. Live cell imaging reveals continuous STAT6 nuclear trafficking. J Immunol. 2010;185(1):64-70.
127. Gingras S, Simard J, Groner B, Pfitzner E. p300/CBP is required for transcriptional induction by interleukin-4 and interacts with Stat6. Nucleic Acids Research. 1999;27(13):2722-9.
128. Litterst CM, Pfitzner E. Transcriptional Activation by STAT6 Requires the Direct Interaction with NCoA-1*. Journal of Biological Chemistry. 2001;276(49):45713-21.
129. Goenka S, Kaplan MH. Transcriptional regulation by STAT6. Immunologic Research. 2011;50(1):87-96.
130. Mentz M, Keay W, Strobl CD, Antoniolli M, Adolph L, Heide M, et al. PARP14 is a novel target in STAT6 mutant follicular lymphoma. Leukemia. 2022;36(9):2281-92.
131. Wurster AL, Rodgers VL, White MF, Rothstein TL, Grusby MJ. Interleukin-4-mediated protection of primary B cells from apoptosis through Stat6-dependent up-regulation of Bcl-xL. J Biol Chem. 2002;277(30):27169-75.
132. Pesu M, Takaluoma K, Aittomäki S, Lagerstedt A, Saksela K, Kovanen PE, Silvennoinen O. Interleukin-4-induced transcriptional activation by stat6 involves multiple serine/threonine kinase pathways and serine phosphorylation of stat6. Blood. 2000;95(2):494-502.
133. Kaplan MH, Schindler U, Smiley ST, Grusby MJ. Stat6 is required for mediating responses to IL-4 and for development of Th2 cells. Immunity. 1996;4(3):313-9.
134. Maier E, Duschl A, Horejs-Hoeck J. STAT6-dependent and -independent mechanisms in Th2 polarization. Eur J Immunol. 2012;42(11):2827-33.
135. Spence S, Fitzsimons A, Boyd CR, Kessler J, Fitzgerald D, Elliott J, et al. Suppressors of cytokine signaling 2 and 3 diametrically control macrophage polarization. Immunity. 2013;38(1):66-78.
136. Gaydosik AM, Queen DS, Trager MH, Akilov OE, Geskin LJ, Fuschiotti P. Genome-wide transcriptome analysis of the STAT6-regulated genes in advanced-stage cutaneous T-cell lymphoma. Blood. 2020;136(15):1748-59.
137. Wang X, Li Y, Luo D, Wang X, Zhang Y, Liu Z, et al. Lyn regulates mucus secretion and MUC5AC via the STAT6 signaling pathway during allergic airway inflammation. Scientific Reports. 2017;7(1):42675.
138. Büttner C, Skupin A, Rieber EP. Transcriptional activation of the type I collagen genes COL1A1 and COL1A2 in fibroblasts by interleukin-4: analysis of the functional collagen promoter sequences. J Cell Physiol. 2004;198(2):248-58.
139. Ritz O, Rommel K, Dorsch K, Kelsch E, Melzner J, Buck M, et al. STAT6-mediated BCL6 repression in primary mediastinal B-cell lymphoma (PMBL). Oncotarget. 2013;4(7):1093-102.

140. Häberle MT, Kelsch E, Dorsch K, Möller P, Ritz O. Knock-down of BCL6 / STAT6 sensitizes primary B cell lymphoma cells for treatment with current therapeutic agents. Oncoscience. 2014;1(4):283-6.
141. Ritz O, Guiter C, Castellano F, Dorsch K, Melzner J, Jais JP, et al. Recurrent mutations of the STAT6 DNA binding domain in primary mediastinal B-cell lymphoma. Blood. 2009;114(6):1236-42.
142. Chapuy B, Stewart C, Dunford AJ, Kim J, Wienand K, Kamburov A, et al. Genomic analyses of PMBL reveal new drivers and mechanisms of sensitivity to PD-1 blockade. Blood. 2019;134(26):2369-82.
143. Viganò E, Gunawardana J, Mottok A, Van Tol T, Mak K, Chan FC, et al. Somatic IL4R mutations in primary mediastinal large B-cell lymphoma lead to constitutive JAK-STAT signaling activation. Blood. 2018;131(18):2036-46.
144. Yildiz M, Li H, Bernard D, Amin NA, Ouillette P, Jones S, et al. Activating STAT6 mutations in follicular lymphoma. Blood. 2015;125(4):668-79.
145. Okosun J, Bödör C, Wang J, Araf S, Yang CY, Pan C, et al. Integrated genomic analysis identifies recurrent mutations and evolution patterns driving the initiation and progression of follicular lymphoma. Nat Genet. 2014;46(2):176-81.
146. Skinnider BF, Elia AJ, Gascoyne RD, Patterson B, Trumper L, Kapp U, Mak TW. Signal transducer and activator of transcription 6 is frequently activated in Hodgkin and Reed-Sternberg cells of Hodgkin lymphoma. Blood. 2002;99(2):618-26.
147. Baus D, Nonnenmacher F, Jankowski S, Döring C, Bräutigam C, Frank M, et al. STAT6 and STAT1 are essential antagonistic regulators of cell survival in classical Hodgkin lymphoma cell line. Leukemia. 2009;23(10):1885-93.
148. Alig SK, Shahrokh Esfahani M, Garofalo A, Li MY, Rossi C, Flerlage T, et al. Distinct Hodgkin lymphoma subtypes defined by noninvasive genomic profiling. Nature. 2024;625(7996):778-87.
149. Sharma M, Leung D, Momenilandi M, Jones LCW, Pacillo L, James AE, et al. Human germline heterozygous gain-of-function STAT6 variants cause severe allergic disease. J Exp Med. 2023;220(5).
150. Minskaia E, Maimaris J, Jenkins P, Albuquerque AS, Hong Y, Eleftheriou D, et al. Autosomal Dominant STAT6 Gain of Function Causes Severe Atopy Associated with Lymphoma. J Clin Immunol. 2023;43(7):1611-22.
151. Zou S, Liu B, Feng Y. CCL17, CCL22 and their receptor CCR4 in hematologic malignancies. Discover Oncology. 2024;15(1):412.
152. Weigert M, Schmidt U, editors. Nuclei Instance Segmentation and Classification in Histopathology Images with Stardist. 2022 IEEE International Symposium on Biomedical Imaging Challenges (ISBIC); 2022 28-31 March 2022.
153. Bankhead P, Loughrey MB, Fernández JA, Dombrowski Y, McArt DG, Dunne PD, et al. QuPath: Open source software for digital pathology image analysis. Scientific Reports. 2017;7(1):16878.
154. Greenwald NF, Miller G, Moen E, Kong A, Kagel A, Dougherty T, et al. Whole-cell segmentation of tissue images with human-level performance using large-scale data annotation and deep learning. Nat Biotechnol. 2022;40(4):555-65.

155. Goldsborough T, O'Callaghan A, Inglis F, Leplat L, Filby A, Bilen H, Bankhead P. A novel channel invariant architecture for the segmentation of cells and nuclei in multiplexed images using InstanSeg. bioRxiv. 2024:2024.09.04.611150.
156. Dayao MT, Brusko M, Wasserfall C, Bar-Joseph Z. Membrane marker selection for segmenting single cell spatial proteomics data. Nature Communications. 2022;13(1):1999.
157. Zhao Y, Shen M, Wu L, Yang H, Yao Y, Yang Q, et al. Stromal cells in the tumor microenvironment: accomplices of tumor progression? Cell Death & Disease. 2023;14(9):587.
158. Jenkins L, Jungwirth U, Avgustinova A, Iravani M, Mills A, Haider S, et al. Cancer-Associated Fibroblasts Suppress CD8+ T-cell Infiltration and Confer Resistance to Immune-Checkpoint Blockade. Cancer Res. 2022;82(16):2904-17.
159. Mariathasan S, Turley SJ, Nickles D, Castiglioni A, Yuen K, Wang Y, et al. TGFβ attenuates tumour response to PD-L1 blockade by contributing to exclusion of T cells. Nature. 2018;554(7693):544-8.
160. Santiago R, Johnson N, Dmitrienko S, Papadakis A, Benlimame N, Mercier F, et al. Changes in Tumor Immune Micro-Environment in Diffuse Large B-Cell Lymphoma (DLBCL): A Comparative Study of Relapsed Versus Diagnostic DLBCL. Blood. 2019;134(Supplement_1):3968-.
161. Takeuchi I, Yanagi K, Takada S, Uchiyama T, Igarashi A, Motomura K, et al. STAT6 gain-of-function variant exacerbates multiple allergic symptoms. Journal of Allergy and Clinical Immunology. 2023;151(5):1402-9.e6.
162. Kindon N, Andrews G, Baxter A, Cheshire D, Hemsley P, Johnson T, et al. Discovery of AZD-2098 and AZD-1678, Two Potent and Bioavailable CCR4 Receptor Antagonists. ACS Med Chem Lett. 2017;8(9):981-6.
163. Viney JM, Andrew DP, Phillips RM, Meiser A, Patel P, Lennartz-Walker M, et al. Distinct conformations of the chemokine receptor CCR4 with implications for its targeting in allergy. J Immunol. 2014;192(7):3419-27.
164. Imai T, Chantry D, Raport CJ, Wood CL, Nishimura M, Godiska R, et al. Macrophage-derived chemokine is a functional ligand for the CC chemokine receptor 4. J Biol Chem. 1998;273(3):1764-8.
165. Lin R, Choi YH, Zidar DA, Walker JKL. β-Arrestin-2-Dependent Signaling Promotes CCR4-mediated Chemotaxis of Murine T-Helper Type 2 Cells. Am J Respir Cell Mol Biol. 2018;58(6):745-55.
166. Perros F, Hoogsteden HC, Coyle AJ, Lambrecht BN, Hammad H. Blockade of CCR4 in a humanized model of asthma reveals a critical role for DC-derived CCL17 and CCL22 in attracting Th2 cells and inducing airway inflammation. Allergy. 2009;64(7):995-1002.
167. Tang J-T, Gao K-C, Zhang Y, Zhou X-Y, Yang L-H, Kuang Y-Q, Li Y-Y. ERK/STAT3 activation through CCL17/CCR4 axis-mediated type 2 cytokine-involved signaling pathways in Th2 cells regulates cutaneous drug reactions. International Immunopharmacology. 2024;130:111712.
168. Liu LB, Xie F, Chang KK, Shang WQ, Meng YH, Yu JJ, et al. Chemokine CCL17 induced by hypoxia promotes the proliferation of cervical cancer cell. Am J Cancer Res. 2015;5(10):3072-84.

169. Zhao H, Bo Q, Wang W, Wang R, Li Y, Chen S, et al. CCL17-CCR4 axis promotes metastasis via ERK/MMP13 pathway in bladder cancer. J Cell Biochem. 2019;120(2):1979-89.
170. Zhang A, Xu Y, Xu H, Ren J, Meng T, Ni Y, et al. Lactate-induced M2 polarization of tumor-associated macrophages promotes the invasion of pituitary adenoma by secreting CCL17. Theranostics. 2021;11(8):3839-52.
171. Goldie SJ, Cottle DL, Tan FH, Roslan S, Srivastava S, Brady R, et al. Loss of GRHL3 leads to TARC/CCL17-mediated keratinocyte proliferation in the epidermis. Cell Death & Disease. 2018;9(11):1072.
172. Marshall LA, Marubayashi S, Jorapur A, Jacobson S, Zibinsky M, Robles O, et al. Tumors establish resistance to immunotherapy by regulating T<sub>reg</sub> recruitment via CCR4. Journal for ImmunoTherapy of Cancer. 2020;8(2):e000764.
173. Higuchi T, Matsuo K, Hashida Y, Kitahata K, Ujihara T, Taniguchi A, et al. Epstein-Barr virus-positive pyothorax-associated lymphoma expresses CCL17 and CCL22 chemokines that attract CCR4-expressing regulatory T cells. Cancer Lett. 2019;453:184-92.
174. Duvic M, Pinter-Brown LC, Foss FM, Sokol L, Jorgensen JL, Challagundla P, et al. Phase 1/2 study of mogamulizumab, a defucosylated anti-CCR4 antibody, in previously treated patients with cutaneous T-cell lymphoma. Blood. 2015;125(12):1883-9.
175. Watanabe K, Gomez AM, Kuramitsu S, Siurala M, Da T, Agarwal S, et al. Identifying highly active anti-CCR4 CAR T cells for the treatment of T-cell lymphoma. Blood Advances. 2023;7(14):3416-30.
176. Kasamon YL, Chen H, de Claro RA, Nie L, Ye J, Blumenthal GM, et al. FDA Approval Summary: Mogamulizumab-kpkc for Mycosis Fungoides and Sézary Syndrome. Clinical Cancer Research. 2019;25(24):7275-80.
177. Nakayama S, Yokote T, Hirata Y, Iwaki K, Akioka T, Miyoshi T, et al. Aberrant expression of CCR4 in diffuse large B-cell lymphoma, not otherwise specified. Leukemia. 2013;27(12):2382-5.
178. Colombo AR, Hav M, Singh M, Xu A, Gamboa A, Lemos T, et al. Single-cell spatial analysis of tumor immune architecture in diffuse large B-cell lymphoma. Blood Adv. 2022;6(16):4675-90.
179. Joffe E, Vardhana SA, Kumar A, Abedi M, Hoeg R, Sharon E, Younes A. A phase I and randomized phase II etctn study of KW-0761 (Mogamulizumab) and MK-3475 (Pembrolizumab) in relapsed and refractory diffuse large B-cell lymphoma. Journal of Clinical Oncology. 2020;38(15_suppl):TPS8072-TPS.
180. Binnemars-Postma K, Bansal R, Storm G, Prakash J. Targeting the Stat6 pathway in tumor-associated macrophages reduces tumor growth and metastatic niche formation in breast cancer. Faseb j. 2018;32(2):969-78.
181. Li X, Han Z, Wang F, Qiao J. The STAT6 inhibitor AS1517499 reduces the risk of asthma in mice with 2,4-dinitrochlorobenzene-induced atopic dermatitis by blocking the STAT6 signaling pathway. Allergy, Asthma & Clinical Immunology. 2022;18(1):12.
182. Kim M-J, Lee Y-J, Yoon Y-S, Lim Jae H, Park E-M, Chong Young H, Kang Jihee L. A STAT6 Inhibitor AS1517499 Reduces Preventive Effects of Apoptotic Cell Instillation on

Bleomycin-Induced Lung Fibrosis by Suppressing PPARγ. Cellular Physiology and Biochemistry. 2018;45(5):1863-77.
183. Jiao B, An C, Tran M, Du H, Wang P, Zhou D, Wang Y. Pharmacological Inhibition of STAT6 Ameliorates Myeloid Fibroblast Activation and Alternative Macrophage Polarization in Renal Fibrosis. Frontiers in Immunology. 2021;12.
184. Mendoza-Rodríguez MG, Sánchez-Barrera CÁ, Callejas BE, García-Castillo V, Beristain-Terrazas DL, Delgado-Buenrostro NL, et al. Use of STAT6 Phosphorylation Inhibitor and Trimethylglycine as New Adjuvant Therapies for 5-Fluorouracil in Colitis-Associated Tumorigenesis. International Journal of Molecular Sciences. 2020;21(6):2130.
185. He K, Barsoumian HB, Puebla-Osorio N, Hu Y, Sezen D, Wasley MD, et al. Inhibition of STAT6 with Antisense Oligonucleotides Enhances the Systemic Antitumor Effects of Radiotherapy and Anti-PD-1 in Metastatic Non-Small Cell Lung Cancer. Cancer Immunol Res. 2023;11(4):486-500.